Low temperature plasma deposition of III-V semiconductors (GaN) on Si

Lakshman Srinivasan

To cite this version:

Lakshman Srinivasan. Low temperature plasma deposition of III-V semiconductors (GaN) on Si. Engineering Sciences [physics]. Institut Polytechnique de Paris, 2024. English. NNT : 2024IPPAX052 . tel-04765565

HAL Id: tel-04765565
https://theses.hal.science/tel-04765565v1

Submitted on 4 Nov 2024

INSTITUT
POLYTECHNIQUE
DE PARIS

NNT : 2024IPPAX052

Thèse de doctorat

ÉCOLE
POLYTECHNIQUE

IP PARIS

Low-temperature plasma deposition of III-V semiconductors (GaN) on Si

Thèse de doctorat de l'Institut Polytechnique de Paris
préparée à l'Ecole Polytechnique

École doctorale n°626 Institut Polytechnique de Paris (ED IP Paris)
Spécialité de doctorat : Physique

Thèse présentée et soutenue à Palaiseau, le 29/04/2024, par

LAKSHMAN SRINIVASAN

Composition du Jury:

M. Khaled HASSOUNI Professeur, Université Sorbonne Paris Nord	Rapporteur
M. Alexandre TALLAIRE Directeur de recherche, Chimie ParisTech - PSL	Rapporteur
Mme Angelique BOUSQUET Enseignant-Chercheur, Universite Clermont Auvergne	Examinateur
M. Farid MEDJDOUB Charge de recherche, IEMN, University of Lille	Examinateur
Mme Rachel OLIVER Professeur, University of Cambridge	Examinateur
M. Guillaume LOMBARDI Professeur, Université Sorbonne Paris Nord	Membre Invite
M. Pere Roca i Cabarrocas Professeur, Ecole Polytechnique	Directeur de thèse
M. Karim Ouaras Charge de recherche, Ecole Polytechnique	Co-directeur de thèse

“I learned very early the difference between knowing the name of something and knowing something.”

Richard Feynman, 1945

Acknowledgements

I am profoundly grateful to have had the unwavering support and guidance of my supervisor, Dr. Karim Ouaras, throughout this transformative journey. Karim has been more than just an academic mentor; he has been a constant source of inspiration and encouragement; more like a big brother to me. From the earliest stages of conceptualizing this project to the final revisions, his expertise, wisdom, and unwavering commitment have been instrumental in shaping both the direction and the depth of my work. Beyond his invaluable guidance in navigating the complexities of research and academia, he has also been a pillar of support during the inevitable challenges and uncertainties that arose along the way. His patience and belief in my potential have instilled in me a newfound confidence and resilience that extends far beyond the pages of this thesis. I am deeply grateful for the countless hours dedicated to reviewing drafts, providing constructive feedback, and engaging in thoughtful discussions that have enriched my understanding and strengthened my arguments. Moreover, Karim has been a source of personal inspiration, demonstrating through his own examples, the impact that dedication can have on both scholarly pursuits and interpersonal relationships. His mentorship has not only shaped my academic trajectory but has also left an indelible mark on my character and aspirations. To Karim, I extend my deepest gratitude for believing in me, for pushing me to reach beyond my comfort zone, and for fostering an environment of intellectual curiosity and growth. This thesis would not have been possible without your guidance and encouragement and for that, I am truly grateful. Anyone would be lucky to have you as their supervisor.

In the journey of completing this thesis, I've been fortunate enough to have had the guidance and support of Pere Roca, my thesis director, who has been nothing short of a father figure to me. Pere's wisdom has been a constant source of inspiration throughout this endeavor. His sharp intellect and boundless curiosity have defied time, reminding me that passion and enthusiasm know no bounds. He is a role model whom I aspire to emulate. Pere's dedication to his craft and his relentless pursuit of knowledge serve as a constant reminder of the kind of scholar and person I hope to become. It is an honor and privilege to have had him by my side on this journey, and I am profoundly grateful for his guidance and support. To Pere, I extend my deepest gratitude for believing in me, for nurturing my growth, and for inspiring me to reach beyond my perceived limitations. This thesis is a testament to your mentorship, and I am forever grateful for the profound impact you have had on my life. I will miss the long scientific discussions that we have on a regular basis.

A heartfelt thank you to the BEER group at the LPICM lab for their invaluable assistance and camaraderie throughout my research journey. John Charles, your help in automating our reactor was invaluable. You have always supported me and been kind to me. Thank you for that. Cyril, your expertise in managing the vacuum systems and reactor, coupled with your willingness to offer insights and engage in friendly chats, has been instrumental to the success of my project. Marc and Jonathan, your support throughout the tenure of my thesis have not only facilitated my experiments but have also enriched my overall experience in the lab. I am thankful for your assistance and friendship.

I would like to thank Pavel for his constant guidance and knowledge in assisting me whenever I needed. Your expertise helped me in a lot of ways and I am very grateful. I would also like to thank Abder and Fathima, even though we were from a different department, I always felt inspired by both of you. A special mention to Erik and Junkang who I admire for their sound knowledge. They have been of constant help, be it discussion, experiments or projecting ideas.

I would like to extend my thanks to Florian Hilt and Stephane Collin from IPVF for constantly guiding me through the PhD and providing support and keeping me on track whenever needed. I would like to extend my gratitude to Mirella Al Katrib and Alexandre Blaizot from IPVF for helping me with XPS and SEM characterization. For SIMS measurements, I would like to thank Francois Jomard from UVSQ.

Special mention to Laurent Invernizzi, Kristaq Gazeli, Swaminathan Prasanna and Dimitris from the lab LSPM at Villetaneuse. The two months that I spent there at the lab was an enriching experience that guided my thesis towards an extremely interesting and profound trajectory of plasma diagnostics. All of your enthusiasm and willingness was an inspiration to me. No wonder Karim speaks highly about all of you.

I would like to thank all of my friends from the lab, starting with my two officemates – Hindia and Michel. You have been a pillar of support and a constant source of happiness throughout my thesis. I would like to extend my thanks to

Lise, my partner in the III-V department. You were an inspiration to me in certain ways to push myself forward, and I wish you all the best in your thesis. Hope we always remain in touch. Others include Amir Habibi, Inaas, Christian, Chandralina, Mbaye, Mateusz, Aymeric, Guili, Monalisa, El Mehdi, Joseph, Pingping, Shiwei, Ntiin, John and Kritika. You guys made my stay here a pleasant experience. I apologize If I might have missed someone, but know that you have been an integral part in my journey.

Lastly, I would like to thank my parents, my sister and her baby Krina. Words cannot express the depth of my gratitude for your unwavering love, support, and encouragement throughout my academic journey. From the earliest days of my education to the completion of this thesis, you have been my pillars of strength, always believing in me even when I doubted myself. Your sacrifices, guidance, and boundless affection have shaped me into the person I am today, and I am endlessly thankful for your unwavering presence in my life. To my beloved sister, congratulations on the arrival of your precious newborn baby! As I embark on this milestone of completing my thesis, I am reminded of the joy and inspiration that your growing family brings to our lives. Your strength and support have been a constant source of motivation for me, and I am grateful for the bond we share. Welcoming your little one into the world fills my heart with immeasurable joy, and I am honored to be an uncle to such a beautiful soul.

Table of Contents

List of acronyms vi

Abstract vii

Résumé viii

General Introduction ix

Chapter 1 - Introduction 1

1.1 Gallium Nitride 4

1.1.1 GaN band structure & properties 4

1.1.2 GaN crystallinity 6

1.2 Processing methods for GaN growth 8

1.2.1 Conventional processing methods 8

1.2.2 Need for a low temperature growth process 10

1.2.3 Plasma assisted processing methods 10

1.3 Plasma discharge 11

1.3.1 Cold Plasmas 11

1.3.2 Low-pressure plasma systems 13

1.3.3 Reactive sputtering for GaN growth (Ar-N_2 plasma facing Ga target) 13

1.4 Building blocks & outline of this PhD 15

REFERENCES 16

Chapter 2 – Experimental Procedures and Characterization Techniques 19

2.1 Plasma based sputtering 20

2.1.1 Basics of sputtering 20

2.1.2 Sputtering deposition of GaN 21

2.1.3 Nucleation & growth 22

2.2 The Plasma PVD reactor 23

2.2.1 Reactor overview 23

2.2.2 The growth chamber 24

2.2.3 Plasma operating conditions 25

2.3 Substrates preparation 26

2.3.1 Si Substrate selection for GaN deposition 26

2.4 Material characterization 28

2.4.1 X-Ray diffraction (XRD) 28

2.4.2 Scanning electron microscopy (SEM) 30

2.4.3 Atomic force microscopy (AFM) 31

2.4.4 Transmission electron microscopy (TEM) 32

2.4.5 X-ray photoelectron spectroscopy (XPS) 33
2.4.6 Cathodoluminescence (CL) 35
2.4.7 Raman spectroscopy 37
2.4.8 Secondary ion mass spectrometry (SIMS) 38
2.4.9 Glow discharge optical emission spectroscopy (GD-OES) 39
2.5 Conclusion 40
REFERENCES 41

Chapter 3 – Plasma diagnostics 43
3.1 TALIF diagnostic: on the determination of the N-atom density 44
3.1.1 TALIF diagnostic setup 45
3.1.2 N atom density calibration using Kr gas 47
3.1.3 Fluorescence signal measurement 49
3.1.4 Fluorescence lifetime & quenching 51
3.1.5 Quadratic regime identification 52
3.1.6 N-atom density estimation 52
3.2 Microwave Interferometry (MWI): on the measurement of electron density 53
3.2.1 MWI diagnostic setup 53
3.2.2 Electron density measurements (n_e) 55
3.3 Optical emission spectroscopy (OES) 55
3.3.1 Main emission features of the plasma 56
3.3.2 Estimating the characteristic temperatures of an Ar/N_2 plasma using OES 57
3.3.2.1 Estimation of the gas temperature using rotational lines 57
3.3.2.2 Estimation of the vibrational temperature 60
3.3.2.3 Estimation of the excitation temperature 61
3.4 Plasma qualification & optimizations 63
3.4.1 Plasma stability 63
3.4.2 Plasma contamination 64
3.4.3 Plasma characteristics: density & temperatures 66
3.5 Conclusion 68
REFERENCES 70

Chapter 4 – Characterization of GaN thin films deposited on Si at room temperature 75
4.1 An overview of the properties of GaN film 77
4.2 Influence of the working pressure 79
4.2.1 Surface morphology, structure & crystalline fraction: pressure effect 80
4.2.2 Estimating the Ga atom flux and average energy at the substrate 83
4.2.3 Interdependence of the flux & energy of Ga atom on the GaN film structure – pressure effect 88
4.3 Influence of the N_2 gas flow variation 90

4.3.1 Surface morphology, structure & crystalline fraction 91
4.3.2 Interdependence of the flux & energy of Ga atoms on the GaN film structure – N_2 flow effect 93
4.4 Influence of the RF power 95
4.4.1 Surface morphology, structure & crystalline fraction 95
4.4.2 Interdependence of the flux & energy of Ga atom on the GaN film structure – RF power effect 97
4.5 Chemical composition investigation of polycrystalline GaN films 99
4.5.1 GaN surface analysis-using XPS 99
4.5.2 Composition profile analysis using XPS & SIMS 101
4.5.3 Oxygen contamination – do reactor & plasma cleaning help? 103
4.6 TEM analysis on the crystalline structure of GaN 104
4.7 Cathodoluminescence analysis of GaN films grown at room temperature 105
4.7.1 Potential origin of the GaN CL peaks in undoped GaN 106
4.7.2 Observations & analysis of the CL peaks of GaN grown at room temperature 107
REFERENCES 113

Chapter 5 – Characterization of GaN thin films on Si at various growth temperatures 118
5.1 Influence of the substrate temperature 118
5.1.1 Effect of growth temperature on the surface morphology 119
5.1.2 Effect of growth temperature on the crystalline structure 120
5.1.3 Effect of temperature on the chemical structure 121
5.1.4 Impact of growth temperature on the luminescence features of the films 123
5.2 A summary of the growth temperature series of GaN thin film deposition on Si 125
REFERENCES 127

Summary & perspectives 128
Summary 128
Perspectives 130
REFERENCES 132
Scientific contributions 133

List of acronyms

AFM atomic force microscopy

CL cathodoluminescence

EDX energy-dispersive X-ray spectroscopy

EDF energy distribution function

GaN gallium nitride

GIXRD grazing incidence x-ray diffraction

LT low temperature

MWI microwave interferometry

MOCVD metal-organic chemical vapor deposition

MBE molecular beam epitaxy

OES optical emission spectroscopy

PVD physical vapor deposition

PEM peak excitation method

RT room temperature

RF radio frequency

SEM scanning electron microscope

SIMS secondary ion mass spectrometry

TALIF two photon absorption laser induced fluorescence

TEM transmission electron microscopy

UHV ultra-high vacuum

WZ wurtzite

XPS x-ray photoelectron spectroscopy

ZB zinc blende

Abstract

The importance of the deposition of Gallium Nitride (GaN) thin films on Silicon substrates at reduced temperatures (< 500°C) stems from the increasing demand of the semiconductor industry in mitigating inherent drawbacks associated with high-temperature processing arising from the thermal mismatch between the film and the substrate. This doctoral thesis, done at LPICM in collaboration with IPVF, undertakes a comprehensive exploration of a low-temperature processing methodology, focusing on Plasma based Physical Vapor Deposition (PVD) as a promising avenue for circumventing the constraints of conventional growth techniques such as MOCVD and MBE. The newly custom-built plasma PVD reactor paves way to explore low-cost III-V deposition by plasma, which is a novel topic at the lab. The work delineates a systematic approach encompassing deposition processes, plasma diagnostics, material characterization, and growth optimization strategies for GaN films deposited at room temperature (RT). Plasma diagnostics play a pivotal role when investigating the intricate nuances of Ar-N_2 plasmas used in the deposition process. The plasma discharge is characterized via optical emission spectroscopy (OES), two-photon absorption laser-induced fluorescence (TALIF), and microwave interferometry (MWI) to obtain parameters related to plasma temperatures and density. From the plasma diagnostics, two important parameters were estimated - the flux of the sputtered Ga atoms (φ_{Ga}) and their average energy at the substrate ($\overline{E_{Ga}^{sub}}$). This allowed us to address the interplay between plasma characteristics and GaN film properties such as their growth rate and crystalline fraction. The assessment of GaN thin films deposited at room temperature was done using characterization techniques such as SEM, AFM & GIXRD, XPS and Cathodoluminescence (CL). Noteworthy findings include the successful growth of hexagonal wurtzite polycrystalline GaN exhibiting growth rates of ~ 2 Å/s and crystalline fractions of ~ 60% at an optimized sputtering condition (6.6 Pa, 40% N_2 and 100 W), elucidating the profound influence of process parameters such as the working pressure, RF power and the N_2 flow rate on the morphological, structural & optical properties. It was found that the growth rate estimated through calculations (~ 2.4 Å/s) was in good agreement with experiments, highlighting the validity of our method. Similarly, $\overline{E_{Ga}^{sub}}$ of Ga correlated well with the crystalline fraction of the GaN films. Further investigation into the influence of substrate temperature from RT to 500°C emphasized the role of thermal energy in enhancing adatom mobility and crystalline quality with the best crystalline fraction of almost ~ 95% obtained at a substrate temperature of 400°C. Overall, this doctoral thesis provides an extensive understanding of the challenges, methodologies, and advancements underpinning the low-temperature processing of GaN thin films via Plasma PVD, by offering tangible insights into its optimization and control.

Résumé

L'importance du dépôt de couches minces de Nitrure de Gallium (GaN) sur des substrats de silicium à des températures réduites (< 500°C) découle de la demande croissante de l'industrie des semi-conducteurs pour atténuer les inconvénients associés au traitement à haute température, tels que la diffusion d'atomes et les contraintes mécaniques dues à l'incompatibilité thermique entre le film et le substrat. En effet, les méthodes conventionnelles comme la MOCVD (Metal Organic Chemical Vapor Deposition) et la MBE (Molecular Beam Epitaxy) impliquent généralement des températures élevées, ce qui peut entraîner des défauts structurels et une dégradation des dispositifs. Ainsi, la recherche de méthodes alternatives de dépôt à basse température devient cruciale pour améliorer l'intégrité des dispositifs électroniques et optoélectroniques à base de GaN. Cette thèse, réalisée en collaboration avec le LPICM et l'IPVF, explore une méthodologie de croissance à basse température pour le dépôt de GaN. Elle se concentre sur le Dépôt Physique en Phase Vapeur (PVD) assisté par plasma (pulvérisation) basé sur un magnétron (RF), qui se présente comme une voie prometteuse pour contourner les limitations des techniques de croissance traditionnelles. Le réacteur PVD-plasma, récemment développé au LPICM, est conçu pour explorer le dépôt de semi-conducteurs III-V à faible coût par plasma, rendant ce projet un nouvel axe de recherche novateur au laboratoire. Ce travail repose sur une approche méthodologique systématique, intégrant la compréhension des processus de dépôt en couplant les diagnostics plasma, la caractérisation des matériaux et les stratégies d'optimisation de la croissance des films de GaN à température ambiante (RT). Les diagnostics plasma ont été déployés pour analyser le plasma Ar-N_2 utilisé. La décharge de plasma a été caractérisée par des techniques avancées telles que la spectroscopie d'émission optique (OES), la fluorescence induite par laser à deux photons (TALIF) et l'interférométrie micro-ondes (MWI). Ces techniques ont permis d'obtenir des paramètres cruciaux liés aux températures et à la densité du plasma, fournissant une compréhension approfondie des mécanismes de dépôt. Les données obtenues ont permis d'estimer deux paramètres critiques pour la croissance : le flux des atomes de Ga pulvérisés et leur énergie moyenne au niveau du substrat. Cette estimation a facilité l'étude de l'interaction entre les caractéristiques du plasma et les propriétés des films de GaN déposés, telles que le taux de croissance et la fraction cristalline. La caractérisation des films minces de GaN, déposés à température ambiante, a été réalisée à l'aide de techniques variées telles que la microscopie électronique à balayage (SEM), la microscopie à force atomique (AFM), la diffraction des rayons X en incidence rasante (GIXRD), la spectroscopie de photoélectrons X (XPS) et la cathodoluminescence (CL). Parmi les résultats notables, nous avons obtenu des couches minces de GaN polycristallin de structure wurtzite hexagonale avec des taux de croissance de ~ 2 Å/s et des fractions cristallines de ~ 60 % dans des conditions de pulvérisation optimisées : une pression de travail de 6,6 Pa, un ratio de 60/40 % Ar/N_2 et une puissance RF de 100 W. En outre, l'influence de ces paramètres a été systématiquement étudiée, mettant en évidence leur rôle crucial dans les propriétés morphologiques, structurales et optiques des films déposés.

Il a été démontré que la vitesse de croissance estimée par les calculs (~ 2,4 Å/s) concordait bien avec celle déterminée expérimentalement, confirmant l'efficacité de notre méthode. De plus, nous avons montré que l'énergie moyenne des atomes de Ga au substrat est corrélée avec la fraction cristalline des films de GaN déterminée expérimentalement. Une étude approfondie de l'influence de la température du substrat (de RT à 500°C) a révélé le rôle essentiel de l'énergie thermique dans l'amélioration de la mobilité des atomes déposés et de la qualité cristalline, la meilleure fraction cristalline de près de ~ 95% étant obtenue à une température de substrat de 400°C. Globalement, cette thèse, essentiellement expérimentale, a permis de mieux comprendre les défis, les méthodologies et les progressions qui sous-tendent le traitement à basse température des films minces de GaN par PVD-plasma. Elle offre des aperçus concrets sur l'optimisation et le contrôle de la qualité du dépôt, ouvrant ainsi la voie à des développements futurs dans le domaine des semi-conducteurs à basse température. En intégrant des diagnostics plasma avancés et des techniques de caractérisation sophistiquées, ce travail contribue à l'avancement des connaissances et des technologies dans le domaine du dépôt de GaN, avec des implications significatives pour l'industrie des semi-conducteurs.

General Introduction

Gallium Nitride (GaN) has emerged as a pivotal semiconductor material in the current industry due to its multifaceted advantages. One of its primary strengths lies in its efficiency compared to traditional silicon as GaN devices can operate at higher voltages (>1000V) and frequencies (GHz). This characteristic facilitates the development of energy-efficient electronic devices, extending battery life in smartphones and reducing electricity consumption in households. Moreover, the material's prowess in power conversion applications is noteworthy leading to the creation of smaller, lighter, and more cost-effective power electronics used in various sectors, including electric vehicles and renewable energy systems. Gallium Nitride on Silicon (GaN on Si) technology holds significant importance and offers several advantages. Firstly, silicon is widely available and relatively inexpensive, its use as a substrate would facilitate cost-effective production of GaN-based devices. This association with existing silicon manufacturing infrastructure enables seamless integration of GaN technology into established semiconductor fabrication facilities, reducing the barriers to adoption and driving scalability.

Conventional methods for growing GaN on Si substrates typically involve techniques such as metalorganic chemical vapor deposition (MOCVD) and molecular beam epitaxy (MBE). These processing methods have been widely established and explored for GaN growth on Si, each with its own set of advantages and challenges. One of the most prominent challenges with such methods is the use of high growth temperatures (700°C – 1100°C) which can be detrimental in several aspects. Among the challenges associated with the above-mentioned high temperature process, the most important one is thermal mismatch issues induced by the difference in thermal expansion coefficient between these two materials. In addition, the lattice mismatch between GaN and Si coupled to high temperature growth can even more enhanced the occurrence of cracks and defects during post-growth cooling.

One solution, considered in the present work is plasma-assisted growth processes that offer very distinct advantages compared to conventional methods, lowering the temperature being only one of the numerous benefits. Unlike high-temperature approaches, which require heating the entire substrate to allow for the dissociation of the gas precursors, plasma allows for an efficient dissociation of gases by electron impact at room temperature, resulting in more efficient energy transfer and lower material temperatures. This enables processing at significantly reduced temperatures. Furthermore, plasma processing allows precise control over ion energy and flux, offering an extra parameter to provide energy to the growing film. In addition, plasma can be used for performing in situ cleaning of the substrate, allowing reduction in the number of processing steps involved in device production. It also enables the use of low gas/precursor inputs; especially physical vapor deposition (PVD) which is easily scalable as it is already widely spread in the semiconductor industry. If one talks about thin films and its crystalline quality, polycrystalline and amorphous films may find attractive applications, which are not native to epitaxial films. Hence, it could be interesting to explore such avenues. In this work, we developed a new reactor that aims at this purpose. It relies on plasma based PVD, i.e. reactive sputtering to deposit GaN on Si substrates. Starting from scratch, we developed the reactor and then explore its capability in producing GaN thin films. We explore the influence of process parameters such as the working pressure, N_2 flow rate and the RF power on the GaN thin film deposition at room temperature (without intentionally heating the Si substrates). This thesis marks the initial phase in a broader pursuit undertaken at LPICM aimed at achieving epitaxial growth of GaN on Si at reduced temperatures. The approach commenced with a systematic investigation into room temperature growth to discern and characterize the underlying conditions, followed by a gradual integration of heating to enhance the film quality. The primary objective is to delve into the fundamental aspects governing GaN growth, iteratively refining deposition conditions to pinpoint optimal parameters while minimizing temperature requirements. Equal importance has been given towards the characterization of both the plasma discharge (Ar-N_2 plasmas) and the GaN thin film thereby emphasizing on the influence of plasma parameters towards understanding the growth mechanisms of the GaN layer in terms of morphology & crystalline structure.

The thesis is composed of five chapters:

Chapter 1 serves as an introduction to the focus material, Gallium Nitride (GaN), providing an overview of its properties, advantages, and applications. It discusses the significance of crystalline quality and outlines epitaxial and polycrystalline thin film structures. The chapter also delves into the different growth processes for GaN thin films, emphasizing the need for low-temperature methods and introducing plasma-assisted physical vapor deposition as a potential solution. Additionally, it introduces plasma discharge basics, focusing on low-pressure cold plasma systems and an Ar-N_2 plasma system. Lastly, it outlines the structure of the thesis and previews the core chapters.

Chapter 2 details the process and experimental procedures for GaN thin films deposition. It introduces the basics of sputtering process, and presents the new plasma PVD reactor system that was fully designed and developed at LPICM. The chapter details the specifics of the plasma reactor, its main components and discuss GaN growth on various silicon substrates. It also introduces the solid-state characterization techniques used for GaN film properties assessment such as SEM, XRD, XPS and cathodoluminescence (CL).

The core of this doctoral work, that encompasses Chapter 3 to 5, is illustrated in Figure 1. The three constituting blocks were consecutively carried out to eventually reach one goal: achieving a high crystalline quality GaN films that could be obtained at substrate temperatures as low as possible using the plasma PVD growth method.

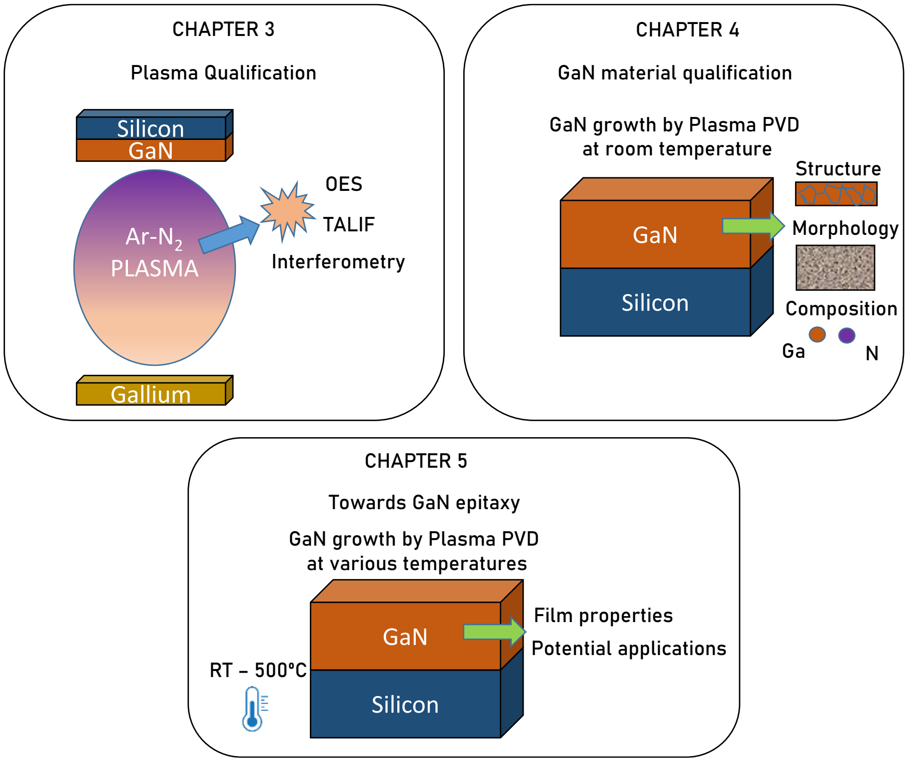

Figure 1: Different building blocks of the PhD thesis.

Chapter 3 focuses on presenting a comprehensive analysis of the Ar-N_2 plasma (facing the Ga target) under deposition conditions. It first provides a short literature overview of various existing plasma diagnostic techniques , then elaborates the one used in the present thesis, namely two-photon absorption laser-induced fluorescence (TALIF), microwave interferometry (MWI), and optical emission spectroscopy (OES), that were respectively used to determine the absolute N-atoms density, electron density and plasma characteristic temperatures (T_{gas}, T_{vib}, T_{exc}). The chapter concludes with a discussion on plasma stability, density, and temperature qualification, emphasizing the critical role of these parameters in optimizing the plasma PVD process for GaN thin film growth.

Chapter 4 presents a comprehensive assessment of the morphological, topographical, chemical and optical properties of GaN thin films deposited at room temperature via plasma PVD as a function of (i) the pressure, (ii) Ar/N_2 ratio and

(iii) plasma power, which are known to be influent parameters in sputtering discharge. Notably, the chapter deals with the correlation between the gas phase (plasma) properties to that of the grown films. In particular, it explores the influence of both Ga-atoms flux and average energy (calculated from the knowledge of plasma parameters – chapter 3) on the growth rate and crystalline fraction of the films, respectively.

Chapter 5 focuses on the characterization of GaN thin films deposited at varying substrate temperatures, highlighting the importance of temperature control in optimizing film quality. It discusses the influence of growth temperature on morphology, crystalline structure, chemical composition, and luminescence of GaN films, providing detailed insights into the effect of temperature variations on film properties. The chapter concludes with a summary of findings on the influence of temperature on the film quality and perspectives for optimizing growth conditions for GaN thin film deposition.

Finally, a summary of the main findings from this thesis and potential perspectives related to reactor improvement, growth improvement and integration towards applications are presented.

Chapter 1 - Introduction

Table of Contents

Chapter 1 - Introduction 1
1.1 Gallium Nitride 4
1.1.1 GaN band structure & properties 4
1.1.2 GaN crystallinity 6
1.2 Processing methods for GaN growth 8
1.2.1 Conventional processing methods 8
1.2.2 Need for a low temperature growth process 10
1.2.3 Plasma assisted processing methods 10
1.3 Plasma discharge 11
1.3.1 Cold Plasmas 11
1.3.2 Low-pressure plasma systems 13
1.3.3 Reactive sputtering for GaN growth (Ar-N_2 plasma facing Ga target) 13
1.4 Building blocks & outline of this PhD 15
REFERENCES 16

The first chapter comprises mainly of four parts:
We first introduce the material at focus here - Gallium nitride (GaN). We start by explaining its properties, advantages, uses and applications. A general overview of the material is presented. Then, we discuss briefly on the structure and the importance of crystalline quality of GaN giving an overview of the different crystalline structures of a thin film.
In the second section, we discuss about the different growth processes used to obtain GaN thin films. We start by introducing the conventional methods, underlie the problem at hand using such methods and focus on why we want to use low temperature methods for processing. We state that the use of a plasma assisted physical vapor deposition (PVD) could be one viable solution.
In the third section, we introduce the basics of plasma discharge, explain about low-pressure cold plasma systems and discuss about an Ar-N_2 plasma system such as ours.
At the end of this chapter, we discuss about the building blocks and outline of this PhD thesis. We give a brief overview on the core of the four chapters that are later presented in this thesis.

The current market for compound semiconductors has surpassed US$ 100 billion, and there are optimistic predictions for its significant growth in the future (US$ 150 billion by 2030) [1] with an anticipated annual growth rate of 3.8% through the forecast period [2]. The global trend for a span of 10 years has been predicted by the "Advance Materials" sector and the graph is shown on Figure 1.1.A. One can observe a dominant position of III-V semiconductors in the compound semiconductor market (Figure 1.1.A&B), which are due to several compelling reasons. First, these materials offer superior performance characteristics compared to traditional silicon-based semiconductors, including higher electron mobility, better power handling capabilities, and enhanced efficiency at high frequencies. Their unique properties make them particularly well-suited for applications in industries such as telecommunications and optoelectronics [3]. Additionally, III-V materials exhibit excellent radiation resistance, making them ideal for use in harsh environments such as space exploration and military applications [4]. Furthermore, ongoing advancements in fabrication techniques and material quality have continued to improve the performance and cost-effectiveness of III-V semiconductors, further solidifying their dominance in the market and extending their needs to several application fields.

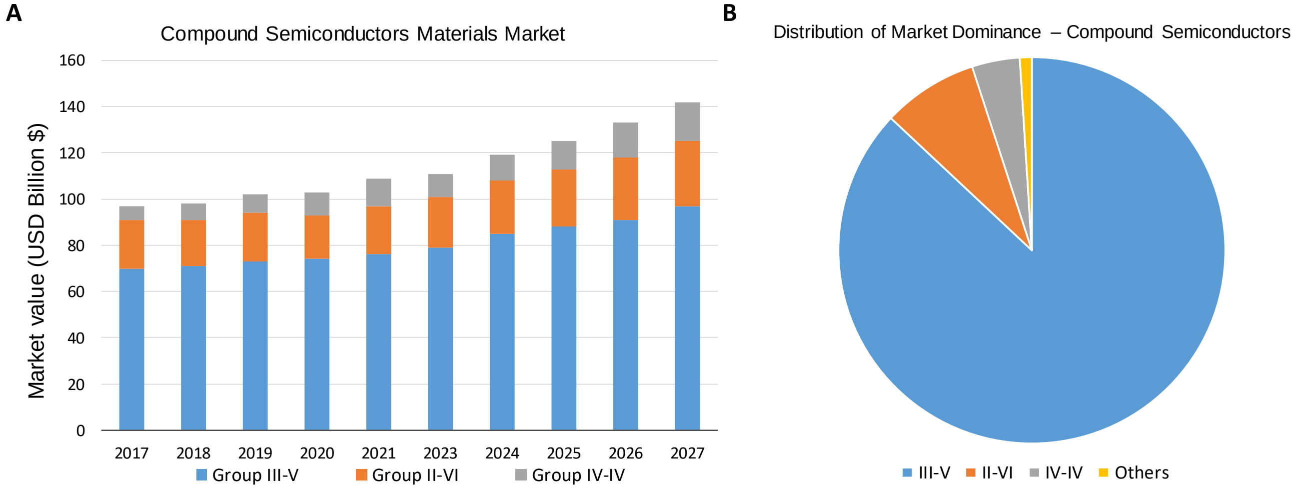

Figure 1.1: A. The global compound semiconductor industry spending over a span of 10 years B. Distribution of the market dominance of compound semiconductors. Both the graphs have been adapted and modified from the *Trends analysis for compound semiconductors* conducted by the *Grand View Research corporation* [5].

Majority of the applications that are focused today in the diverse field of micro-electronics, telecommunications and medical industry owe a part to the III-V semiconductor material group [6], [7]. The market dependence on the field of applications is shown in Figure 1.2. These applications vary from 3D Sensing for mobiles & computers to medical wearables. they possess a high electron mobility when compared to semiconductors like Silicon, which is crucial for high-speed applications such as RF amplifiers and high-frequency transistors [8]. Within the global semiconductor industry, the optoelectronics segment currently holds the largest market share accounting for about 10% of the total market [3]. The semiconductor market industry dominates the optoelectronic industry in terms of evolution and performance. In terms of electronics, the market is set to benefit from the increasing utilization of III-V materials in a range of applications, including electronic film coatings, electronic wafers, and integrated circuits.

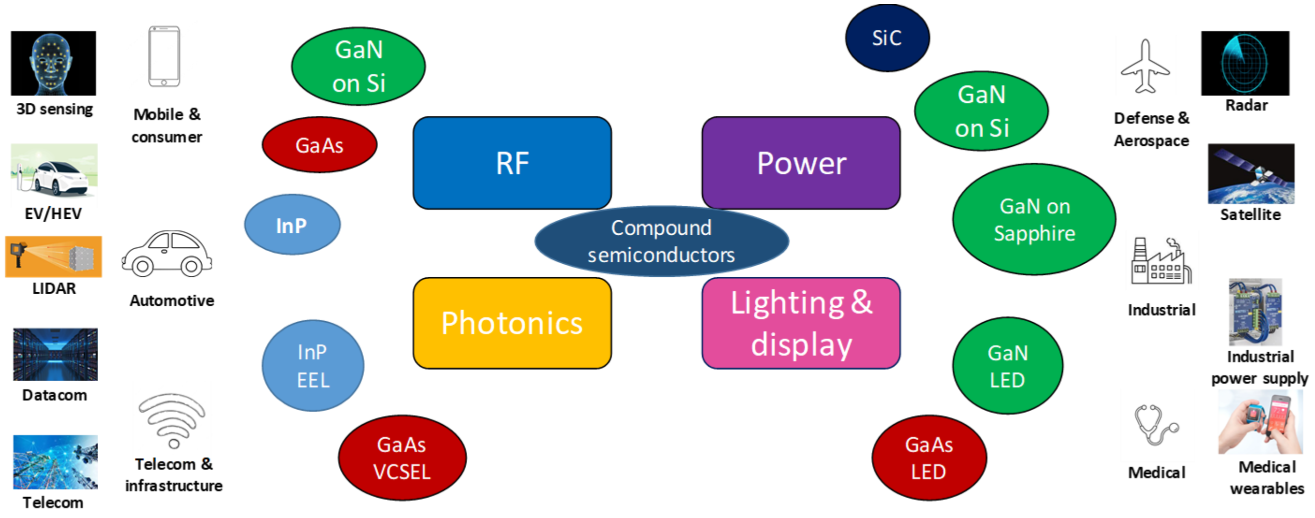

Figure 1.2: Diverse fields of applications for the compound semiconductors and their dominance on the market. Adapted from the *Yole intelligence report on compound semiconductor market evolution* [9].

Moreover, the direct bandgap of III-V materials allows for efficient light emission and absorption, which makes them ideal for optoelectronic applications like lasers, LEDs and photodetectors. III-V compounds can be engineered to have a wide range of bandgap energies by varying the elemental composition [10], [11] as shown in the bandgap engineering matrix for III-V semiconductors (Figure 1.3). This flexibility allows for the design of semiconductors tailored to specific applications, including solar cells and photodetectors that can operate across various parts of the electromagnetic spectrum [12].

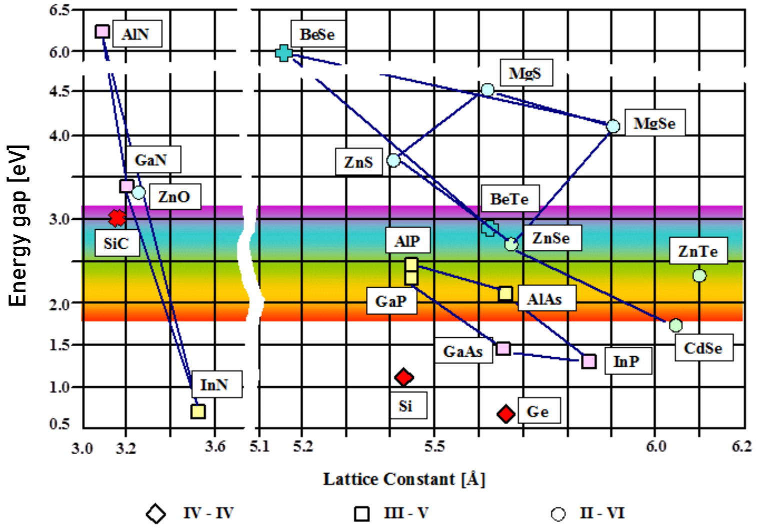

Figure 1.3: Wavelength engineering matrix. Bandgap vs lattice constant for IV-IV, III-V and II-VI semiconductors [13].

A subset of the III-V semiconductor group are the III-Nitride semiconductors. These materials are composed of elements from group III combined with Nitrogen. They possess similar properties as that of III-V, namely a direct bandgap, excellent thermal & mechanical properties [14], high radiation resistance and a high electron mobility [15]. This once again makes them a prime candidate to focus on a wide array of applications including high-speed electronics, optoelectronics and solar cells [16], [17]. One important material within the III-N semiconductor group and the main protagonist in this study is Gallium Nitride (GaN).

1.1 Gallium Nitride

Gallium nitride (GaN) is a semiconductor material with a wide bandgap that has found numerous uses across various technologies. The study of GaN began in the 1960s, but it was only from the 1980s that researchers successfully grew high-quality GaN crystals [18, p. 1], [19], [20]. The initial development laid the foundation for its commercial applications, wherein the early 1990s, researchers from Nichia in Japan, namely Shuji Nakamura, Isamu Akasaki, and Hiroshi Amano made a groundbreaking discovery [21] when they developed the first practical blue LED using GaN-based materials [20], [22], which eventually was a turning point as it completed the RGB (red, green, blue) color spectrum, allowing for the production of white LEDs, which revolutionized the lighting industry. From this point, GaN becomes vital in high-power electronics, such as power amplifiers and RF transistors, due to its high electron mobility and ability to handle high temperatures owing to its high break down voltage since voltage stresses can be significant at high temperatures. It also plays a key role in the production of high-efficiency LEDs, enabling energy-efficient lighting and displays. GaN's properties make it essential in high-frequency applications like radar and wireless communication, contributing to advancements in 5G networks and satellite technology [23]. Moreover, its high radiation resistance makes it ideal for use in space technology, while ongoing research explores its potential in emerging fields such as quantum computing. As of now, GaN's versatility and efficiency still continue to drive the innovation in electronics, optoelectronics, and beyond [24].

1.1.1 GaN band structure & properties

Group III-nitrides can form crystals in two different structures known as wurtzite and zinc blende (Figure 1.4). The main distinction between them lies in their stacking sequences. In the wurtzite phase (Figure 1.4.A), the stacking sequence is represented as ...ABAB... along the [0001] axis, whereas in the zinc-blende phase (Figure 1.4.B), the sequence is ...AABB... along the [111] axis [25]. The capital letter A represents the distinctive position of group III cations (ex: Ga^{3+}), while the capital letter B represents the position of nitrogen anions (N^{3-}) in the triangular lattice on the (0001) plane. The wurtzite hexagonal close packed structure is the most common and stable crystal structure of GaN. It is thermodynamically favored under certain growth conditions, especially in thin films and nanostructures [26].

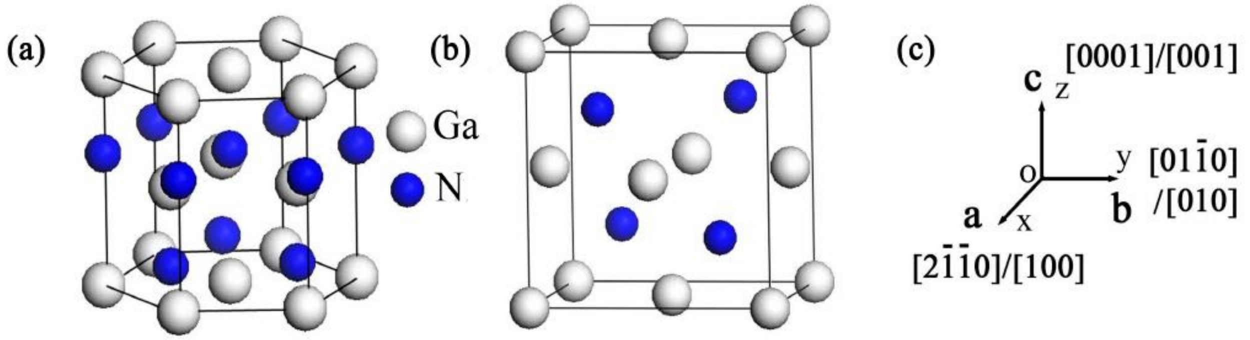

Figure 1.4: Crystal structure of: A. Wurtzite GaN ; B. Zinc-blende GaN ; C. relationship between the axes and crystallographic directions [27].

The zinc blende structure is less common for GaN but still important, especially when GaN is grown on substrates with a cubic lattice structure like silicon (Si). In the zinc blende structure, gallium and nitrogen atoms form a face-centered cubic (FCC) lattice arrangement, similar to the structure of diamond [28]. However, this structure typically has an indirect bandgap, which makes it less suitable for optoelectronic applications. It is worth noting that the choice of crystal structure depends on the growth conditions, substrate materials, and the intended application of GaN-based devices.

It is important to note that commonly, the wurtzite structure is favored for light-emitting devices, while the less common zinc blende has potential applications in areas such as spintronics and quantum computing [29].

The physical and optical properties of GaN along with some common III-V nitrides are listed in Table 1.1. GaN is a hard, brittle material with high mechanical stability. It can withstand harsh environments and is used in a variety of applications where durability is crucial [30], [31]. GaN, with its wide bandgap and low thermal expansion coefficient when compared with other III-N materials is a potentially suitable material to combine with other useful semiconductors such as Silicon.

Table 1.1: Properties of wurtzite III-N materials [31], [32], [33]

Parameter	GaN	AlN	InN
Energy band gap (**eV**) (300K)	3.39	6.2	0.7
Lattice constant a(**Å**) (300K)	3.189	3.112	3.545
Lattice constant c(**Å**) (300K)	5.186	4.982	5.703
Thermal conductivity ($\mathbf{Wcm^{-1}K^{-1}}$)	1.3	2.0	-
Thermal expansion coefficient α_a ($\mathbf{10^{-6}K^{-1}}$)	4.3	5.27	5.6
Refractive index n (**632 nm**)	2.38	2.15	3.15
Dielectric constant ε	8.9	8.5	15.3

Apart from the conventional properties listed in Table 1.1, several other important properties are important to consider: the critical breakdown voltage, the thermal conductivity, the melting point, and the electron (saturation) velocity. These allows to directly contrast the performance between semiconductors as shown in Figure 1.5 that compares the electronic properties of GaN with those of Si and SiC which are both dominant materials in the semiconductor industry. As can be clearly seen in Figure 1.5, GaN-based devices offer considerable benefits in terms of operating at high voltage, high frequency, and high temperature.

It is clear that GaN leads in high frequency and high voltage areas. SiC seems to be the superior semiconductor in the area of thermal conductivity and silicon is largely outmatched. GaN has a higher speed capability, can operate at higher voltages and can operate well at high temperatures.

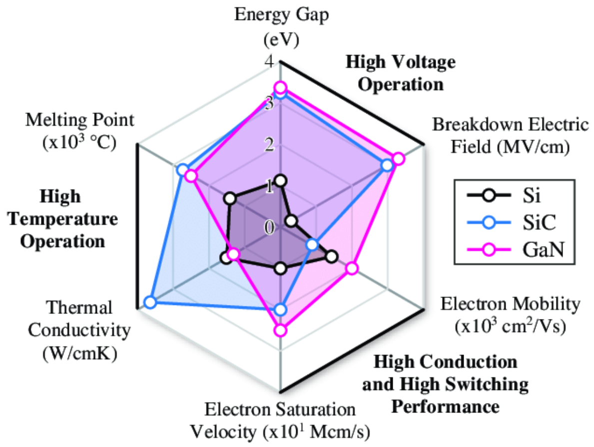

Figure 1.5: Radar chart of physical and electronic properties of GaN compared with Si and SiC [34]

Among the applications discussed above for GaN-based devices, one always considers a high quality epitaxial GaN film grown with least defects to obtain a high performance. Essentially, it is important to consider that the road to obtain a high quality epitaxial thin film often comes down with attaining a film with lower quality at first. Although, this enables one to broaden the scope of such material towards different applications. The huge success of crystalline GaN as an electronic and optical material has motivated an enormous effort to explore all aspects of the material, seek improved means of growth, and explore avenues of finding applications to fulfill necessities that does not require epi-grade layers.

1.1.2 GaN crystallinity

The crystallinity of GaN is essential because it affects its electronic, optical, and thermal properties. On the one hand, single-crystal GaN, with a well-defined crystalline structure, is highly desirable for high-performance applications due to its superior electrical and thermal properties. A high quality epitaxial film is ideally characterized by its electron diffraction pattern, which should depict growth along a single crystal plane thereby announcing the material as a single crystal layer. Figure 1.6.A shows one such example where a high quality epitaxial GaN thin film was grown on Sapphire. The epitaxial growth of electronic grade GaN (0001) onto c-plane Al_2O_3 from Figure 6.A was processed using a reactive DC-MSE (magnetron sputter epitaxy) at 700°C. The epitaxial grade quality of the film was confirmed using the selective area electron diffraction pattern (SAED) obtained from TEM micrograph as shown in Figure 6.A [35]. The SAED pattern (inset of Figure 6.A) is characteristic of a single crystal GaN epi-layer on sapphire with the relation: $[11\bar{2}0]_{GaN} \,||\, [1\bar{1}00]_{Al2O3}$ which depicts a lattice matched growth from the substrate. The lattice constants of the deposited GaN were measured via the reciprocal space mappings (RSMs) obtained from X-ray diffraction measurements, which are shown in Figure 1.6.B.

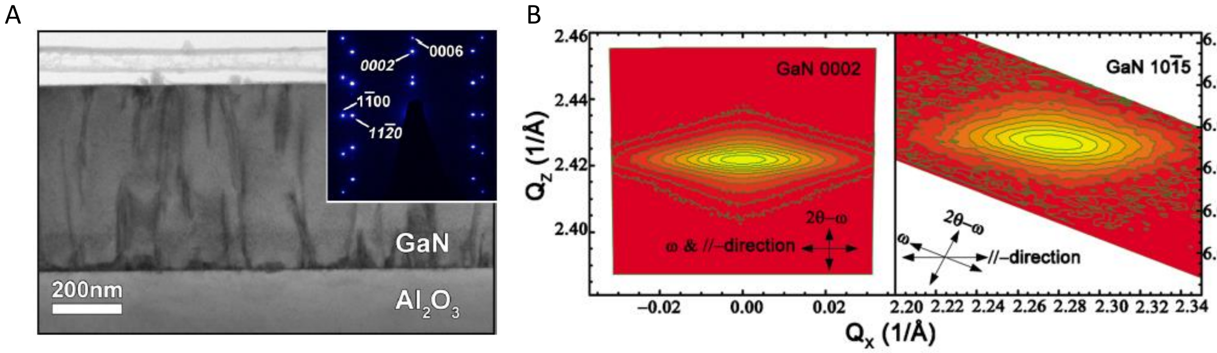

Figure 1.6: Growth of a high-quality epitaxial GaN thin film on Al_2O_3. A. XTEM micrograph and selected area electron diffraction Pattern of the film and substrate; B. Reciprocal space mapping around the GaN 0002 and $10\bar{1}5$ reflections. Figures taken from the work of M. Junaid [35].

Both these reflections recorded the same azimuth depicting a growth in the same direction. The positions from the RSM graphs yield lattice constants a and c ~3.187Å and 5.190Å which are very close to a bulk single crystal GaN thereby confirming the single crystal nature of the film. On the other hand, polycrystalline thin films are materials with a structured arrangement of multiple crystalline grains within a thin, flat layer. Unlike single-crystal thin films, which have a uniform and continuous lattice structure, polycrystalline thin films are composed of numerous small crystalline regions with different orientations. These grains are separated by grain boundaries, where the atomic arrangement transitions from one grain to another [36]. The microstructure of a polycrystalline thin film is shown in Figure 1.7 depicting the crystal orientation and grain boundaries.

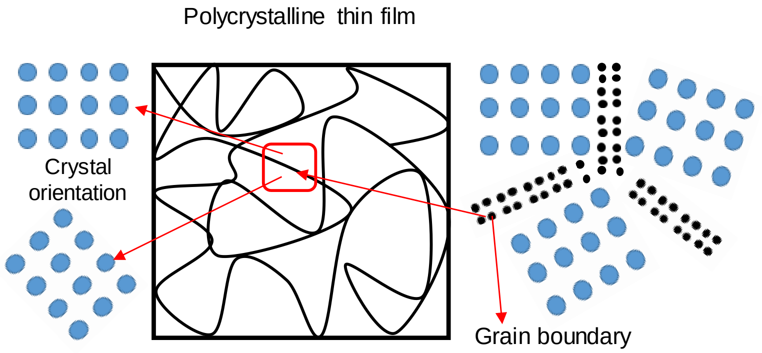

Figure 1.7: Microstructure of a polycrystalline thin film material.

Although the quality lags with respects to an epitaxial thin film, there are numerous advantages of a polycrystalline film. Indeed, they can be processed at lower growth temperatures, making them suitable for flexible electronics, displays, and sensors [37]. In addition, due to the presence of grain boundaries and imperfections, polycrystalline thin films typically have lower thermal conductivity than their single-crystal counterparts do [38] which can be advantageous in applications where thermal insulation is required.

Figure 1.8 presents the work of Jadyn K. Sprenger [39], who managed to grow polycrystalline (pc) GaN on Si (100) substrate using atomic layer deposition (ALD) at 100°C. A typical pc-GaN film has growth orientations across several crystal planes that could be identified with the grain orientation from a TEM micrograph (Figure 1.8.A) or from XRD patters (Figure 1.8.B). The XRD pattern shows the growth along several crystal facets confirming the polycrystalline nature of the thin film. The Si (100) peak has the highest intensity, as the grown GaN film is thin (<200 nm) and so the x-ray penetrates the single crystal substrate.

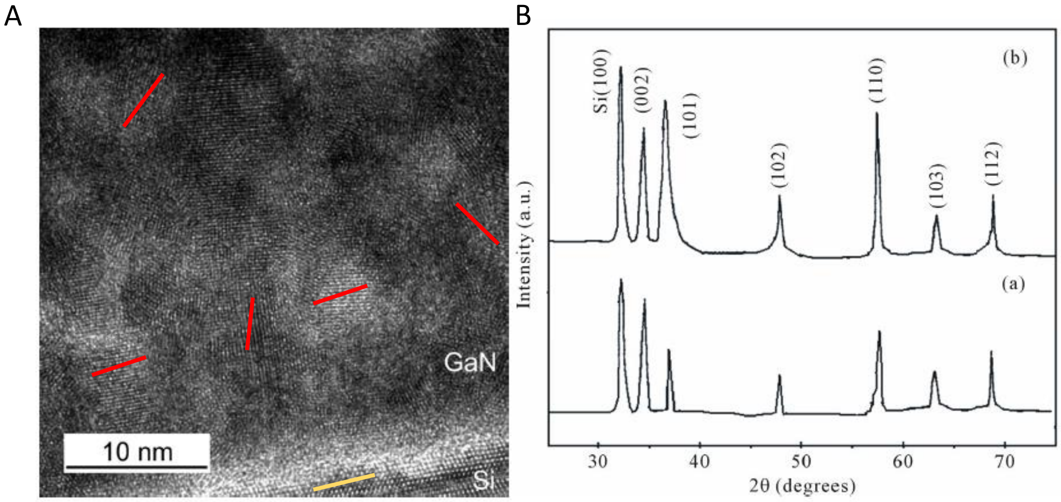

Figure 1.8: A. TEM image of GaN grown on Si (100). B. XRD pattern of a pc-GaN grown at room temperature and 100°C using ALD. Reproduced from the work of JK. Sprenger [39].

Over the past few decades, the interest in polycrystalline GaN is slowly growing since its deposition conditions are more lenient than those of epitaxial GaN. A limited amount of research has been done so far to study the growth of polycrystalline GaN using plasmas at growth temperatures ranging from room temperature up to 550°C [40], [41], [42], [43], [44], [45], [46]. Recent works by H. Wei et al (2019) [47] and P. Qui et al (2020) [48] demonstrate the use of polycrystalline GaN as an electron transport layer (ETL) in perovskite solar cells, paving its way towards photovoltaic applications. The ability to use diverse substrates, to deposit at lower temperatures opens the door to flexible devices fabrication, and to be able to grow GaN directly on the substrate without using a buffer layer, are some of the important reasons for this interest.

The quality of the GaN thin film be it epitaxial or polycrystalline entirely depends on the process method used to grow the film. Some methods can yield a high quality layer, but require more energy input to achieve such high substrate temperatures and can be complex for large scale processing. On the other hand, some processing methods could be simpler, less complex and may require less energy, but compromise on the quality of the thin film. Hence, it is essential to focus on the right processing method that can accommodate the quality of the film, energy aspects of the growth and focus on application compatibility.

1.2 Processing methods for GaN growth

1.2.1 Conventional processing methods

Conventionally, there are two common processing methods to grow high-quality GaN namely metal organic chemical vapor deposition (MOCVD) and molecular beam epitaxy (MBE).

MOCVD

Metal Organic Chemical Vapor Deposition (MOCVD) is a widely used technique for the epitaxial growth of Gallium Nitride (GaN) thin films and device structures. This process is crucial for the production of high-quality GaN materials used in various applications, including light-emitting diodes (LEDs), high-power electronics, and laser diodes. The schematic of an MOCVD system is shown in Figure 1.9.

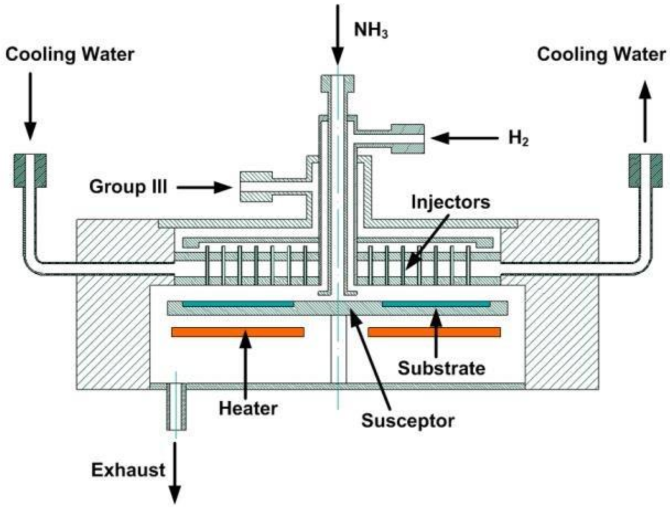

Figure 1.9: Reactor schematics of a typical MOCVD system for the deposition of a group III-nitride [49].

MOCVD is a chemical vapor deposition technique where volatile metal organic precursors (TMGa) and ammonia (NH_3) react on the substrate at elevated temperatures to produce epitaxial GaN thin films. The reaction is typically carried out in a reactor chamber with controlled temperature and pressure conditions. The substrate holder is heated to the desired growth temperature, typically in the range of 800°C to 1100°C, using resistive or induction heating elements.

During growth, the metal organic precursors adsorb onto the substrate surface releasing gallium atoms while ammonia undergoes pyrolysis to release nitrogen atoms. These atoms react on the substrate surface to form a monolayer, which then serves as the nucleation site for further GaN growth. Epitaxial GaN layers are built up one atomic layer at a time, allowing precise control over layer thickness, composition, and doping. After growth, the sample is gradually cooled to room temperature to avoid thermal stress.

This growth method has several attractive features as it provides a high growth rate ~ 7Å/s [50] and large area deposition. It provides us with an epitaxial quality material with a very low defect density (~ 10^5 cm^{-2}) and has an excellent control over film thickness, composition and doping.

Despite its attractive features, the one area, which is considered a challenge in such growth method, is the use of high temperatures for deposition, which is usually followed by a long cooling down of the sample, which might introduce a significant amount of defects in the thin film.

MBE

MBE is a highly precise thin-film deposition technique used for the epitaxial growth of various semiconductor materials. MBE is known for its ability to produce high quality, low-defect density films with atomic-level control. It operates in ultra-high vacuum conditions and utilizes atomic beams of source materials to deposit thin layers of GaN on a substrate. The process uses effusion cells to contain and heat the source materials, typically gallium and ammonia source, which is, cracked either thermally or via RF plasma. Knudsen cells or electron-beam evaporators are commonly employed. These cells control the flux of material onto the substrate. A schematic of a usual MBE system is shown in Figure 1.10. Ga and N source materials are heated in their respective effusion cells. The molecular or atomic beams impinge on the substrate surface and GaN growth occurs atom by atom to form a crystalline layer. Ga and N fluxes are carefully controlled to achieve the desired stoichiometry.

MBE allows for precise control over layer thickness and composition by adjusting the flux rates and growth temperature.

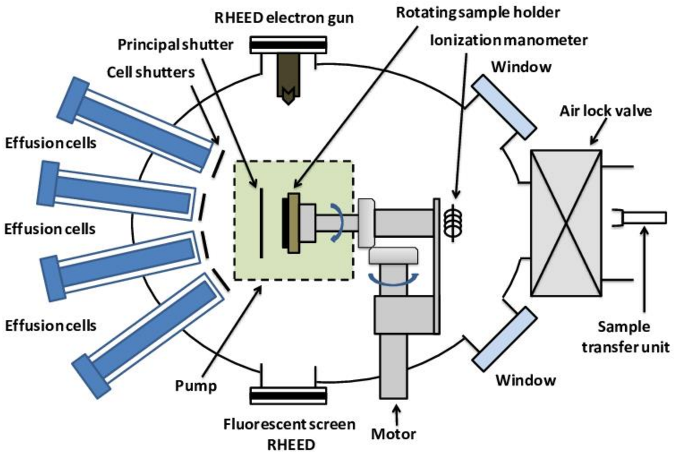

Figure 1.10: Schematic of a typical Molecular beam epitaxy (MBE) growth chamber consisting of the effusion cells with the shutters, the UHV chamber, the turbo pump, the reflected high-energy electron diffraction (RHEED) gun and the substrate equipped to a magnetic manipulator [51].

MBE has several attractive features such as its exceptional control over film thickness, stoichiometry, and crystalline quality. The ability to produce low defect density and high crystal quality and it precision to control doping profiles. Its only drawback is that the use of ultra-high vacuum (UHV) equipment is technically demanding and expensive. This limits its exposure and scalability in industry. Hence, mostly utilized in lab-scale research, molecular beam epitaxy (MBE) processes are continuously refined by researchers to cater to the increasing demands of advanced semiconductor applications.

There are several other methods such as hydride vapor phase epitaxy (HVPE) [52] , sublimation of gallium and nitrogen sources (physical vapor transport) [53] and ammonothermal growth [54] which are less extensively used when compared to the above conventional methods and hence are not widely discussed in this thesis.

Each of these methods has its advantages and disadvantages, and the choice of a specific method depends on the intended application, cost, and equipment availability. The most common point amongst all the growth methods is the use of high growth temperature (> 700°C). It is therefore important to identify to which extent such high temperatures can be detrimental to the thin film and how it can be avoided.

1.2.2 Need for a low temperature growth process

The utilization of a low-temperature process (< 500°C), relative to the conventional methods paves the way to mitigate several drawbacks, some of which are:

I) Thermal mismatch at high temperatures – it occurs when two materials with different coefficients of thermal expansion (hetero-epitaxy) are subjected to changes in temperature (usually cooling post growth) [55]. The differential expansion of materials can create strain and stress within the crystal structure [56]. These stresses can cause deformation and structural damage if they exceed the material's mechanical limits causing cracks and fractures. For instance, when considering the hetero-epitaxy of GaN on Si, one have to handle a lattice mismatch of ~ 17% which basically induce the issues illustrated in Figure 1.11.A (reveals high stacking faults in GaN near the interface with a Si substrate) If we include the post growth cooling effects by considering the thermal expansion coefficients at high temperature growth processes, then the grown layer will have cracks and defects. Consequently, low-temperature growth allows for more gradual lattice relaxation and can mitigate these issues [56]. Blah

II) Processing for temperature sensitive applications - Certain semiconductor devices and applications, such as flexible electronics and organic semiconductors are highly sensitive to temperature. Low-temperature growth is essential to ensure the functionality and integrity of these devices [57]. In some cases, semiconductor materials must be integrated with other materials to create tandem devices in which the latter material cannot withstand high temperatures. In these cases, a low-temperature growth process is necessary to achieve compatibility and integration [58].

III) Elevated energy input at high temperatures – the demands of high-energy inputs can be explained in terms of the necessary aspects that are responsible. The high temperature required in conventional growth processes (~ 1000°C) necessitates significant energy input to heat the growth chamber or substrate. Moreover, high temperatures can lead to increased material wastage through evaporation or decomposition of precursors. The importance for low energy consumption can be linked to the ecological impacts wherein reducing the energy consumption means reduced greenhouse gas emissions and less reliance on fossil fuels for energy generation, thus contributing to mitigating climate change.

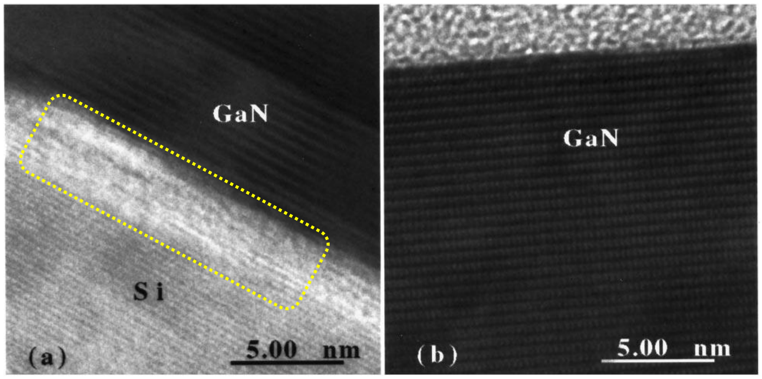

Figure 1.11: High resolution TEM micrographs of (a) GaN/Si hetero-interface and (b) GaN away from the interface[59].

As there are several drawbacks in growing semiconductors at high temperatures, we look towards processing methods that uses substrate temperatures as low as possible while ensuring and optimizing the growth of GaN thin films. Would low-pressure plasma be the solution?

1.2.3 Plasma assisted processing methods

Figure 1.12 shows the schematics of a plasma-assisted processing method. Plasma-assisted growth processes have several advantages over conventional growth methods. Plasma assistance can circumvent the requirement of high temperature processing. Conventional high-temperature methods involve heating the entire material or substrate to achieve the desired reactions or material transformation. In contrast, plasma processing primarily heats the gas, which has a much lower thermal mass. This means that the energy transfer to the material being processed is more efficient, and the overall temperature of the material can be maintained at a much lower level.

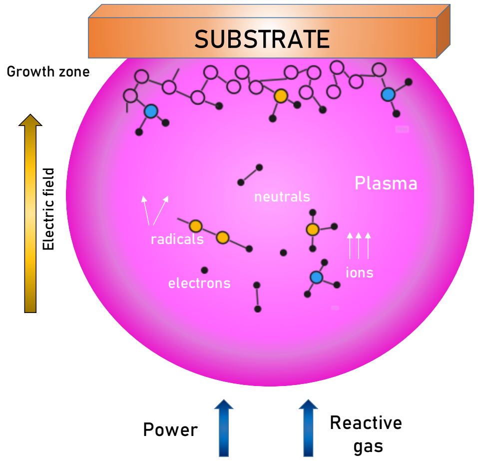

Figure 1.12: Schematics of a plasma-based processing method.

Secondly, plasma can dissociate and ionize reactive gases, allowing chemical reactions to occur at lower temperatures on the substrate. Plasma processes also offer a control over the ion energy and ion flux impinging to the substrate [60]. By adjusting the applied electric fields within the plasma processing equipment, it is possible to control the trajectories and energies of ions. This allows for precise manipulation of ion to suit the specified deposition.

There are several types of plasma-assisted processing methods such as Plasma-Enhanced Chemical Vapor Deposition (PECVD) [61], Plasma-Assisted Molecular Beam Epitaxy (PA-MBE) [62], remote plasma atomic layer deposition (RP-ALD) [63], etc. However, in this thesis, the focus is made on one such method known as Reactive Sputtering, which belong to the PVD class.

1.3 Plasma discharge

Plasmas are classified according to their density of charged particles and their temperature. They are visible on earth and in their natural state (at very high temperature) such as in lightning and polar aurora [64]. At the inverse, non-equilibrium plasmas produced in laboratory generally operate at near room temperature conditions.

Hereafter, we introduce some basics of plasma discharge trough the description of some usual parameters that define plasma systems.

1.3.1 Cold Plasmas

Cold plasma, also called non-thermal plasma, is a unique and the fourth state of matter that sets it apart from the usual (solid, liquid, and gas). Unlike traditional plasmas linked to high temperatures seen in stars or lightning, cold plasma occurs at or close to room temperature. It comprises of charged particles like electrons, ions, and excited atoms or molecules, yet it does not notably raise the temperature of its surroundings. Usually, microwave, DC and radiofrequency excitation are the two common methods used to excite and sustain plasmas.

Cold plasmas can be generated by applying an electrical discharge between two electrodes, namely the cathode and anode, within a low-pressure gas environment. The electric field accelerates the charged particles, thereby increasing their energy [65]. Due to the electrons' lower mass, they experience greater acceleration by the electric field, resulting in a temperature difference between electrons, ions, and neutrals. Cold plasmas find applications in industries such as microelectronics and surface treatment, including processes like Physical Vapor Deposition (PVD) such as ours.

Plasma density

Density in a plasma refers to the number of particles per unit volume. It comprises of ions, electrons and neutrals. In equilibrium, a plasma generally remains neutral (charge neutrality) where the following equation is obeyed:

$$n_{e^-} + n_{i^-} = n_{i^+} \tag{1.1}$$

where *n* is the density and e^-,i^-, i^+ are the electrons, negative and positive ions respectively.

The different species within the plasma are continuously engaged in interactions [66]. Each species exhibits directional motion towards the electric field and possesses its own energy, determined by its mass and collisions with the surrounding gas.

The velocity profiles of particles are described by a probability distribution function. In many cases, the distribution function is approximated using the Maxwell-Boltzmann type, which allows for the translation of the probability density function. This translation ensures that the quantity (dN ~ change in the number of particles in a given volume) of a particular species has an energy between *E* and *E* + *dE* [65]. Mathematically, it is represented as:

$$f(E) = \frac{dN}{N} = \frac{1}{\Pi^2}\frac{1}{(K_B T_j)^{\frac{3}{2}}}\exp\left(-\frac{E}{K_B T_j}\right)\sqrt{E}\,dE \tag{1.2}$$

where, the symbol k_B represents the Boltzmann constant, and T_j denotes the absolute temperature corresponding to the population *j* (where *j* can represent electrons, ions, or neutrals). As an initial approximation, equation (1.2) describes the distribution function of the species found in the plasma.

The level of ionization in a plasma, represented by the parameter *a*, quantifies the proportion of charged species relative to the total density. It is defined as follows:

$$\alpha = \frac{n_i}{n_o + n_i} \tag{1.3}$$

where n_o and n_i are the neutral and ion densities respectively.

Mean free path

The mean free path refers to the average distance that particles travel between two collisions. It is influenced by the density of particles and the likelihood of their interactions with each other [67]. Mathematically, it is represented as:

$$\lambda = \frac{1}{\sigma . n} \tag{1.4}$$

where *n* is the particle density and *σ* is the collisional cross-section. On elaborating this, we obtain a relation of the mean free path with respect to pressure:

$$\lambda = 8.34\ x\ 10^{14} p \frac{(\varphi_a + \varphi_g)^2}{4}\sqrt{1 + \frac{M_a}{M_g}} \tag{1.5}$$

The diameters (φ_a, φ_g) and atomic masses (M_a, M_g) of the atoms in the material or gas, along with the working pressure *p*, are involved in determining the mean free path.

Typically, the mean free path between an argon atom and an electron changes with pressure. At 300K and an electron energy of 10 eV, with a cross section of 1.66×10^{-16} cm^2 (value close to our reactor system), at 50 mTorr (6.6 Pa) and 100 mTorr (13.3 Pa) pressures, the mean free paths are 0.5 cm and 0.25 cm, respectively. For gallium atoms colliding with an electron, it's approximately 0.2 cm.

In plasma, electrons play a crucial role in the excitation and dissociation processes due to their lighter weight. Additionally, ion bombardment, chemical reactive recombination, and metastable energy transfer can also contribute to the emission processes. Thus, plasma emission can occur through several mechanisms listed as follows:

a) Electron impact excitation,

$$A + e^- \rightarrow A^* + e^- \tag{1.6}$$

$$A^* \rightarrow A + hv$$

b) Electron impact dissociation,

$$AB + e^- \rightarrow A^* + B + e^- \tag{1.7}$$

$$A^* \rightarrow A + hv$$

c) Ion impact processes,

$$A^+ + e^-(+M) \rightarrow A^*(+M) \tag{1.8}$$

$$A^* \rightarrow A + hv$$

d) Chemiluminescent recombination reaction,

$$A + BC \rightarrow AB^* + C \tag{1.9}$$

$$AB^* \rightarrow AB + hv$$

A, B and C are atoms or molecules, e^- is an electron, $e^-(+M)$ may be a neutral species, a negative ion, an electron plus a third body or a surface (e.g. electrodes, reactor walls or particles in the plasma) [68].

1.3.2 Low-pressure plasma systems

Plasma based systems operate over a wide range of working pressure ranging from a few Pascals to atmospheric pressure. Low pressure plasmas are generated in a vacuum based environment. They have low particle densities, resulting in a less frequent collision between charged particles/reactive species which reduces the chance of energy losses through collisions leading to a more stable and controlled plasma [69]. Typically, low pressure plasma systems are used for materials processing, thin film deposition, etching and surface modification. Some of its applications include magnetron based sputtering for thin film deposition, reactive ion etching (RIE) for semiconductor processing and PECVD for thin film growth.

High-pressure plasmas have high particle densities, more collisions and are generally used for surface cleaning, cutting, welding and dielectric barrier discharge for ozone generation (DBD) [70]. For relevance based on the context of this thesis, we will focus on low pressure reactive sputtering at a working pressure of a few Pascal, where the sputtered atoms undergo lesser collisions in the discharge leading to reduced energy losses and hence have a better probability of reaching the substrate. For GaN growth, Ar and N_2 were employed as sputtering gases, with N_2 primarily serving as the source of nitrogen atoms, and hereafter, we offer further insights on this process.

1.3.3 Reactive sputtering for GaN growth (Ar-N_2 plasma facing Ga target)

Efficient sputtering of Ga atoms is essential for the growth of our GaN thin films. The use of a pure N_2 gas for deposition usually requires an additional reactive evaporation step of the Gallium target, which makes the deposition process more complex. Moreover, if we use a pure N_2 plasma, the process of nitridation (plasma breaks apart the N_2 molecules, generating reactive nitrogen species such as atomic nitrogen and nitrogen ions) can be challenging due to the strong triple bond present in N_2 [71] [72].

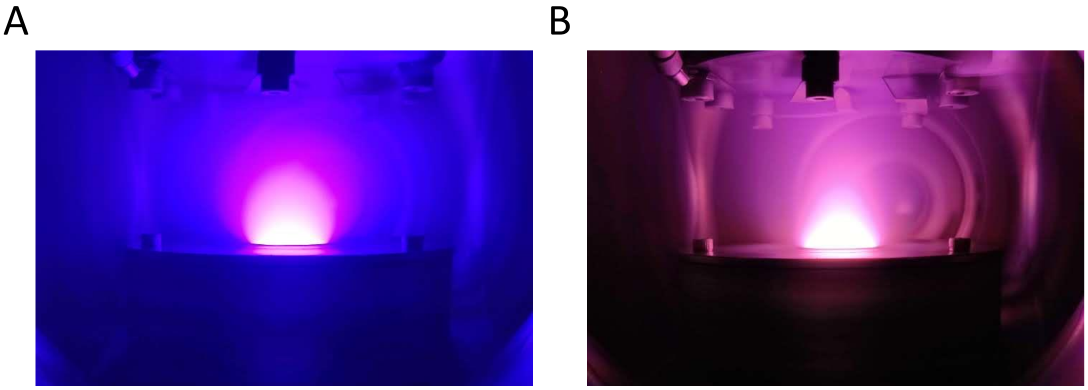

Figure 1.13: Plasma discharge from the growth chamber in our plasma PVD reactor. A. Pure Ar plasma B. Ar-N_2 plasma standard process conditions.

It is crucial to optimize the production of the active species such as nitrogen atoms in order to control surface interactions during film growth and achieve high-quality films A simple solution would be to use Argon as a sputtering gas and keep the nitrogen as a sputtering cum reactive gas. Addition of inert gases such as Ar in a pure N_2 plasma might increase the density of the active species by ionization and excitation (Penning) processes [73] and because of its heavy molecular weight, it can be primarily used for sputtering the Ga target. For the deposition of GaN thin films, in our custom-built reactor, we use both Ar and N_2 as the process gases and the corresponding plasma generated in a pure Ar and pure N_2 environment is shown in Figure 1.13.A&B.

Research works done so far in understanding GaN growth by magnetron sputtering using Ar-N_2 plasmas

Magnetron sputtering epitaxy of GaN (gallium nitride) using Ar-N_2 plasma has been an area of extensive research, focusing on improving the quality of GaN films for various applications, especially in optoelectronics and high-power electronics. Early works by F. Hernández-Maldonado et al. demonstrated the feasibility of growing GaN films using reactive sputtering with an Ar-N_2 mixture, emphasizing the significance of nitrogen incorporation and its impact on film quality and crystallinity. Subsequent studies delved deeper into optimizing the sputtering parameters.
For instance, research by K. Matsubara et al. investigated the effects of substrate temperature, RF power, and gas flow ratios on the structural and optical properties of GaN films, highlighting the critical role of precise control over these parameters to achieve high-quality epitaxial layers. Additionally, L. Dai et al. explored the influence of substrate choice and surface preparation on the epitaxial growth, demonstrating that substrates like sapphire and silicon carbide (SiC) significantly affect the growth mode and defect densities in GaN films.

The introduction of advanced characterization techniques, as seen in the works of J. S. Speck et al., provided deeper insights into the defect structures and strain states in GaN films, offering pathways to mitigate defects through optimized sputtering conditions and post-growth treatments. Moreover, recent advancements by Y. Takeda et al. in plasma diagnostics and control have further refined the process, enabling the production of GaN films with superior electronic properties suitable for high-frequency and high-power device applications.

M. Junaid et al. provided a comprehensive study on the film properties and growth mechanisms, revealing how different sputtering conditions influence the crystalline quality and surface morphology of GaN films, which is crucial for device performance. Similarly, S. Motomura et al. investigated the impact of sputtering power and nitrogen partial pressure on the properties of GaN films, identifying optimal conditions for achieving low defect densities and high luminescence efficiency, thus pushing the boundaries of material quality for optoelectronic applications. Collectively, these studies underscore the significant progress made in magnetron sputtering epitaxy of GaN with Ar-N_2 plasma, paving the way for its widespread adoption in advanced electronic and optoelectronic systems and to further explore the nuances of the basic understanding on the GaN deposition process using magnetron sputtering.

1.4 Building blocks & outline of this PhD

The introduction chapter focused on three main parts – the material (GaN), the problem at hand (low temperature growth process) and the potential solution (Plasma PVD of GaN). It stated the importance and dominance of GaN in the semiconductor industry especially for applications in the field of optoelectronics & power electronics. The conventional growth process and their limitations were discussed, introducing the reason why we considered plasma based methods as an alternative way that has to be further investigated: the goal of my thesis.

This PhD thesis is divided into 4 chapters. **Chapter 2** first introduces the custom-built plasma PVD reactor at LPICM to deposit GaN, which is a novel topic for the lab. A good part of the first year of the thesis was spent on developing the plasma reactor. Consequently, the chapter focuses on explaining the growth process, thereby explaining about the process of sputtering, the plasma operation, the main process parameters involved, the substrate used and the growth chamber properties. As far as thin film properties are concerned, we used several ex-situ solid-state characterization techniques that will be introduced.

Chapter 3 named "Plasma diagnostics" is entirely focused on the qualification of Ar-N_2 plasma under growth regime. An extensive focus is made on the description of plasma diagnostics such as optical emission spectroscopy (OES), two-photon absorption laser induced fluorescence (TALIF) and microwave interferometry (MWI). The methodology and procedure behind each in-situ method is thoroughly explained. Some results such as the nitrogen density and electron density are discussed to have an insight on the growth process. Additionally, the contamination by oxygen in the reactor is briefly discussed paving way to the GaN material qualification.

Chapter 4 focuses on the material qualification of the GaN films. It focused on describing the main features of the GaN thin film that has been deposited at room temperature. The structure, morphology, chemical quality and the composition profile have been analyzed. We report our first successful growth of polycrystalline GaN at room temperature and discuss its main properties. The chapter revolves around process optimization. Hence, the trends in the quality of the thin film at various process parameters such as the RF power, working pressure and N_2 flow variation have been extensively investigated. An anomaly was observed while characterizing our GaN films, which was the presence of high concentration of oxygen contaminant present in the bulk. Implementation of additional plasma & reactor cleaning steps helped reducing the contaminant to an extent, but not completely. This led to the question of whether increasing the growth temperature might help us towards mitigating contaminants and improving the GaN film quality, which paves the way towards Chapter 5. **Chapter 5** focuses on the parametric study of GaN on Si at various substrate temperatures (from RT to 500^{o}C). We present the optimized best quality GaN thin film that could be obtained while working at such temperatures using plasma PVD.

REFERENCES

[1] O. Burkacky, M. de Jong, and J. Dragon, "Strategies to lead in the semiconductor world," *McKinsey Artic. URL*, 2022, Accessed: Mar. 05, 2024. [Online]. Available: http://worldtradescanner.com/JJ%20strategies-to-lead-in-the-semiconductor-world_final.pdf

[2] T. Li, M. Mastro, and A. Dadgar, *III–V Compound Semiconductors: Integration with Silicon-Based Microelectronics*. CRC Press, 2010.

[3] F. Dimroth, "High-efficiency solar cells from III-V compound semiconductors," *Phys. Status Solidi C*, vol. 3, no. 3, pp. 373–379, 2006, doi: 10.1002/pssc.200564172.

[4] F. Malerba, *The Semiconductor Business: The Economics of Rapid Growth and Decline*. Univ of Wisconsin Press, 1985.

[5] "Compound Semiconductor Materials Market Size Report, 2027." Accessed: Sep. 28, 2023. [Online]. Available: https://www.grandviewresearch.com/industry-analysis/compound-semiconductor-materials-market

[6] J. F. Geisz and D. J. Friedman, "III–N–V semiconductors for solar photovoltaic applications," *Semicond. Sci. Technol.*, vol. 17, no. 8, p. 769, Jul. 2002, doi: 10.1088/0268-1242/17/8/305.

[7] R. Chau, S. Datta, and A. Majumdar, "Opportunities and challenges of III-V nanoelectronics for future high-speed, low-power logic applications," in *IEEE Compound Semiconductor Integrated Circuit Symposium, 2005. CSIC '05.*, Oct. 2005, p. 4 pp.-. doi: 10.1109/CSICS.2005.1531740.

[8] S. Adachi, *Properties of Semiconductor Alloys: Group-IV, III-V and II-VI Semiconductors*. John Wiley & Sons, 2009.

[9] S. Leroy, "Compound semiconductor substrate market set to double: how are companies competing in this space?," Yole Group. Accessed: Sep. 28, 2023. [Online]. Available: https://www.yolegroup.com/strategy-insights/compound-semiconductor-substrate-market-set-to-double-how-are-companies-competing-in-this-space/

[10] V. L. Rideout, "A review of the theory and technology for ohmic contacts to group III–V compound semiconductors," *Solid-State Electron.*, vol. 18, no. 6, pp. 541–550, Jun. 1975, doi: 10.1016/0038-1101(75)90031-3.

[11] M. P. Mikhailova, K. D. Moiseev, and Yu. P. Yakovlev, "Discovery of III–V Semiconductors: Physical Properties and Application," *Semiconductors*, vol. 53, no. 3, pp. 273–290, Mar. 2019, doi: 10.1134/S1063782619030126.

[12] D. Z. Ting *et al.*, "Advances in III-V semiconductor infrared absorbers and detectors," *Infrared Phys. Technol.*, vol. 97, pp. 210–216, Mar. 2019, doi: 10.1016/j.infrared.2018.12.034.

[13] S. Nakamura, "Background story of the invention of efficient blue InGaN light emitting diodes (Nobel Lecture): Invention of the efficient blue InGaN LEDs," *Ann. Phys.*, vol. 527, no. 5–6, pp. 335–349, Jun. 2015, doi: 10.1002/andp.201500801.

[14] R. F. Davis, "III-V nitrides for electronic and optoelectronic applications," *Proc. IEEE*, vol. 79, no. 5, pp. 702–712, May 1991, doi: 10.1109/5.90133.

[15] S. N. Mohammad and H. Morkoç, "Progress and prospects of group-III nitride semiconductors," *Prog. Quantum Electron.*, vol. 20, no. 5, pp. 361–525, Jan. 1996, doi: 10.1016/S0079-6727(96)00002-X.

[16] H. J. Joyce *et al.*, "III–V semiconductor nanowires for optoelectronic device applications," *Prog. Quantum Electron.*, vol. 35, no. 2, pp. 23–75, Mar. 2011, doi: 10.1016/j.pquantelec.2011.03.002.

[17] C. R. Eddy Jr., N. Nepal, J. K. Hite, and M. A. Mastro, "Perspectives on future directions in III-N semiconductor research," *J. Vac. Sci. Technol. A*, vol. 31, no. 5, p. 058501, Jul. 2013, doi: 10.1116/1.4813687.

[18] J. I. Pankove and T. D. Moustakas, "Chapter 1 Introduction: A Historical Survey of Research on Gallium Nitride," in *Semiconductors and Semimetals*, vol. 50, J. I. Pankove and T. D. Moustakas, Eds., in Gallium Nitride (GaN) I, vol. 50. , Elsevier, 1997, pp. 1–10. doi: 10.1016/S0080-8784(08)63082-3.

[19] H. P. Maruska and W. C. Rhines, "A modern perspective on the history of semiconductor nitride blue light sources," *Solid-State Electron.*, vol. 111, pp. 32–41, Sep. 2015, doi: 10.1016/j.sse.2015.04.010.

[20] S. Nakamura and M. R. Krames, "History of Gallium–Nitride-Based Light-Emitting Diodes for Illumination," *Proc. IEEE*, vol. 101, no. 10, pp. 2211–2220, Oct. 2013, doi: 10.1109/JPROC.2013.2274929.

[21] D. W. Runton, B. Trabert, J. B. Shealy, and R. Vetury, "History of GaN: High-Power RF Gallium Nitride (GaN) from Infancy to Manufacturable Process and Beyond," *IEEE Microw. Mag.*, vol. 14, no. 3, pp. 82–93, May 2013, doi: 10.1109/MMM.2013.2240853.

[22] S. Nakamura and S. F. Chichibu, *Introduction to Nitride Semiconductor Blue Lasers and Light Emitting Diodes*. CRC Press, 2000.

[23] "Energies | Free Full-Text | Gallium-Nitride Semiconductor Technology and Its Practical Design Challenges in Power Electronics Applications: An Overview." Accessed: Oct. 17, 2023. [Online]. Available: https://www.mdpi.com/1996-1073/12/14/2663

[24] M. A. Khan, G. Simin, S. G. Pytel, A. Monti, E. Santi, and J. L. Hudgins, "New Developments in Gallium Nitride and the Impact on Power Electronics," in *2005 IEEE 36th Power Electronics Specialists Conference*, Jun. 2005, pp. 15–26. doi: 10.1109/PESC.2005.1581596.

[25] K. Miwa and A. Fukumoto, "First-principles calculation of the structural, electronic, and vibrational properties of gallium nitride and aluminum nitride," *Phys. Rev. B*, vol. 48, no. 11, pp. 7897–7902, Sep. 1993, doi: 10.1103/PhysRevB.48.7897.

[26] R. Wang, P. P. Ruden, J. Kolnik, I. Oguzman, and KF. Brennan, "DIELECTRIC PROPERTIES OF WURTZITE AND ZINCBLENDE STRUCTURE GALLIUM NITRIDE," *J. Phys. Chem. Solids*, vol. 58, no. 6, pp. 913–918, Jun. 1997, doi: 10.1016/S0022-3697(96)00219-3.

[27] H. Qin, X. Luan, C. Feng, D. Yang, and G. Q. Zhang, "Mechanical, Thermodynamic and Electronic Properties of Wurtzite and Zinc-Blende GaN Crystals," *Materials*, vol. 10, p. 1419, Dec. 2017, doi: 10.3390/ma10121419.

[28] T. S. Cheng, L. C. Jenkins, S. E. Hooper, C. T. Foxon, J. W. Orton, and D. E. Lacklison, "Selective growth of zinc-blende, wurtzite, or a mixed phase of gallium nitride by molecular beam epitaxy," *Appl. Phys. Lett.*, vol. 66, no. 12, pp. 1509–1511, Mar. 1995, doi: 10.1063/1.113671.

[29] D. J. As, "Cubic group-III nitride-based nanostructures—basics and applications in optoelectronics," *Microelectron. J.*, vol. 40, no. 2, pp. 204–209, 2009.

[30] I. Bhat, "3 - Physical properties of gallium nitride and related III–V nitrides," in *Wide Bandgap Semiconductor Power Devices*, B. J. Baliga, Ed., in Woodhead Publishing Series in Electronic and Optical Materials. , Woodhead Publishing, 2019, pp. 43–77. doi: 10.1016/B978-0-08-102306-8.00003-4.

[31] D. Ueda, "Properties and Advantages of Gallium Nitride," in *Power GaN Devices: Materials, Applications and Reliability*, M. Meneghini, G. Meneghesso, and E. Zanoni, Eds., in Power Electronics and Power Systems. , Cham: Springer International Publishing, 2017, pp. 1–26. doi: 10.1007/978-3-319-43199-4_1.

[32] F. Roccaforte and M. Leszczynski, "Introduction to Gallium Nitride Properties and Applications," in *Nitride Semiconductor Technology*, John Wiley & Sons, Ltd, 2020, pp. 1–39. doi: 10.1002/9783527825264.ch1.

[33] J. I. Pankove, "Properties of Gallium Nitride," *MRS Online Proc. Libr. OPL*, vol. 97, p. 409, Jan. 1987, doi: 10.1557/PROC-97-409.

[34] G. Iannaccone, C. Sbrana, I. Morelli, and S. Strangio, "Power electronics based on wide-bandgap semiconductors: Opportunities and challenges," *IEEE Access*, vol. 9, pp. 139446–139456, 2021.

[35] M. Junaid *et al.*, "Electronic-grade GaN(0001)/Al2O3(0001) grown by reactive DC-magnetron sputter epitaxy using a liquid Ga target," *Appl. Phys. Lett.*, vol. 98, no. 14, p. 141915, Apr. 2011, doi: 10.1063/1.3576912.

[36] C. R. M. Grovenor, "Grain boundaries in semiconductors," *J. Phys. C Solid State Phys.*, vol. 18, no. 21, p. 4079, Jul. 1985, doi: 10.1088/0022-3719/18/21/008.

[37] K. Wasa, M. Kitabatake, and H. Adachi, *Thin film materials technology: sputtering of control compound materials*. Springer Science & Business Media, 2004.

[38] W. S. Wong and A. Salleo, *Flexible Electronics: Materials and Applications*. Springer Science & Business Media, 2009.

[39] J. K. Sprenger, A. S. Cavanagh, H. Sun, K. J. Wahl, A. Roshko, and S. M. George, "Electron enhanced growth of crystalline gallium nitride thin films at room temperature and 100 C using sequential surface reactions," *Chem. Mater.*, vol. 28, no. 15, pp. 5282–5294, 2016.

[40] E. C. Knox-Davies, J. M. Shannon, and S. R. P. Silva, "The properties and deposition process of GaN films grown by reactive sputtering at low temperatures," *J. Appl. Phys.*, vol. 99, no. 7, 2006.

[41] T. Maruyama and H. Miyake, "Gallium nitride thin films deposited by radio-frequency magnetron sputtering," *J. Vac. Sci. Technol. A*, vol. 24, no. 4, pp. 1096–1099, Jun. 2006, doi: 10.1116/1.2208988.

[42] T. Miyazaki, T. Fujimaki, S. Adachi, and K. Ohtsuka, "Properties of GaN films deposited on Si (111) by radio-frequency-magnetron sputtering," *J. Appl. Phys.*, vol. 89, no. 12, pp. 8316–8320, 2001.

[43] N. Elkashef, R. S. Srinivasa, S. Major, S. C. Sabharwal, and K. P. Muthe, "Sputter deposition of gallium nitride films using a GaAs target," *Thin Solid Films*, vol. 333, no. 1–2, pp. 9–12, 1998.

[44] C. G. Zhang, W. D. Chen, L. F. Bian, S. F. Song, and C. C. Hsu, "Preparation and characterization of GaN films by radio frequency magnetron sputtering and carbonized-reaction technique," *Appl. Surf. Sci.*, vol. 252, no. 6, pp. 2153–2158, Jan. 2006, doi: 10.1016/j.apsusc.2005.03.209.

[45] Q. X. Guo, A. Okada, H. Kidera, T. Tanaka, M. Nishio, and H. Ogawa, "Heteroepitaxial growth of gallium nitride on (1 1 1) GaAs substrates by radio frequency magnetron sputtering," *J. Cryst. Growth*, vol. 237, pp. 1079–1083, 2002.

[46] Y. Sato, A. Kurosaki, and S. Sato, "Low-temperature growth of GaN and InxGa1- xN films on glass substrates," *J. Cryst. Growth*, vol. 189, pp. 42–46, 1998.

[47] H. Wei *et al.*, "Plasma-enhanced atomic-layer-deposited gallium nitride as an electron transport layer for planar perovskite solar cells," *J. Mater. Chem. A*, vol. 7, no. 44, pp. 25347–25354, 2019, doi: 10.1039/C9TA08929B.

[48] P. Qiu *et al.*, “Plasma-enhanced atomic layer deposition of gallium nitride thin films on fluorine-doped tin oxide glass substrate for future photovoltaic application,” *Ceram. Int.*, vol. 46, no. 5, pp. 5765–5772, Apr. 2020, doi: 10.1016/j.ceramint.2019.11.026.

[49] S. Liu, S. Zhou, K. Wang, Z. Chen, Z. Gan, and X. Luo, “Several co-design issues using DfX for solid state lighting,” presented at the ICEPT-HDP 2011 Proceedings - 2011 International Conference on Electronic Packaging Technology and High Density Packaging, Aug. 2011, pp. 1–5. doi: 10.1109/ICEPT.2011.6067038.

[50] B. Beaumont, M. Vaille, T. Boufaden, B. el Jani, and P. Gibart, “High quality GaN grown by MOVPE,” *J. Cryst. Growth*, vol. 170, no. 1, pp. 316–320, Jan. 1997, doi: 10.1016/S0022-0248(96)00635-5.

[51] J. L. Puebla Nunez, “Spin phenomena in semiconductor quantum dots,” PhD Thesis, University of Sheffield, 2013. Accessed: Feb. 26, 2024. [Online]. Available: https://etheses.whiterose.ac.uk/4026/

[52] M. Bockowski, M. Iwinska, M. Amilusik, M. Fijalkowski, B. Lucznik, and T. Sochacki, “Challenges and future perspectives in HVPE-GaN growth on ammonothermal GaN seeds,” *Semicond. Sci. Technol.*, vol. 31, no. 9, p. 093002, Aug. 2016, doi: 10.1088/0268-1242/31/9/093002.

[53] D. Siche *et al.*, “PVT growth of GaN bulk crystals,” *J. Cryst. Growth - J CRYST GROWTH*, vol. 318, pp. 406–410, Mar. 2011, doi: 10.1016/j.jcrysgro.2010.10.030.

[54] M. Zajac *et al.*, “Basic ammonothermal growth of Gallium Nitride – State of the art, challenges, perspectives,” *Prog. Cryst. Growth Charact. Mater.*, vol. 64, no. 3, pp. 63–74, Sep. 2018, doi: 10.1016/j.pcrysgrow.2018.05.001.

[55] C. T. Hsu, “Epitaxial growth of II–VI compound semiconductors by atomic layer epitaxy,” *Thin Solid Films*, vol. 335, no. 1, pp. 284–291, Nov. 1998, doi: 10.1016/S0040-6090(98)00950-X.

[56] “Strain-induced enhancement of near-infrared absorption in Ge epitaxial layers grown on Si substrate | Journal of Applied Physics | AIP Publishing.” Accessed: Sep. 11, 2023. [Online]. Available: https://pubs.aip.org/aip/jap/article/98/1/013501/796040/Strain-induced-enhancement-of-near-infrared

[57] A. C. Arias, J. D. MacKenzie, I. McCulloch, J. Rivnay, and A. Salleo, “Materials and applications for large area electronics: solution-based approaches,” *Chem. Rev.*, vol. 110, no. 1, pp. 3–24, 2010.

[58] H. Sirringhaus, “Device physics of solution-processed organic field-effect transistors,” *Adv. Mater.*, vol. 17, no. 20, pp. 2411–2425, 2005.

[59] D. Zubia, S. H. Zaidi, S. R. J. Brueck, and S. D. Hersee, “Nanoheteroepitaxial growth of GaN on Si by organometallic vapor phase epitaxy,” *Appl. Phys. Lett.*, vol. 76, no. 7, pp. 858–860, Feb. 2000, doi: 10.1063/1.125608.

[60] A. Anders, “Plasma and ion sources in large area coating: A review,” *Surf. Coat. Technol.*, vol. 200, no. 5–6, pp. 1893–1906, 2005.

[61] N. A. Fichtenbaum, *Growth of nitrogen-face gallium nitride by MOCVD*. University of California, Santa Barbara, 2008.

[62] S. Fernández-Garrido, J. Grandal, E. Calleja, M. A. Sánchez-García, and D. López-Romero, “A growth diagram for plasma-assisted molecular beam epitaxy of GaN nanocolumns on Si(111),” *J. Appl. Phys.*, vol. 106, no. 12, p. 126102, Dec. 2009, doi: 10.1063/1.3267151.

[63] C. Ozgit-Akgun, I. Donmez, and N. Biyikli, “(Invited) Plasma-Enhanced Atomic Layer Deposition of III-Nitride Thin Films,” *ECS Trans.*, vol. 58, no. 10, p. 289, Aug. 2013, doi: 10.1149/05810.0289ecst.

[64] “PLA volume 28 issue 3 Cover and Back matter,” *J. Plasma Phys.*, vol. 28, no. 3, pp. b1–b10, Dec. 1982, doi: 10.1017/S0022377800000350.

[65] F. F. Chen, *Introduction to Plasma Physics*. Springer Science & Business Media, 2012.

[66] H. S. Butler and G. S. Kino, “Plasma Sheath Formation by Radio-Frequency Fields,” *Phys. Fluids*, vol. 6, no. 9, p. 1346, 1963, doi: 10.1063/1.1706905.

[67] D. A. Gurnett and A. Bhattacharjee, *Introduction to Plasma Physics: With Space and Laboratory Applications*. Cambridge University Press, 2005.

[68] V. Suendo, A. V. Kharchenko, and P. R. i Cabarrocas, “The effects of RF plasma excitation frequency and doping gas on the deposition of polymorphous silicon thin films,” *Thin Solid Films*, vol. 451, pp. 259–263, 2004.

[69] G. Franz, *Low Pressure Plasmas and Microstructuring Technology*. Springer Science & Business Media, 2009.

[70] L. Bárdos and H. Baránková, “Cold atmospheric plasma: Sources, processes, and applications,” *Thin Solid Films*, vol. 518, no. 23, pp. 6705–6713, Sep. 2010, doi: 10.1016/j.tsf.2010.07.044.

[71] S. Agarwal, B. Hoex, M. C. M. Van de Sanden, D. Maroudas, and E. S. Aydil, “Absolute densities of N and excited N 2 in a N 2 plasma,” *Appl. Phys. Lett.*, vol. 83, no. 24, pp. 4918–4920, 2003.

[72] N. K. Bibinov, A. A. Fateev, and K. Wiesemann, “On the influence of metastable reactions on rotational temperatures in dielectric barrier discharges in He-N2 mixtures,” *J. Phys. Appl. Phys.*, vol. 34, no. 12, p. 1819, 2001.

[73] I. Sugimoto, S. Nakano, and H. Kuwano, “Enhanced saturation of sputtered amorphous SiN film frameworks using He- and Ne-Penning effects,” *J. Appl. Phys.*, vol. 75, no. 12, pp. 7710–7717, Jun. 1994, doi: 10.1063/1.356602.

Chapter 2 – Experimental Procedures and Characterization Techniques

Table of Contents

Chapter 2 – Experimental Procedures and Characterization Techniques 19
2.1 Plasma based sputtering 20
2.1.1 Basics of sputtering 20
2.1.2 Sputtering deposition of GaN 21
2.1.3 Nucleation & growth 22
2.2 The Plasma PVD reactor 23
2.2.1 Reactor overview 23
2.2.2 The growth chamber 24
2.2.3 Plasma operating conditions 25
2.3 Substrates preparation 26
2.3.1 Si Substrate selection for GaN deposition 26
2.4 Material characterization 28
2.4.1 X-Ray diffraction (XRD) 28
2.4.2 Scanning electron microscopy (SEM) 30
2.4.3 Atomic force microscopy (AFM) 31
2.4.4 Transmission electron microscopy (TEM) 32
2.4.5 X-ray photoelectron spectroscopy (XPS) 33
2.4.6 Cathodoluminescence (CL) 35
2.4.7 Raman spectroscopy 37
2.4.8 Secondary ion mass spectrometry (SIMS) 38
2.4.9 Glow discharge optical emission spectroscopy (GD-OES) 39
2.5 Conclusion 40
REFERENCES 41

In this chapter, we present the process and the experimental procedures used/developed to deposit GaN thin films. We first introduce some basics of sputtering processes. Then we present the plasma PVD reactor system that was developed at LPICM during my thesis, including the reactor chamber and various important parts such as the substrate holder, the liquid Ga target and the magnetron system. Section 3 is dedicated to the growth of GaN on various types of Silicon (different orientations) to identify it effects on GaN growth quality. We finally introduce all the solid-state characterization methods/ techniques used to qualify our GaN film.

2.1 Plasma based sputtering

2.1.1 Basics of sputtering

Sputtering involves the removal of atoms from a material by bombarding it with high-energy ions. The material being bombarded is referred to as the target, which can be either solid or liquid. In this thesis, we used a liquid Gallium target. To create the ions necessary for sputtering, a sputtering gas, usually a heavy and inert atom such as Ar is introduced into a vacuum chamber. The positive ions in the plasma are then accelerated towards the target material that is negatively biased. When the ions collide with the target material, they transfer energy to the atoms of the target. The energy exchange, $E_{transfer}$ is given by a formula involving the mass of the incident ion, M_i and the target atom M_t:

$$E_{transfer} = \frac{4M_iM_t}{(M_i + M_t)^2} \tag{2.1}$$

When the energy transferred to the atoms of the target exceeds the surface binding energy, the atoms are sputtered off. The sputtering yield, which is the number of atoms ejected per incident particle, is an important measure of the sputtering process efficiency [1]. Figure 2.1.A illustrates the sputtering process. Besides atom ejection, the interaction between ions and the target surface generates secondary electrons and reflected neutrals.

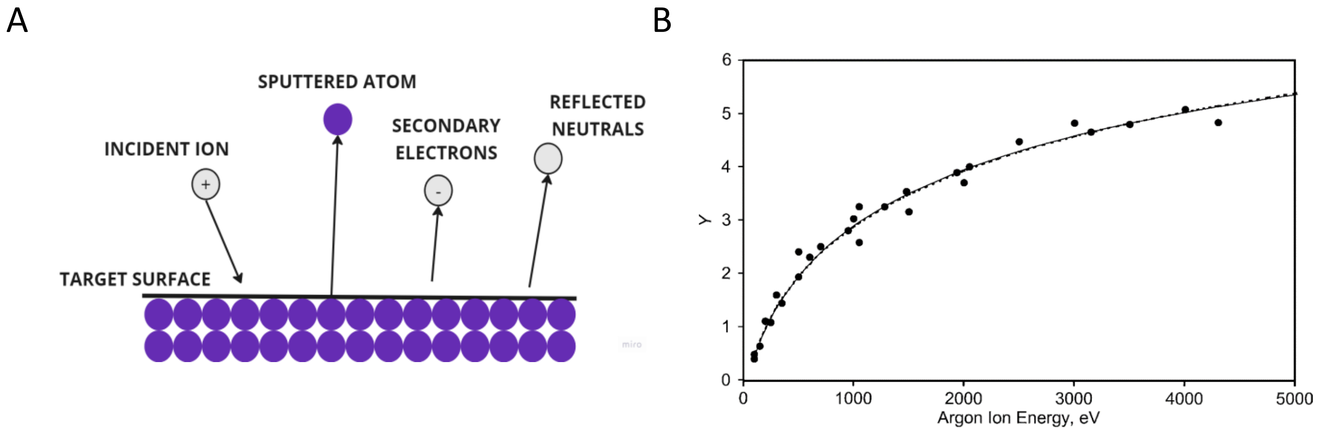

Figure 2.1: A. Illustration of the sputtering process. B. Sputter yield of a metallic target (Cu) with Ar^+ ions [2].

The impacting ions can also become implanted in the target material when their impinging energy is of the order of a few keV range, either with or without the ejection of target atoms. The secondary electrons, repelled by the negative potential applied to the target, play a crucial role in sustaining the discharge by aiding the gas ionization process. The sputtered atoms from the target material eventually reach the substrate and form a thin film on its surface. An example of a sputter yield of a Cu target with the Ar^+ ions is shown in Figure 2.1.B. We define an important parameter here known as the threshold energy for sputtering. This threshold energy is crucial because sputtering efficiency strongly depends on it. Below this threshold, the incident particles do not have enough energy to dislodge atoms from the surface effectively. Above the threshold, the sputtering yield (the number of atoms ejected per incident particle) increases significantly with increasing energy until saturation is reached. Typical threshold energies for sputtering often are in the range of a few tens of eVs. For systems consisting of gas mixtures involving an inert (e.g. Ar) and a reactive gas (e.g. N_2), it is essential to monitor the sputtering rate at different gas fractions to maintain an efficient sputtering of the target.

Magnetron based sputtering

Magnetron sputtering is a method that enhances the ionization process during sputtering by utilizing a magnetic field. sustained by permanent magnets positioned on the backside of the target where two common configurations are shown in Figure 2.2 (balance A and unbalanced B). When subjected to both magnetic and electrical fields, the secondary electrons ejected from the target follow a cycloid path near the target surface due to the Lorentz force acting on them [3].

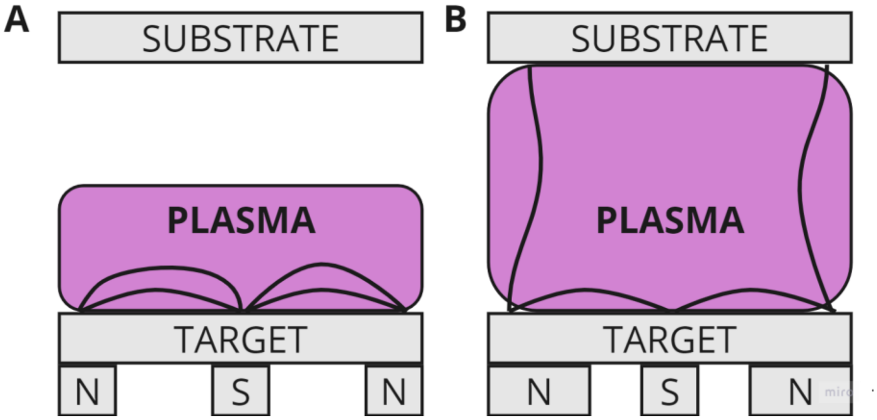

Figure 2.2 : Types of magnetron effecting the shape of the magnetic field. A. Balanced magnetron; B. Unbalanced magnetron

An unbalanced magnetron features stronger outer poles and weaker inner poles. As a result, the electrons become trapped near the target. The trapped electrons in this region significantly increase the probability of ionizing the gas atoms. By using a magnetron source, a sputtering plasma can be sustained at much lower gas pressures [4].

2.1.2 Sputtering deposition of GaN

The schematics of a sputtering process for growing GaN is shown in Figure 2.3.A. In this illustration, Argon (Ar) is used as the sputtering gas and Nitrogen (N_2) acts both as a sputtering and a reactive gas providing the source of N-atoms in the medium. The target is made of liquid Gallium, which is placed in a crucible. The cathode for our reactor system is supported by an unbalanced magnetron.

As the processes gases are introduced into the growth chamber, an RF voltage bias is applied to the sputtering target to start the gas ionization process. During half of the cycle, an applied RF voltage induces a substantial electron current toward the powered electrode, while the second half of the cycle witnesses a minor ion current. Consequently, the capacitively coupled RF electrode accumulates a negative charge, reaching a specific self-bias V_{DC}. Eventually, the electron current, prompted by the positive voltage exceeding the plasma potential (V_P) in one-half of the cycle (as depicted in Figure 2.3.B), equals the net ion current in the other half, when the electrode potential is below V_P.

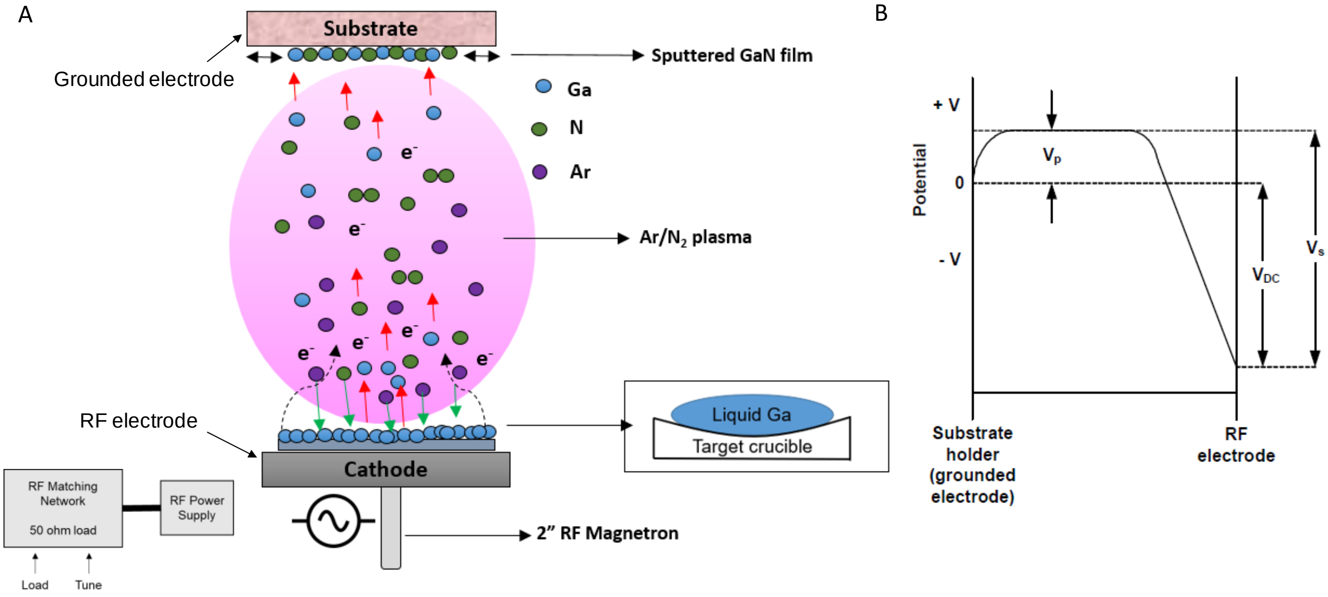

Figure 2.3: A. Schematics of the plasma enhanced PVD process to grow GaN thin films. B. Spatial distribution of average potential in a RF glow discharge reactor [5]. Here, V_P, V_{DC} and V_S are the plasma, DC and sheath potential respectively.

In Figure 2.3.B, the spatial distribution of the average potential in an RF discharge reactor is illustrated, wherein the sheath potential (V_S) equals V_{DC} + V_P on the powered electrode. Once the RF power is applied, the ionized Ar/N_2 gas forms a plasma consisting of electrons, ions, neutrals and radicals. Due to the target's negative bias, the ions in the plasma are accelerated towards the target and bombard with a kinetic energy proportional to the target bias. When subjected to magnetic and electrical fields, the electrons that are ejected exhibit a cycloidal trajectory near the surface of the target, influenced by the Lorentz force acting upon them. Consequently, these electrons become confined in proximity to the target. This confinement enhances the likelihood of ionization for gas atoms within this vicinity. The sputtered Ga atoms and ions travel through the plasma onto the substrate surface. Momentum transfer between these positive ions and the adatoms results in an increase in the kinetic energy to the film growth and can thus improve the film quality. The dissociated nitrogen ions travel to the substrate and react with the gallium atoms to form GaN thin film on the surface of the substrate.

2.1.3 Nucleation & growth

Thin film growth can be classified into three categories – A) layer-by-layer growth mode, B) 3-D growth mode or Island growth mode and C) Combination of 2-D and 3-D growth mode [6]. The illustrations of the three growth modes are shown in Figure 2.4. Layer-by-layer growth mode involves sequential deposition of atoms or molecules, resulting in smooth, continuous layers. 3-D growth mode leads to the formation of clusters or islands initially, which grow independently into rough, discontinuous structures. Island growth mode combines aspects of both, starting with island formation and progressing to continuous film formation as deposition continues.

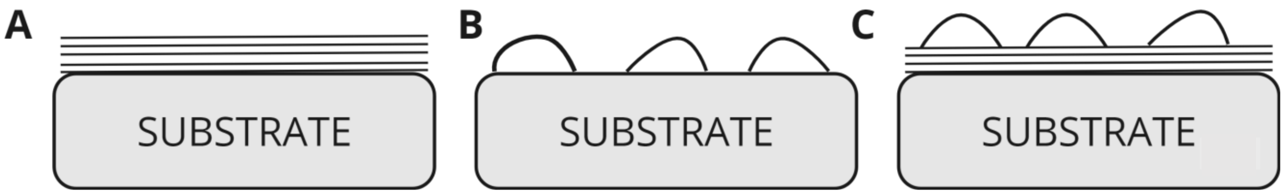

Figure 2.4: Illustration of the different growth modes to form a thin film.

During the sputtering process, the sputtered species are transferred from the target to the substrate in a vapor phase. The adatoms diffuse on the surface, influenced by their energy, and interact with the substrate surface. Alternatively, they may leave the surface through re-evaporation or desorption. Over time, the adatoms gather to form small clusters. These clusters continuously form and disintegrate, but only those exceeding a critical size become stable nuclei and continue to grow. This nucleation stage persists until a maximum number density is achieved [7]. The density of these primary nuclei decreases as the growth temperature rises, thereby increasing the probability of adatom mobility. As the growth process proceeds, these islands merge in a process called coalescence, ultimately resulting in the formation of a thin film.

2.2 The Plasma PVD reactor

2.2.1 Reactor overview

Figure 2.5 shows the custom-built homemade plasma PVD reactor designed and installed at LPICM during my thesis. It consists of a RF (13.56 MHz) magnetron sputtering. Typically, a turbo molecular pump was used to evacuate the reactor. The base pressure before deposition was kept at 10^{-7} mbar. A butterfly valve was used to maintain the desired working pressure in the range of 1-100 mTorr (1-13.3 Pa). Argon (Ar) (99.999% purity) was primarily used as the sputtering gas and Nitrogen (N_2) (99.999% purity) was used as a sputtering cum reactive gas. The sputtering target was a group of pure metallic Ga pellets (99.9999% purity) melted to occupy/fill the shape of a homemade concave target crucible.

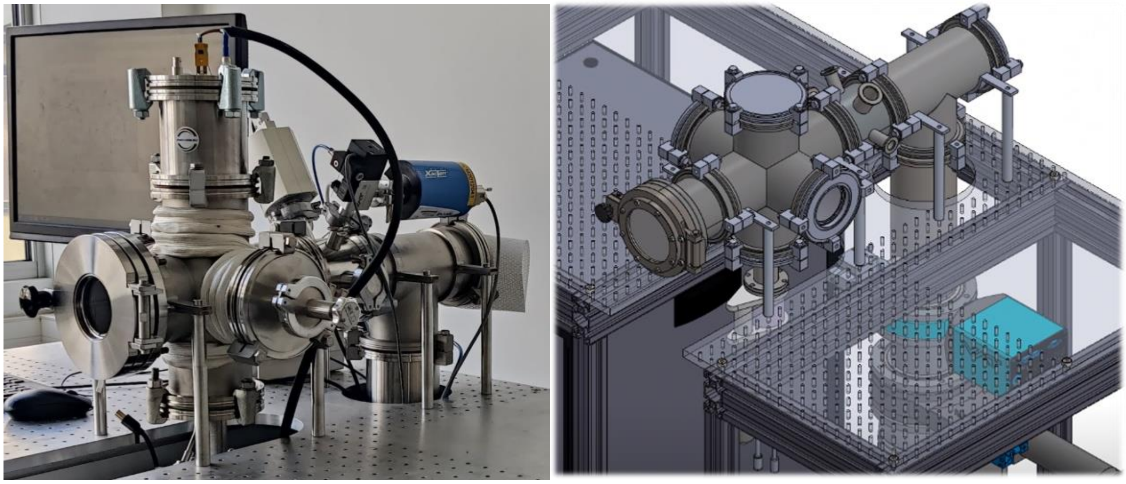

Figure 2.5: The real-view and the schematic of the custom built plasma PVD reactor.

The magnetron is equipped with a water-based cooling system to ensure the safety of the equipment and a smooth operation even at high power conditions (~ 150W). The precursor gases (Ar & N_2) are fed into the reactor in a controlled manner with the help of mass flow controllers (MFCs) that ensures an accurate flow rate. The maximum range of flows for the gases is set at 20 sccm each. The entire reactor pumping system and the MFCs are automated with the help of a Beckhoff system and was controlled using a LABVIEW interface.

The PVD reactor was built to be easily transportable to be able to do experiments in other labs. The deposition is contained in a specific area of the reactor close to the cathode and this area is otherwise known as the growth chamber or the reaction chamber as specified in Figure 2.6.

2.2.2 The growth chamber

Figure 2.6 depicts the growth chamber in our plasma reactor. It consists of a target in a crucible attached to the cathode that uses a 2-inch RF based magnetron sputtering system. A shutter is implemented close to the substrate holder to avoid any deposition on the substrate during plasma cleaning or conditioning. The distance between the target and the substrate is varied typically in a range from 5 ~10 cm.

The growth chamber also consists of three large optical glass windows, which has multiple purposes. These windows can either be used for visual inspection of the plasma or more essentially, can be used to analyze the emissions from the plasma using an optical emission spectrometer. Plasma is ideally contained within the region of the target crucible (typically ~ 1-2 inch) and is useful for concentrated depositions on the substrate thereby exposing the reactor walls to a minimum.

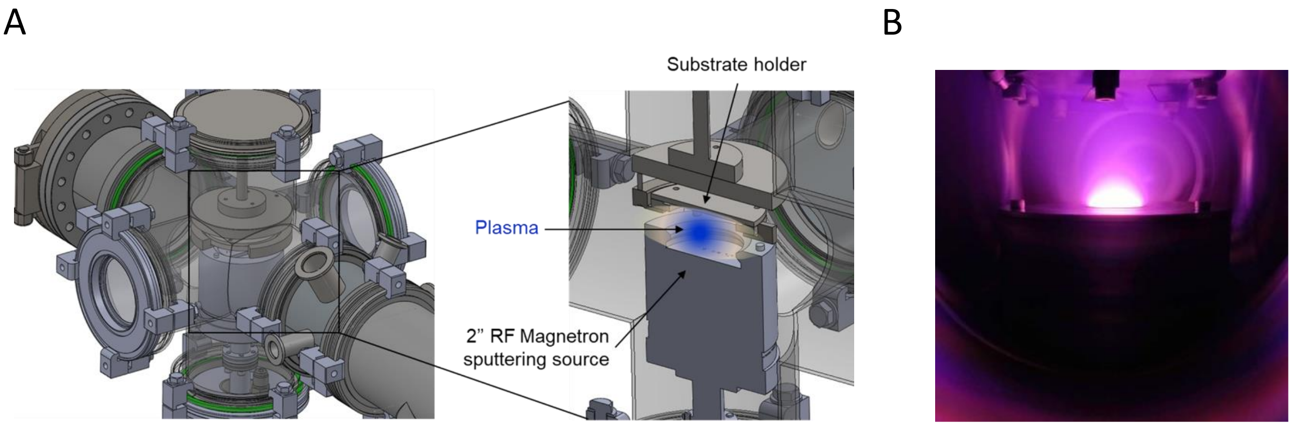

Figure 2.6: Reaction chamber of the plasma PVD reactor. A. Schematics showing the area where the plasma is ignited. B. Real view of the reaction chamber with the plasma.

The substrate holder is attached to a heating element. Three designs of substrate holders were used in this thesis, each having its own purpose.

Substrate holder

Throughout this thesis, various forms of substrate holder were accommodated as shown in Figure 2.7. Figure 2.7.A depicts the basic custom designed substrate holder to accommodate 2-inch Si/Sapphire/Glass wafers. This particular holder was not equipped with a heating element and was primarily used for depositions at room temperature. A specific variation of the holder at room temperature is depicted in Figure 2.7.B. This type of holder was used to test multiple substrates at once processed at the same conditions.

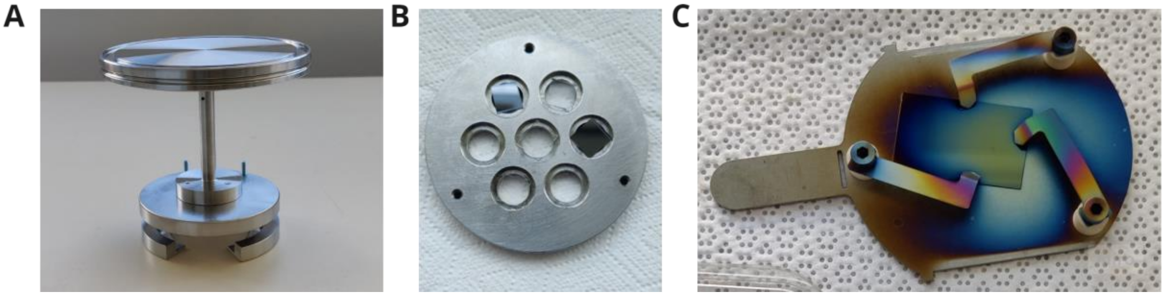

Figure 2.7: Variations of the substrate holder. A. Custom built design to hold 2-inch wafers (RT). B. Designed to hold multiple substrates at once (RT). C. Design compatible with the heating element.

Once the heating element was installed, the substrate holder was modified according to its needs. The holder at Figure 2.7.C represents the design compatible with the heating element. It could also hold multiple substrates at once. These variations were necessary, as the substrate was placed on the top electrode while the target had to be placed on the bottom electrode due to the use of liquid Ga as the target.

Liquid Ga Target

Pure liquid gallium has a high surface tension and does not wet any surface easily [8], [9]. The selected material for the crucible to hold liquid Ga should be ultra-high vacuum (UHV) compatible and its surface should be easily dampened by liquid Ga. Stainless steel (SS) is a proven material to contain liquid Ga. Apart from the material selection, the shape of the crucible should also be taken into account. It is essential to prevent the formation of air pockets in the target and maintain a flat surface.

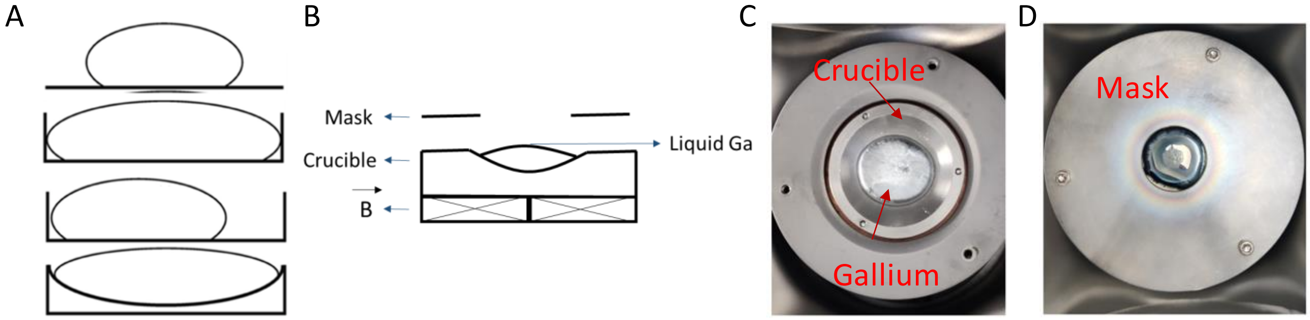

Figure 2.8: A. Schematics showing liquid Ga droplet on various stainless steel surfaces - Flat, cylindrical & concave shaped trough [8]. B. Schematics of Liquid Ga target on our target crucible and a mask exposing the Ga to the plasma. C. Real-view of the crucible and Ga on the cathode. D. Real-view of the Mask on top of the target crucible.

Even though liquid Ga wets stainless steel (SS) well when compare with other materials like molybdenum and graphite, it still does not spread on the surface easily. Rather, it forms a large droplet similar to Figure 2.8.A. In cylindrical shaped crucible from Figure 2.8.B, Ga remains in a big droplet form and some parts of the SS is exposed to the plasma and can be sputtered. Another problem from using a cylindrical crucible is that there will be some empty spaces in the corner. The concave SS crucible from Figure 2.8.A&B is the most optimized shape. A large target area is formed without any voids. Figure 2.8.C represents the real view of the crucible placed on the cathode. We used a mask on top of the target crucible to avoid any unwanted exposure of stainless steel to the plasma as shown in Figure 2.8.D.

2.2.3 Plasma operating conditions

The deposition process of a GaN thin film by sputtering relies on the interplay of various process parameters.In general, the parameters that are well-known to affect the growth include total working pressure, partial pressure of the gas mixture, the RF power and the substrate temperature. As it was the first time that this reactor was operated, we wanted to determine the conditions that ensure stable plasma conditions and in the same time verifying that Ga was efficiently sputtered. For this purpose, we performed a campaign during which we ignited a plasma for the same duration of X min, using OES when it comes to probing Ga emission efficiency. This was done as a function of the pressure and the RF power while fixing the Ar/N_2 ratio and total flow. To determine the Ga-atoms efficiency, we used Optical emission spectroscopy (OES) to probe the Ga atomic line at lambda – 403, 417 nm using an AVANTES Avaspec-4 ULS4096 CL-EVO starline spectrometer that has a slit width of 10 μm /SMA-RS has a spectral coverage in the UV-VIS region and a potential range from 200-750 nm. The resolution (FWHM) of the spectrometer is 0.7 nm. This set-up was also used, in as a qualitative manner, to analyze N_2 emission lines and to characterize the plasma temperatures.

Power (W) Pressure (mTorr)	10	25	50	75	100	125	150
5	🟥 ×	🟥 ×	🟥 ×	🟥 ×	🟥 ×	🟥 ×	🟧 ✓*
10	🟥 ×	🟥 ×	🟧 ✓*	🟧 ✓*	🟧 ✓*	🟧 ✓*	🟧 ✓*
20	🟥 ×	🟧 ✓*	🟧 ✓*	🟨 ✓*	🟨 ✓*	🟨 ✓*	🟨 ✓*
30	🟥 ×	🟧 ✓*	🟧 ✓*	🟨 ✓*	🟨 ✓*	🟨 ✓*	🟨 ✓*
50	🟧 ✓*	🟧 ✓*	🟧 ✓*	🟩 ✓	🟩 ✓	🟩 ✓	🟩 ✓
75	🟧 ✓*	🟧 ✓*	🟩 ✓	🟩 ✓	🟩 ✓	🟩 ✓	🟩 ✓
100	🟧 ✓*	🟧 ✓*	🟩 ✓	🟩 ✓	🟩 ✓	🟩 ✓	🟩 ✓

🟥 × → No plasma
🟧 ✓* → Weak Plasma with no Ga emission
🟨 ✓* → Plasma ON after ignition at high pressure and power.
🟩 ✓ → Plasma ON

Figure 2.9: Plasma ignition conditions in our custom built plasma PVD reactor. This was done at a fixed mixture of Ar/N_2 (60/40) at a total flow rate of 20 sccm.

Figure 2.9 shows a panorama of the effect of RF power and pressure on plasma operation, highlighting the conditions at which the plasma (i) does not ignite, (ii) exhibit poor Ga emission efficiency, (iii) ignites after switching back from a stable condition and (iv) stable condition where plasma ignites. From Figure 2.9, it appears that the plasma does not ignite at very low-pressure values (< 30 mTorr (~ 4 Pa)) until a strong RF Power is applied (> 125 W). Subsequently, we found out that the plasma was stable and Ga from the target sputtered effectively at conditions with a working pressure above 20mTorr andan RF power above 75 W. Based on the plasma ignition conditions and considering the stability, we chose an optimized window of conditions for our deposition represented by the blue box in Figure 2.9. The working pressure range was from 20 to 100 mTorr (2.6 Pa – 13.3 Pa), the RF power was varied from 75 W to 125 W and the Ar/N_2 gas flows were kept constant at a ratio of 60/40 with a total flow of 20sccm.

2.3 Substrates preparation

Various GaN substrates are now accessible for growing homoepitaxial films of GaN, but they are very expensive. Therefore, the majority of GaN-based devices are grown on foreign substrates such as Si, SiC and Al_2O_3 that are the most commonly used for heteroepitaxial growth of GaN. Table 2.1 presents the lattice mismatch and dislocation densities of commercial GaN epilayers grown on different substrates [10].

Table 2.1: Bulk GaN vs foreign substrates [11]

Properties	GaN on bulk GaN	GaN on Si	GaN on SiC	GaN on Al_2O_3
Lattice mismatch	0%	17%	3.5%	16%
Dislocation density (cm^{-2})	10^4 ~5 x 10^6	1 x 10^{11}	5 x 10^9	5 x 10^9

The majority of this thesis focus on the optimization of the growth parameters for depositing GaN especially on Si as it cheap and more convenient when it comes to applications. In this thesis, as the focus is made on optimizing the process, we mostly tested Si substrates of different orientations. However, for the sake of comparison, we also performed some depositions on sapphire substrates when the optimal growth conditions were validated with Silicon.

2.3.1 Si Substrate selection for GaN deposition

In this thesis, we tested three different orientations of Si substrates: (100), (110) and (111). Commercially, Si (111) is the most common wafer used to deposit GaN. This is due to the fact that the preferred orientation of h-GaN on Si (111) is more easily formed than on Si (100) substrates [12]. Visually, the impact of the substrate orientation towards the growth is presented in Figure 2.10 with a schematic of the layer-by-layer growth of GaN on **(a)** Si (100) and **(b)** Si (111).

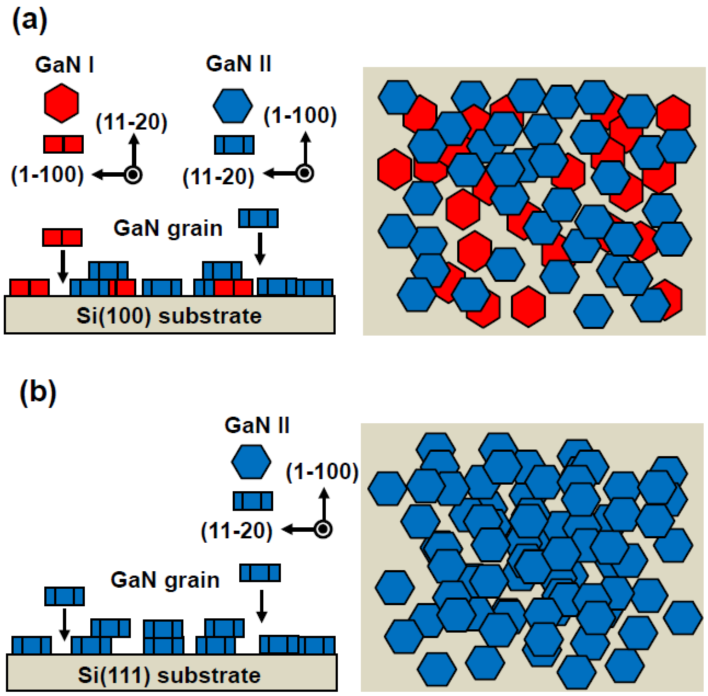

Figure 2.10: Illustration of h-GaN deposition on A. Si (100) and B. Si (111) [12].

In both Figure 2.10.A&B, we consider the two most common GaN growth patterns, namely the GaN-I (growth directions in [0001] and [10$\bar{1}$0]) and the GaN-II (growth directions in [0002] and [11$\bar{2}$0]. At the beginning of the growth, both GaN-I and GaN-II appear on the surface of Si (100). As time progresses, GaN-II dominates the crystalline growth process. The growth mode transforms from an island to layer-by-layer growth. However, for the Si (111) substrate, the template matches with h-GaN and hence only GaN-II is observed from the start of the growth. This is the reason why Si (111) is preferred in the industry over Si (100).

Besides Si (111), Si (110) is also considered as an interesting substrate for GaN but its possibilities are scarcely explored. Figure 2.11 presents the XRD data for GaN deposited on Si (110) and Si (111) for the same process conditions using MOCVD or MBE.

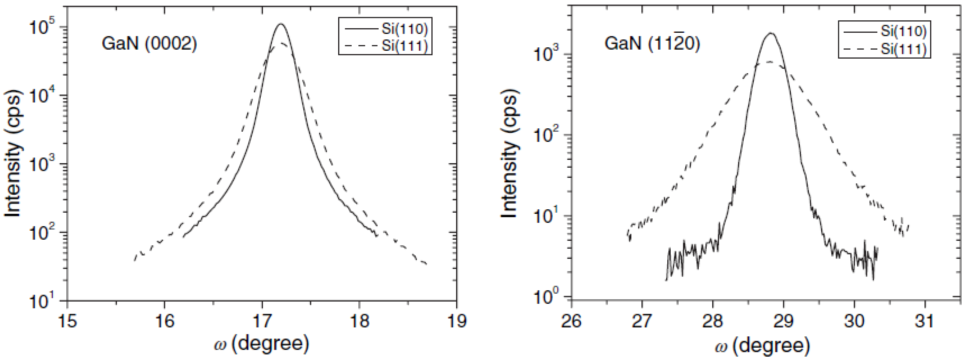

Figure 2.11: XRD ω-scan for the (0002) and (1120) reflection for GaN on Si (110) and Si (111) [13].

The results shows improvement in the crystalline quality of GaN grown on Si (110), especially in the GaN [11$\bar{2}$0] growth direction as indicated by the reduction of the FWHM. Additional advantages of using Si (110) include simplified cleavage along different directions compared to Si (111) due to the presence of primary {111} cleavage planes perpendicular to the (110) plane. It also facilitates etching, particularly for thin film devices that require substrate removal [13]. During this thesis, we tried depositing GaN on all the three orientations of Si substrates ((111), (110) and (100)). Moreover, it is also important to take note here that for our measurements, the orientation of Si substrates did not have any influence on the intensity and the FWHM of the crystalline peaks of GaN obtained from 2θ XRD measurements; they were identical.

Substrate cleaning

Si wafers always have a native oxide layer formed on them. A common method of removing them is to perform a Hydrofluoric acid (HF) dip using a highly diluted (1:20) HF solution [14]. Before any deposition, the Si wafers, irrespective of the orientation ((100), (111), (100)) were soaked in the HF solution for about 30seconds. Finally, the wafer was blown dried with Nitrogen (N_2) to ensure a clean surface. The clean samples are then quickly loaded onto the reactor for deposition of GaN.

2.4 Material characterization

In this thesis, we used several ex-situ material characterization techniques that aided us in determining the structural, optical, morphological, electrical and chemical quality of the material. Some essential methods were elaborated in this section with particular emphasis on GaN thin films and the adaptation of such techniques to tailor the material.

2.4.1 X-Ray diffraction (XRD)

XRD is a technique used to study the crystalline structure of materials by analyzing their texture and degree of crystallinity. The atoms of a crystal belong to families of parallel reticular planes denoted (hkl), which are characterized by an inter-reticular distance d_{hkl} between each of them. When a parallel monochromatic X-ray beam of wavelength λ is radiated onto the crystalline material, making an incidence angle θ with the planes, this angle is called the Bragg angle. This relationship between the crystal lattice structure and X-ray diffraction phenomena forms the basis for understanding the principles of crystallography and determining material properties through diffraction analysis.[15]. If the diffracted waves are in phase, they will constructively interfere in certain directions, meaning that the diffracted intensity will be non-zero only if the contributions of the successive planes are in phase. The schematic representation of Bragg's law is shown in Figure 2.12.

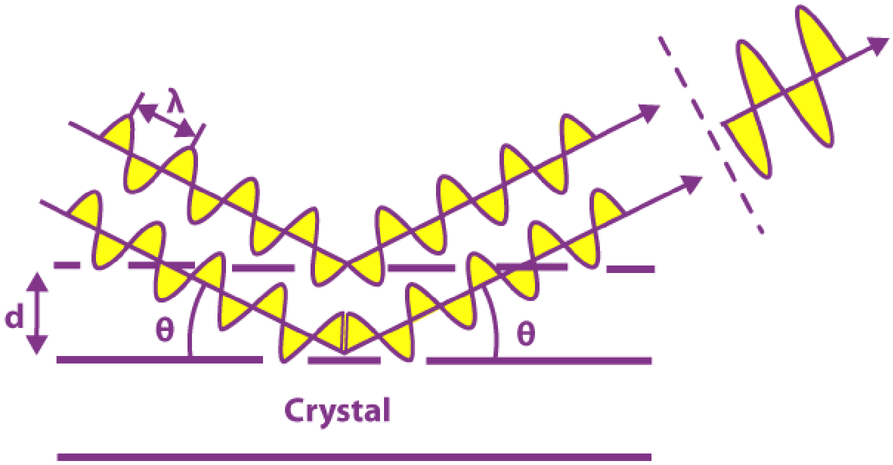

Figure 2.12: Schematic representation of X-ray diffraction from a part of a single crystal obeying Bragg's law [16].

Bragg's law is represented as:

$$n\lambda = 2d_{hkl}sin\theta \tag{2.2}$$

where λ is the wavelength of radiation, d_{hkl} the inter-planar spacing or lattice spacing of (hkl) planes, θ the angle between the incident ray and the crystal plane, and *n* the order of diffraction. By adjusting the crystal orientation through changing θ, one can arrange for diffraction to happen for a given set of planes.

Determining the crystallite size and lattice parameters

In the field of X-ray diffraction and crystallography, the Scherrer equation is used that connects the broadening of a peak in a diffraction pattern to the size of sub-micrometer crystallites within a solid material [17]. The Scherrer equation can be expressed as:

$$D = K\lambda/\beta cos\theta \tag{2.3}$$

where *D* is the mean size of the crystallites which may be smaller or equal to the grain size, *K* s a dimensionless shape factor that has a constant value of ~0.9, *λ* the x-ray wavelength, *β* the FWHM of the corresponding peak, *θ* the Bragg angle. Apart from the size of the crystallites, XRD can also be used to calculate the lattice constants. The lattice constants of a hexagonal (two lattice parameters – *a* and *c*) and cubic material (single lattice parameter - *a*) can be determined if the quantity d_{hkl} (inter-planar spacing) is known [17]. The relation is as follows:

$$\text{(Cubic)} \quad \frac{1}{d_{hkl}^2} = \frac{h^2 + k^2 + l^2}{a^2} \tag{2.4}$$

$$\text{(Tetragonal)} \quad \frac{1}{d_{hkl}^2} = \frac{h^2 + k^2}{a^2} + \frac{l^2}{c^2} \tag{2.5}$$

The inter-planar spacing (d_{hkl}) can be determined from the Bragg's relation. The lattice parameters estimated from XRD can be used to comment on the defects and strain in the layer.

Grazing incidence x-ray diffraction (GIXRD)

One of the advantages of GIXRD over conventional XRD is that, when analyzing the thin films, most of the incident beam is confined within the grown thin film since the penetration depth is significantly reduced due to the low angle of incidence thereby reducing the intensity of the diffracted signal coming from the substrate [18]. GIXRD involves directing a beam of X-rays at a very shallow angle of incidence onto a sample surface (typically less than 1°). This shallow angle of incidence allows the X-rays to penetrate only a few nanometers into the sample, making GIXRD particularly useful for the analysis of thin films. The difference in geometries between XRD and GIXRD is depicted in Figure 2.13.

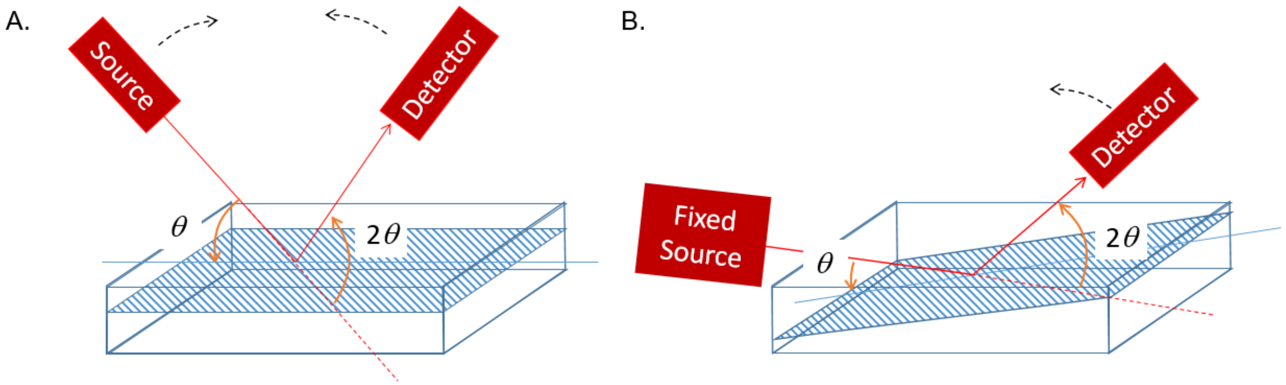

Figure 2.13: Source-detector geometries of A. X-ray diffraction B. Grazing incidence X-ray diffraction.

In this thesis, we majorly use GIXRD to analyze the crystallinity of our samples (especially those deposited at room temperature) as the thin films were in the range of a few hundreds of nm.

2.4.2 Scanning electron microscopy (SEM)

Figure 2.14 depicts the schematic of an SEM system. This technology works on the principle of impinging the fine beam of high-energy electrons on the surface of the specimen and obtaining a signal from the surface of the specimen/ material to determine its properties. The accelerated electrons in SEM carry a large amount of kinetic energy. This energy, when impinges on the surface dissipates a variety of signals due to electron-specimen interaction. The combination of signals includes secondary electrons, backscattered electrons, diffracted backscattered electrons, photons, visible light, and heat. These signals are used to obtain different information about the specimen surface and in the case of SEM, the secondary electrons and backscattered electrons are mostly used in producing the image of the specimens [19]. Secondary electrons mainly carry the morphology and topographical information whereas backscattered electrons are used to determine the contrasts in the composition of multiphase samples. The use of energy-dispersive X-ray spectroscopy (EDX), in conjunction with a scanning electron microscope, allows for the identification of the elemental composition of a substance. EDX has the ability to detect elements with atomic numbers higher than boron, even at concentrations as low as 0.1%. Its applications include material assessment and identification, identification of contaminants, spot analysis of regions up to 10 cm in diameter, quality control screening, and various other uses [20]. Although it is just used to know the surface composition and not the depth, it is a quick and easy tool to quantify the composition roughly. Each element has a unique atomic structure giving it a set of unique peaks on its X-ray emission spectrum.

Throughout our thesis, we used a Zeiss Merlin compact SEM system to comment on the surface morphology and cross-section of our GaN films deposited at varying process conditions. Based on the thickness range of our samples (~ a few hundred nanometers), the operating voltage varied between 5 to 10 kV.

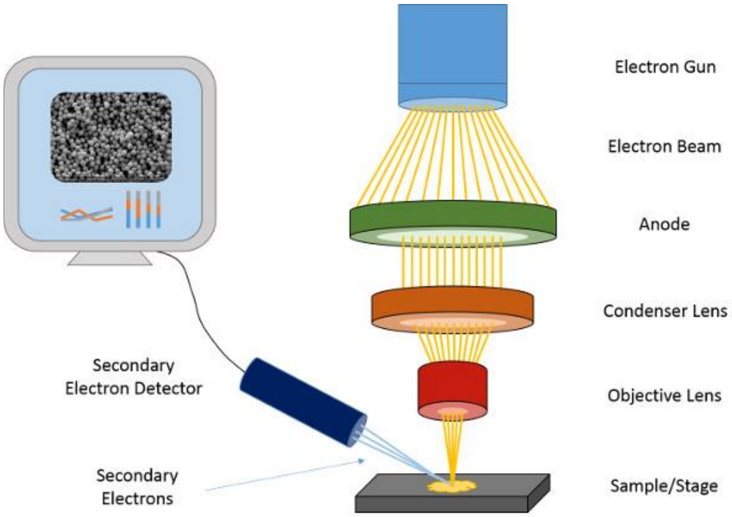

Figure 2.14: Schematics of an SEM system [21]. The computerized image of the sample is obtained by interpreting the data fed through the secondary electron detector.

The thickness of our GaN films were measured via observing the cross-sectional SEM images and were verified using a dekTAK profilometer. Contact profilometers are utilized in this instance, wherein a probe is placed in contact with the surface to record its height. This is accomplished mechanically using a feedback loop that monitors the force exerted by the sample as it moves across the surface while pressing against the probe. Furthermore, our GaN samples exhibited non-uniformity in thickness across a sample space of ~ 2 inches, which was monitored using a profilometers at various points across the sample surface.

2.4.3 Atomic force microscopy (AFM)

AFM is an advanced form of scanning probe microscopy that can precisely measure surface topography and roughness with an accuracy of less than 1 nm. This non-invasive technique can be utilized to evaluate the roughness of materials [22]. Figure 2.15 shows the basic schematic of an AFM system.

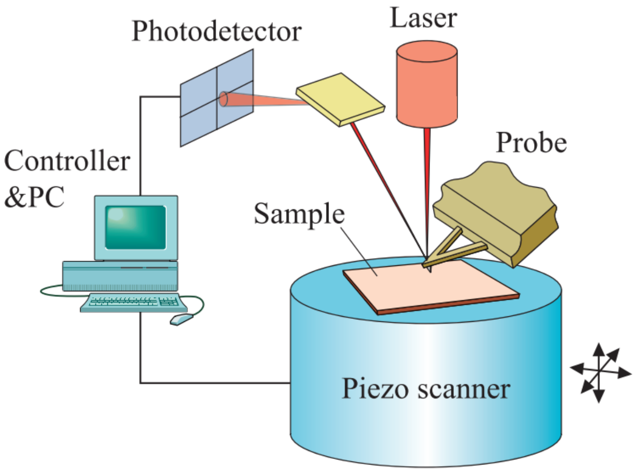

Figure 2.15: Schematic diagram of the atomic force microscope [23].

AFM instruments function based on the concept of surface detection using an extremely sharp tip located at the end of a micro machined silicon probe. This sharp tip is employed to create an image of a sample by systematically scanning across the surface in a line-by-line fashion, although the approach can significantly differ between distinct operational modes, i.e. contact mode and dynamic, often called tapping mode [24].

The fundamental principle of AFM involves connecting this nanoscale tip to a small cantilever, which essentially acts as a spring. When the tip makes contact with the surface, the cantilever flexes, and this bending is identified using a laser diode and a split photodetector. The extent of this bending indicates the force of interaction between the tip and the sample. In contact mode, the tip is pressed onto the surface, and an electronic feedback system constantly monitors the force of interaction to ensure a consistent deflection as the scanning progresses. Another mode, known as 'tapping' offers a compromise between contact mode and non-contact mode. It involves oscillating the AFM tip at or near its resonant frequency while scanning the sample surface [22]. As the tip approaches the surface, it momentarily taps the sample, and then retracts during the upward part of the oscillation cycle. This tapping action reduces the force between the tip and the sample, limiting the potential for damage or wear on both the tip and the sample. Additionally, because tapping mode operates at a frequency slightly higher than the resonant frequency, it can minimize the effects of surface adhesion and capillary forces. For these purposes, we used an Agilent Picoscan 3000 AFM setup based on a tapping mode scheme to measure our GaN films.

2.4.4 Transmission electron microscopy (TEM)

TEM is a method of microscopy that involves directing a concentrated stream of electrons through a slim sample, typically less than 100 nm thick[25]. This technique enables precision at the atomic level, allowing for the identification of the arrangement of atoms, and the contrast between them can differentiate the various species of atoms. Figure 2.16 shows a simple schematic of a classical TEM system. The microscope column comprises a sequence of electromagnetic lenses and apertures designed to focus the electron beam onto the sample, magnifying the TEM image onto the viewing screen (or detectors). To maintain the necessary vacuum levels within the column, a vacuum system is employed. At the column's upper part resides the electron gun, linked to a high voltage source responsible for determining the kinetic energy of the electron beam. Standard accelerating voltages typically range from 80 kV to 300 kV.

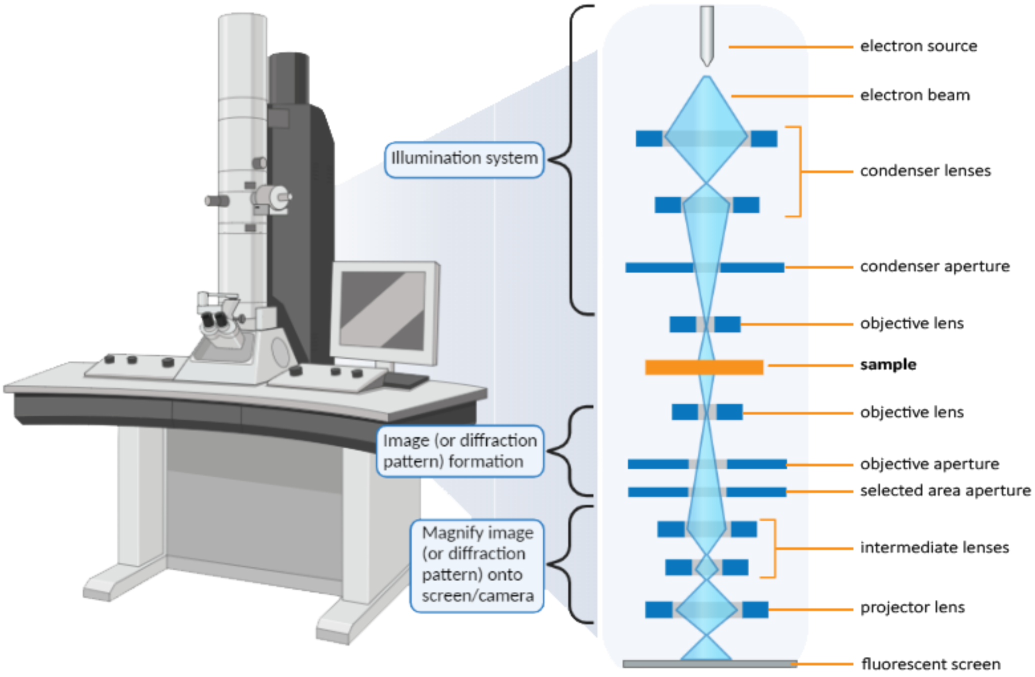

Figure 2.16: A simplified schematic of a TEM setup highlighting the major components through the column [26].

Figure 2.17 shows the work of Jiminez et.al. [27], where the structure of a GaN layer grown on an AlN buffer layer was investigated. The analysis yielded results from which the structure and the crystallinity of the GaN film were deduced from high resolution TEM (HR-TEM). The films are polycrystalline with several growth orientations that were observed from the selective area diffraction pattern. The films were columnar and the atomic stacking of the individual elements along the growth directions could be observed.

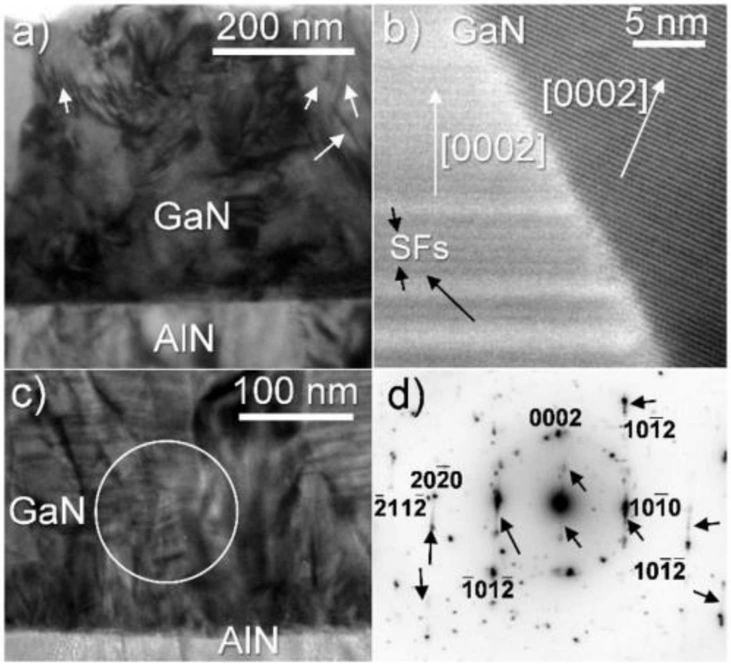

Figure 2.17: TEM images for a cross-section of GaN layers [27]. A. TEM micrograph of a GaN layer grown on a buffer AlN layer. B. HR-TEM micrograph of a grain boundary between two grains with different orientations. C&D. TEM micrograph and the corresponding selective area diffraction pattern (SAED) showing different growth orientations.

In this work, we use TEM to analyze the structure and crystallinity of our GaN films. For this purpose, the structure of the thin films was analyzed using a Thermo Fisher Themis High-resolution TEM (HRTEM), working at 300 kV. For HRTEM, the films were scratched, and a residue was placed onto a carbon-coated copper grid. TEM was carried out thanks to access to the Interdisciplinary Center for Electron Microscopy of Ecole Polytechnique (CIMEX).

2.4.5 X-ray photoelectron spectroscopy (XPS)

XPS is a surface-sensitive analytical technique that is used to study the chemical composition of materials. XPS works by directing a beam of X-rays at a sample, which causes electrons to be emitted from the surface of the material. The energy and number of these emitted electrons are then measured using an electron analyzer. By analyzing the energy of the emitted electrons, one can determine the elements present in the material and the chemical states of those elements. One of the key advantages of XPS is its ability to provide information about the surface chemistry of materials. Because the technique is sensitive to the material's surface, it can provide information about surface contaminants, surface functionalization, and chemical changes that occur at the surface. The working schematic of a typical XPS system is shown in Figure 2.18.

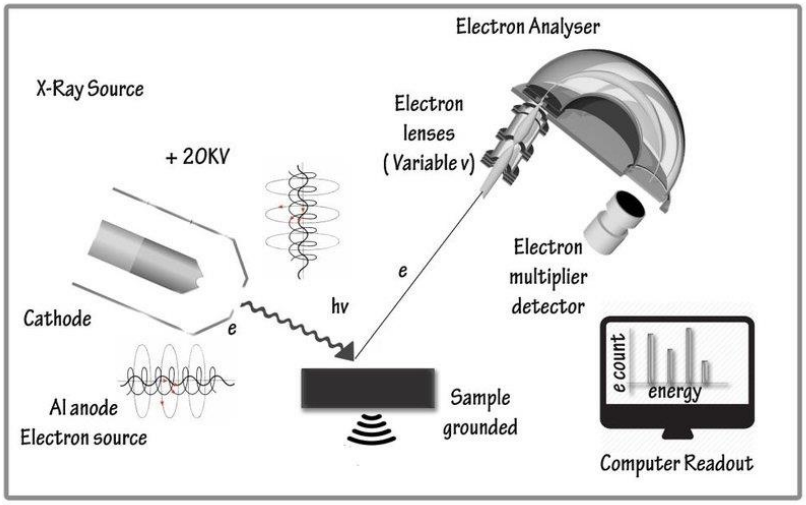

Figure 2.18: Schematic representation of an XPS system [28]

A depth profile can also be made by sputter etching the thin film and analyzing the exposed surface. Ideally, the system is able to detect most of the elements in the periodic table.

Binding energies of Gallium

Ga2p or Ga3d are typically used to quantify elemental gallium. Usually, the Ga2p peak is used to provide a better depth resolution for sputter profiling [29]. This is because the Ga3d electrons have a higher kinetic energy than the Ga2p electrons and therefore have a better sampling depth. Hence, the Ga3d is more useful for surface and chemical analysis. The Auger peaks of Ga (Ga LLM) are spread out between 300-600 eV and they overlap with several peaks from other elements.

GaN reference peak fit

Quantifying GaN through XPS is always considered as a challenge. This is due to the fact that the strongest peak of Nitrogen (N1s) superimposes with the Auger peaks of Ga (Ga LLM) in the binding energy range between 380~400eV [30]. The superimposed peaks are shown in Figure 2.19.

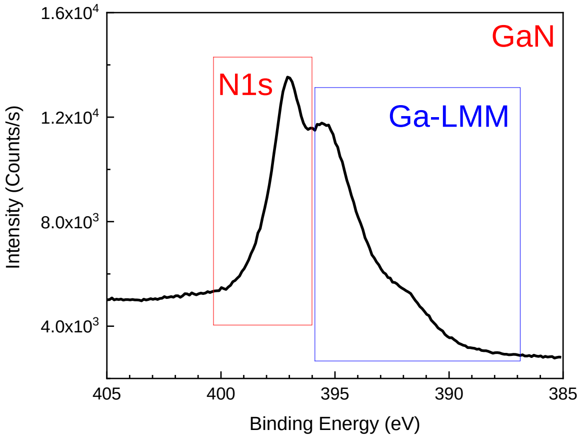

Figure 2.19: Superposition of N1s peak with the Auger peak of Ga. The measured XPS spectra corresponds to one of our GaN films.

The deconvoluted N1s peak is shown in Figure 2.20 along with all the other Auger Ga peaks and the corresponding quantification of the Ga and N elements are shown in Table 2.2. It is important to note here that superposition of the Ga Auger peaks with the N1s peak of nitrogen hinders the accurate quantification of the composition of Nitrogen as the intensity of the XPS signal of N1s might also be influenced by the Ga peaks. However, the composition values can be used to compare growth at different process conditions.

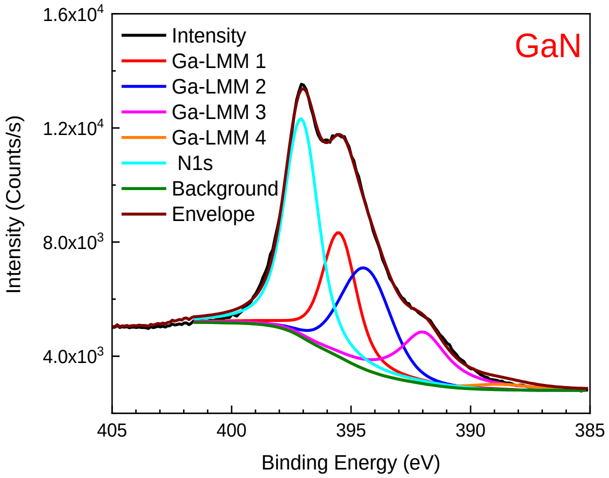

Figure 2.20: Deconvolution of N1s peak from the Ga Auger peaks (LMM). The measured XPS spectra corresponds to one of our GaN films.

Table 2.2: Quantification of GaN by comparing Ga3d and Ga2p peaks

Name	Peak BE (eV)	FWHM (eV)	Area (P) CPS.eV	Atomic %
Ga3d	21.11	1.69	39354.52	48.5
N1s	398.44	1.52	39433.72	51.5
Ga2p	1119.09	1.76	210558.71	46.27
N1s	398.44	1.52	39433.72	53.73

On comparing the two peaks of Ga (Ga3d and Ga2p), the quantification is slightly different. The low energy peak (Ga3d) gives a better atomic ratio than the high-energy peak (Ga2p). Another reason for choosing Ga3d is that it is in the same binding energy range as N1s, so they have similar escape depths and there is a significant attenuation of superficial contamination [31], which is commonly observed while combining elements with a large energy gap. Hence, for further XPS analysis in the upcoming sections, we use Ga3d peak to quantify Gallium. XPS was carried out in collaboration with Institut Lavoisier de Versailles (ILV).

2.4.6 Cathodoluminescence (CL)

CL spectroscopy is a useful technique for studying the optical and structural properties of semiconductors and optoelectronic devices. It is an optical phenomenon where the electrons interacting with a luminescent material (GaN in our case) results in the emission of photons. The principle is the inverse of the photoelectric effect where the electron emission is induced by photon irradiation. The schematics of CL on a GaN/Si sample is shown in Figure 2.21 [32].

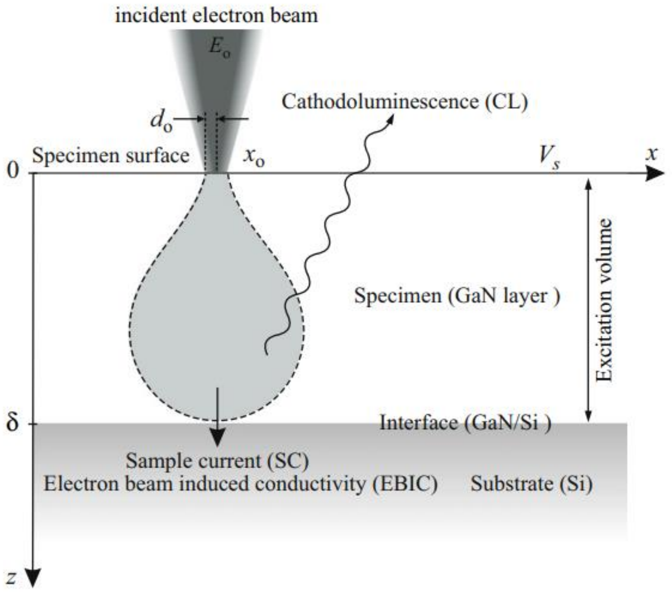

Figure 2.21: Schematic representation of spatial CL excitation by e-beam irradiation of a GaN thin film on Si substrate [33].

We use CL in scanning mode to examine the morphology and defect related bands of GaN films films. The CL intensity from our samples is obtained by integrating the excess minority carriers in time and electron absorption [33] and it can be mathematically represented by:

$$I_{CL} = \int_{z_d}^{\infty} \frac{\Delta n(z)}{\tau_n} \exp(-\alpha_b z)\, dz \tag{2.6}$$

where Δn are the excess minority carriers in the neutral region, τ_n is the electron lifetime constant, z_d is the depletion width and α_b is the luminescence absorption coefficient.

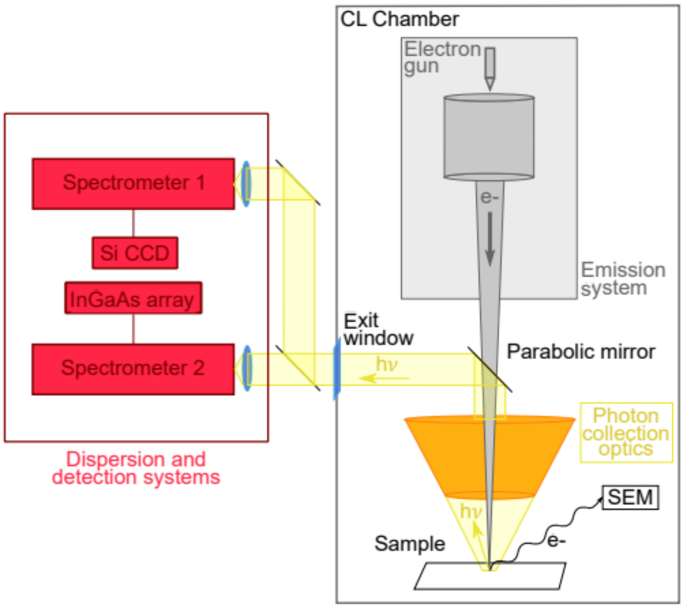

Figure 2.22: Schematics of the cathodoluminescence (CL) set-up used. Three distinct ensembles can be distinguished: the emission system (grey), the light collection optics (yellow), and the detection and dispersion system (red). Adapted from the thesis of Capucine and from the works of Bidaud, (2021) [34], [35].

The CL measurements for our GaN/Si samples were carried out in collaboration with the Center for Nanoscience and nanotechnology (C2N). The schematics involving the measurement setup is shown in Figure 2.22. The system comprises of the electron emission, light collection optics and the detection system. The e-beam was irradiated at 6kV and 1.2A with an aperture of ~ 100μm. The spectrometer and the CCD had an entrance slit of 5000 μm with a variable grating of 150/500. The central wavelength was kept at 500nm. The spectrometer had a readout of 50 kHz and the integration time was varied between 50~200 milliseconds. The samples were measured at 300K~ room temperature (RT) and at 77K (liquid nitrogen).

A typical CL spectrum of epitaxial GaN grown on Si substrate extracted from [27] is shown in Figure 2.23. The spectra show the band edge (BE) emission of GaN with a peak energy of 3.39eV at 300K and 3.46eV at 77K. This band is identified as the donor-bound exciton transition [36]. It is also considered as the primary band of GaN. Additionally, the CL spectra exhibits a broad yellow luminescence ~2.2 eV at both 300K and 77K. This is considered as a defect band that could potentially originate from either Ga vacancies, oxygen or carbon impurities, or intrinsic point defects [37].

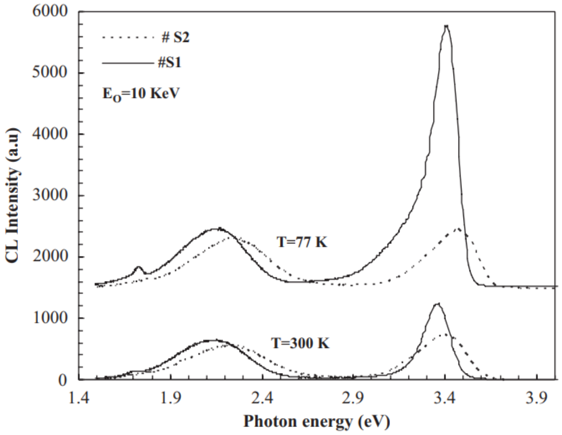

Figure 2.23: CL spectra of GaN on Si substrate at 77K and 300K [33].

In this thesis, for CL analysis, we use the above spectrum from Figure 2.23 as a reference for comparison with the spectra from our measurements. Although a majority of our samples is polycrystalline and does not exhibit the same behavior as an epitaxial film, it is a good starting point to compare the intensities and shifts in the bands at both RT and 77K.

2.4.7 Raman spectroscopy

Raman spectroscopy gives information on the structural properties of GaN and provides a qualitative analysis on the crystallinity of the thin films. It is a non-invasive technique, which involves directing a laser beam at a sample, and the light interacts with molecular vibrations and phonons, which causes a change in photon energies scattered by the material compared to the incoming photon energy. This variation provides information about the vibrational modes in the system [38]. For instance, it can be used to determine the crystallinity of a silicon sample. In our case, it was mainly used as a fast mean to verify the presence of GaN characteristics peaks given in Table 2.3.

Table 2.3: Phonon modes in wurtzite GaN & cubic zinc blende GaN [39]

Mode	Wurtzite GaN	Cubic ZB GaN
E_2(high)	569	552
A_1(LO)	735	739

At the Γ point (Brillouin zone center), for a hexagonal structure of GaN, six sets of the optical phonon modes are active. For a cubic zinc blende (ZB) GaN structure, only 2 phonon modes are active. The scattering geometry has a huge influence on the selection of these phonon modes. For a Raman system with a backscattering geometry such as ours, only the E_2 (high) and the A_1 (LO) modes are allowed, the rest are forbidden [39].

Figure 2.24.A shows a typical Raman setup. When a laser beam is illuminated on the sample, the Raman-shifted light (colored red) is filtered out from the laser light by a dichroic mirror, and dispersed along a vertical line on the two dimensional CCD detector. In slit-scanning mode, many spectra are acquired simultaneously: each position along the line on the sample produces a spectrum along the CCD detector.

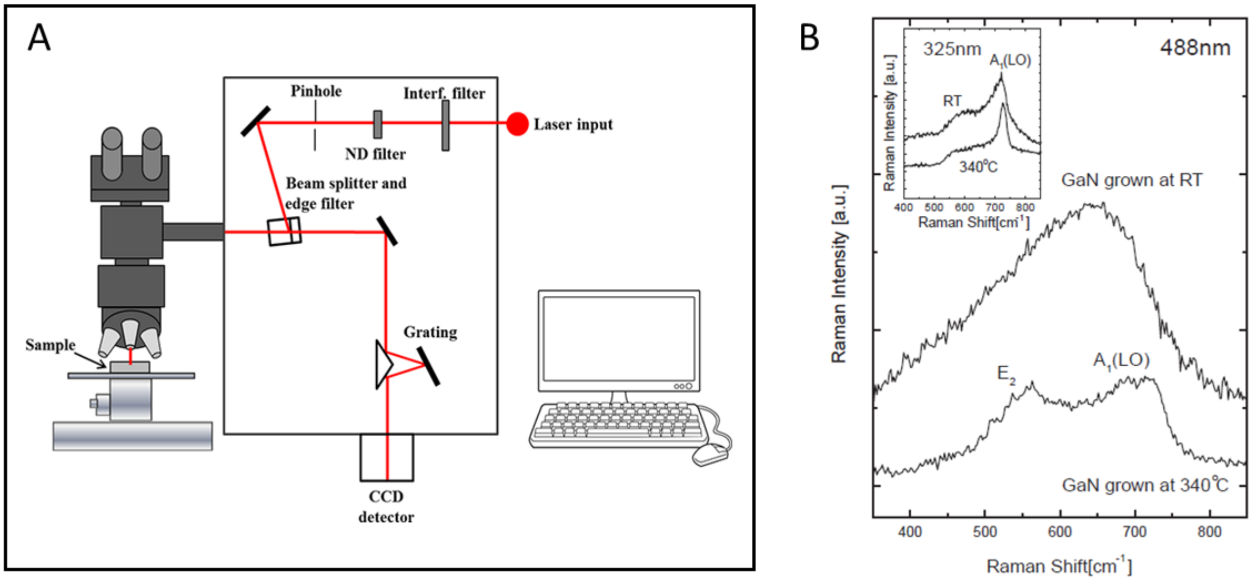

Figure 2.24: A. Schematic of Raman spectrometer. The displayed setup focuses the illuminating laser down to a spot on the sample (GaN) [40]; B. Raman spectra of a GaN film grown at room temperature and at 340°C recorded under UV excitation (488 nm). Inset shows the Raman spectra at 325 nm excitation [41].

In our case, we used the cylindrical mode and focus on a spot on the sample. Three different laser wavelengths were used to analyze the GaN samples: 532 nm (Green), 630 nm (red) and 405 nm (Ultra violet). Figure 2.24.B presents a typical Raman spectrum of a GaN thin film that is amorphous in nature. A 325 nm excitation would have been better, but our setup was limited to 405 nm excitation.

2.4.8 Secondary ion mass spectrometry (SIMS)

In our thesis, we used SIMS to characterize the elemental depth profile of our GaN samples and particularly to gain information about the profile at the GaN/Si wafer interface. The secondary ions generated by sputtering are then gathered and measured by a mass spectrometer [42]. This methodology is critical for analyzing atoms that are present in trace amounts and do not form part of the crystal structure, such as impurities like O, H, or C or dopant atoms.

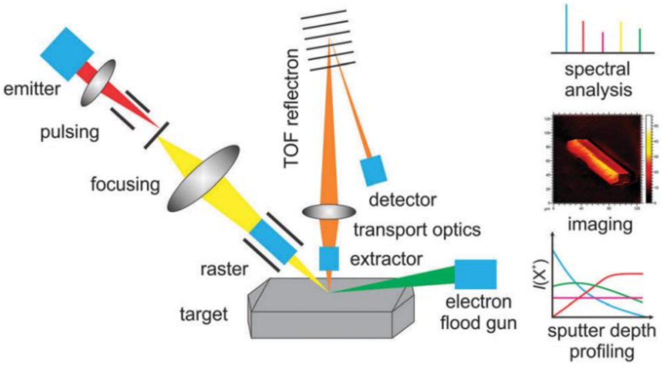

Figure 2.25: Schematics of the functional principle of a SIMS instrument and options for surface and bulk analysis of solid thin films. The images on the right depicts the mass spectrometric analysis, imaging of the lateral distribution of secondary ion and the sputter depth profiling could be analyzed. Adapted from JP. Hofmann, 2014 [43].

SIMS is a powerful analytical technique used to determine the elemental and isotopic composition of solid surfaces and thin films, which is complementary with XPS regarding the information they provide in chemical composition SIMS operates on the principle of ionizing and analyzing secondary ions emitted from the surface of a solid sample. Figure 2.25 shows the schematics and the information that could be obtained using SIMS.

2.4.9 Glow discharge optical emission spectroscopy (GD-OES)

GD-OES, as SIMS, enables the analysis of a sample's elemental composition. GD-OES is however easier and faster to use than SIMS, even tough is it not as sensitive as SIMS. This method can analyze layers with thicknesses ranging from thin (<50 nm) to thick (several hundred µm), and it can be used on a variety of materials such as metals, semiconductors, glass, ceramics, and polymers [44]. In a glow-discharge, a chamber is filled with a low-pressure gas. Upon activating RF power, an electric plasma is generated. The sample undergoes layer-by-layer sputtering by Ar ions, and neutral species enter the plasma. The atoms that are extracted from the material are introduced into the plasma, become excited through collisions with electrons or metastable carrier gas atoms. The spectrometer measures the characteristic spectrum emitted by these excited atoms.

This is a dynamic process: the plasma continually receives new species as sputtering progresses, causing the spectrum to evolve with each layer being sputtered. Figure 2.26.A shows the schematics of a GD-OES setup and the corresponding depth profile of a GaN layer on a sapphire substrate.

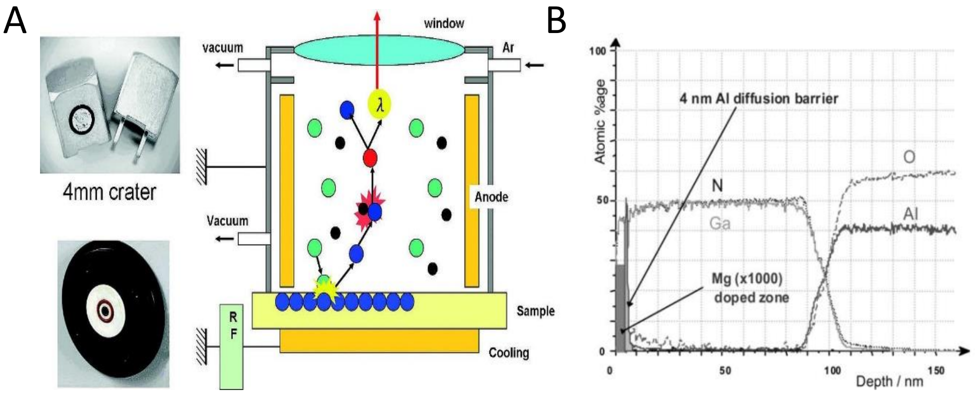

Figure 2.26: A. Schematic and the components of the analytical glow-discharge source from Horiba [45]. Here, the schematics show the Ar ions (green) sputtering the target atom (blue) which are then ionized in the plasma. B. Depth profile of a 100 nm thick GaN film on a sapphire substrate [44].

A high resolution of the depth profile can be obtained through GD-OES as observed from Figure 2.26.B. The profile shows a uniform elemental composition of Ga and N with stoichiometric ratios followed by a gradual decrease in the signal once the sputter-etch reaches the substrate, where the elements of the substrate are then sputtered. From GD-OES, we can analyze the elemental composition uniformity of the thin film and the sharpness of the interface of the thin film with the substrate.

In this PhD study, we used a HORIBA pulsed GD-OES system which was mainly used to get a fast insight on the composition profile of the GaN layer and to monitor the oxygen impurity in the layer due to contamination within the reactor (Chapter 4).

2.5 Conclusion

This chapter has presented three main parts related to experiments in general: A) the sputtering growth process, B) the Plasma PVD design and working and C) the material characterization. At first, the basics of sputtering was presented emphasizing on GaNdeposition. Then, we moved on towards the plasma PVD reactor developed during this thesis. We introduced of the main features of the reactor system and its essentials such as the liquid Ga target design, the various forms of substrate holders that were used and then, gave an overview of the process parameters window defined for running GaN deposition under stable and Ga-ejection efficient plasma conditions. The choice in the Silicon substrates used throughout this study and the impacts of using these substrates and their orientations towards a standard GaN growth were analyzed from a bibliographical standpoint. The final part of this chapter dealt with the main characterization techniques that were used to study/ analyze the GaN thin films. The next chapter will be dedicated to the diagnostic techniques used to qualify the plasma.

REFERENCES

[1] D. Depla and S. Mahieu, *Reactive sputter deposition*, vol. 109. Springer, 2008.

[2] A. Anders and J. Andersson, "Sputtering in vacuum: A technology for ultraclean metallization and space propulsion," in *2008 23rd International Symposium on Discharges and Electrical Insulation in Vacuum*, Bucharest, Romania: IEEE, Sep. 2008, pp. 561–566. doi: 10.1109/DEIV.2008.4676856.

[3] R. Payling and T. Nelis, *Glow Discharge Optical Emission Spectroscopy: A Practical Guide*. Royal Society of Chemistry, 2007.

[4] H. Fager, "Growth and Characterization of Amorphous TiAlSiN and HfAlSiN Thin Films," 2012.

[5] V. Suendo, "Physico-Chimie des plasmas de silane pour la formation de nacocristaux de silicium a tempétature ambiante: application à des dispositifs.," PhD Thesis, Ecole Polytechnique X, 2005. Accessed: Nov. 28, 2023. [Online]. Available: https://pastel.hal.science/pastel-00001909/

[6] M. Ohring, *Materials Science of Thin Films: Depositon and Structure*. Elsevier, 2001.

[7] M. A. Signore, A. Sytchkova, D. Dimaio, A. Cappello, and A. Rizzo, "Deposition of silicon nitride thin films by RF magnetron sputtering: a material and growth process study," *Opt. Mater.*, vol. 34, no. 4, pp. 632–638, Feb. 2012, doi: 10.1016/j.optmat.2011.09.012.

[8] A. Prabaswara, J. Birch, M. Junaid, E. A. Serban, L. Hultman, and C.-L. Hsiao, "Review of GaN Thin Film and Nanorod Growth Using Magnetron Sputter Epitaxy," *Appl. Sci.*, vol. 10, no. 9, p. 3050, Apr. 2020, doi: 10.3390/app10093050.

[9] G. H. Wagner and W. H. Gitzen, "Gallium," *J. Chem. Educ.*, vol. 29, no. 4, p. 162, 1952.

[10] "GaN Substrates (Bulk, C-Plane)." Accessed: May 11, 2023. [Online]. Available: https://kymatech.com/products-services/materials/gan-related-iii-n-materials/634-bulk-gan-c-plane-substrates

[11] M. Junaid, "Magnetron Sputter Epitaxy of GaN Epilayers and Nanorods," 2012, Accessed: May 11, 2023. [Online]. Available: https://urn.kb.se/resolve?urn=urn:nbn:se:liu:diva-84655

[12] W.-K. Wang and M.-C. Jiang, "Growth behavior of hexagonal GaN on Si(100) and Si(111) substrates prepared by pulsed laser deposition," *Jpn. J. Appl. Phys.*, vol. 55, no. 9, p. 095503, Sep. 2016, doi: 10.7567/JJAP.55.095503.

[13] A. Dadgar *et al.*, "Epitaxy of GaN on silicon - Impact of symmetry and surface reconstruction," *New J. Phys.*, vol. 9, p. 389, Oct. 2007, doi: 10.1088/1367-2630/9/10/389.

[14] S.-E. MicroSi, "Silicon Wafer Cleaning," Shin-Etsu MicroSi. Accessed: May 15, 2023. [Online]. Available: https://www.microsi.com/blog/silicon-wafer-cleaning/

[15] G. E. M. Jauncey, "The Scattering of X-Rays and Bragg's Law," *Proc. Natl. Acad. Sci.*, vol. 10, no. 2, pp. 57–60, Feb. 1924, doi: 10.1073/pnas.10.2.57.

[16] "Bragg's Law." Accessed: May 04, 2023. [Online]. Available: http://pd.chem.ucl.ac.uk/pdnn/powintro/braggs.htm

[17] "The reflection of X-rays by crystals | Proceedings of the Royal Society of London. Series A, Containing Papers of a Mathematical and Physical Character." Accessed: May 11, 2023. [Online]. Available: https://royalsocietypublishing.org/doi/abs/10.1098/rspa.1913.0040

[18] I. M. Kötschau and H. W. Schock, "Compositional depth profiling of polycrystalline thin films by grazing-incidence X-ray diffraction," *J. Appl. Crystallogr.*, vol. 39, no. 5, pp. 683–696, Oct. 2006, doi: 10.1107/S002188980601987X.

[19] R. K. says, "Scanning Electron Microscope - About Tribology." Accessed: Oct. 17, 2023. [Online]. Available: https://www.tribonet.org/wiki/scanning-electron-microscope/

[20] "Chapter 9 - Scanning Electron Microscopy (SEM) and Energy-Dispersive X-Ray (EDX) Spectroscopy | Elsevier Enhanced Reader." Accessed: Apr. 27, 2023. [Online]. Available: https://reader.elsevier.com/reader/sd/pii/B9780444637765000097?token=6DAF015DE8B55887F69961ADC08CCC24A376F81AD05CCC3DABC6496CA5DE92D4F9DA69F8C36CF2CBEE120EE45FF456E2&originRegion=eu-west-1&originCreation=20230427114900

[21] M. Abd Mutalib, M. A. Rahman, M. H. D. Othman, A. F. Ismail, and J. Jaafar, "Chapter 9 - Scanning Electron Microscopy (SEM) and Energy-Dispersive X-Ray (EDX) Spectroscopy," in *Membrane Characterization*, N. Hilal, A. F. Ismail, T. Matsuura, and D. Oatley-Radcliffe, Eds., Elsevier, 2017, pp. 161–179. doi: 10.1016/B978-0-444-63776-5.00009-7.

[22] F. J. Giessibl, "Advances in atomic force microscopy," *Rev. Mod. Phys.*, vol. 75, no. 3, pp. 949–983, Jul. 2003, doi: 10.1103/RevModPhys.75.949.

[23] N. Ishida and V. S. Craig, "Direct measurement of interaction forces between surfaces in liquids using atomic force microscopy," *KONA Powder Part. J.*, vol. 36, pp. 187–200, 2019.

[24] P. Eaton and K. Batziou, "Artifacts and Practical Issues in Atomic Force Microscopy," in *Atomic Force Microscopy: Methods and Protocols*, N. C. Santos and F. A. Carvalho, Eds., in Methods in Molecular Biology. , New York, NY: Springer, 2019, pp. 3–28. doi: 10.1007/978-1-4939-8894-5_1.

[25] M. Hayat, *Basic Techniques For Transmission Electron Microscopy*. Elsevier, 2012.

[26] "Transmission Electron Microscopy | Nanoscience Instruments." Accessed: Nov. 28, 2023. [Online]. Available: https://www.nanoscience.com/techniques/transmission-electron-microscopy/

[27] J. J. Jiménez *et al.*, "Comprehensive (S)TEM characterization of polycrystalline GaN/AlN layers grown on LTCC substrates," *Ceram. Int.*, vol. 45, no. 7, pp. 9114–9125, May 2019, doi: 10.1016/j.ceramint.2019.01.250.

[28] C. Cushman, S. Chatterjee, G. Major, N. Smith, A. Roberts, and M. Linford, "Trends in Advanced XPS Instrumentation. 1. Overview of the Technique, Automation, High Sensitivity, Imaging, Snapshot Spectroscopy, Gas Cluster Ion Beams, and Multiple Analytical Techniques on the Instrument.," *Vac. Technol. Coat.*, Nov. 2016.

[29] "Gallium | XPS Periodic Table - FR." Accessed: May 11, 2023. [Online]. Available: https://www.thermofisher.com/fr/fr/home/materials-science/learning-center/periodic-table/other-metal/gallium.html

[30] Y.-H. Lai, C.-T. Yeh, J.-M. Hwang, H.-L. Hwang, C.-T. Chen, and W.-H. Hung, "Sputtering and Etching of GaN Surfaces," *J. Phys. Chem. B*, vol. 105, no. 41, pp. 10029–10036, Oct. 2001, doi: 10.1021/jp011728k.

[31] A. Jablonski and C. Powell, "Information depth and the mean escape depth in Auger electron spectroscopy and X-ray photoelectron spectroscopy," *J. Vac. Sci. Technol. Vac. Surf. Films*, vol. 21, pp. 274–283, Feb. 2003, doi: 10.1116/1.1538370.

[32] F. B. Nasr, A. Matoussi, R. Salh, S. Guermazi, H.-J. Fitting, and Z. Fakhfakh, "Cathodoluminescence study of undoped GaN films: Experiment and calculation," *Phys. E Low-Dimens. Syst. Nanostructures*, vol. 41, no. 3, pp. 454–459, 2009.

[33] "doi:10.1016/j.physe.2008.09.010 | Elsevier Enhanced Reader." Accessed: May 11, 2023. [Online]. Available: https://reader.elsevier.com/reader/sd/pii/S1386947708003615?token=8A052E9311B72D709D729E5E494D1368BBD3465F01B639DB49B430B2C8CFC8C7829FE60D2E8926577D8DEC0E8AC635D5&originRegion=eu-west-1&originCreation=20230511112238

[34] T. Bidaud, "Characterization of nanomaterials by cathodoluminescence for photovoltaic applications," phdthesis, Université Paris-Saclay, 2021. Accessed: Oct. 17, 2023. [Online]. Available: https://theses.hal.science/tel-03283375

[35] C. Tong, "III-V-on-Si nanowire-based solar cells for tandem applications," These de doctorat, université Paris-Saclay, 2023. Accessed: Feb. 27, 2024. [Online]. Available: https://www.theses.fr/2023UPAST044

[36] B. J. Skromme, J. Jayapalan, R. P. Vaudo, and V. M. Phanse, "Low-temperature luminescence of exciton and defect states in heteroepitaxial GaN grown by hydride vapor phase epitaxy," *Appl. Phys. Lett.*, vol. 74, no. 16, pp. 2358–2360, Apr. 1999, doi: 10.1063/1.123850.

[37] Z. Chine, B. Piriou, M. Oueslati, T. Boufaden, and B. El Jani, "Anti-Stokes photoluminescence of yellow band in GaN: evidence of two-photon excitation process," *J. Lumin.*, vol. 82, no. 1, pp. 81–84, Jul. 1999, doi: 10.1016/S0022-2313(99)00014-9.

[38] L. A. K. Staveley, *The Characterization of Chemical Purity: Organic Compounds*. Elsevier, 2016.

[39] C. Wetzel and I. Akasaki, "Raman and IR studies of GaN".

[40] A. Downes and A. Elfick, "Raman spectroscopy and related techniques in biomedicine," *Sensors*, vol. 10, no. 3, pp. 1871–1889, 2010.

[41] M. K. I. Westwood, "Amorphous GaN Grown by Room Temperature Molecular Beam Epitaxy," *Jpn. J. Appl. Phys.*, vol. 39, no. 8R, p. 4753, Aug. 2000, doi: 10.1143/JJAP.39.4753.

[42] A. Benninghoven, F. G. Rudenauer, and H. W. Werner, "Secondary ion mass spectrometry: basic concepts, instrumental aspects, applications and trends," Jan. 1987, Accessed: Apr. 27, 2023. [Online]. Available: https://www.osti.gov/biblio/6092161

[43] J. P. Hofmann, M. Rohnke, and B. M. Weckhuysen, "Recent advances in secondary ion mass spectrometry of solid acid catalysts: large zeolite crystals under bombardment," *Phys. Chem. Chem. Phys.*, vol. 16, no. 12, pp. 5465–5474, Feb. 2014, doi: 10.1039/C3CP54337D.

[44] J. Angeli, A. Bengtson, A. Bogaerts, V. Hoffmann, V.-D. Hodoroaba, and E. Steers, "Glow discharge optical emission spectrometry : moving towards reliable thin film analysis–a short review," *J. Anal. At. Spectrom.*, vol. 18, no. 6, pp. 670–679, 2003, doi: 10.1039/B301293J.

[45] "Instrument Introduction." Accessed: Nov. 27, 2023. [Online]. Available: https://www.horiba.com/sgp/scientific/technologies/glow-discharge-optical-emission-spectroscopy/instrument-introduction/

Chapter 3 – Plasma diagnostics

Table of Contents

Chapter 3 – Plasma diagnostics 43
3.1 TALIF diagnostic: on the determination of the N-atom density 44
3.1.1 TALIF diagnostic setup.. 45
3.1.2 N atom density calibration using Kr gas 47
3.1.3 Fluorescence signal measurement 49
3.1.4 Fluorescence lifetime & quenching.. 51
3.1.5 Quadratic regime identification... 52
3.1.6 N-atom density estimation.. 52
3.2 Microwave Interferometry (MWI): on the measurement of electron density 53
3.2.1 MWI diagnostic setup.. 53
3.2.2 Electron density measurements (n_e).. 55
3.3 Optical emission spectroscopy (OES) 55
3.3.1 Main emission features of the plasma 56
3.3.2 Estimating the characteristic temperatures of an Ar/N_2 plasma using OES 57
3.3.2.1 Estimation of the gas temperature using rotational lines 57
3.3.2.2 Estimation of the vibrational temperature... 60
3.3.2.3 Estimation of the excitation temperature 61
3.4 Plasma qualification & optimizations.. 63
3.4.1 Plasma stability... 63
3.4.2 Plasma contamination... 64
3.4.3 Plasma characteristics: density & temperatures 66
3.5 Conclusion 68
REFERENCES.. 70

Chapter 3 comprises of 4 sections. The three first sections elaborate on three specific plasma diagnostics, each of it aiming at determining useful quantities for understanding underlying processes behind the growth of GaN: (**3.1**) the N-atoms density, (**3.2**) the electron density and (**3.3**) temperatures (of molecules and electrons). The final section is on the overall qualification of the plasma, summarizing its main attributes in regards to the quantities mentioned above.

Before the first section, a small introductory part is presented providing an overview of the needs and applications of various plasma diagnostic techniques to characterize such discharge.

The first section is dedicated towards explaining the methodology of two-photon absorption laser induced fluorescence (TALIF) used to obtain the N-atom density. Details about the density calibration, lifetime decay and validation of the choice of laser energy is elaborately explained in this section.

The second section focuses on Microwave interferometry (MWI) diagnostics used to determine the electron density. The diagnostic setup along with the electron density variation across the pressure are presented.

The third section is dedicated to the characterization of our plasma using optical emission spectroscopy (OES). We first present the setup, give an overview of the main emissive species identified in our Ar/N_2 plasma discharge, and discuss on the effective sputtering of Ga atoms from the target. Then, we elaborate on the characteristic temperatures of the plasma under growth conditions, such as the kinetic gas temperature, the vibrational and the excitation temperature.

Finally, at the end of this chapter, we provide a qualification of the plasma across four parameters – plasma stability, plasma density, the plasma temperature and thin film contamination due to O impurities in the discharge.

For the deposition of GaN using plasma sputtering, precise knowledge of plasma characteristics is crucial for understanding and controlling the growth process. The characteristics comprises of a wide range of parameters, some of which important are the density of the reactive species (N, Ga, Ar), density and temperature of electrons, gas temperature, ion flux and ion energy distribution [1], [2]. Many different techniques are being employed for measuring the spatial profile and evolution of such parameters. Although most of them are already well established, plasma diagnostics is still a very challenging and vivid discipline[3]. In our case, we limit our discussion to laser aided diagnostics, emission spectroscopy and microwave diagnostics and we characterize our RF magnetron based Ar/N_2 plasma discharge using: i) Two photon absorption laser induced fluorescence (TALIF), ii) Microwave interferometry, and iii) Optical emission spectroscopy (OES).

As the main objective of the thesis is to obtain high quality GaN films, it is crucial to be able to understand and identify the conditions that affects the most it properties such as its uniformity and structure. A well-qualified plasma process represents the way to have a control of the grown film properties. The above-mentioned plasma diagnostic techniques helped us toward this goal. It is important to mention here that all the plasma characterizations were performed under regular conditions of growth, i.e. always with the presence of gallium target.

3.1 TALIF diagnostic: on the determination of the N-atom density

Atomic nitrogen's ground state is only accessible in the vacuum ultraviolet (VUV) range, which can be probed using absorption spectroscopy. This is however not straightforward since UV radiation source is required. To circumvent the need for VUV facilities, two-photon absorption laser-induced fluorescence (TALIF) was introduced [4], [5] and successfully used to probe the density of N atoms in our RF plasma discharge. Instead of directly absorbing a VUV photon, TALIF uses two lower-energy photons whose combined energy matches that of a single VUV photon. These photons are typically in the visible or near-infrared range, which are more readily available with standard laser systems. It is well known that the dissociation of N_2 molecules to generate atomic nitrogen species in a plasma is a tough task to achieve due to the strong N≡N bond. Therefore, most of the time, N_2 is mixed with argon to enhance its dissociation [6], [7]. For instance, Tabbal *et al.* have measured a dissociation degree of 2.5% at a pressure of 7.5 Torr (~ 1000 Pa) with Ar mixing ratio of 95% in a surface-wave-sustained plasma [8]. Many authors have characterized N_2 plasmas using several methods such as calibrated OES [9], OES actinometry[6], NO titration[10], VUV-absorption[11] or TALIF [12], [13]. However, these were mainly conducted in plasma discharges working under moderate- to high-pressure regimes (from hundreds of Pa to atmospheric pressure) such as inductively couple plasma (ICP)[14] or micro-hollow cathode discharges [15]. As far as magnetron-sputtering discharges are concerned, only a few studies are dealing with N-atoms density determination especially when considering the restriction on detection limit inherent to the low-pressure conditions. Even if TALIF seems to be well adapted to low-pressure plasmas since collisional quenching of excited states that prevails at high pressures can be discarded, the major drawback at lower pressures is that the strong background emission from N_2 FPS overlaps with weaker fluorescence signal due to lower density of N-atoms and thus making the measurement of the N-atoms absolute density challenging. In this work, we use nanosecond (ns)-TALIF to probe N atoms in a low-pressure plasma (~ a few Pascal) such as ours.

3.1.1 TALIF diagnostic setup

Figure 3.1 shows the experimental ns-TALIF schematic. The representation can be divided into two main parts: the laser and the fluorescence collection system.

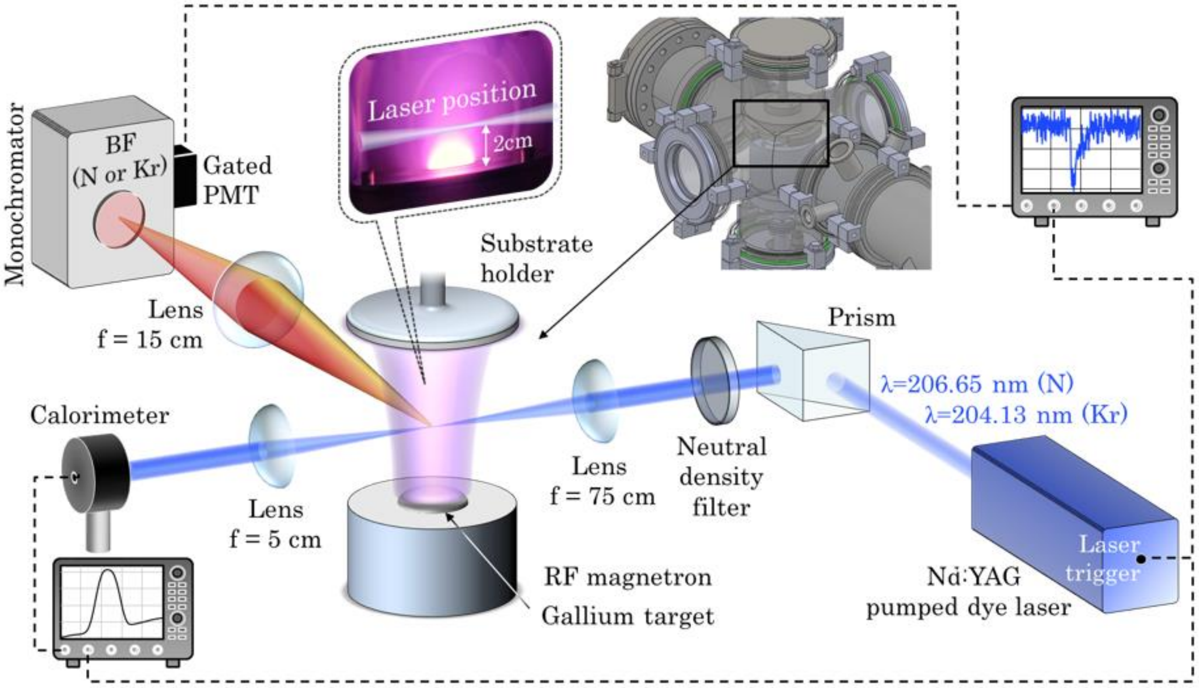

Figure 3.1: The schematic of a ns-TALIF experimental setup involving the Plasma PVD reactor.

The laser system

A tunable dye laser (Cobra-Stretch-Sirah Lasertechnik) was used for the ns-TALIF setup which is then pumped by the second harmonic of a 500mJ/pulse Nd:YAG laser YAG laser at 10 Hz that provides a pulse with a width of 10 ns (Quanta-Ray Lab-Series170-10 - Spectra-Physics). The dye laser beam was processed by two Beta Barium Borate (BBO) crystals, which yielded a laser beam with three harmonics separated using two fused silica Pellin-Broca prisms. We selected the desired third harmonic that was tuned in the regions of interest, i.e., 204 and 207 nm for Kr (204.221 nm) and N (206.767 nm) atoms, respectively. A typical energy value obtained for this harmonic is about 0.2 mJ.pulse^{-1}. The obtained pure UV-C radiation, that entered the reactor through a UV-fused silica window 2 cm above the cathode, was focused in order to have a beam diameter of 500 μm in the center of the reactor thanks to a lens with a 750 mm focal length (Figure 3.1). Subsequently, the laser beam exits the reactor through a second UV-fused silica window. Its diameter was adjusted using a 50 mm focal length lens to illuminate the calorimeter sensor (J-10MB-LE - Coherent) connected to an oscilloscope (TDS 3052, 500 MHz, 5 GS s^{-1} - Tektronix) that was placed at the laser line's end, ensuring continuous measurement of the laser's energy. Beforehand, it was confirmed that the plasma did not absorbs the laser, resulting in no discernible difference in measured energy with or without the presence of plasma. In contrast, the optical windows of the reactor partially absorb the laser radiation, affecting the laser beam's energy inside the reactor. To calculate the laser beam's energy in the reactor, we have taken into account the optical windows' transmittance by comparing it to the energy measured outside the reactor.

The fluorescence collection system

To determine the absolute density of N-atoms, we used the same experimental procedure as that thoroughly described in the work of E. Bisceglia *et al.*[16]. Once stimulated by the laser, the N-atoms undergo de-excitation, resulting in the emission of a fluorescence signal. This signal is then collected using a detection system, which consists of a monochromator (Model SP-2155, Princeton Instruments) and a gated photomultiplier tube (PMT - Hamamatsu, H11526-20-NF). The fluorescence is directed onto the monochromator positioned in front of the PMT with the aid of a 15-centimeter focal-length lens as described in Figure 3.1. The monochromator is equipped with a band pass filter used to select the appropriate wavelength range for the fluorescence of N (Semrock FF02-740/13-25) or Kr (Semrock FF02-586/15-25), the last being used for calibration purpose as detailed later. This configuration effectively enhances the Signal-to-Noise Ratio (SNR) of the TALIF signal by reducing the amount of background noise collected by the PMT. The fluorescence signal from the gated PMT was recorded by an oscilloscope.

Laser trigger and time delays

The visible portion of the dye laser beam was used in order to align the laser pulse with the gated PMT. This beam is directed towards a photo-diode, which is linked to an oscilloscope. The oscilloscope then generates a signal, which is sufficiently long (~ 1ms) to trigger a multi-function I/O device (National instruments USB). This additional step is necessary because the nanosecond signal produced by the laser is too small. Consequently, this device produces the necessary triggers for the PMT, taking into account the response times of all components and the length of the connecting cables. The laser trigger, laser pulse, the gate and the fluorescence signal from the PMT are depicted in the schematic from Figure 3.2.

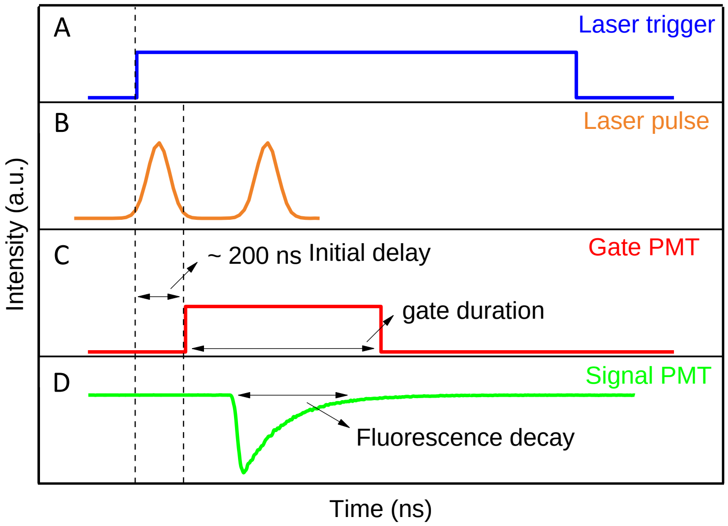

Figure 3.2: The different types of waveforms observed from the oscilloscope during the TALIF measurement. A. The laser trigger; B. the laser pulse; C. signal from the gate for the PMT and D. signal from the PMT.

The overall response time of the system, considering these factors, is approximately 200 nanoseconds. This, in conjunction with the previously mentioned 1ms signal, means that two laser pulses are required to conduct TALIF measurements (see Figure 3.2.B). The first pulse initiates the data collection system, while the second pulse generates the recorded fluorescence signal. An appropriate delay is thus introduced between the initial laser pulse and the gate of the PMT. The entire system, encompassing control of the laser, data collection, and data processing, is managed through a specialized LabVIEW program.

The gate is usually opened a few ns (~ 100 ns) before recording the signal from the PMT to avoid any stray oscillations during the de-excitation process (Figure 3.2.C). Specifically, for nitrogen with its low intensity signal, this process is necessary. The fluorescence decay rate is typically in the range of a few tens of ns. Once the laser is triggered, the gate and the signal from the PMT are aligned, and then we start measuring the fluorescence signal (Figure 3.2.D).

3.1.2 N atom density calibration using Kr gas

Before the N-atom density measurements, it is important to perform a calibration procedure to ensure that the measurements obtained from the TALIF setup are accurate, reliable and potentially identify any systematic deviations. Goehlich et al.[17] first introduced a calibration technique that uses a noble gas of known quantity to perform quantitative measurements of atomic densities using TALIF. This technique was used in this thesis to calculate the absolute nitrogen atom density. This approach relies on comparing TALIF measurements conducted in a noble gas with a known density to those of a specific atomic species of interest for which we aim at determining its density. The TALIF excitation processes for these two species should closely match in terms of laser excitation and emitted fluorescence wavelengths. This ensures minimal disparity in the laser setup and fluorescence collection optics between the two measurements. When dealing with nitrogen (N) atoms, krypton (Kr) gas is often chosen and commonly employed for calibration purposes [18]. Figure 3.3 represents the two-photon excitation and fluorescence scheme of krypton and nitrogen atoms.

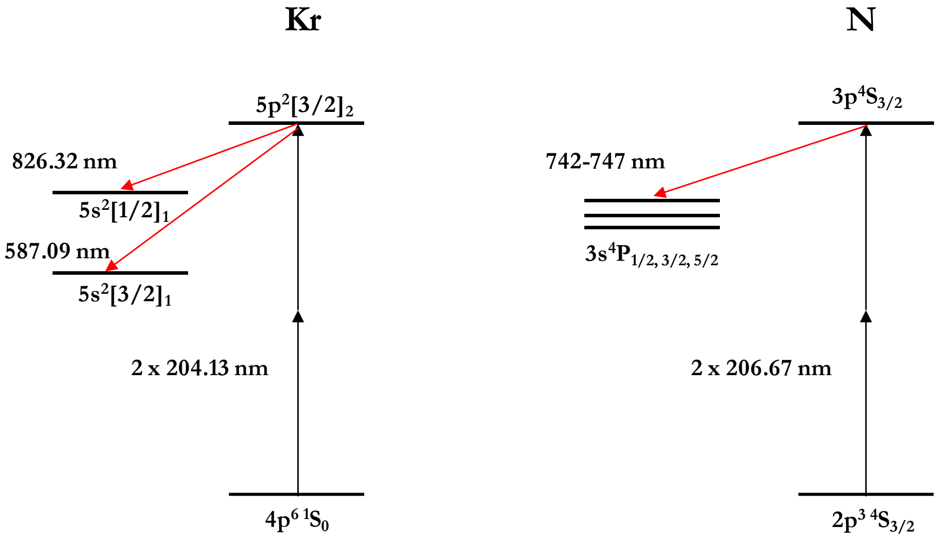

Figure 3.3: Two-photon excitation and fluorescence scheme of Krypton and Nitrogen atom. Adapted from the works of *E. Bisceglia, 2021* [19].

The two-photon-absorption wavelength values (approximately 2×204.13 nm) of Krypton closely match those of nitrogen atoms (~ 206.67 nm). Therefore, the same dye (Rhodamine 640) for TALIF measurements on nitrogen and krypton is used. In the krypton $5p^2[3/2]_2$ state, the primary fluorescent emissions are detected at 826.32 nm and 587.09 nm. Even though the radiative decay at 826.32 nm is more pronounced, the 587.09 nm line is chosen to capture krypton's fluorescence signal due to the potential for the 826.32 nm radiation to contain undesired Kr radiation lines stemming from other excited states of krypton [20], [21]. For nitrogen, the de-excitation from 3p $^4S_{3/2}$ to the states 3s $^4P_{1/2,3/2,5/2}$ produces three fluorescence lines at 742.364, 744.230, and 746.831 nm, which are collected by the PMT.

For quantifying the absolute atomic nitrogen density, we measured the fluorescence signal of nitrogen and compared its intensity with the fluorescence signal of Krypton. For calibration measurements, a cuvette filled with Kr at defined pressure was used [22]. However, for accuracy related to cross-section of the two-photon excitation and its fluorescence, we also filled the reactor with Krypton gas at a fixed pressure of 2 mbar and measure its fluorescence.
An equation comparing the fluorescence intensity of the gas with the known quantity (Krypton) and the gas with the species of interest (nitrogen) was proposed by S. Schröter et. al. (2020) [22] and we used it to determine the absolute atom nitrogen atom density:

$$\frac{S_{F,x}}{S_{F,cal}} = \frac{\eta(\lambda_{F,x})}{\eta(\lambda_{F,cal})}\frac{T_f(\lambda_{F,x})}{T_f(\lambda_{F,cal})}\frac{1}{T_c(\lambda_{F,cal})}\frac{a_{ik,x}}{a_{ik,cal}}\frac{\sigma_x^{(2)}}{\sigma_{cal}^{(2)}}\frac{n_x}{n_{cal}}\left(\frac{E_x\lambda_{L,x}}{(E_{cal}/T_c(\lambda_{L,cal}))\lambda_{L,cal}}\right)^2 \tag{3.1}$$

In equation (3.1), the terms denoted with 'x' refers to the values of nitrogen and the terms denoted with 'cal' refers to the values of Krypton. λ_F and λ_L refer to the wavelength of either the laser or fluorescence radiation. $S_{F,x}$ and $S_{F,cal}$ refer to the spectrally and temporally integrated fluorescence signals (integrals over wavelength and time). Here, $S_{F,x}$ and $S_{F,cal}$ are only the temporally integrated fluorescence intensities of nitrogen and krypton respectively since we consider the peak excitation method (PEM) to calculate the N-atom densities [19]. $\eta(\lambda)$ refers to the quantum efficiency of the detector system (PMT & monochromator) at the specific fluorescence wavelengths of krypton and nitrogen. $T_f(\lambda)$ is the transmission of the interference filter placed in front of the detector system for the respective fluorescence wavelengths of Kr and N. $T_c(\lambda)$ is single-wall transmission of the cuvette used for calibration. It is considered to be 1 as we don't use a cuvette to measure Krypton's fluorescence). $\sigma_{x,cal}^{(2)}$ refers to the two-photon excitation cross-section and $E_{x,cal}$ is the laser pulse energy. Assuming the laser-excited fluorescence state is denoted by the letter i, the branching ratio of the transmission into the lower start k is described as:

$$a_{ik} = \frac{A_{ik}}{\sum_k A_{ik} + \sum_q k_q^i n_q} = \frac{A_{ik}}{A_i + Q_i} = \frac{A_{ik}}{A_i}\frac{A_i}{A_i + Q_i} = b_{ik}\frac{\tau_{eff}}{\tau_{nat}} \tag{3.2}$$

a_{ik} is the decay rate for the transition from state i to k. τ_{nat} is the natural lifetime of the decay from the excited state which is the inverse of the sum of decay rates into all possible lower states $\tau_{nat} = (\sum_k A_{ik})^{-1}$ of the state i. The natural lifetime of Kr (5p[3/2]$_2$) is 34.1 ns [23]. b_{ik} is the purely optical branching ratio into a specific state k and τ_{eff} is the effective lifetime of the laser excited state. n_{cal} is the absolute krypton density that we measure and n_x is the absolute nitrogen density that we calculate. All the literature values used to calculate the N atom density from the above equations have been taken from the NIST atomic spectra database [24], which are represented in Table 3.1. The term $g_{v_{peak(X)}}$ from Table 3.1 refers to the measured two-photon absorption profile of the unknown gas (nitrogen) and the ratio $g_{v_{peak(Kr)}}/g_{v_{peak(N)}}$ corresponds to the inversed ratio of the FWHM ($FWHM_{(N)}/FWHM_{(Kr)}$[25]) corresponding to the laser energy profile, which is adapted to fit equation (3.1).

Table 3.1: Detailed list of the parameters used for N-atoms determination. "Meas." and "Manuf." stand for experimentally measured and manufacturer data, respectively

Parameter	$\int_t S_{F_{peak(X)}}$		η_X		T_X		$\frac{\sigma_{Kr}}{\sigma_N}$	A_X		τ_X		E_X		λ_X		$g_{v_{peak(X)}}$	
Unit	a.u.		no unit		no unit		no unit	s^{-1}		ns		µJ		nm		s	
X species	Kr	N	Kr	N	Kr	N	**NA**	Kr	N	Kr	N	Kr	N	Kr	N	Kr	N
Value	$7.96\text{x}10^{-9}$	Variable	0.468	0.4836	0.92	0.92	0.62	$1.17\text{x}10^{6}$	$3.38\text{x}10^{6}$	28.7	Pressure dependent	≈127	≈259	204.221	206.767	$6.28\text{ x}10^{-12}$	$7.12\text{ x}10^{-12}$
Uncertainty (%)	10	10	10	10	5	5	50	6	12	10	10	8	8	None	None	14	16
Reference	Meas.		Manuf.		Manuf.		Niemi *et al.*[23]	Niemi *et al.*[23]	Meas.	Meas.		Meas.		Meas.		Meas.	Meas.

3.1.3 Fluorescence signal measurement

The calculation of N-atoms density using TALIF is generally done using the full excitation method (FEM) [17], [26], [27]. The use of FEM requires the knowledge of the profiles of the laser beam and the absorption lines of N-atom and Kr-atom. In particular, the absorption line profiles depend on the local plasma conditions and are not always easy to determine from experiments [21], [28], [29]. It requires calculating terms such as the Doppler broadening of the absorption lines and the gas temperature. Additionally, the use of FEM requires the determination of the time and frequency integrated fluorescence signals for each density value measurements. A simplified process for measurement is to use the peak excitation method (PEM) [19]. In this method, the N-atoms density can be readily determined using a single laser shot at a central wavelength of the krypton's and nitrogen's fluorescence. This is done by capturing the fluorescence signals of Kr and N generated by several laser pulses over a range of central wavelength values and integrating each fluorescence signal temporally over the whole central wavelength range. The use of the peak value of the temporal integral of the fluorescence signal enables achieving the maximum overlap between the laser and the absorption lines, thereby limiting the uncertainties of the measured N-atoms density [30].

PEM is valid as long as the spectral profiles of the absorption lines chosen for TALIF measurements do not change over the investigated plasma conditions. The approach seems to be particularly suitable for low temperature and low-pressure plasmas where the change in line broadening width due to Doppler and Stark effects remain limited [19], [29]. The difference between the FEM and PEM methods are explained thoroughly elsewhere [19]. Hence, to calculate the N atom densities, we use the peak excitation method (PEM) scheme.

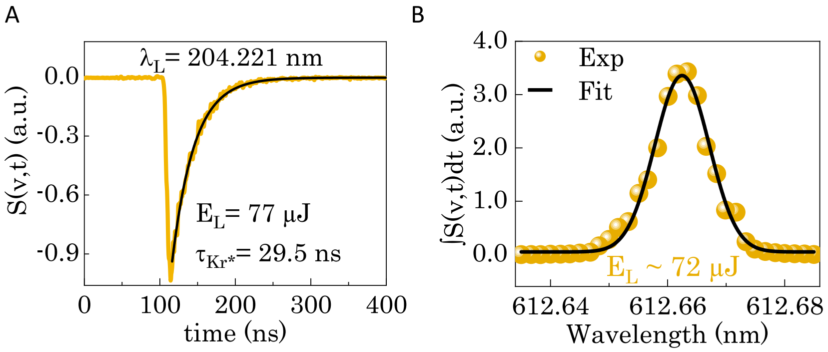

Figure 3.4: Krypton fluorescence measurements at a pressure of 200 Pascal, laser energy E_L ~ 77µJ and excited at a laser central wavelength λ_L~ 204.221 nm. A. Krypton Fluorescence signal with an effective lifetime ($\tau_{eff,Kr}$) of 29.5 ns. B. Temporally integrated fluorescence signal of Krypton over a range of laser central wavelengths.

For our measurements, at each process conditions, we calculated the N-atom density by considering the peak value of the temporal integral of the fluorescence signal from N and Kr. Figure 3.4 represents the fluorescence measurements obtained for Krypton gas at a defined pressure of 2 mbar ~ 200 Pascal. Figure 3.4.A depicts the signal captured by the gated PMT, which is the de-excitation of the excited Kr atom that produces the fluorescence. The black line here indicates the decay of the fluorescence signal from which the decay of the population of the upper state Kr* ($\tau_{eff,Kr}$) is calculated to be ~ 29.5 ns. The data points from Figure 3.4.B represent the temporally integrated fluorescence signal; these points are measured over a range of laser central wavelength. The corresponding Gaussian fit of the profile is shown by the black curve. For calculating the N-atom density from equation (3.1), the peak value of the Gaussian fit was chosen for $S_{F,cal}$.

Figure 3.5 represents the fluorescence measurements obtained for nitrogen in the Ar/N$_2$ plasma at a few tens of Pascals. The central laser wavelength λ_L was kept at ~ 206.767 nm. The fluorescence decay of the populated excited state of nitrogen (N*) yielded an effective lifetime ($\tau_{eff,N}$) of 27.1 ns (depicted by the yellow line in Figure 3.5.A). Similar to Krypton, the temporal integral of the fluorescence signal at different wavelengths was measured and plotted as shown in Figure 3.5.B. The peak value of the Gaussian fit (black line) was chosen to represent $S_{F,x}$ from equation (3.1), which was essential for calculating the N-atom density.

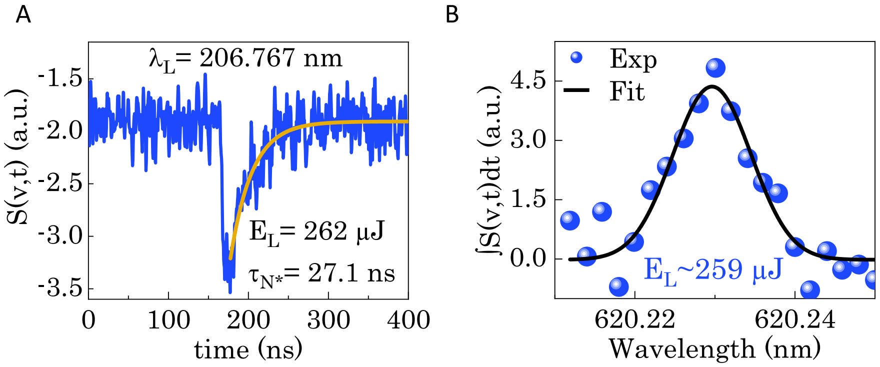

Figure 3.5: Nitrogen fluorescence measurements at a pressure of ~ 20 Pascal, laser energy E_L ~ 262 μJ and excited at a laser central wavelength λ_L~ 206.767 nm. A. Nitrogen Fluorescence signal with an effective lifetime ($\tau_{eff,N}$) of 27.1 ns. B. Temporally integrated fluorescence signal of nitrogen over a range of laser central wavelengths.

It is important to note here that the fluorescence signal intensity (PMT signal observed in oscilloscope in terms of voltage) of nitrogen comprises of a strong background emission unlike krypton. This is because Kr gas exists in its atomic state while nitrogen gas exists in its molecular state. The scarcity of enough N atoms at such a low-pressure system (~ a few Pascal) makes it difficult to extract the fluorescence signal necessary to calculate the absolute N-atom densities.

Error estimation and uncertainties

There are several error factors to be considered while obtaining the N-atom density using TALIF. The basic ones are the systematic and statistical errors. The systematic error arises due to the reproducibility of the measurement itself. In our case, for each process parameter variation (RF Power, Pressure and N$_2$ flow variation, the TALIF measurement process was repeated thrice and the grouped standard deviation was calculated and this value was considered as the systematic error. The statistical error arises due to the individual variables from equation (3.1), which is used to calculate the N-atom density. The uncertainties on the time integrated peak fluorescence intensity ($\int S(v,t)\,dt$) using the PEM scheme correspond to around 10-15% of the global relative error on the density [19], [31]. We consider this value to be 15% of the calculated N-atom density for all our measurements. Apart from this, the largest contribution to the relative error on nitrogen atom density comes by far from the uncertainty on the ratio of the two-photon absorption cross-sections for nitrogen and krypton, which amounts to ~ 50% [19], [32]. The second error source comes from the uncertainty on the krypton radiative lifetime, which is 20% [31]. In the following, the systematic error associated with each determined N-atoms density will not be shown as it is close to 60%, mainly due to the 50% uncertainty of the value of the two-photon absorption cross section ratio. Therefore, only the average values are displayed along with the statistical error obtained by calculating the standard deviation from three independent measurements.

3.1.4 Fluorescence lifetime & quenching

The effective lifetime (τ_{eff}) of the laser excited state from equation (3.1), is an important factor that needs to be measured in our experiment. The precise knowledge of the effective lifetime for the excited states of both Kr and N is essential for reliable quantitative measurements of the N atom density. It is measured by fitting the exponential decay of the fluorescence signal of the desired species (Kr or N) obtained from the PMT that corresponds to the decay of the population of the excited state of Kr or N. τ_{eff} takes both the natural lifetime and the radiation-less collisional de-excitation (quenching) via collisions of the excited states into account. For the Krypton gas, the calibration measurements were performed at 200 Pa and the measured effective lifetime was ~ 29 ns. This value is very close to the value obtained when computing the Kr excited state radiative lifetime from the Einstein coefficient recommended by the NIST database [24] which is ~ 28.5 ns. At 200 Pa, we can therefore consider the quenching of the Kr atom to be negligible and the radiative lifetime of the Kr excited state is almost equal to the fluorescence decay time ($\tau_{eff,Kr}$) of Krypton.

For nitrogen, Figure 3.5.A shows the fluorescence signal. Fitting the exponential decay of the signal from the PMT gives us the N* decay rate(τ_{N^*}) which is the effective lifetime. This is calculated to be approximately 27 ns. The effective lifetime for nitrogen (τ_{N^*}) is expressed as [33]:

$$\frac{1}{\tau_{N^*}} = \frac{1}{\tau_{r,N^*}} + k_{qN_2}[N_2] + k_{qAr}[Ar] \tag{3.3}$$

$$= \frac{1}{\tau_{r,N^*}} + P \times \frac{10^{-2}}{k_B T} \times [k_{qN_2}x_{N_2} + k_{qAr}(1 - x_{N_2})] \tag{3.4}$$

Here, k_{qN_2} and k_{qAr} are the quenching rates of excited N atom (N*) by N_2 and Ar respectively in cm^3s^{-1}; [N_2] and [Ar] the densities of N_2 and Ar respectively in cm^{-3}. P is the working pressure in Pascal; k_B is the Boltzmann constant in JK^{-1}; T is the gas temperature in K; and x_{N_2} is the fraction of N_2 in the gas mixture. τ_{r,N^*} is the natural radiation de-excitation decay of the excited level (N*). τ_{r,N^*} can be calculated using the Stern-Volmer plot [34], [35] which is the inverse of the intercept from equation (3.4) for different fractions of N_2 in the Ar/N_2 gas mixture. The Stern-Volmer plot measured in our case was taken for a pure N_2 gas with no Ar (100% N_2 ~ x_{N_2}=1) which is shown in Figure 3.6.

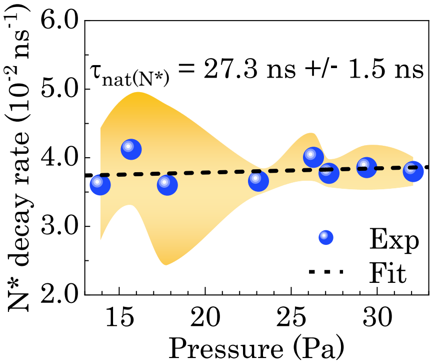

Figure 3.6: Stern-Volmer plot depicting the excited N atom's decay rate during the fluorescence emission w.r.t the working pressure (Pa). Each data point (blue circle) represents the lifetime of the de-excitation process, which produces the fluorescence (τ_{N^*}). The yellow gradient in the background depicts the error bar of the data set.

The natural radiative de-excitation decay ($\tau_{r,N^*} = \tau_{nat(N^*)}$) of the excited level is measured to be ~ 27.3 ns. On comparing the effective lifetime and the natural radiative lifetime of the excited N atom (τ_{N^*} and τ_{r,N^*}), we find out that they both have a similar value close to 27 ns. Looking back at equation (3.3), this reveals that quenching rate of the excited N atom N* by N_2 (k_{qN_2}) is considered to be negligible at these low pressures (a few tens of Pascal). Although, it is important to note that at higher pressure (a few thousand Pascal), the quenching rates have a significant value that distinguishes the effective lifetime from the radiative lifetime and needs to be considered.

3.1.5 Quadratic regime identification

The validity of equation (3.1) mentioned above to calculate the absolute nitrogen atom density depends on the assumption that the laser-atom interaction is dominated by the two-photon laser absorption. But it is important to consider that several phenomenon such as stimulated emission, photo-ionization (when a third photon is absorbed by the already excited atom) and photo-dissociation can occur if the instantaneous laser power and the local power density are too high [27], [36]. The range of laser energy where there is a dominance of the two-photon laser absorption is called the quadratic regime. The power dependence factor is a useful term that ensures the above conditions are fulfilled [37]. It can be mathematically represented as the linear fit of the integral of the TALIF signal versus the square of the laser energy. When the two-photon laser absorption dominates over the other phenomena, the power dependence factor is usually close to 1. Figure 3.7 represents the log-log plot of the temporally integrated TALIF signal at various values of the squared laser energies for krypton and nitrogen.

The laser energy was varied using neutral density filters placed on the path of the laser beam. The linear fits for both krypton and nitrogen are plotted in Figure 3.7. The slope of the linear fit is equal to 1 (1 ± 0.04) for Krypton and almost equal to 1 (1.17 ± 0.16) for Nitrogen with a slight deviation.

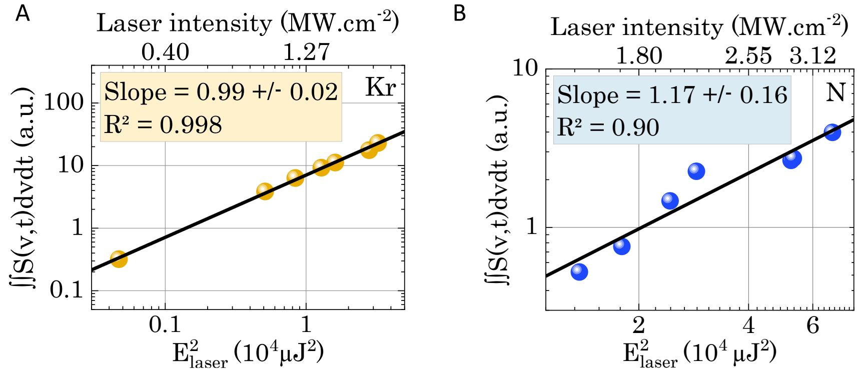

Figure 3.7: Temporally integrated TALIF signal as a function of the square of the laser energy for A. Krypton and B. Nitrogen. *The black line corresponds to the associated linear fit of the data points.*

The deviation might be due to the weak fluorescence signal measured for nitrogen, which is almost 100 times lower in intensity when compared with the fluorescence signal of Krypton. Nevertheless, the power dependence factor is still close to 1 and it could be agreed that for both krypton and nitrogen, the laser-atom interaction is dominated by the two-photon absorption. Thus, equation (3.1) can be used for the determination of absolute nitrogen atom density in the plasma discharge in this particular energy range.

3.1.6 N-atom density estimation

TALIF experiments were conducted at a pressure range of 16-32 Pa. This was mainly due to the fact that at low pressures (< 15 Pa), we could not obtain the fluorescence signal of nitrogen atom and hence could not calculate the atomic density. An important point to note here is that the GaN growth window with respect to pressure in our reactor was between 2-15 Pa, so unfortunately, the exact estimation of N-atom densities at the growth conditions of GaN could not be performed. However, the estimated density trends at a slightly higher working pressure could still yield us with useful information.

Figure 3.8 represents the N-atom density across the pressure range of 15-35 Pa. The fluorescence signal obtained at each pressure is marked in the inset of the figure.

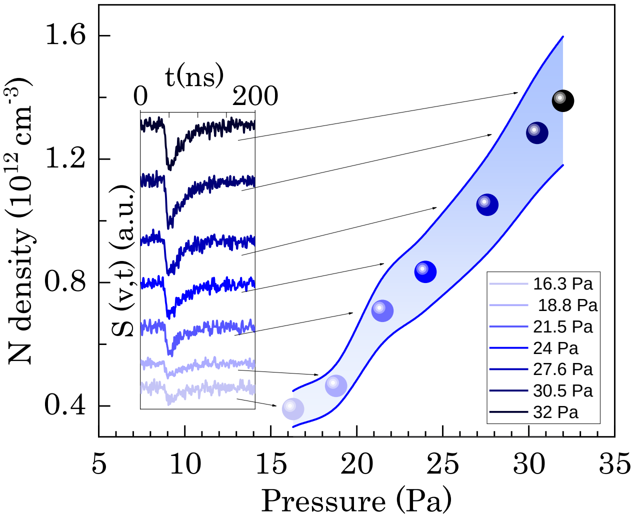

Figure 3.8: Nitrogen atom density plotted at a pressure range of 15-35 Pa. The inset shows the fluorescence signal obtained during the TALIF measurement at each pressure.

In our plasma discharge, the N-atom density ranges from 10^{11} cm^{-3} ~ 10^{12} cm^{-3} which is in the same range other process involving Ar/N_2 plasma in process conditions close to ours [38]. Regarding the trends w.r.t pressure, we observe a progressive increase of the N-atoms density from 4×10^{11} to 1.4×10^{12} cm^{-3} by varying the pressure from 16 Pa to 32 Pa, respectively. Within the investigated pressure range, the N-atoms density increases by a factor of 3.25 while the pressure increases by a factor of 2. It is noteworthy that the operation of such plasma source at pressures as high as 30 Pa may be beneficial for applications in which the strong production of N-atoms is desirable. For instance, this would represent a way to increase the growth rate of nitride-based coatings or to improve the efficiency of nitridation processes while working at relatively low pressure that ensures low-level of contamination.

A possible cause leading to the increase of the N-atoms density as a function of the pressure may be the enhancement of the electron density, which induces a larger dissociation degree of N_2 through direct (i.e., $e^- + N_2 \rightarrow N + N$) or indirect mechanisms, e.g., through electron collisions with vibrationally excited N_2 molecules[14]. To examine such cause, we measure the electron density as a function of the pressure, which is presented in the next section.

3.2 Microwave Interferometry (MWI): on the measurement of electron density

Electron density measurements are usually performed using Langmuir probe [39]. However, in reactive deposition plasmas such as ours, the deposition on the probe surface makes it practically unusable as it leads to misinterpretation. At the contrary, Microwave interferometry (MWI) is a non-invasive technique, makings it an attractive system and hence used in a wide array of plasma systems from low temperature vacuum deposition to fusion experiments [40], [41]. Additionally, the interpretation of the measurements in a MWI system is much simpler when compared to Langmuir probe, where information about ion composition and plasma sheaths are required. Basically, MWI relies on the uses microwave radiation to infer plasma dielectric properties which are related directly to the electron density. In a simplified explanation, it is inferred from phase shift and attenuation of the microwaves by the plasma.

3.2.1 MWI diagnostic setup

We used a Miwitron MWI 2650 system for our measurements loaned by the "Réseau des Plasmas Froids", the national French plasma network in collaboration with Cédric Noel from Institut Jean Lamour. The schematic of the system is presented in Figure 3.9. The system comprises of two microwave units with antennas, one is emitting a microwave beam at 26.5 GHz, and the other acting as a receiver. For this purpose, the reactor was equipped with BK7 windows on either sides transparent to microwave radiation. The transmitting and the receiving units were connected together using coaxial cables. The transmitting unit is connected to the control unit using a coaxial cable. The control unit contains a digital unit to display the value of electron density being measured. The calibration of the system was done by entering value of plasma length (plasma size or width parallel to the line of transmission). As the plasma path length varies as a function of the process conditions, we recorded a picture of the plasma for each investigated process conditions and determined the path length, i.e. the plasma diameter along the line of sight of the microwave radiations (shown in Figure 3.9).

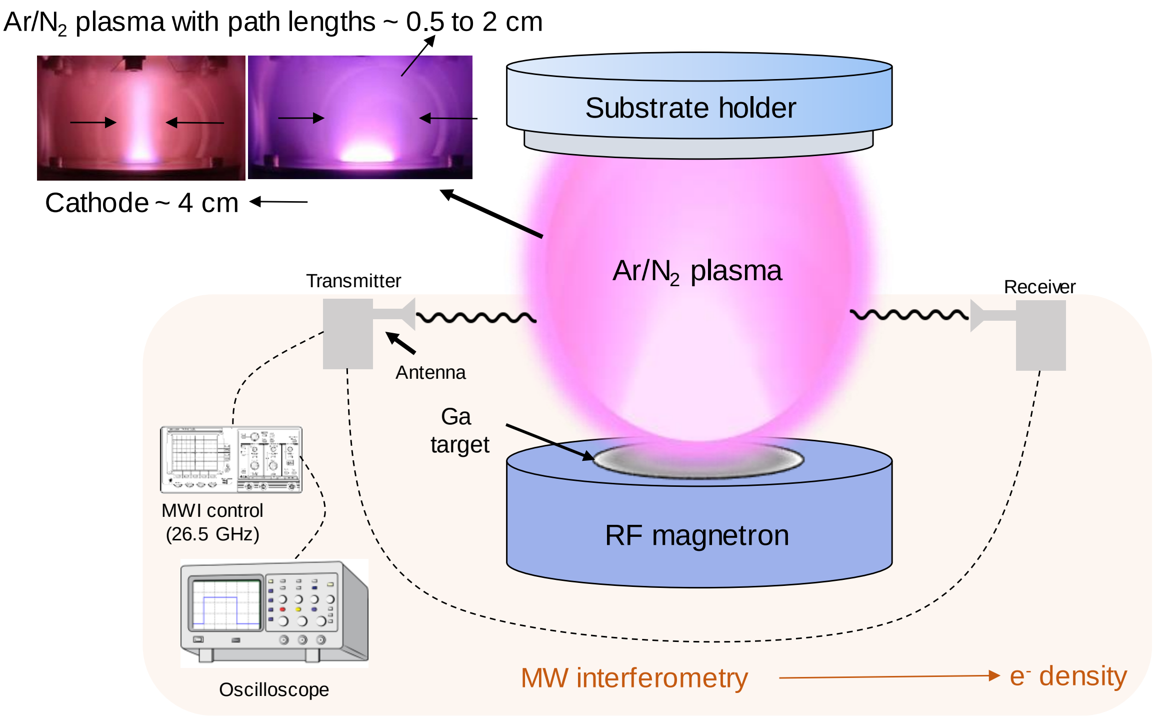

Figure 3.9: Schematics of the Microwave interferometry (MWI) setup adjusting to our plasma PVD reactor system. The transmitter and the receiver units are connected via coaxial cables and are placed just outside the windows on either sides.

We the measures the phase shift of microwave radiation produced by the Ar/N$_2$ plasma placed in the primary transmission path of the interferometer in respect to a phase of a radiation taken from an auxiliary transmission path of the interferometer serving for the phase reference. Since we used a low-pressure plasma, this phase shift is essentially a function of the plasma electron density alone. As the phase shift is calibrated, we can do continuous measurement of density between the upper limit of strong refraction effects near the plasma critical density and the low limit of phase sensitivity of the interferometer [42], [43]. Since the measured signal was integrated along the transmission path of microwaves in plasma, the value of electron density determined is averaged over the transmission path length. The minimum phase shift angle that the control unit can go is 0.1^{o}; which corresponds to the minimum electron density that could be measured ~ 1 x 10^{-9} cm^{-3}. The minimum path length provided by the control unit is 5.5 cm. For even shorter plasma path lengths, we use a correction factor by dividing the path length limit (5.5 cm) by the actual plasma path length. The average electron density is calculated using the formula:

$$\bar{n} = 5.4 \times 10^{10} \times \Delta\varphi \left[\frac{1}{L}\right] cm^{-3} \tag{3.5}$$

$\bar{n}$ is the average electron density, $\Delta\varphi$ the phase shift and L the plasma path length. It is important to ensure the base limit is levelled before each measurement. The electron density is displayed directly on the control unit. However, the base limit also called as the zero point fluctuates frequently and is hard to keep track. For accuracy, we connect an oscilloscope to the control unit and measure the voltage across time. The phase shift from equation 3.5 can be calculated using the relation 1mV = 0.1°. This is true for a path length of 5.5 cm. We then use the correction factor and determine the plasma electron density at various process conditions.

3.2.2 Electron density measurements (n_e)

As an example, we present the n_e measured across varying a single process parameter - the working pressure. Figure 3.10 depicts the electron density measurements at a pressure range 1-35 Pa. Within this range, the n_e ranges from 10^{10} ~ 10^{11} cm^{-3}, which is again in agreement with that measured in typical low pressure Ar-N_2 plasma discharge [44], [45]. Unlike TALIF where no fluorescence was observed at low pressure ranges (1-15 Pa), the electron density values could be measured for the entire pressure range (1-35 Pa) thereby focusing also on the growth range of GaN (2-15 Pa). Since we have estimated electron density at this range and know the trends of both N-atom densities and electron densities, one could extrapolate the values of N-atom densities from TALIF at low pressures (< 15 Pa) using modeling studies.

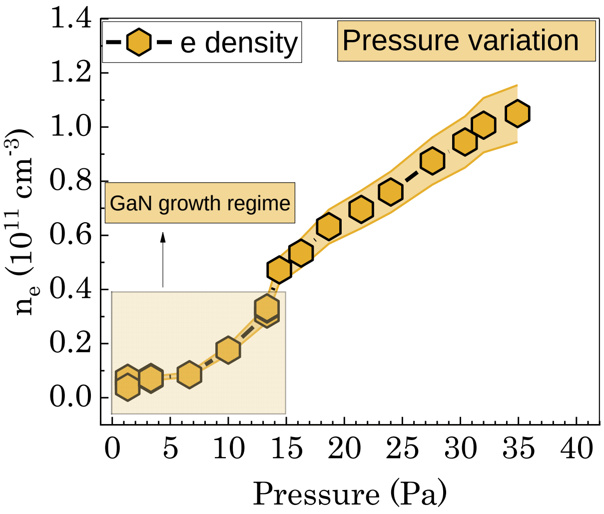

Figure 3.10: Electron density (n_e) plotted vs the working pressure range of 0-35 Pa. The patterned inset from 2-15 Pa depicts the growth regime that was used to deposit GaN.

Throughout the pressure range, the electron density keeps increasing. This might be due to the increased collision frequency between the plasma species as the pressure increases [44]. It is important to note here that, apart from the working pressure, process parameters such as the N_2 flow and the RF power were also considered for the electron and N-atom density estimation, which will be useful to link the trends in growth quality of GaN films and will be presented in Chapter 4.

3.3 Optical emission spectroscopy (OES)

In this thesis, we extensively used OES for several purposes:

(i) to globally qualify the discharge, especially when the reactor was launched, in order to monitor the main emissive species in the Ar/N_2 discharge and also to identify the conditions at which the Ga-atoms ejection was maximal.

(ii) we are interested in measuring the gas, vibrational and electron temperatures as a function of main growth process parameters and hence we use OES to characterize the plasma temperature.

Also, for purpose of process optimization, OES was used to optimize the process as we faced oxygen contamination of the samples due to impurities present in the plasma. This will be discussed in the last section of this chapter dedicated to plasma qualification and optimization. Hereafter, we will focus on the point (i) and (ii).

3.3.1 Main emission features of the plasma

As introduced in chapter 1, in sputtering process, Argon (Ar) is primarily utilized for its substantial mass, which maximizes the ejection of Gallium (Ga) atoms, while nitrogen (N_2) serves as a source of nitrogen atom precursors in the gaseous phase. Nevertheless, achieving a high concentration of nitrogen atoms is a known to be challenging due to the strong triple bond (bond energy ~ 945 kJ/mol) connecting the two atoms of N_2 [46]. Therefore, the role of argon in the discharge extends beyond simply facilitating sputtering; it may also contribute to augmenting nitrogen atom production through an energy transfer process involving Ar metastable species [47], [48]. To assess the conditions that favor gallium sputtering while ensuring robust N_2 emission, we employed Optical Emission Spectroscopy (OES) as a straightforward and non-intrusive qualitative technique. Optical emission spectroscopy (OES) was performed using an AVANTES Avaspec-ULS4096 CL-EVO spectrometer that has a slit width of 10 µm, a resolution (FWHM) of 0.7 nm and a spectral coverage in the UV-VIS region (from 200-750 nm).

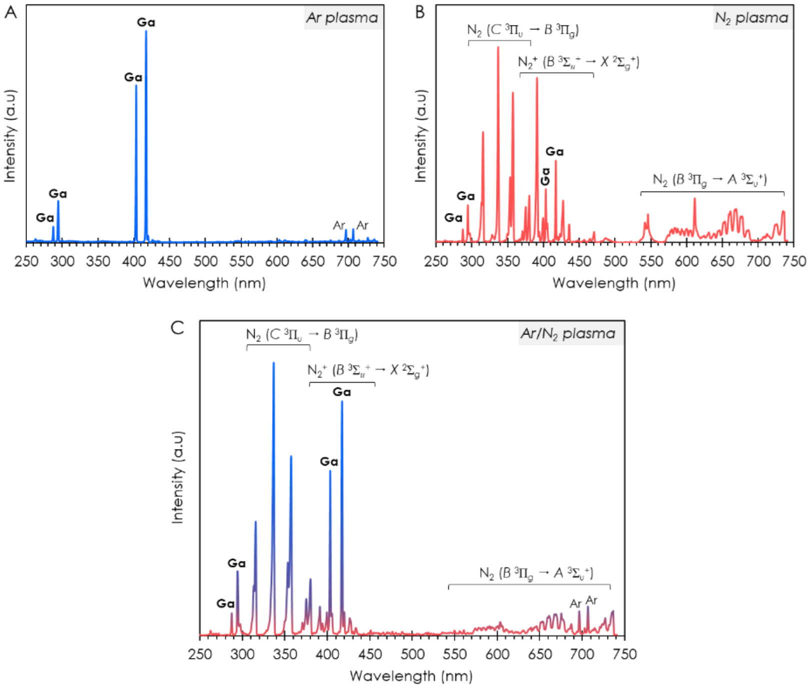

Figure 3.11: Optical emission spectra from the plasma PVD reactor. A. Ar plasma at 50mTorr, 100W depicting the atomic Ga lines. B. N_2 plasma at 50mTorr, 100W depicting the molecular and atomic nitrogen lines and atomic Ga lines. C. Ar/N_2 plasma at 50mTorr, 100W showing strong atomic Ga lines along with the nitrogen emission lines.

Figure 3.11 illustrates the optical emission spectra of three different plasma types: pure Ar plasma (A), pure N_2 plasma (B), and Ar/N_2 plasma used for GaN film deposition (C). These spectra are presented for the purpose of peaks identification and to highlight the advantages of combining Ar to N_2 to enhance Ga sputtering. It is evident that while pure N_2 plasma induces the ejection of Ga atoms (Figure 3.11.B), the addition of Ar further enhances this process and leads to strong N_2 emission (Figure 3.11.C).

The prominent peaks observed in the wavelength range of 300-400 nm (Figure 3.11.C) correspond to various transition lines from the N_2 second positive band system (SPS).

The major peaks observed in these spectra correspond to transition lines associated with molecular nitrogen, gallium, and argon. Figure 3.11.C exhibits molecular features originating N_2 second positive band system (SPS): $(C^3\Pi_u(\nu') \rightarrow B^3\Pi_g(\nu''))$, N_2^+ first negative system (FNS): $(B^2\Sigma_u^+(\nu') \rightarrow X^2\Sigma_g^+(\nu''))$ and N_2 first positive system (FPS):

$(B^3\Pi_g(\nu') \rightarrow A^3\Sigma_u^+(\nu''))$, where ν' and ν'' are the vibrational quantum numbers of the upper and lower states [44]. The intense emission lines within the 300 to 370 nm range in the SPS region indicate excitation and quenching processes from the ground state, facilitated by collision with metastable species. This results in the overpopulation of $N_2(C^3\Pi_u)$. In contrast, the peaks from FNS are weaker due to the higher threshold energies required for excitation compared to SPS. The resonant transitions of gallium [49] are also evident, with sputtered Ga atoms in the Ar-N_2 plasma being excited to the metastable ($5s^2S_{1/2}$) level through collisions with excited species, followed by radiative decay with emissions at 403.3 and 417 nm [50]. Again, these observations highlight the advantages of using an Ar/N_2 mixture over pure N_2, as the addition of Ar not only promotes Ga atom ejection but also results in strong N_2 emission.

3.3.2 Estimating the characteristic temperatures of an Ar/N$_2$ plasma using OES

Glow discharges at low gas pressures (a few Pa) are non-equilibrium plasmas where the electron temperature (T_e) is always higher than the neutral gas temperature (T_{gas}). Given that our plasma system possesses a low electron density (~10^9 - 10^{11} cm^{-3} as measured from interferometry) , wherein radiative processes prevail over collisional processes, it falls within the corona balance category and is acknowledged as a non-local thermal equilibrium (LTE) plasma [51]. Molecular gases such a N_2 in our discharge can be characterized by their vibrational T_{vib} and rotational temperatures T_{rot} in addition to the electron and gas temperatures. The characteristic temperatures generally follow a classical inequality [52] : $T_e > T_{vib} > T_{rot} \sim T_{gas}$. In this study, we try to estimate three different characteristic temperatures in our Ar-N_2 discharge – I) the rotational temperature (T_{rot}) – provides us with an estimate of the gas temperature. As electrons have limited effectiveness in imparting rotational energy to molecules due to their small mass, the distribution of rotational states is regulated by collisions with heavier particles [53] . II) Vibrational temperature (T_{vib}) & III) Excitation temperature (T_{exc}) – since both vibrational and excitation transitions are primarily dominated by electronic collisions, their populations provides an insight into the electron temperature (T_e) [51].

In this study, to estimate the rotational temperatures of N_2 (SPS & FNS), we used a high-resolution OES setup (HR-OES) with a resolution of 0.006 nm. The experiments to determine the vibrational temperature of N_2 SPS and excitation temperature of our plasma system were done using a low-resolution spectrometer (AVANTES) with a resolution of 0.3 nm. The whole study was carried out at the Laboratoire des Sciences des Procédés et des Matériaux (LSPM) at Villetaneuse.

3.3.2.1 Estimation of the gas temperature using rotational lines

Gas temperature measurements in non-equilibrium plasmas are frequently acquired through emission spectroscopy, specifically by analyzing the population distribution across rotational levels of excited states in diatomic molecules (referred to as rotational temperature). This approach has been successfully employed for many years [54], [55]. We particularly focus on the rotational levels of N_2. The rotational temperature (T_{rot}) of N_2 can be established by utilizing any rotational band within the emission spectrum of nitrogen or a similar molecular gas. In the case of nitrogen, this determination is feasible by employing specific bands, such as the second positive system (SPS) bands at 337.4 or 380.4 nm or the first negative system at 391.4 nm (FNS) [56]. As mentioned before, we use a high-resolution spectrometer for this purpose and for determining the rotational temperature; we use the 337 nm spectra of N_2 SPS and the 391.4 nm spectra from N_2 FNS.

Donnelly et al [57], described that the T_{rot} can be determined by comparing the experimental spectrum of a particular rovibrational band to a synthetic spectrum calculated for various rotational temperatures. In order to determine T_{rot}, the recorded rotational emission spectrum is fitted with a simulated spectrum generated by the software "Massive-OES" [58]. A typical spectrum of the (0, 0) band at 337 nm (N_2 SPS) and the N_2^+ FNS is presented in Figure 3.12.A&B. The rotational temperature was obtained by comparing the relative intensities of the various lines of the emission band. A conventional Boltzmann plot method can be used to determine the rotational temperature. As an example, if we consider the 337 nm emission band, for a transition from a rotational level J' in the upper vibronic state $(C^3\Pi_u, \upsilon')$, to a rotational level J'' in the lower vibronic state $(B^3\Pi_g, v'')$, the relation between the intensity of the emission line and the rotational temperature can be expressed as: [59]

$$I(J',J'') = aS(J',J'')\exp\left(-E(J')/k_BT_{rot}\right) \tag{3.6}$$

where a is a constant that depends on the spectral response of the imaging system, $S(J',J'')$ is the line strength for each transition, $E(J')$ is the rotational energy of the level, J' and k_B is the Boltzmann constant. The above relation can be expressed in terms of wavelength and transition probability [60]:

$$\ln\left(\frac{I\lambda}{AG}\right) = B - \frac{E_k}{k_BT_{rot}} \tag{3.7}$$

where, I denotes the total intensity, A refers to the transition probability. G is the degeneracy of the upper level (statistical weight), λ is the wavelength and E_k is the excitation energy. T_{rot} is calculated from the slope of the Boltzmann plot between $\ln\left(\frac{I\lambda}{AG}\right)$ vs the excitation energy E_k from equation (3.7).

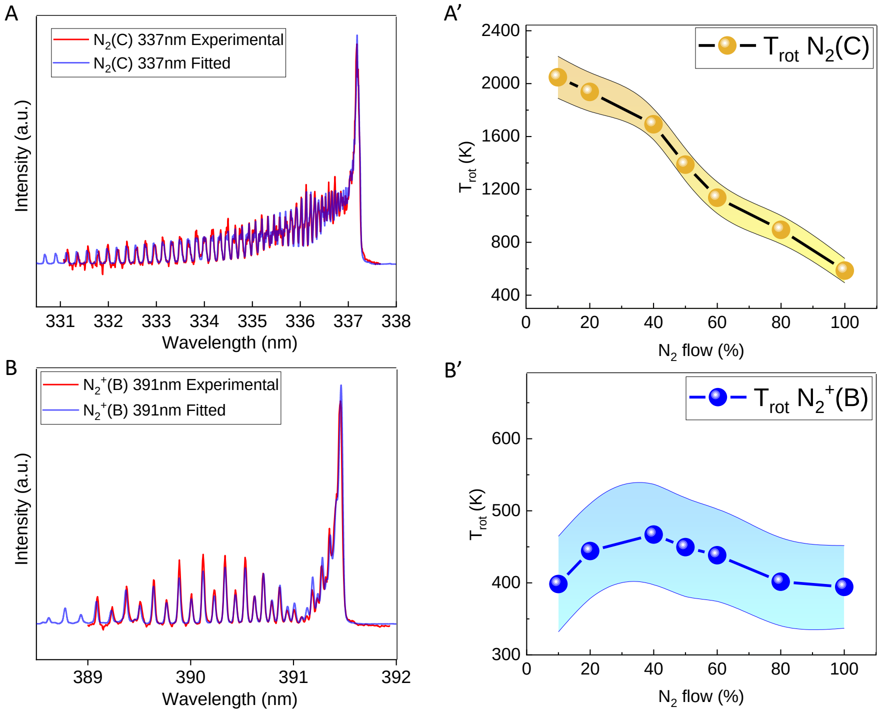

Figure 3.12: A. Experimental (red) and the simulated (blue) time-averaged rotational emission spectra of the N_2 (SPS) at 337.4 nm used to determine the rotational temperature ((T_{rot} N_2 (C)). A'. The corresponding T_{rot} N_2 (C) vs N_2 fraction in the Ar/N_2 gas mixture. B. The time averaged rotational emission spectra of the N_2^+ (FNS) at 391.4 nm used to determine the rotational temperature (T_{rot} N_2^+ (B)). B'. The T_{rot} N_2^+ (B) vs N_2 fraction in the Ar/N_2 gas mixture.

Figure 3.12.A&B represents the measured and fitted spectra of the N_2(C) and N_2^+(B) state respectively. The corresponding T_{rot} is plotted in Figure 3.12.A'&B' as a function of the N_2 fraction in the Ar/N_2 gas mixture. The T_{rot}(N_2(C)) is observed to be in a wide range of temperature (400 K ~ 2200 K) whereas the T_{rot} (N_2^+(B)) is uniform around 450 K ± 150 K. The error in the temperature estimation arises from the simulated fitting of the emission spectra and the accuracy of the Boltzmann plot distribution.

Ideally, when the N_2(C) excitation occurs exclusively through electron impact dissociation, its rotational distribution is assumed to be in equilibrium with the translational motion of the neutral gas species (N_2). Hence, the T_{rot} calculated from N_2(C) can be used as an estimation of the gas temperature ($T_{rot} \sim T_{gas}$) [61], [62]. Same goes for the other molecular transition occurring at the FNS of N_2^+(B), assuming a dominance of the electron impact excitation, the rotational temperature can be used as an estimation for the gas temperature ($T_{rot} \sim T_{gas}$) [63], [64]. However, on observing Figure 3.12.A'&B', the T_{rot} distribution across various N_2 flows is entirely different. For N_2(C), the T_{rot} values are much higher than N_2^+(B) and follows a decreasing trend as the N_2 flow increases. Generally, the gas temperature (T_{gas}) is in the order of a few hundreds of Kelvin [65]. While T_{rot} ($N_2^+(B)$) could be an estimation of T_{gas}, in our case, $T_{rot}(N_2(C))$ might not correspond to the gas temperature (T_{gas}) as discussed below.

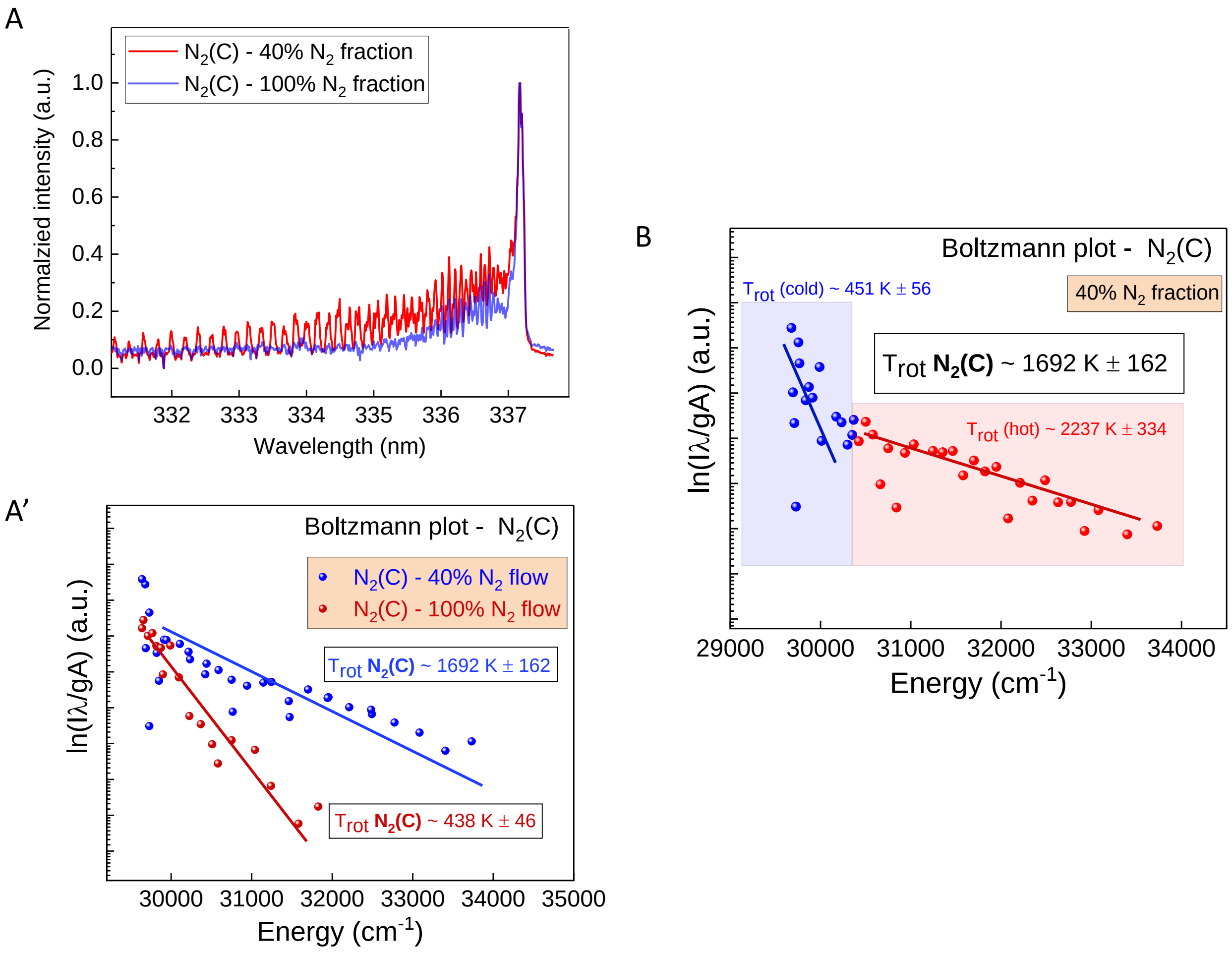

Figure 3.13: A. The rotational emission spectra of the N_2 (SPS) at 337.1 nm at two different N_2 fractions in the Ar/N_2 gas mixture (40% and 100%). A'. The corresponding Boltzmann plot obtained from the two different N_2 fractions and the calculated T_{rot} $N_2(C)$. B. The Boltzmann plot at N_2 ~ 40% split in to a hot and cold zone depicting two different mechanisms that causes the T_{rot} to rise to ~ 1692 K.

The only condition where $T_{rot}(N_2(C))$ ~ T_{rot} ($N_2^+(B)$) is at a N_2 flow of 100% (pure N_2, no Ar) where the T_{rot} ~ 450 K. One could say that the $T_{rot}(N_2(C))$ is influenced by the Ar gas where a process apart from the electron impact excitation is dominant. To investigate this, we considered the $N_2(C)$ emission SPS emission band at two different N_2 flows (40% and 100%) which is shown in Figure 3.13.A. At 40% N_2 (red spectra), the rotational bands extend over a wide range from 337 nm beyond 332 nm whereas at 100% N_2, the bands stop at ~ 335 nm. The corresponding Boltzmann plots are shown in Figure 3.13.A' where the measured T_{rot} are ~1700 K at 40% N_2 and ~438 K at 100% N_2. At 40% N_2, most probably, the production of $N_2(C)$ through metastable energy transfer is expected to be dominant which results in a rotational temperature that is higher than that of the gas temperature [62], [66], [67], [68].

The $N_2(C)$ is therefore predominantly populated by two processes [69]:

$$e^- + N_2(X) \rightarrow N_2(C) + e^- \tag{3.8}$$

$$Ar^*_{meta}(3P_2) + N_2(X) \rightarrow Ar + N_2(C) \tag{3.9}$$

The threshold energy for equation (3.9) of the Ar* metastable states is ~11.5 eV which is very close to the threshold energy of the electron impact dissociation of N_2 (X) to N_2(C) in equation (3.8) ~ 11.1 eV [69]. Comparing the respective energies, we state that the excitation of N_2(X) to N_2(C) by the Ar* metastable is valid. So, in our case, at lower N_2 fractions (higher Ar concentration), the N_2(C) is excited to higher rotational levels by a) electron impact excitation and b) via Ar* metastables where the populated rotational states are non-thermalized. This is why the T_{rot} ~1700 K predicted using the N_2(C) band is overestimated in the discharge region. The Boltzmann distribution of T_{rot} for the hot and cold process is shown in Figure 3.13.B. T_{rot} (cold) is ~ 450 K which is in the range of T_{rot} obtained from the N_2^+(B). T_{rot} (hot) due to the Ar* metastable is ~ 2237 K and does not represent the gas temperature.

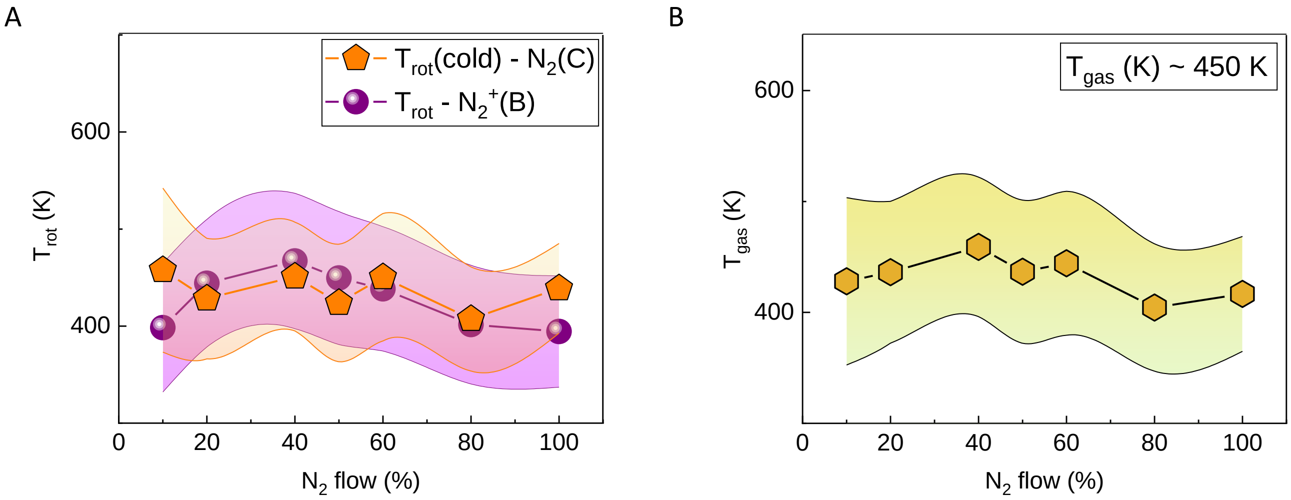

Figure 3.14: A. The rotational temperature T_{rot} of N_2^+ (FNS) and the cold part of the N_2 (SPS) showing similar trends at various N_2 fractions in the Ar/N_2 gas mixture. B. The estimated gas temperature (T_{gas}) vs N_2 flow obtained from averaging the rotational temperatures of the N_2^+ (FNS) and N_2 (SPS).

So, to estimate the gas temperature of the Ar-N_2 discharge, we can either consider the T_{rot} from N_2^+(B) or the T_{rot}(cold) from N_2(C). A comparison of the T_{rot} from the N_2^+(B) and N_2(C) bands is shown in Figure 3.14.A at different N_2 fractions in the Ar-N_2 gas mixture. T_{rot} is uniform at ~ 450 K ± 150 K with subtle variation throughout the entire range of N_2 flows. Considering both the SPS and the FNS bands, we estimate the T_{gas} ~ 450 K. The estimated T_{gas} at various N_2 flows is shown in Figure 3.14.B. The gas temperature does not vary significantly at various N_2 fractions.

3.3.2.2 Estimation of the vibrational temperature

The vibrational temperature (T_{vib}) of molecular nitrogen can also be determined based on the SPS of the nitrogen emission spectrum similar to the rotational temperature. Here, we consider the radiation transition between the C and B electronic states: $N_2(C^3\Pi_u) \rightarrow N_2\left(B^3\Pi_g\right) + h\nu$. We use the vibrational sequence $\Delta\upsilon$ = -2 of the N_2 SPS in the wavelength range 365-385 nm and we assume that the emission follows a Boltzmann distribution [62]. Figure 3.15.A depicts the measured vibrational spectrum for the N_2 SPS. It is important to note here that for measuring T_{vib}, we used a low-resolution spectrometer (~ 0.3 nm) and hence we do not see the rotational bands within the three observed vibrational bands. Although, this resolution is enough to detect the vibrational transitions at 371.05 nm, 375.05 nm and at 380.49 nm which corresponds to the transitions from ($v' = 2, v" = 4$), (($v' = 1, v" = 3$) and (($v' = 0, v" = 2$) respectively. The line intensity corresponding to a vibrational transition ($I^{v'}_{v''}$)is given by [62], [70]:

$$I^{v'}_{v''} \ \alpha \ f^{v'}_{v''} A^{v'}_{v''} \exp\left(-\frac{G_{v'}}{k_B T_{vib}}\right) \qquad (3.10)$$

where $f_{v''}^{v'}$ is the transition frequency, $A_{v''}^{v'}$ is the Einstein spontaneous emission probability, $G_{v'}$ is the energy of the upper vibrational state and k_B is the Boltzmann constant. Figure 3.15.A' shows the slope of the Boltzmann plot from equation (3.10), which gives us the vibrational temperature T_{vib}. The characteristic constants used in equation (3.10) needed to determine T_{vib} are mentioned elsewhere [62]. The estimated T_{vib} in our Ar-N_2 plasma discharge is ~ 4200 K ± 400 K (~ 0.35 eV). Figure 3.15.B shows the trend in T_{vib} across various N_2 fractions. There is a slight non-uniformity with T_{vib} ~ 4300 K at 10% N_2 and ~ 3950 K at 100% N_2. For a fixed RF Power and pressure, we could say that the T_{vib} is higher at lower concentration of N_2 in the discharge. This might be due to the fact that with the increase in Ar percentage, the Ar* metastable population increases. This increases the probability of the Penning excitation from equation (3.9) because of the lower excitation threshold energy of N_2(C) (E_{th} (N_2 (C) ~ 11.1 eV, E_{th} (Ar*) ~ 11.55 eV & 11. 72 eV). Nevertheless, considering the errors during calculation, this does not constitute to a significant change and the overall range of T_{vib} is from 3800 K to 4600 K across various N_2 fractions.

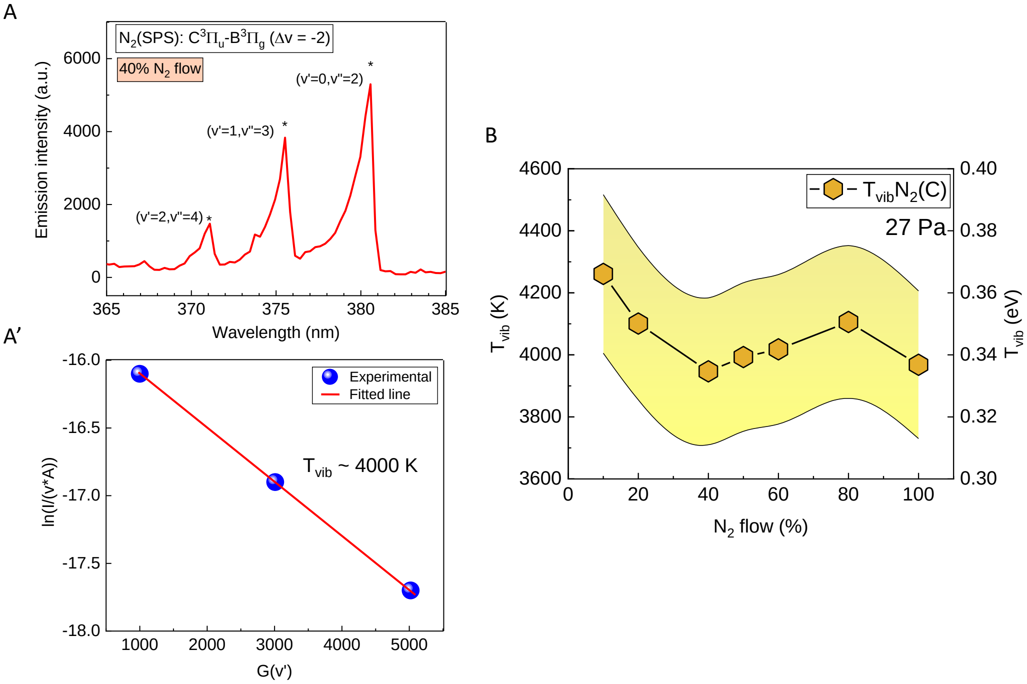

Figure 3.15: A. The vibrational emission spectrum of the SPS of N_2 (vibrational sequence $\Delta\upsilon$ = -2) obtained at 40% N_2 fraction. A'. The corresponding Boltzmann plot used for the determination of the vibrational temperature of N_2(C). B. Variation of the vibrational temperature (T_{vib} N_2(C)) as a function of the N_2 fraction.

If electron collisions predominantly govern vibrational excitations, a rise in T_{vib} signifies an elevation in electron temperature (T_e). Considering similar RF magnetron discharges such as ours from literature, the T_e is typically in the range of 0.3 eV ~ 1 eV [68], [69]. The measured T_{vib} illustrated in Figure 3.15.B ranges from 0.3 to 0.4 eV, indicating a notably lower value but still in the T_e range from literature. So, the vibrational temperature T_{vib} of N_2(C) alone cannot be employed to directly monitor the electron temperature due to the possibility of N_2(C) excitation arising from collisions with electrons and Ar* metastables [52].

The fundamental significance of both vibrational and rotational temperatures in plasma processes lies in their distinct roles. Rotational excitation serves as a plasma thermometer (monitoring the gas temperature), while vibrational excitation, owing to its adiabatic nature, acts as an energy reservoir. This reservoir is crucial for sustaining energy and plays a pivotal role in the chemical reactions occurring within the plasma [52].

3.3.2.3 Estimation of the excitation temperature

The electronic excitation temperature T_{exc} represents the distribution of electronic energy states within the excited states. These excited states are achieved through collisions with electrons, and ideally, the energy distribution in these excited states can be characterized by the electron energy distribution function (EEDF), leading to $T_e = T_{exc}$. Unfortunately, for a non-equilibrium plasma such as ours, due to inadequate time for electron distribution to reach equilibrium with electronic excitation distribution, the validity of the $T_e = T_{exc}$ relationship becomes questionable [73], [74]. Presently, there are many ongoing discussions on methods to estimate T_e in non-thermal plasmas [75], [76], [77]. However, if we assume that the upper levels of atomic transitions that we selected are in local thermal equilibrium (LTE), i.e. it will follow the Boltzmann approximation, the estimation of T_{exc} could still give us a rough estimation of the electron temperature to study its trend under various process conditions [78]. This is useful especially in atmospheric pressure plasmas (high electron density) and magnetized plasmas (such as ours) where Langmuir probe cannot be used. The electron excitation temperature (T_{exc}) can be calculated through the Boltzmann-plot method using sequences of different Ar lines [79], [80], [81].

The Boltzmann plot expressed used to determine T_{exc} is given as [80] :

$$\ln\left(\frac{I_{ij}\lambda_{ij}}{g_i A_{ij}}\right) = -\frac{E_i}{k_B T_{exc}} + C \qquad (3.11)$$

Where I_{ij} is the relative intensity of the selected Ar-I emission line between level *i* and *j*. λ_{ij} is the wavelength in nm, g and A are the statistical weight and the transition probability of a selected transition. In our studies, we use 14 emission lines of Ar to calculate the T_{exc}. They are listed in Table 3.2 along with the values of the other constants required to determine T_{exc}.

Table 3.2: The spectra parameter of the observed Ar-I emission lines from 696 nm to 853 nm. The corresponding constants are taken from literature [81].

Wavelength (nm)	A_{ij} x 10^7 (s^{-1})	E_i (eV)	E_j (eV)	Transition	g_i
696.5	0.63	11.54	13.32	$4p_1 - 4s_2$	3
706.7	0.38	11.54	13.30	$4p_2 - 4s_2$	5
727.3	0.18	11.62	13.32	$4p_1 - 4s_1$	3
738.4	0.84	11.62	13.30	4p−4s	5
750.4	4.45	11.82	13.47	$4p_0 - 4s_1$	5
751.5	4.02	11.62	13.27	$4p_0 - 4s_1$	1
772.4	0.51	11.54	13.15	$4p_1 - 4s_2$	5
794.8	1.86	11.72	13.28	$4p_1 - 4s_0$	3
801.5	0.92	11.54	13.09	$4p_2 - 4s_2$	5
810.4	2.5	11.62	13.15	$4p_1 - 4s_1$	5
811.3	3.31	11.54	13.07	$4p_3 - 4s_2$	3
826.5	1.53	11.82	13.32	$4p_1 - 4s_1$	7
842.5	2.15	11.62	13.09	$4p_2 - 4s_1$	5
852.1	1.89	11.82	13.28	$4p_1 - 4s_1$	5

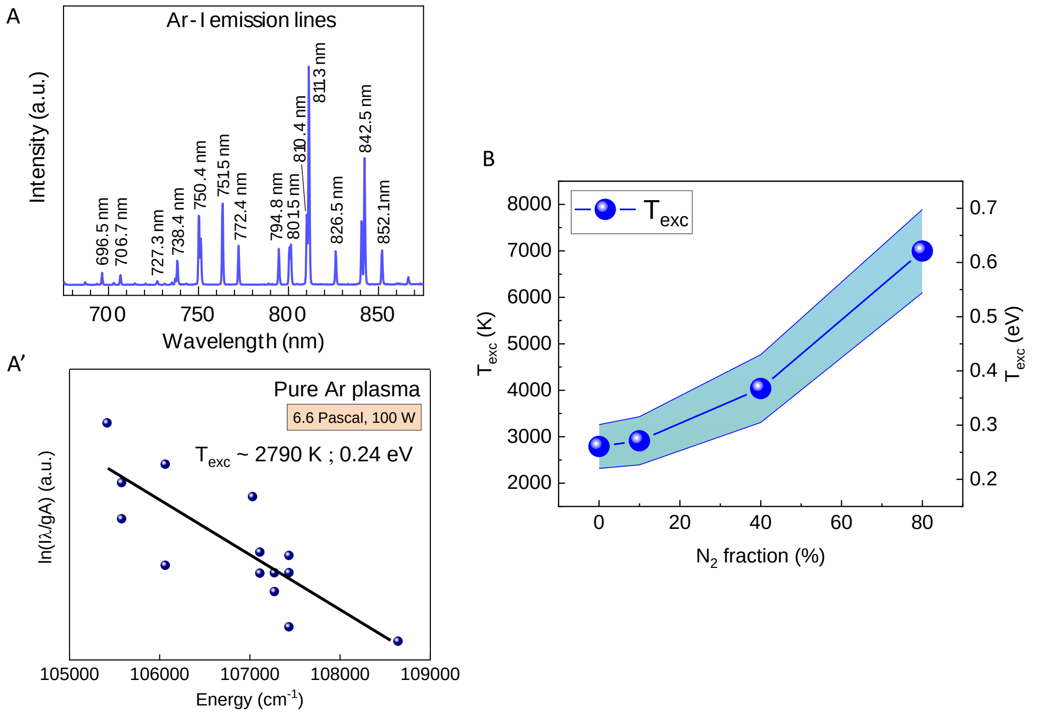

Figure 3.16: A. Emission spectrum showing the Ar-I lines that were considered for determining the excitation temperature (T_{exc}) using line-ratio method. A'. The Boltzmann plot at an N_2 fraction of 10%. B. The trends in the T_{exc} at various N_2 fractions in the Ar/N_2 gas mixture.

Figure 3.16.A represents the Ar emission lines used for our measurements from Table 3.2. By calculating the slope from equation (3.11), we obtain the T_{exc} as depicted by the Boltzmann-plot from Figure 3.16.A'. At various N_2 fractions in the Ar-N_2 gas mixture, we estimate T_{exc} to be in a wide range from 2500 K to 8000 K (0.2 eV ~ 0.7 eV) as shown in Figure 3.16.B. As mentioned before, for RF magnetron discharges such as ours, the electron temperature T_e is typically in the range of 0.3 ~ 1 eV [71], [72]. Form what we observe; the T_{exc} values are in the range of the values of T_e from literature and T_{exc} along with T_{vib} could be used to monitor the electron temperature T_e in our discharge.

3.4 Plasma qualification & optimizations

Plasma qualification is an important step prior to the growth of GaN. There are several features of our plasma that were discussed in this chapter which when put together would help us in optimizing the growth process and to obtain a good quality GaN film. We divide the plasma qualification into three sub-sections: i) plasma stability, ii) plasma density (electron and N-atom density) and iii) plasma characteristic temperatures.

3.4.1 Plasma stability

We distinguish the stability of our Ar/N_2 plasma for durations corresponding either to the growth (longer duration ~ 1-2 hours) or plasma diagnostics (shorter durations ~ 10-20 minutes). Figure 3.17 presents the matrix informing us of the plasma stability at various RF power (10W to > 150W) and working pressure (0.66 Pa to >40 Pa). The stability in our case depicts the ability of a specific process condition to produce a plasma and remain stable throughout the deposition.

The growth regime of GaN is defined as the pressure and power ranges in which the plasma remains stable for longer durations. On observing the matrix, we could say that for RF powers above 75W and below 150W and working pressures above 2.66 Pa and below 13.33 Pa, the plasma remains stable. Most of our GaN deposition will be focused on this range of pressure and power. At higher RF power and pressure (> 150W and > 13.33 Pa), the plasma is stable but only for shorter durations, typically a few tens of minutes. GaN growth at this regime would provide us with a very thin layer (<~ 50nm) on which solid-state diagnostics (ex-situ characterization) would be difficult to perform and hence the quality of the film could not be properly analyzed. At RF power range above 150 W, the plasma becomes completely unstable. However, at pressures greater than 15 Pa and less than 40 Pa, the plasma remains stable for shorter durations and we explore these conditions with the help of the plasma diagnostic techniques that were used in this chapter.

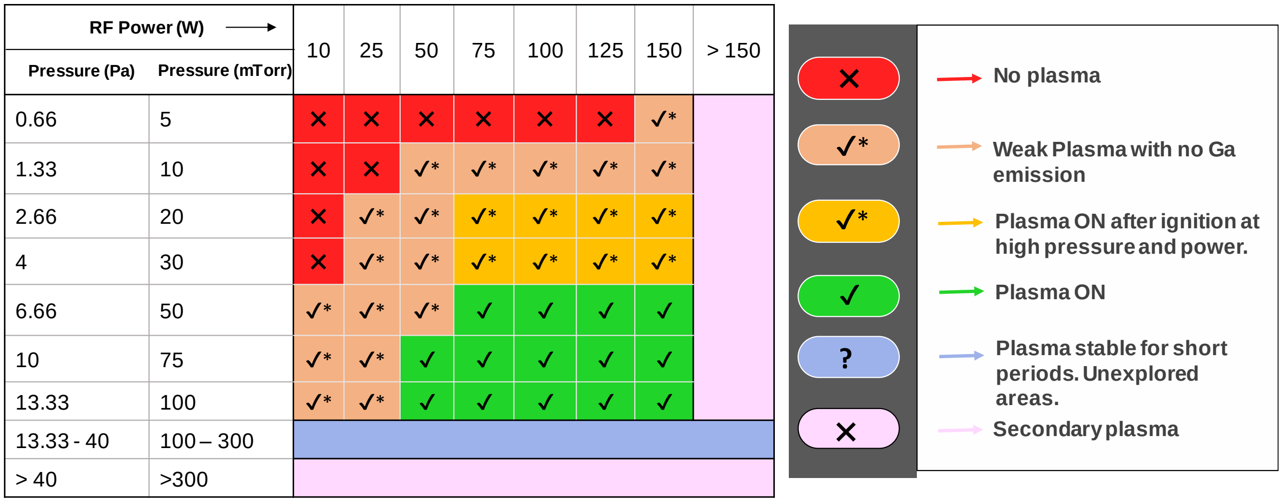

RF Power (W) →		10	25	50	75	100	125	150	> 150
Pressure (Pa)	Pressure (mTorr)								
0.66	5	✗	✗	✗	✗	✗	✗	✓*	
1.33	10	✗	✗	✓*	✓*	✓*	✓*	✓*	
2.66	20	✗	✓*	✓*	✓*	✓*	✓*	✓*	
4	30	✗	✓*	✓*	✓*	✓*	✓*	✓*	
6.66	50	✓*	✓*	✓*	✓	✓	✓	✓	
10	75	✓*	✓*	✓	✓	✓	✓	✓	
13.33	100	✓*	✓*	✓	✓	✓	✓	✓	
13.33 - 40	100 – 300								
> 40	>300								

✗ → No plasma
✓* → Weak Plasma with no Ga emission
✓* → Plasma ON after ignition at high pressure and power.
✓ → Plasma ON
? → Plasma stable for short periods. Unexplored areas.
✗ → Secondary plasma

Figure 3.17: A broad overview of the plasma process conditions (Pressure, RF Power) in terms of plasma stability. Each matrix cell is defined by its ability to produce a stable plasma at that specific process conditions.

3.4.2 Plasma contamination

An interesting feature that we observed during the optical emission spectroscopy measurements of the plasma system was the presence of OH emission lines. There are two possibilities for such an observation – a) the plasma interacts with the reactor walls which may release a steady supply of adsorbed gases such as water and oxygen [82] or b) the use of liquid Ga as a target enables the dissolution of oxygen into the gallium [83], [84]. In either case, the presence of a foreign species in the plasma could be detrimental for the GaN samples with significant chemical contamination.

Figure 3.18.A reveals the OH spectra centered at 309 nm in an Ar/N_2 plasma environment. The broad peak represents the overlapping of the OH spectra along with the 317 nm peak of the second positive system (SPS) of N_2 emission spectra. To monitor the OH lines without the presence of N_2 emission lines, a pure Ar plasma was used. Figure 3.18.B depicts the OH peak at 309 nm recorded over a range of time at three different base pressures – 10^{-5}, 10^{-6} and 10^{-7} mbar. It is important to note here that the working pressure and RF power during the plasma was kept the same (50 mTorr, 100W) for all the three conditions. The time series spectra of OH reveals that for a high base pressure (~ 10^{-5} mbar), the OH intensity is almost tenfold in intensity w.r.t the intensity value at a low base pressure (10^{-7} mbar). This points out to the fact that pumping overnight to reach a base pressure value ~ 10^{-7}mbar yields a lesser concentration of OH in the plasma and thereby lesser contamination.

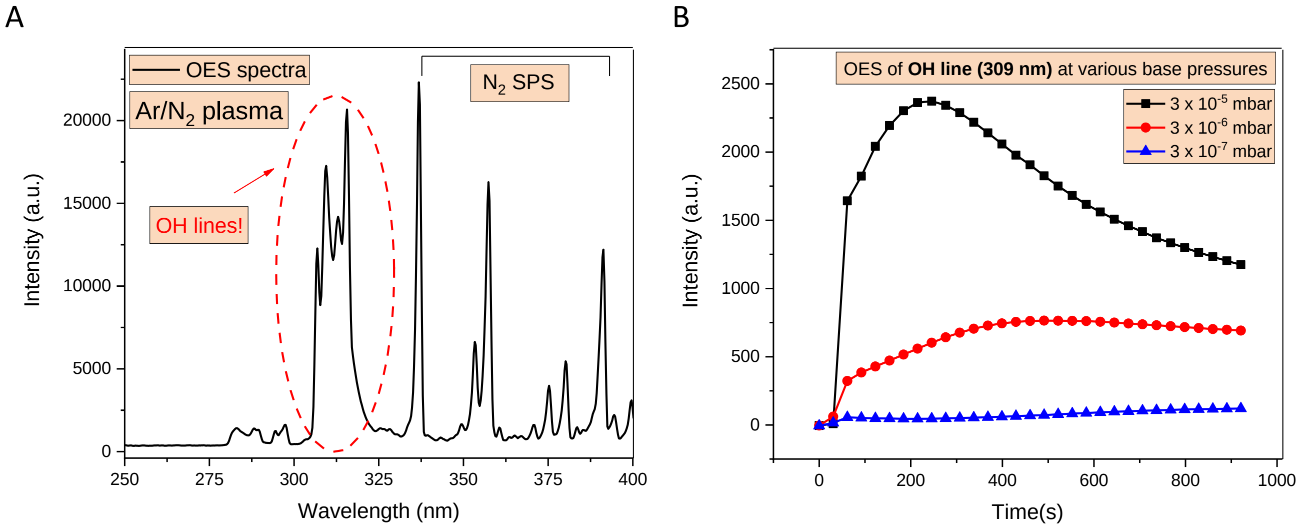

Figure 3.18: A. Strong OH emission spectra detected at 309 nm measured by optical emission spectroscopy (OES) in an Ar/N$_2$ plasma environment. B. Temporal monitoring of the OH spectra peak at various base pressures of 10^{-5}, 10^{-6} and 10^{-7} mbar.

Our plasma PVD reactor is currently in its early stages and a load-lock system is yet to be installed. Therefore, every time a sample is loaded or recovered, the Ga target and the reactor walls are exposed to atmosphere and thereby prone to contamination. A temporary solution to mitigate the presence of contamination in the reaction chamber was to implement a reactor and target cleaning process. A simple cleaning process was introduced whose steps are depicted as a flow chart in Figure 3.19. The first step was to heat the reactor walls close to the deposition area thereby creating an accelerated desorption of O_2 and H_2O off the reactor walls. This step involved heating the reactor walls up to 200°C using a heating cable wrapped around the deposition chamber. The heating was carried out in four short cycles of 30 minutes each as depicted on the inset of the reactor wall heating process in Figure 3.19.

The first cycle revealed a sharp increase in the base pressure upon turning the heating system ON, which indicated a strong desorption of contaminants of the reactor walls. The following cycles presented a trend of decreased base pressures from 10^{-5} mbar until 10^{-7} mbar at the end of the fourth cycle. Upon further heating, the base pressure did not rise and remained at 10^{-7} mbar indicating the removal of contaminants from the walls. The second step was to focus on the liquid Gallium target. When oxygen is present in gallium, it can lead to the formation of gallium oxide (Ga_2O_3). These oxide layers can develop on the surface of the gallium target, reducing the sputter yield during deposition. Plasma treatment the gallium target with inert gases such as Argon to displace the oxygen is a potential solution that has been used often [83], [85]. In the cleaning step, similar to step 1, four successive cycles of pure Ar plasma sputtering was carried out for 30 minutes each. The corresponding OH emission line was recorded during these cycles and shown in the inset of target cleaning in Figure 3.19. The trends of the OH line for the first cycle presented an increase in the emission intensity during the first half and a gradual decrease in the second half. The successive cycles 2, 3 and 4 produced results where a low intense OH emission was visible and was uniform throughout the cycle. This provided us with a notion that a single cycle of the target-cleaning step was sufficient to reduce the contamination of the Ga target.

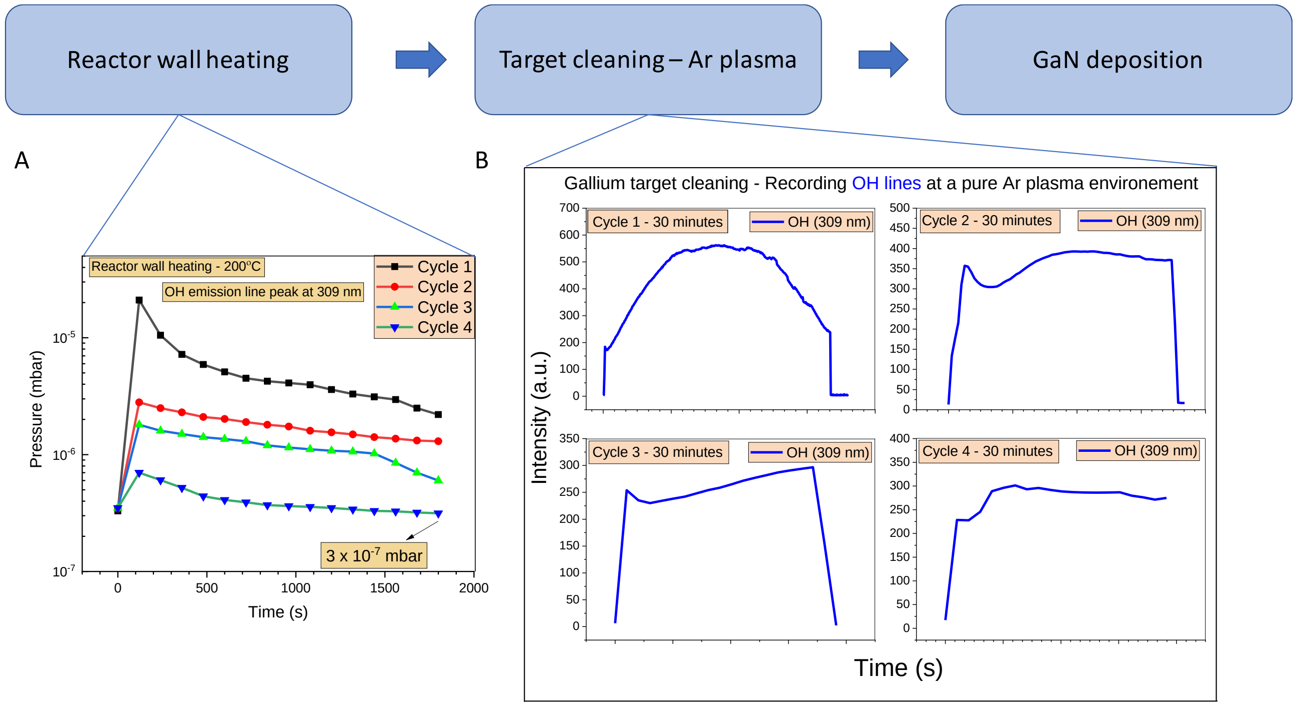

Figure 3.19: An overview of the reactor and plasma cleaning process to mitigate the presence of Oxygen. 1. A flow chart describing the steps required for the cleaning procedure – i) Reactor wall heating; ii) Target cleaning. A. OH emission spectra monitored during 4 repeated cycles of reactor wall heating at 200ºC. B. OH emission intensity monitored during 4 repeated cycles of target cleaning which involves a pure Ar plasma sputtering the liquid Ga target.

The above plasma cleaning steps were introduced prior to each GaN deposition irrespective of the process conditions used. Although the emission from the plasma yielded a low intense signal of OH, this was in no way sufficient to correlate with any oxygen contamination in the deposited GaN sample. For that, a thorough ex-situ chemical analysis of the GaN sample was necessary. The next chapter is dedicated on investigating the quality of the GaN thin film in terms of structure, morphology and its chemical properties. The oxygen contamination of GaN thin film will be elaborated in the chemical composition section.

3.4.3 Plasma characteristics: density & temperatures

To characterize the density of species in our discharge, we consider the N-atom density (N) and the electron density (n_e) measurements obtained from TALIF and MWI respectively. Figure 3.20 represents the N and n_e across a pressure range from 15-35 Pa, which is above the growth regime (see Figure 3.17). This is because from TALIF alone, the extrapolation of the N atom density can only be done within the higher-pressure ranges (15-35 Pa) and the atomic density at the growth regime of GaN (0-15 Pa) is unknown. However, if we consider the comparison of the trends in electron density and N atom density from Figure 3.20.A&B, both the N atom density and the electron density follow a similar rising trend with an increase in pressure up to 35 Pa.

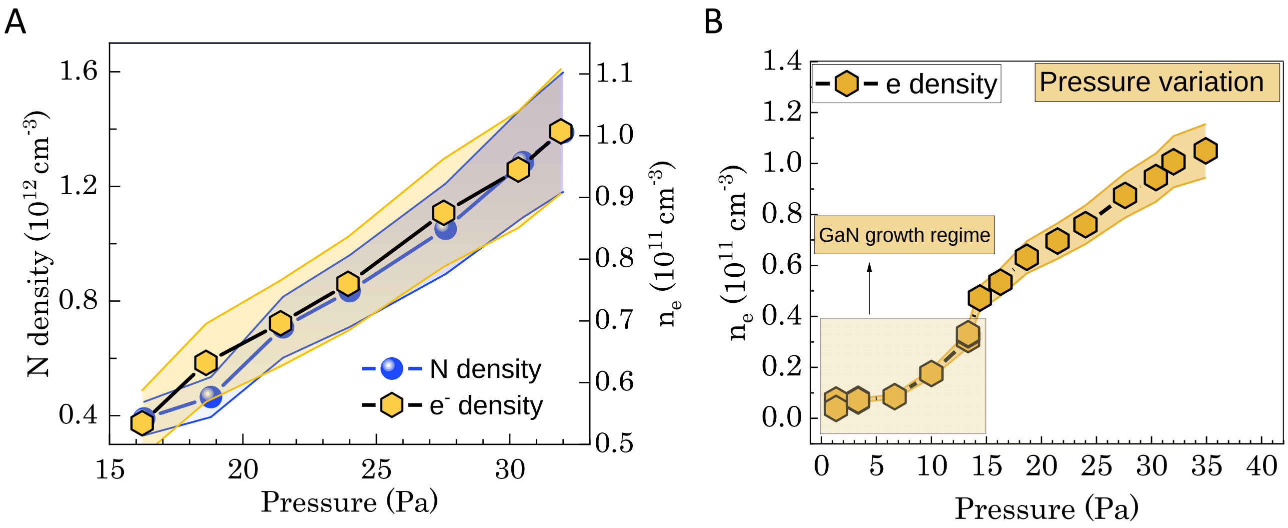

Figure 3.20: A. N-atom density and the plasma electron density plotted a pressure range of 15-35 Pa. B. electron density plotted at an extended pressure range of 0-35 Pa.

Unlike TALIF, the electron density measurements were not limited to 15 Pa and the density follows a decreasing trend as the pressure range is extended from 15 Pa into the growth regime (0-15 Pa) – Figure 3.20.B. We could say that the N atom density might also follow a similar trend and at the growth regime (> 13.3 Pa ~ 100mTorr), the atomic density could be less than 4 x 10^{11} cm^{-3} (density value at 15 Pa). Another way of estimating the N-atom density within the growth regime could be from the fluorescence signal itself. During measurements, we observed that the fluorescence signal directly correlated with the N-atom density (see Figure 3.8). The signal became stronger as the N-atom density increased. Since, no fluorescence was observed at the growth regime (> 13.3 Pa ~ 100mTorr), we could say that the N atom density at this range could be lower than 4 x 10^{11} cm^{-3} (density value at 15 Pa).

As the pressure increases, the N atom density and the electron density increase collinearly. The maximum N atom density and electron density is obtained at a pressure of 35 Pa with respective values of 1.4 x 10^{12} cm^{-3} and 1.1 x 10^{11} cm^{-3}. With respect to the working pressure in the growth regime, the electron density is in the range of 1-4 x 10^{10} cm^{-3} and the nitrogen atom density is less than 4 x 10^{11} cm^{-3}. Our measurements indicate a similar variation trend of the electron density n_e with that of the N-atoms density (**Error! Reference source not found.**.b) except that the electron density is doubled between 16 Pa and 32 Pa, i.e., from 0.5×10^{11} cm^{-3} to 1×10^{11} cm^{-3}, respectively, while N-atoms density increases by a factor of 3.25. Therefore, while the enhancement of the production of N-atoms is likely to be attributed to the increase of the electron density, it seems that other processes may also enter into play. For instance, one may think about reactions that involved Argon ions and N_2 molecules trough charge exchange reactions ($Ar^+ + N_2 \rightarrow Ar + N_2^+$) followed by dissociative recombination ($e^- + N_2^+ \rightarrow N + N$) or that would be the consequence of reactions of Ar metastable with N_2[19]. This enhancement of N-atoms production when working at such low-pressure range would be beneficial for applications that target high growth rates.

We use OES to determine the characteristic temperatures of our Ar-N_2 plasma discharge and preliminarily analyze the different temperatures w.r.t varying N_2 fractions in the gas mixture. We qualify the plasma in terms of the gas temperature, rotational and vibrational temperatures of the N_2 molecule and the electron excitation temperature. The bar graph of the different temperatures is shown in Figure 3.21. The gas temperature T_{gas} is estimated to be ~ 550 K ±150 K and remains uniform at varying gas flows. $T_{rot}N_2(C)$ in our case does not correspond directly to the gas temperature. It is also influenced by the metastable energy transfer of Ar* which results in a rise of the temperature from 550 K up to ~ 2400 K.

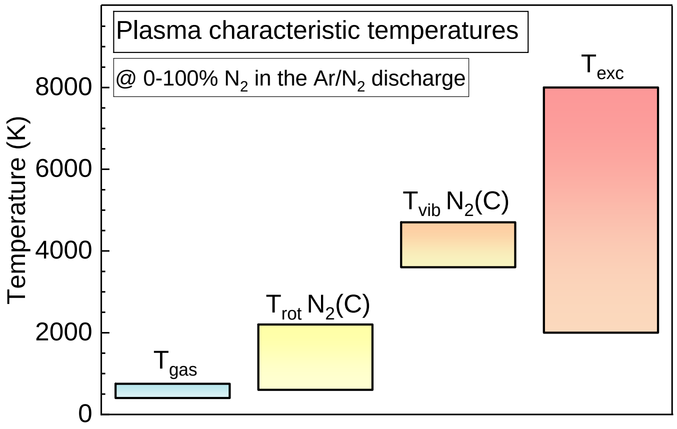

Figure 3.21: The plasma characteristic temperatures measured using OES in our Ar-N2 discharge. Four temperatures (T_{gas}, $T_{rot}N_2(C)$, $T_{vib}N_2(C)$ and T_{exc}) are presented along with their trends w.r.t varying N_2 fraction in the gas mixture.

The vibrational temperature $T_{vib}N_2(C)$ does not vary significantly with N_2 flow variation and remains uniform ~ 4000 K ± 400 K. The excitation temperature T_{exc} however increases from 2000 K at pure Ar discharge (0% N_2) to ~ 8000 K at high N_2 fractions (80% N_2). Both $T_{vib}N_2(C)$ and T_{exc} are generally considered as factors that can provide an approximate estimate of the electron temperature in a discharge [53]. But since, both the temperatures follow a different trend at varying N_2 flows, we will further consider the electron density variation as the governing factor to choose a specific temperature ($T_{vib}N_2(C)$ or T_{exc}) that could be used as an estimate of the electron temperature. That will depend on the process parameter that we choose to analyze which will be extensively discussed in the coming chapters.

The results of N-atom density, electron density and plasma temperatures at various plasma process parameters obtained through the course of this chapter will be further discussed in the upcoming chapters (4 and 5) to support the observation of trends in the characterization of a GaN thin film and validate the provided hypothesis. Chapters 4 and 5 are dedicated to the growth and solid-state characterization of the GaN film.

3.5 Conclusion

Chapter 3 presented an overview of three plasma diagnostic techniques used to characterize our Ar/N_2 plasma system - TALIF, MWI and OES. Each technique focused on a specific plasma characteristic. TALIF was used to determine the absolute N atom density. The N fluorescence signal obtained was very low in intensity typical of a low-pressure plasma discharge. To determine the atomic density, we use a peak excitation method (PEM) where only the temporally integrated fluorescence signal is considered and repetitive measurements of the signal are avoided. The effective lifetime decay of N and Kr yielded values that enabled us to neglect the effect of quenching rate and consider only the de-excitation through radiative collision. The N-atom density was measured to be ~ 10^{11}-10^{12} cm^{-3}. MWI was used to determine the electron density in the discharge. The electron density was in the range of ~ 10^{10}-10^{11} cm^{-3}.
Density measurements from TALIF and MWI were compared to qualify the plasma characteristics in the growth regime. The electron density and N atom density followed a similar increasing trend w.r.t working pressure. As atomic density measurements could not be performed at lower pressure ranges (<13.3 Pa) due to the absence of fluorescence detection, the trend towards lower pressure ranges was identified by correlating the electron density measurements at low pressures.

OES was used as a tool to identify the trends in the emissive species w.r.t varying process conditions and to monitor efficient sputtering of Ga atoms in the discharge. Additionally, OES was used to identify oxygen-based contaminants in the plasma, which could prove detrimental for the growth process. A temporary plasma and reactor cleaning solution was introduced to mitigate the effect of the contaminants.

Temperature measurements from OES were compared to provide an estimate on the gas temperature and electron temperature in our discharge. The rotational temperature measurements gave a good estimate of the gas temperature ~ 550 K. The electron temperature however could not be directly determined. As an alternative, we measured the vibrational temperature, which was estimated to be ~ 4000 K, and the excitation temperature, which was estimated to be in the range of 2000 K to 8000 K.

The plasma qualification at the growth and extended regime w.r.t pressures leads us towards paving the way for the onset of thin film characterization at these process conditions, which is discussed in Chapter 4.

REFERENCES

[1] I. H. Hutchinson, "Principles of plasma diagnostics," *Plasma Phys. Control. Fusion*, vol. 44, no. 12, pp. 2603–2603, 2002.

[2] H.-J. Kunze, "Plasma Diagnostics," in *Plasma Physics*, vol. 670, A. Dinklage, T. Klinger, G. Marx, and L. Schweikhard, Eds., in Lecture Notes in Physics, vol. 670. , Berlin/Heidelberg: Springer-Verlag, 2005, pp. 349–373. doi: 10.1007/11360360_13.

[3] A. J. H. Donné, "Introduction to Plasma Diagnostics," *Fusion Sci. Technol.*, vol. 45, no. 2T, pp. 383–390, Mar. 2004, doi: 10.13182/FST04-A504.

[4] E. Es-Sebbar, Y. Benilan, A. Jolly, and M. C. Gazeau, "Characterization of an N2 flowing microwave post-discharge by OES spectroscopy and determination of absolute ground-state nitrogen atom densities by TALIF," *J. Phys. Appl. Phys.*, vol. 42, no. 13, p. 135206, 2009.

[5] C. Dumitrache, A. Gallant, N. de Oliveira, C. O. Laux, and G. D. Stancu, "Quantitative fs-TALIF in high-pressure NRP discharges: Calibration using VUV absorption spectroscopy," *Plasma Sources Sci. Technol.*, vol. 31, no. 1, p. 015004, 2022.

[6] T. Czerwiec, F. Greer, and D. B. Graves, "Nitrogen dissociation in a low pressure cylindrical ICP discharge studied by actinometry and mass spectrometry," *J. Phys. Appl. Phys.*, vol. 38, no. 24, p. 4278, Dec. 2005, doi: 10.1088/0022-3727/38/24/003.

[7] N. Kang, F. Gaboriau, S. Oh, and A. Ricard, "Modeling and experimental study of molecular nitrogen dissociation in an Ar–N2 ICP discharge," *Plasma Sources Sci. Technol.*, vol. 20, no. 4, p. 045015, Jun. 2011, doi: 10.1088/0963-0252/20/4/045015.

[8] M. Tabbal, M. Kazopoulo, T. Christidis, and S. Isber, "Enhancement of the molecular nitrogen dissociation levels by argon dilution in surface-wave-sustained plasmas," *Appl. Phys. Lett.*, vol. 78, no. 15, pp. 2131–2133, Apr. 2001, doi: 10.1063/1.1359775.

[9] A. Salmon, N. A. Popov, G. D. Stancu, and C. O. Laux, "Quenching rate of N(2P) atoms in a nitrogen afterglow at atmospheric pressure," *J. Phys. Appl. Phys.*, vol. 51, no. 31, p. 314001, Jul. 2018, doi: 10.1088/1361-6463/aace71.

[10] P. Vašina, V. Kudrle, A. Tálský, P. Botoš, M. Mrázková, and M. Meško, "Simultaneous measurement of N and O densities in plasma afterglow by means of NO titration," *Plasma Sources Sci. Technol.*, vol. 13, no. 4, p. 668, Oct. 2004, doi: 10.1088/0963-0252/13/4/016.

[11] A. Remigy *et al.*, "Cross-comparison of diagnostic and 0D modeling of a micro-hollow cathode discharge in the stationary regime in an Ar/N2 gas mixture," *J. Phys. Appl. Phys.*, vol. 55, no. 10, p. 105202, Dec. 2021, doi: 10.1088/1361-6463/ac3c74.

[12] S. F. Adams and T. A. Miller, "Two-photon absorption laser-induced fluorescence of atomic nitrogen by an alternative excitation scheme," *Chem. Phys. Lett.*, vol. 295, no. 4, pp. 305–311, 1998, doi: https://doi.org/10.1016/S0009-2614(98)00972-5.

[13] T. L. Chng, N. D. Lepikhin, I. S. Orel, N. A. Popov, and S. M. Starikovskaia, "TALIF measurements of atomic nitrogen in the afterglow of a nanosecond capillary discharge," *Plasma Sources Sci. Technol.*, vol. 29, no. 3, p. 035017, Mar. 2020, doi: 10.1088/1361-6595/ab6f9c.

[14] T. Kimura and H. Kasugai, "Experiments and global model of inductively coupled rf Ar/N2 discharges," *J. Appl. Phys.*, vol. 108, no. 3, p. 033305, Aug. 2010, doi: 10.1063/1.3468603.

[15] A. Remigy *et al.*, "Absolute N-atom density measurement in an Ar/N2 micro-hollow cathode discharge jet by means of ns-two-photon absorption laser-induced fluorescence," *Phys. Plasmas*, vol. 29, no. 11, p. 113508, Nov. 2022, doi: 10.1063/5.0110318.

[16] E. Bisceglia *et al.*, "Investigation of N(4S) kinetics during the transients of a strongly emissive pulsed ECR plasma using ns-TALIF," *Plasma Sources Sci. Technol.*, vol. 30, no. 9, p. 095001, Aug. 2021, doi: 10.1088/1361-6595/ac0da1.

[17] A. Goehlich, T. Kawetzki, and H. F. Döbele, "On absolute calibration with xenon of laser diagnostic methods based on two-photon absorption," *J. Chem. Phys.*, vol. 108, no. 22, pp. 9362–9370, 1998.

[18] K. Niemi, V. Schulz-Von Der Gathen, and H. F. Döbele, "Absolute calibration of atomic density measurements by laser-induced fluorescence spectroscopy with two-photon excitation," *J. Phys. Appl. Phys.*, vol. 34, no. 15, p. 2330, 2001.

[19] E. Bisceglia, "Enhancement of nitrogen atom density using microwave pulsed discharges: Methodology combining laser-induced fluorescence and collisional-radiative model," PhD Thesis, Université Paris-Nord-Paris XIII, 2021. Accessed: Oct. 23, 2023. [Online]. Available: https://theses.hal.science/tel-03620582/

[20] C. Y. Duluard and X. Aubert, "Precautions for using krypton as a calibration species for Two-Photon Absorption Laser Induced Fluorescence of hydrogen and nitrogen atoms", Accessed: Oct. 23, 2023. [Online]. Available: https://scholar.google.com/scholar?cluster=7928486647795741955&hl=en&oi=scholarr

[21] S. Mazouffre *et al.*, “Density and temperature of N atoms in the afterglow of a microwave discharge measured by a two-photon laser-induced fluorescence technique,” *Plasma Sources Sci. Technol.*, vol. 10, no. 2, p. 168, 2001.

[22] S. Schröter *et al.*, “The formation of atomic oxygen and hydrogen in atmospheric pressure plasmas containing humidity: picosecond two-photon absorption laser induced fluorescence and numerical simulations,” *Plasma Sources Sci. Technol.*, vol. 29, no. 10, p. 105001, 2020.

[23] K. Niemi, V. Schulz-Von Der Gathen, and H. F. Döbele, “Absolute atomic oxygen density measurements by two-photon absorption laser-induced fluorescence spectroscopy in an RF-excited atmospheric pressure plasma jet,” *Plasma Sources Sci. Technol.*, vol. 14, no. 2, p. 375, 2005.

[24] A. Kramida, Y. Ralchenko, and J. Reader, “NIST Atomic Spectra Database (ver. 5.3),[Online],” *Natl. Inst. Stand. Technol. Gaithersburg MD USA*, 2015.

[25] G. D. Stancu, “Two-photon absorption laser induced fluorescence: rate and density-matrix regimes for plasma diagnostics,” *Plasma Sources Sci. Technol.*, vol. 29, no. 5, p. 054001, May 2020, doi: 10.1088/1361-6595/ab85d0.

[26] S. F. Adams and T. A. Miller, “Surface and volume loss of atomic nitrogen in a parallel plate rf discharge reactor,” *Plasma Sources Sci. Technol.*, vol. 9, no. 3, p. 248, 2000.

[27] G. D. Stancu, “Two-photon absorption laser induced fluorescence: rate and density-matrix regimes for plasma diagnostics,” *Plasma Sources Sci. Technol.*, vol. 29, no. 5, p. 054001, 2020.

[28] E.-T. Es-Sebbar, C. Sarra-Bournet, N. Naudé, F. Massines, and N. Gherardi, “Absolute nitrogen atom density measurements by two-photon laser-induced fluorescence spectroscopy in atmospheric pressure dielectric barrier discharges of pure nitrogen,” *J. Appl. Phys.*, vol. 106, no. 7, 2009, Accessed: Nov. 02, 2023. [Online]. Available: https://pubs.aip.org/aip/jap/article/106/7/073302/896215

[29] S. Hofmann, A. F. H. Van Gessel, T. Verreycken, and P. Bruggeman, “Power dissipation, gas temperatures and electron densities of cold atmospheric pressure helium and argon RF plasma jets,” *Plasma Sources Sci. Technol.*, vol. 20, no. 6, p. 065010, 2011.

[30] E. Bisceglia *et al.*, “Investigation of N (4S) kinetics during the transients of a strongly emissive pulsed ECR plasma using ns-TALIF,” *Plasma Sources Sci. Technol.*, vol. 30, no. 9, p. 095001, 2021.

[31] K. Dzierżęga, U. Volz, G. Nave, and U. Griesmann, “Accurate transition rates for the 5 p − 5 s transitions in Kr I,” *Phys. Rev. A*, vol. 62, no. 2, p. 022505, Jul. 2000, doi: 10.1103/PhysRevA.62.022505.

[32] J. Wolberg, *Data analysis using the method of least squares: extracting the most information from experiments*. Springer Science & Business Media, 2006. Accessed: Nov. 02, 2023. [Online]. Available: https://books.google.com/books?hl=en&lr=&id=BYYe-AYas9AC&oi=fnd&pg=PA1&dq=Wolberg+J+2006+Data+Analysis+Using+the+Method+of+Least+Squares:+Extracting+the+Most+Information+from+Experiments+(Springer+Science+%26+Business+Media),+ISBN:+978-3-540-+31720-3&ots=Hh7N9SBxmb&sig=BufosSRmA7xJyAeQx9hwThOsT1c

[33] A. Remigy, G. Lombardi, X. Aubert, S. Prasanna, N. De Oliveira, and C. Lazzaroni, “Absolute N atom density measurements in an Ar/N 2 Micro-Hollow Cathode Discharge by means of nanosecond Two-Photon Laser Induced Fluorescence,” in *APS Annual Gaseous Electronics Meeting Abstracts*, 2021, pp. GT51-004. Accessed: Nov. 02, 2023. [Online]. Available: https://ui.adsabs.harvard.edu/abs/2021APS..GECG51004R/abstract

[34] M. A. Damen, D. Hage, A. W. van de Steeg, L. M. Martini, and R. Engeln, “Absolute CO number densities measured using TALIF in a non-thermal plasma environment,” *Plasma Sources Sci. Technol.*, vol. 28, no. 11, p. 115006, 2019.

[35] S. F. Adams and T. A. Miller, “Two-photon absorption laser-induced fluorescence of atomic nitrogen by an alternative excitation scheme,” *Chem. Phys. Lett.*, vol. 295, no. 4, pp. 305–311, 1998.

[36] H. F. Döbele, T. Mosbach, K. Niemi, and V. Schulz-Von Der Gathen, “Laser-induced fluorescence measurements of absolute atomic densities: concepts and limitations,” *Plasma Sources Sci. Technol.*, vol. 14, no. 2, p. S31, 2005.

[37] S. Agrup, F. Ossler, and M. Ald�n, “Measurements of collisional quenching of hydrogen atoms in an atmospheric-pressure hydrogen oxygen flame by picosecond laser-induced fluorescence,” *Appl. Phys. B Lasers Opt.*, vol. 61, no. 5, pp. 479–487, Nov. 1995, doi: 10.1007/BF01081277.

[38] N. Kang, F. Gaboriau, S. Oh, and A. Ricard, “Modeling and experimental study of molecular nitrogen dissociation in an Ar–N2 ICP discharge,” *Plasma Sources Sci. Technol.*, vol. 20, no. 4, p. 045015, 2011.

[39] L. J. Overzet and M. B. Hopkins, “Comparison of electron-density measurements made using a Langmuir probe and microwave interferometer in the Gaseous Electronics Conference reference reactor,” *J. Appl. Phys.*, vol. 74, no. 7, pp. 4323–4330, 1993.

[40] C. B. Wharton, *Microwave diagnostics for controlled fusion research*. University of California Radiation Laboratory, 1957. Accessed: Nov. 02, 2023. [Online]. Available: https://books.google.com/books?hl=en&lr=&id=tymrzo6V5SIC&oi=fnd&pg=PA1&dq=microwave+interferometry+in+fusion+experiments&ots=6DSU0A_uIX&sig=IhHJKChLfjR4e2LRHWS1v8kRuzc

[41] P. Shi *et al.*, “Multichannel microwave interferometer for simultaneous measurement of electron density and its fluctuation on HL-2A tokamak,” *Plasma Sci. Technol.*, vol. 18, no. 7, p. 708, 2016.

[42] M. Andrasch, J. Ehlbeck, R. Foest, and K. D. Weltmann, “Electron density measurements on an inductively coupled plasma with a one-port microwave interferometer,” *Plasma Sources Sci. Technol.*, vol. 21, no. 5, p. 055032, 2012.

[43] “-for Vacuum Plasma.” Accessed: Nov. 02, 2023. [Online]. Available: http://www.miwitron.com/pageID_7766911.html

[44] T. H. Chung, Y. W. Lee, H. M. Joh, and M. A. Song, “Pressure dependence of dissociation fraction and optical emission characteristics in low-pressure inductively coupled N_2 -Ar plasmas,” *AIP Adv.*, vol. 1, no. 3, p. 032136, Sep. 2011, doi: 10.1063/1.3628670.

[45] X.-M. Zhu and Y.-K. Pu, “Using OES to determine electron temperature and density in low-pressure nitrogen and argon plasmas,” *Plasma Sources Sci. Technol.*, vol. 17, no. 2, p. 024002, 2008.

[46] I. Sugimoto, S. Nakano, and H. Kuwano, “Enhanced saturation of sputtered amorphous SiN film frameworks using He- and Ne-Penning effects,” *J. Appl. Phys.*, vol. 75, no. 12, pp. 7710–7717, Jun. 1994, doi: 10.1063/1.356602.

[47] J. Muñoz, J. Margot, and M. Chaker, “Argon metastable and resonant densities in a low-pressure Ar–N2 inductively coupled plasma,” *J. Phys. Appl. Phys.*, vol. 46, no. 45, p. 455205, 2013.

[48] W. Park, J. Han, J. Kim, and S. Y. Moon, “The effect of gas composition on the properties of silicon oxynitride thin film prepared by low-pressure inductively coupled Ar/N2 plasma,” *Thin Solid Films*, vol. 764, p. 139629, 2023.

[49] T. Shirai, J. Reader, A. E. Kramida, and J. Sugar, “Spectral Data for Gallium: Ga I through Ga XXXI,” *J. Phys. Chem. Ref. Data*, vol. 36, no. 2, pp. 509–615, Jun. 2007, doi: 10.1063/1.2207144.

[50] C. Corr, R. Boswell, and R. Carman, “Gas phase optical emission spectroscopy during remote plasma chemical vapour deposition of GaN and relation to the growth dynamics,” *J. Phys. Appl. Phys.*, vol. 44, no. 4, p. 045201, Feb. 2011, doi: 10.1088/0022-3727/44/4/045201.

[51] F. U. Khan, N. U. Rehman, S. Naseer, M. Y. Naz, N. A. D. Khattak, and M. Zakaullah, “Effect of Excitation and Vibrational Temperature on the Dissociation of Nitrogen Molecules in Ar-N_2 Mixture RF Discharge,” *Spectrosc. Lett.*, vol. 44, no. 3, pp. 194–202, Mar. 2011, doi: 10.1080/00387010.2010.497527.

[52] N. Britun, M. Gaillard, A. Ricard, Y. M. Kim, K. S. Kim, and J. G. Han, “Determination of the vibrational, rotational and electron temperatures in N2 and Ar–N2 rf discharge,” *J. Phys. Appl. Phys.*, vol. 40, no. 4, p. 1022, 2007.

[53] F. Iza and J. A. Hopwood, “Rotational, vibrational, and excitation temperatures of a microwave-frequency microplasma,” *IEEE Trans. Plasma Sci.*, vol. 32, no. 2, pp. 498–504, 2004.

[54] P. Bruggeman, D. Schram, M. Á. González, R. Rego, M. G. Kong, and C. Leys, “Characterization of a direct dc-excited discharge in water by optical emission spectroscopy,” *Plasma Sources Sci. Technol.*, vol. 18, no. 2, p. 025017, 2009.

[55] S. A. Astashkevich *et al.*, “Radiative characteristics of 3p Σ, Π; 3d Π-, Δ- states of H2 and determination of gas temperature of low pressure hydrogen containing plasmas,” *J. Quant. Spectrosc. Radiat. Transf.*, vol. 56, no. 5, pp. 725–751, 1996.

[56] L. M. Isola, B. J. Gómez, and V. Guerra, “Determination of the electron temperature and density in the negative glow of a nitrogen pulsed discharge using optical emission spectroscopy,” *J. Phys. Appl. Phys.*, vol. 43, no. 1, p. 015202, 2009.

[57] V. M. Donnelly and M. V. Malyshev, “Diagnostics of inductively coupled chlorine plasmas: Measurements of the neutral gas temperature,” *Appl. Phys. Lett.*, vol. 77, no. 16, pp. 2467–2469, 2000.

[58] J. Voráč, L. Kusỳn, and P. Synek, “Deducing rotational quantum-state distributions from overlapping molecular spectra,” *Rev. Sci. Instrum.*, vol. 90, no. 12, 2019, Accessed: Nov. 14, 2023. [Online]. Available: https://pubs.aip.org/aip/rsi/article-abstract/90/12/123102/1018065

[59] J.-S. Poirier, P.-M. Bérubé, J. Muñoz, J. Margot, L. Stafford, and M. Chaker, “On the validity of neutral gas temperature by N_2 rovibrational spectroscopy in low-pressure inductively coupled plasmas,” *Plasma Sources Sci. Technol.*, vol. 20, no. 3, p. 035016, Jun. 2011, doi: 10.1088/0963-0252/20/3/035016.

[60] M. Ashford *et al.*, “Gas Temperature Determination of Nonthermal Plasma Through Boltzmann Plot Method,” in *2019 IEEE Pulsed Power & Plasma Science (PPPS)*, IEEE, 2019, pp. 1–4. Accessed: Nov. 12, 2023. [Online]. Available: https://ieeexplore.ieee.org/abstract/document/9009911/?casa_token=mGRpVwFSsXoAAAAA:KIladniG1kVVsHPUefgn6juHT5JqT88cAb4HOma_LCfyjJ0py75erPoS2lXrAzSEXHX6u-_BLA

[61] V. Martin, G. Bauville, M. Fleury, and V. Puech, "Exciplex emission induced by nanosecond-pulsed microdischarge arrays operating at high repetition rate frequency," *Plasma Sources Sci. Technol.*, vol. 21, no. 6, p. 065001, 2012.

[62] S. Kasri *et al.*, "Experimental characterization of a ns-pulsed micro-hollow cathode discharge (MHCD) array in a N2/Ar mixture," *Plasma Sources Sci. Technol.*, vol. 28, no. 3, p. 035003, 2019.

[63] S. B. Bayram, P. T. Arndt, and M. V. Freamat, "Rotational spectra of N2+: an advanced undergraduate laboratory in atomic and molecular spectroscopy," *Am. J. Phys.*, vol. 83, no. 10, pp. 867–872, 2015.

[64] K. Gazeli, P. Svarnas, B. Held, L. Marlin, and F. Clement, "Possibility of controlling the chemical pattern of He and Ar 'guided streamers' by means of N2 or O2 additives," *J. Appl. Phys.*, vol. 117, no. 9, 2015, Accessed: Nov. 12, 2023. [Online]. Available: https://pubs.aip.org/aip/jap/article/117/9/093302/149351

[65] P. J. Bruggeman, N. Sadeghi, D. C. Schram, and V. Linss, "Gas temperature determination from rotational lines in non-equilibrium plasmas: a review," *Plasma Sources Sci. Technol.*, vol. 23, no. 2, p. 023001, 2014.

[66] M. Šimek, "Optical diagnostics of streamer discharges in atmospheric gases," *J. Phys. Appl. Phys.*, vol. 47, no. 46, p. 463001, 2014.

[67] L. Xu, N. Sadeghi, V. M. Donnelly, and D. J. Economou, "Nickel atom and ion densities in an inductively coupled plasma with an internal coil," *J. Appl. Phys.*, vol. 101, no. 1, 2007, Accessed: Nov. 12, 2023. [Online]. Available: https://pubs.aip.org/aip/jap/article/101/1/013304/916958

[68] Q. Wang, F. Doll, V. M. Donnelly, D. J. Economou, N. Sadeghi, and G. F. Franz, "Experimental and theoretical study of the effect of gas flow on gas temperature in an atmospheric pressure microplasma," *J. Phys. Appl. Phys.*, vol. 40, no. 14, p. 4202, 2007.

[69] N. K. Bibinov, A. A. Fateev, and K. Wiesemann, "On the influence of metastable reactions on rotational temperatures in dielectric barrier discharges in He-N2 mixtures," *J. Phys. Appl. Phys.*, vol. 34, no. 12, p. 1819, 2001.

[70] G. Herzberg, "Spectra of diatomic molecules," *Mol. Spectra Mol. Struct.*, vol. 1, p. 127, 1950.

[71] A. D. Srivastava, M. H. Gordon, and D. G. Bhat, "Optical emission spectroscopy in an inverted cylindrical magnetron plasma," *Surf. Coat. Technol.*, vol. 200, no. 5–6, pp. 1346–1350, 2005.

[72] S. Mathioudaki, C. Vandenabeele, R. Tonneau, A. Pflug, and S. Lucas, "Characterization of a pulsed low pressure argon discharge in a cylindrical magnetron reactor by plasma diagnostic and 3D plasma modeling," *J. Vac. Sci. Technol. A*, vol. 37, no. 3, 2019, Accessed: Nov. 13, 2023. [Online]. Available: https://pubs.aip.org/avs/jva/article-abstract/37/3/031301/910820

[73] J. A. M. Van der Mullen, "Excitation equilibria in plasmas; a classification," *Phys. Rep.*, vol. 191, no. 2–3, pp. 109–220, 1990.

[74] N. Balcon, A. Aanesland, and R. Boswell, "Pulsed RF discharges, glow and filamentary mode at atmospheric pressure in argon," *Plasma Sources Sci. Technol.*, vol. 16, no. 2, p. 217, 2007.

[75] A. Yanguas-Gil, J. Cotrino, and A. R. González-Elipe, "Measuring the electron temperature by optical emission spectroscopy in two temperature plasmas at atmospheric pressure: A critical approach," *J. Appl. Phys.*, vol. 99, no. 3, 2006, Accessed: Nov. 13, 2023. [Online]. Available: https://pubs.aip.org/aip/jap/article/99/3/033104/292558

[76] D. Mariotti, Y. Shimizu, T. Sasaki, and N. Koshizaki, "Gas temperature and electron temperature measurements by emission spectroscopy for an atmospheric microplasma," *J. Appl. Phys.*, vol. 101, no. 1, 2007, Accessed: Nov. 13, 2023. [Online]. Available: https://pubs.aip.org/aip/jap/article/101/1/013307/917079

[77] D. Mariotti, Y. Shimizu, T. Sasaki, and N. Koshizaki, "Method to determine argon metastable number density and plasma electron temperature from spectral emission originating from four 4p argon levels," *Appl. Phys. Lett.*, vol. 89, no. 20, 2006, Accessed: Nov. 13, 2023. [Online]. Available: https://pubs.aip.org/aip/apl/article/89/20/201502/907622

[78] F. J. Gordillo-Vázquez, M. Camero, and C. Gómez-Aleixandre, "Spectroscopic measurements of the electron temperature in low pressure radiofrequency Ar/H2/C2H2 and Ar/H2/CH4 plasmas used for the synthesis of nanocarbon structures," *Plasma Sources Sci. Technol.*, vol. 15, no. 1, p. 42, 2005.

[79] A. Kais, J. Lo, L. Thérèse, and P. Guillot, "Heating power at the substrate, electron temperature, and electron density in 2.45 GHz low-pressure microwave plasma," *Phys. Plasmas*, vol. 25, no. 1, 2018, Accessed: Nov. 13, 2023. [Online]. Available: https://pubs.aip.org/aip/pop/article/25/1/013504/129024

[80] Y. T. Lin, "Enhancement of Selected Species in Nonthermal Atmospheric Pressure Plasma: Implications on Wound Healing Effects," *IEEE Trans. Plasma Sci.*, vol. 47, no. 2, pp. 1134–1144, 2018.

[81] R. Jaafarian and A. Ganjovi, "Using RF inductive rings to improve the efficiency of a designed pulsed plasma jet," *Indian J. Phys.*, vol. 93, no. 6, pp. 799–810, Jun. 2019, doi: 10.1007/s12648-018-1343-9.

[82] E. C. Knox-Davies, J. M. Shannon, and S. R. P. Silva, "The properties and deposition process of GaN films grown by reactive sputtering at low temperatures," *J. Appl. Phys.*, vol. 99, no. 7, 2006.

[83] M. Dinescu, P. Verardi, C. Boulmer-Leborgne, C. Gerardi, L. Mirenghi, and V. Sandu, “GaN thin films deposition by laser ablation of liquid Ga target in nitrogen reactive atmosphere,” *Appl. Surf. Sci.*, vol. 127, pp. 559–563, 1998.

[84] C. Lehrer, L. Frey, S. Petersen, M. Mizutani, M. Takai, and H. Ryssel, “Defects and gallium-contamination during focused ion beam micro machining,” in *2000 International Conference on Ion Implantation Technology Proceedings. Ion Implantation Technology-2000 (Cat. No. 00EX432)*, IEEE, 2000, pp. 695–698. Accessed: Nov. 02, 2023. [Online]. Available: https://ieeexplore.ieee.org/abstract/document/924248/

[85] M. S. Kumar, S. S. Kushvaha, and K. K. Maurya, “Low temperature growth of GaN epitaxial layers on sapphire (0001) by pulsed laser deposition using liquid gallium target,” *Sci. Adv. Mater.*, vol. 6, no. 6, pp. 1215–1220, 2014.

Chapter 4 – Characterization of GaN thin films deposited on Si at room temperature

Table of Contents

Chapter 4 – Characterization of GaN thin films deposited on Si at room temperature 75

4.1 An overview of the properties of GaN film 77

4.2 Influence of the working pressure 79

4.2.1 Surface morphology, structure & crystalline fraction: pressure effect 80

4.2.2 Estimating the Ga atom flux and average energy at the substrate 83

4.2.3 Interdependence of the flux & energy of Ga atom on the GaN film structure – pressure effect............... 88

4.3 Influence of the N_2 gas flow variation 90

4.3.1 Surface morphology, structure & crystalline fraction.................................. 91

4.3.2 Interdependence of the flux & energy of Ga atoms on the GaN film structure – N_2 flow effect............. 93

4.4 Influence of the RF power 95

4.4.1 Surface morphology, structure & crystalline fraction.................................. 95

4.4.2 Interdependence of the flux & energy of Ga atom on the GaN film structure – RF power effect............ 97

4.5 Chemical composition investigation of polycrystalline GaN films 99

4.5.1 GaN surface analysis-using XPS 99

4.5.2 Composition profile analysis using XPS & SIMS 101

4.5.3 Oxygen contamination – do reactor & plasma cleaning help? 103

4.6 TEM analysis on the crystalline structure of GaN 104

4.7 Cathodoluminescence analysis of GaN films grown at room temperature 105

4.7.1 Potential origin of the GaN CL peaks in undoped GaN 106

4.7.2 Observations & analysis of the CL peaks of GaN grown at room temperature 107

4.8 A summary of the qualification of GaN on Si at room temperature 110

REFERENCES.................................. 113

Chapter 4 focuses on the characterization of GaN thin films grown at room temperature using reactive magnetron sputtering in a custom-built plasma PVD reactor. The chapter is structured into seven sections:

1. Contextualizes our work within the framework of GaN growth via sputtering, referencing the Thornton growth model. Characterization of GaN films is conducted using SEM, AFM, and GIXRD, revealing either amorphous or polycrystalline structures under various process conditions.

2. Investigates the impact of working pressure on film quality, correlating trends in growth rate, morphology, and crystallinity with adatom energy and mobility. Plasma diagnostics parameters, including gas temperature and electron density, are utilized to estimate Ga atom flux (φ_{Ga}) and average energy at the substrate ($\overline{E_{Ga}^{sub}}$) to correlate with the growth rate and the crystalline quality of the GaN films.

3. Explores the effects of N_2 flow rate on film properties, extending the analysis from section 2 to a new process parameter.

4. Examines the influence of RF power on film characteristics, building upon insights gained in previous sections to define an optimized sputtering condition for room temperature GaN film deposition.

5. Conducts chemical composition analysis of GaN films using XPS assessing surface chemistry, depth profiles, and the impact of contaminants on lattice structure. It evaluates the efficacy of plasma and reactor cleaning procedures in mitigating oxygen contamination of the grown films.

6. Performs structural analysis of GaN films using TEM, focusing on samples deposited under optimized conditions identified in earlier sections.

7. Presents results from Cathodoluminescence measurements, analyzing spectra for GaN films across pressure and flow series to identify luminescence peaks associated with band-edge and defect-related emissions. Correlates the results from TEM to comment on the grain size and luminescence effects corresponding to the growth condition.

8. Provides a concise summary of GaN film qualification, evaluating the findings from sections 1 to 7.

In this thesis, we aim at harnessing the potential of using a plasma for reducing process temperatures while producing high quality thin films. To do so, a precise control over the process parameters is necessary. In this chapter, we focus on assessing the influence of process parameters such as the working pressure, N_2 flow rate and the RF power. The growth rate, surface morphology, topography and crystalline fraction were used as data levers to determine the quality of the thin film. We first analyze the features of the GaN films; then we analyze the plasma to correlate with the film properties, after which we provide the first insights on the pathway to obtain a film with the best quality in terms of growth rate and crystalline structure. Along the way, we also encounter possible contaminants, which enabled us to concentrate more on the chemical composition of the films and possible ideas on the mitigation methods of such contaminants. Furthermore, the luminescence features of such films deposited at room temperature were also analyzed and certain defects related to growth conditions were explored.

First, we start by presenting a global overview of the GaN film deposited at room temperature using several characterization techniques.

4.1 An overview of the properties of GaN film

Figure 4.1 presents an overview of the characterization data set of a typical GaN thin film deposited on n-type c-Si (100) substrates at room temperature under the following growth conditions: working pressure in the range of 2.3 – 13.3 Pa, RF power varied from 75 W to 125 W and N_2 flow varied from 0-100% in an Ar/N_2 gas mixture. As a reminder, room temperature means that the substrate was not intentionally heated and that the eventual heating would be due to the plasma is fairly limited (less than 50°C), as measured by a thermocouple placed on the substrate holder. A picture of the GaN thin film is shown in Figure 4.1.A along with its corresponding thickness profile across the width of the sample – measured with the help of a profilometer (Figure 4.1.A'). The GaN film is the thickest at the center and subsides uniformly across both edges. This non-uniformity is likely due to target configuration. Indeed, the 2" circular magnetron-sputtering source that holds the liquid Ga target is partially hidden by a 1" circular mask and hence the plasma at the cathode is confined to approximately 1" thereby inducing this non- uniform profile in the 2" rectangular substrate. It is important to note here that the quality of the thin film does not vary across the investigated thickness range and remains consistent as verified by XRD analysis, which show identical XRD patterns for samples of different thickness grown at identical conditions.

Figure 4.1.B&C shows SEM and AFM images representing the surface morphology and the topography of the GaN film, respectively. The thin film exhibits a nanostructured morphology with features at a size range of a few tens of nanometers. The topographical view from AFM depicts a granular morphology with a root mean square (RMS) roughness values in the range of a few nanometers.

Figure 4.1.D&D' depicts the profile of the thin film in terms of composition (D) and morphology (D') that were obtained using GD-OES and cross-section SEM, respectively. The former shows a uniform elemental distribution of gallium and nitrogen within the depth, which confirmed us the efficiency of our plasma process in supplying a sufficient amount of both Ga and N-atoms. As can be seen in Figure 4.1.D, the film exhibits a sharp interface, as evidenced by the sharp decrease in the signal intensities of both Ga and N that occurs concomitantly with the strong increase of the Si signal. The cross-sectional SEM image (Figure 4.1.D') of the thin film depicts a columnar growth, which was most of the time the structure we found for all the films we grown that were of polycrystalline nature, whatever the operating conditions.

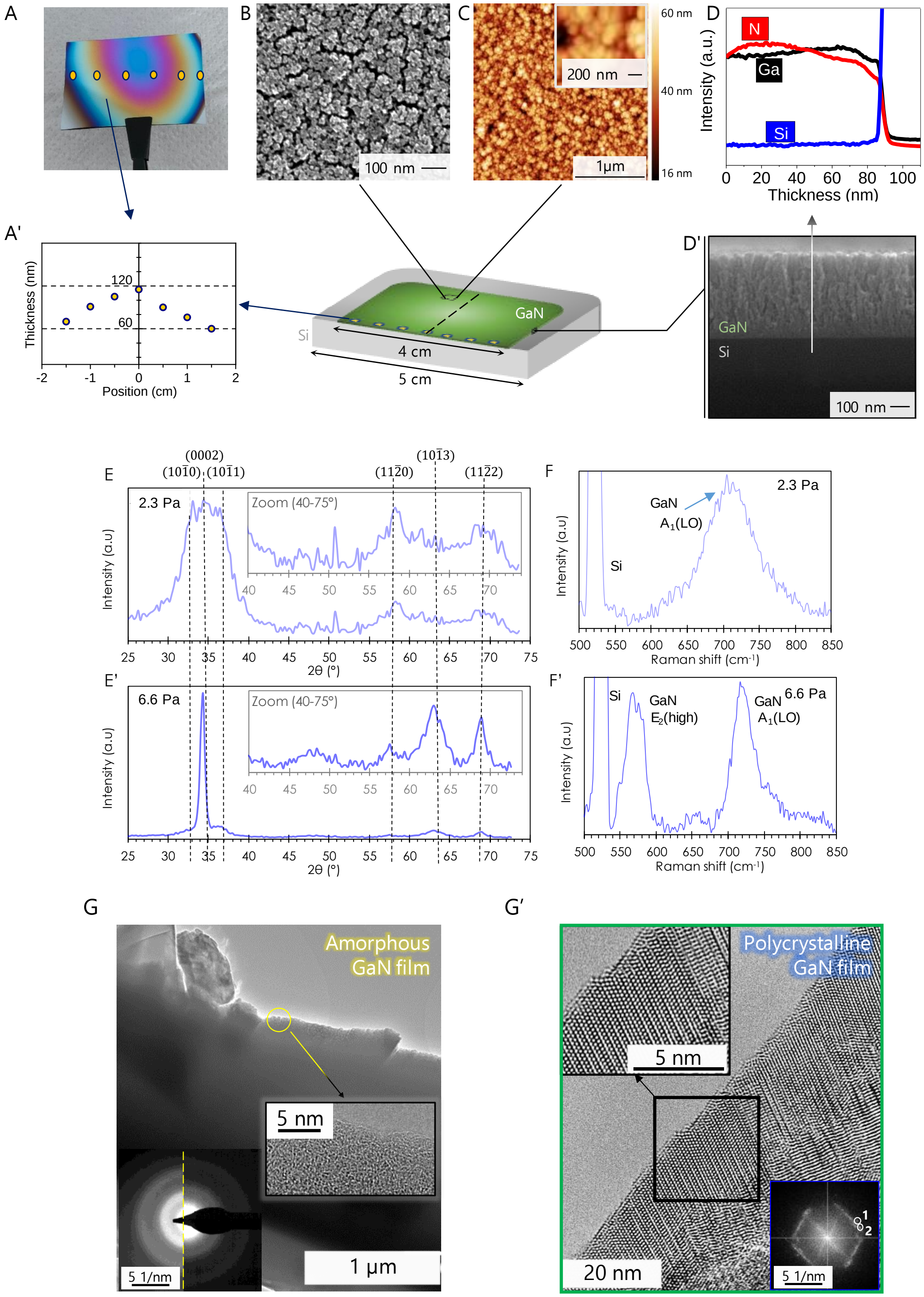

Figure 4.1: The central image represents a schematic of a GaN thin film deposited on a Si substrate. A, A': Picture of a GaN thin film & its corresponding thickness profile across the width of the sample. B: SEM surface profile. C: AFM profile at two different magnifications. D, D': The GD-OES composition profile across the depth of the sample & its corresponding SEM cross-sectional image. E, E': GIXRD spectra of GaN on Si at a working pressure of 2.3 Pa and 6.6 Pa; F, F': Raman spectra of GaN on Si at a working pressure of 2.3 Pa and 6.6 Pa respectively corresponding to an amorphous and polycrystalline GaN film. G, G': High-resolution TEM images of an amorphous and a polycrystalline GaN film. The insets show the diffraction pattern corresponding to the crystalline structure of the film.

In terms of crystalline structure, depending on the variation in the process parameters, we overall got two type of films in this thesis work: amorphous and polycrystalline GaN films as respectively shown in Figure 4.1.E&E' in which peak identification was done using the JCPDS database [1]. In Figure 4.1.E&E', one can clearly observe the distinctive patterns from the amorphous (A) to crystalline (B) phase especially in the region of 25-40°, delineating the change in structure when the pressure is changed from 2.3 Pa to 6.6 Pa. Apart from the dominant peak at 34 corresponding to the (0002) plane of GaN, the analysis reveals peaks corresponding to the $(10\bar{1}1)$ plane, alongside weaker peaks at 57°, 63°, and 69° indicative of the $(11\bar{2}0)$, $(10\bar{1}3)$, and $(11\bar{2}2)$ planes. These findings align with literature values of a hexagonal wurtzite GaN, thereby confirming the dominance of the hexagonal structure of our GaN films. For the polycrystalline sample (Figure 4.1.E'), we used the Sherrer's formula for the (0002) peak to estimate the grain size [2]. We have found that samples have a grain size of ~ 5 to 10 nm. The crystalline structure was also analyzed using Raman spectroscopy and the spectra corresponding to the sample at 2.3 Pa and 6.6 Pa are presented in Figure 4.1.F&F'. For a Raman system with a backscattering geometry such as the one used here, only the E_2 (high) and the A_1 (LO) modes are allowed, the others being forbidden [3]. For the sample grown at 2.3 Pa, the E_2 (high) peak is not observed, while a broad peak centered around 680 cm^{-1} is observed, confirming the amorphous nature of the GaN film. However, for the sample deposited at 6.6 Pa, both the peaks of the E_2 (high) and the A_1 (LO) modes are visible corresponding to the polycrystalline nature of the film. It is important to note here that the peaks of the A_1(LO) mode at ~ 711 cm^{-1} are weak and deviate drastically with respect to the reference values of GaN at 735 cm^{-1}. Although the A_1(LO) mode is allowed, literature suggests that a quantitative analysis with this peak is hardly possible unless an epitaxial GaN layer is deposited [4]. The blue shift of both the E_2(high) and the A_1(LO) mode from a typical crystalline GaN layer may be attributed to numerous factors such as the strain, inhomogeneity in the chemical composition and structural defects [5]. The wurtzite structure of our GaN films have also been confirmed from the diffraction patterns obtained from the TEM measurements as depicted in Figure 4.1.G&G' where the polycrystalline film shows an ordered atomic stacking of elements whereas the amorphous films correspond to a disordered arrangement of atoms.

Throughout the entire range of the process conditions, we observed the same two prominent structures of GaN as mentioned above: a) an amorphous GaN film and b) a polycrystalline GaN film with a hexagonal wurtzite structure. The process parameters (working pressure, Ar/N_2 flow variation and RF Power) played an important role in this transition from an amorphous to a polycrystalline layer. In the coming sections, we aim to explore the dependence of the process parameters not only on this transition, but also on morphology, structural, chemical and luminescence aspects and address towards optimizing the sputtering process to obtain a high-quality GaN. It is imperative to emphasize on the criteria defining high-quality GaN films based on our analysis. **In the context of this thesis, optimal GaN thin film quality encompasses considerations of crystalline fraction, stoichiometry, band-edge luminescence, and achieving a high growth rate with minimal surface roughness.** While electrical conductivity is also indicative of sample quality, preliminary electrical characterization tests conducted on our GaN films, deposited at room temperature, revealed high resistivity of approximately 10^8 Ω.cm. Henceforth, references to high-quality samples in our case will be based solely on the aforementioned features, independent of their electrical characteristics that is a parameter that will be optimized beyond this thesis. A detailed explanation on the influence on the process parameters on the morphology and structure will be given in the coming sections.

4.2 Influence of the working pressure

Figure 4.2 presents the Thornton's structure zone model [6] [7] where the structure of the films is given as a function of the Ar process pressure and a value T/Tm the ratio of substrate temperature (T) to the melting temperature (Tm) of the deposited material (GaN ~ 2700°C). In this model, Zone 1 corresponds to T/Tm values below 0.1, where atoms have low energy, yielding compact films;Zone 2, with T/Tm between 0.4 and 0.8, exhibits improved adatom mobility and crystallinity; Zone 3, spanning T/Tm above 0.8, features enhanced surface diffusion, leading to smoother films.

The Transition Zone occurs when T/Tm is in between 0.1 to 0.4, marking a shift to energy transfer-dominated processes.

From Figure 4.2, we can state that in our typical growth conditions, i.e. working at a fixed temperature close to the room temperature without any significant deviations, corresponding to process condition (~T/Tm < 0.1), and at a pressure range of 10 to 100mTorr, there cannot be any transitions from zone 1 to any other zones. Hence, following this model, the GaN films are expected to have a columnar structure with porous morphology and weakly binding grains [8].

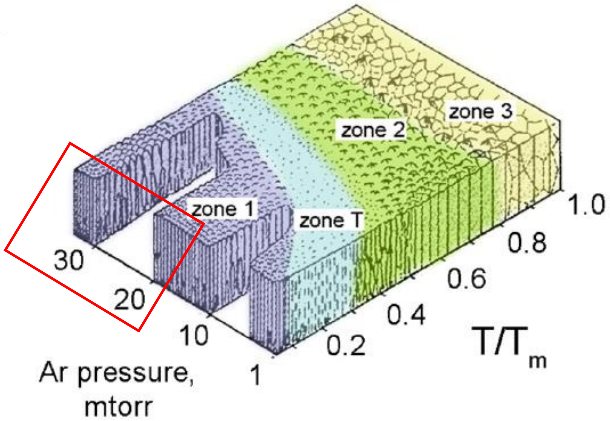

Figure 4.2: Structure zone diagrams of Thornton's zone model recreated from [6], [7], [9] . The area marked in red represents the sputtering pressure conditions that we used (1-15 Pa).

The zone 1 structure results when adatom diffusion is insufficient to overcome the effects of shadowing, which can occur in amorphous and polycrystalline layers [10]. Earlier structure zone models (late 60s) considered only the effect of the substrate temperature to define the structures [11]. Thornton elaborated on the zone classification by taking into account the working pressure. This growth parameter has the potential to alter both the kinetic energy of ions reaching the substrate and the average distance particles travel without collisions. Consequently, it can either increase or decrease the intensity of particle bombardment on the substrate surface, thereby influencing the mobility of adatoms on that surface. Therefore, an efficient way to establish the optimization process is to start by investigating the evolution of the surface morphology and crystalline fraction as a function of the working pressure. This model has its limitations as it fails to account for factors like the introduction of nitrogen (N_2) gas and other crucial parameters such as power, which may introduce discrepancies. In this thesis, we aim to address these limitations by developing our own sputtering model tailored for GaN growth. Our approach involves aligning our criteria with Thornton's model, focusing particularly on morphology and crystallinity as foundational elements.

4.2.1 Surface morphology, structure & crystalline fraction: pressure effect

Figure 4.3 represents the SEM surface micrographs (**A**) and the cross-sectional images (**B**) of GaN films grown on Si at six different pressure values ranging from 2.3 to 13.3 Pa. From the surface micrographs (Figure 4.3.A), we observe that the films are all nanostructured with feature sizes varying as a function of the pressure. Also visible in Figure 4.3.A is the grain structure that overall becomes more porous with more voids visible as the pressure increases. Going back to the Thornton's zone model shown in Figure 4.2, this could be attributed to the fact that at low pressures (2.3 Pa); the reactive species (nitrogen ions, radicals and atoms) close to the substrate have higher energy in a less collisional regime, which in turn increases the adatom mobility on the surface. The mobility of adatoms on the substrate's surface is high enough to produce a dense structure with little separation into individual columns [8]. The trend of the increase in porosity is mostly visible when the pressure is increased from 2.3 Pa to 6.6 Pa, after which the trend seems less clear. However, it is important to note that while analyzing the cross-section of the samples depicted in Figure 4.3.B, a discernible trend of the film densifying (becoming less porous) at lower pressures (2.3 Pa) is not evident, contrary to what Thornton's model would suggest. Instead, all the films display a similar columnar structure overall. It is important to note here that columnar structures and porosity are not inherently linked. Porosity refers to the presence of void spaces or pores within a material, while columnar structures involve the formation of elongated columns or grains within a thin film. While it is possible for columnar structures to exhibit porosity, especially if the growth conditions are not optimized to promote denser packing of atoms, the presence of columnar structures does not necessarily imply porosity. Conversely, dense films can also exhibit columnar structures if the growth conditions favor the formation of such morphology.

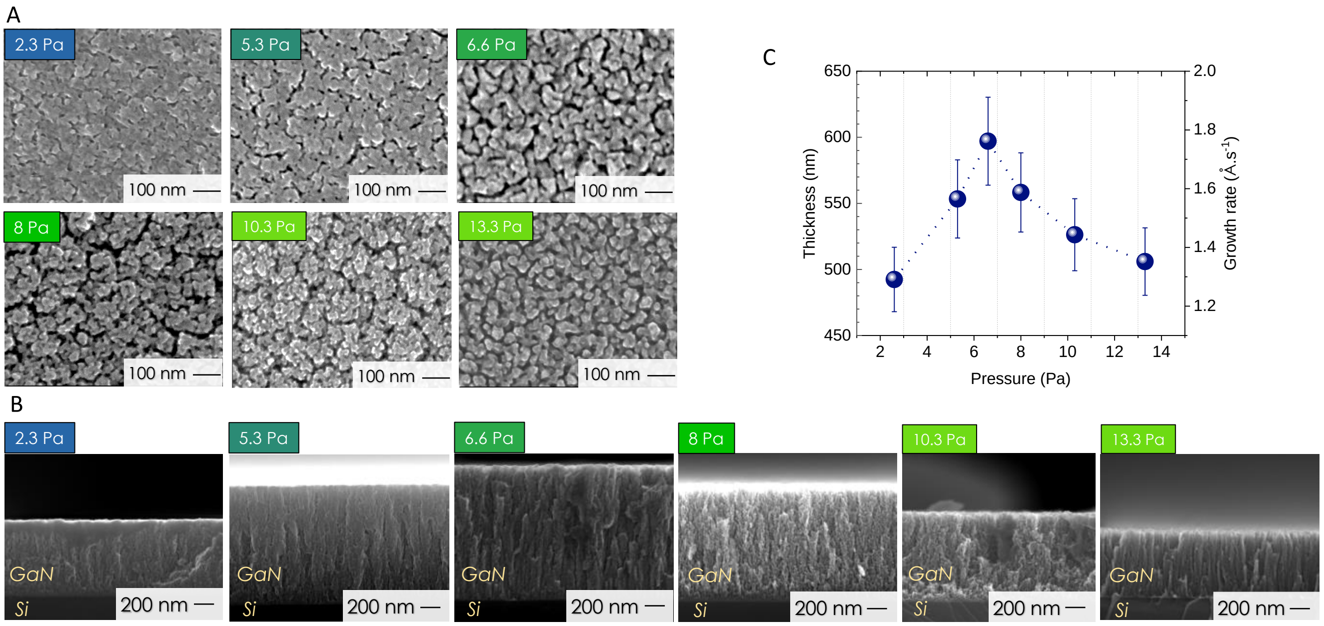

Figure 4.3: SEM images of GaN on Si at varying pressures from 1-15 Pa. A. SEM surface micrographs. B. SEM cross-section images depicting the thin film & the Si substrate. C. The thickness & growth rate obtained from the cross-section images at varying pressures. The RF Power and Ar/N_2 flow were kept constant at 100 W and 12/8 sccm respectively.

At higher-pressure ranges such as ours, the longer the distance travelled by the reactive species to reach the substrate, the more they collide and lose energy and the relation between the pressure and the energy becomes more complex and could depend on other factors such as the gas temperature. The dependence on the energy of Ga-atoms on the growth structure will be explained in detail in the coming sections.

To gain more insights on the deposition process, the growth rate as a function of the pressure has been measured from the film thickness values extracted from cross-section SEM images (Figure 4.3.B). Overall, the growth rate is of the order of a few Å/s with the highest growth rate achieved at 6.6 Pa with a value of 1.8 Å/s. This value is much higher than those reported for a sputtering process which uses a GaN target and a pure Ar plasma (~ 0.4 Å/s) [12], whereas it is similar to a conventional deposition process such as MBE that has an average growth rate of ~ 1-2 Å/s at 700°C [13]. The variation of the growth rate could be related to the flux of the incoming reactive species. To get more insights into the morphology, we further explore the AFM micrographs and analyze the surface roughness of the films.

Figure 4.4 represents the AFM images at varying pressures from 2.3 Pa to 13.3 Pa. The root mean square (RMS) roughness values were calculated from the surface micrographs in Figure 4.4.A and the trend is presented in Figure 4.4.B.

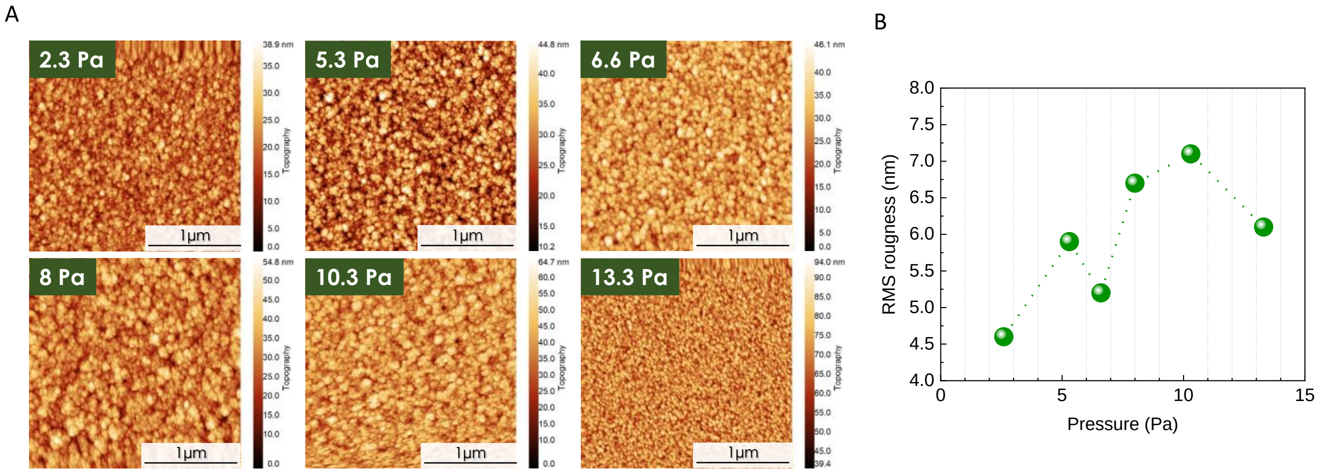

Figure 4.4: AFM images of GaN on Si at varying pressures from 1-15 Pa. A. AFM surface micrographs. B. The root mean square (RMS) roughness obtained from AFM topography at varying pressures. The RF Power and Ar/N_2 flow were kept constant at 100 W and 12/8 sccm respectively.

The RMS surface roughness values are in the range of ~ 4-8 nm which is comparable to the roughness values reported in the literatures (~5nm) for GaN deposition at room temperature [14], [15]. What could be interpreted here is that compared to conventional epitaxial samples as grown by MBE (RMS ~ 1-2 nm)[16], our polycrystalline samples with structural imperfections are inherent to a relatively rougher surface, however, from the observed trends, pressure only has a limited effect on the overall roughness. This could be beneficial while focusing on applications as we concretely modify several parameters without worrying too much about modifying the roughness. Keeping this in mind, we now look into the crystalline structure of the thin films, which were interpreted using GIXRD.

Figure 4.5.A represents the GIXRD spectra measured at different pressures. From the GIXRD spectra, we calculate the crystalline fraction (F_c). which is calculated by integrating the crystalline area below the crystalline peak ((0002) peak at 34° in our case) and dividing it by the overall area comprising of the crystalline & amorphous phases [17]. Figure 4.5.B depicts the F_c at various working pressures.

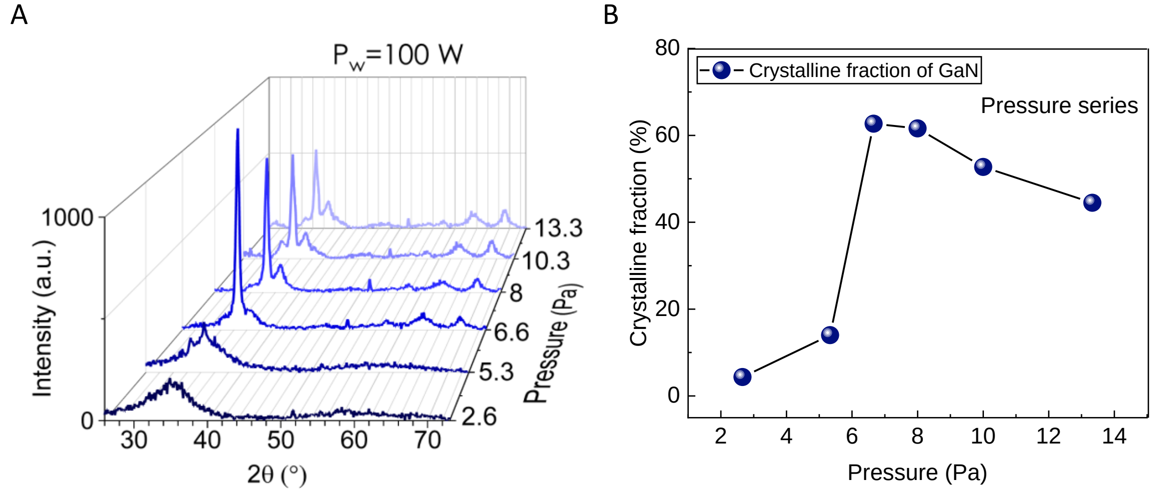

Figure 4.5: A. GIXRD profile at varying pressure ranges from 1-15 Pa. B. Crystalline fraction calculated from the corresponding GIXRD spectra from A. The RF Power and Ar/N_2 flow were kept constant at 100 W and 12/8 sccm respectively.

There are two important observations that can be made from Figure 4.5: (i) as the pressure increases from 2.6 – 6.6 Pa, the GaN film undergoes a transition from an amorphous to a polycrystalline film as evident from the emergence of the 0002 peak peaks (Figure 4.5.A). This is also evidenced from the increase of F_c growing from ~5% at 2.6 Pa to 60% at

6.6 Pa (Figure 4.5.B); (ii) as the pressure further increases from 6.6 Pa to 13.3 Pa, the film remains polycrystalline even though the crystalline fraction decreases from 60% to ~45%, respectively.

From these observations, we can say that the impact of working pressure on the transition from an amorphous to a polycrystalline film is substantial. To better understand the relation, we consider the energy model proposed by Losbichler & Mitterer [18], who correlated the growth rate along crystalline features of the film to the energy & mobility of the impinging adatoms. In our case, the impinging adatoms are those of gallium and nitrogen. Therefore, estimating the adatoms' energy and flux at the substrate will help us to understand the trends in the crystalline quality and the growth rate at varying process conditions. However, from the TALIF measurements (Chapter 3), we were not able to obtain an estimate of the N atom density at our working conditions (0-13 Pa) as the fluorescence signal was too low. Moreover, the source of nitrogen atoms is the N_2 gas and the plasma enables complex reactions involving the formation of N from N_2, which could in turn complicate the correlation between the plasma parameters and the film properties. Considering the flux and energy of Ga atoms would still be valuable as it is the only sputtered component, and we can directly interpret the correlation of the sputtered atoms towards the film deposition. Therefore, we estimated the target atom's (Ga) flux and average energy at the substrate for varying process conditions and correlate it with the growth rate and the crystalline fraction obtained from SEM-cross section and GIXRD respectively. The next section elaborates on the methodology adopted to estimate the Ga atom's flux and energy at the substrate.

4.2.2 Estimating the Ga atom flux and average energy at the substrate

To estimate the flux and energy of the Ga atoms from the target, we go back to the basics of sputtering, where the physics of interaction of an incoming ion with the atoms of a material (target) is described. Depending on the colliding ion's kinetic energy, successive phenomena occur at the surface of the target which results in the ejection of a Ga atom [19]. For estimating the Ga flux and energy in a reactive magnetron sputtering process with Ar and N_2 as the process gases and Ga as the target, we make certain assumptions. These assumptions are:

a) The ion energies of Ar^+ and N_2^+ are directly estimated from the dc-bias potential (V_{DC} ~ 650 V to 850 V). The ion energies are dependent on the self-bias and the plasma potential [20]. As the plasma potential for an RF magnetron sputtering system similar to ours is typically a few tens of eV [21], [22], [23], [24], we neglect any changes occurring in the plasma potential and consider only the self-bias at the cathode.

b) From the N_2 gas, we only consider N_2^+ ions contributing towards sputtering of Ga. Ideally, for modelling an Ar-N_2 plasma-target interaction, N_2^+, N^+ and N^0 species are considered to interact with the target. But, it has been shown that the dominant species among the nitrogen ions and radicals is the N_2^+ ion [25] and hence for reducing complexity in our analysis, we assume that the Ga target is bombarded only by N_2^+ and Ar^+ ions.

c) The incoming Ar^+ and N_2^+ ions incident at the target and the sputtered Ga atom are all normal to the target surface [26].

d) The sputtered Ga particles are all neutral atoms in the ground state.

e) The sputtered Ga atoms only collide with the neutral Ar background gas and these collisions are elastic. This is because there is no proper information on the interaction potential for the interaction with a molecular N_2 gas. This assumption is often considered for all plasma modelling investigations in an Ar-N_2 plasma discharge [27].

f) The energy losses for the sputtered Ga atoms from the target to the substrate occurs only in a pathway normal to the substrate's surface without accounting for angular effects [28], [29].

Apart from these general assumptions, we make some more specific assumptions, which will be explained as we progress.

Ga-atoms energy at the substrate ($\overline{E_{Ga}^{sub}}$)

Figure 4.6.A depicts a schematic of the interaction of the Ar^+ and N_2^+ ions at the Ga target followed by the ejection/sputtering of Ga atoms from the target. The sputtering yield Y(E) of the Ga atoms can be calculated using Bohdansky's empirical formula [30] by knowing the incident ion energies of Ar^+ and N_2^+:

$$Y(E) = 0.0064\,.\; M_2\,.\; \gamma^{\frac{5}{3}}\,.\; E^{\frac{1}{4}}\,.\; \left(1-\frac{E_{th}}{E_i}\right)^{\frac{7}{2}} \qquad (4.1)$$

where $\gamma = \frac{4M_1M_2}{(M_1+M_2)^2}$, is the energy transfer factor in a direct collision, M_1, M_2 the masses of the incident ion (Ar^+ and N_2^+) and the target material (Ga), E_{th} is threshold energy equal to $8E_s/\left({}^{M_1}/{}_{M_2}\right)^2$, E_s the surface binding energy of Ga atoms ~ 2.8 eV [31], E_i the incident ion energy ~ (650~850 eV) for our sputtering system. At an incident ion energy of 700eV, the Ga sputtering yield *Y(E)* calculated from equation (4.1) for an Ar^+ ion is ~ 2.4 Ga atoms/ion and for a N_2^+ ion is ~ 1.5 Ga atoms/ion. Depending on the process condition variation, the ion energy towards the target varies (650~850V), thereby the sputter yield *Y(E)* also varies.

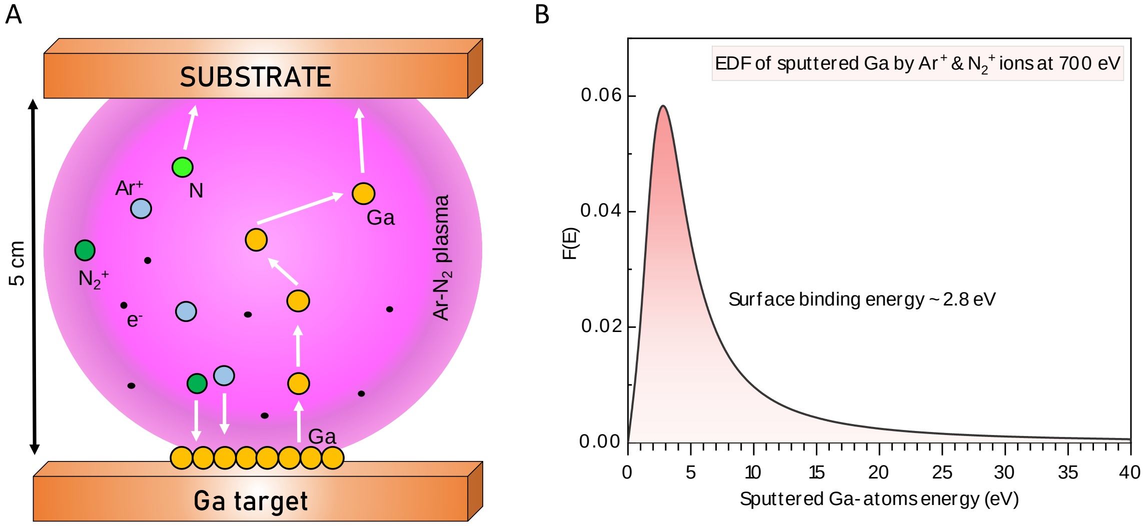

Figure 4.6: A. Schematic showing the Ar^+ and N_2^+ ions bombarding the Ga target normal to the surface. B. The Thompson energy distribution function (EDF) of sputtered Ga atom by Ar^+ and N_2^+ ions calculated at a kinetic energy of 700 eV. The Ga atoms are not sputtered for an energy less than the surface binding energy of Ga ~ 2.8 eV.

Once the Ga atoms are sputtered, they undergo several collisions before reaching the substrate. An important parameter to consider here is the sputtered atom energy distribution function (EDF), since it describes the energy with which the Ga atoms travels the path from target to substrate. For estimation the energy of the sputtered Ga atom, we consider the Thompson energy distribution function (EDF) F(E) [32] :

$$F(E)\begin{cases} \propto \dfrac{1-\left(\dfrac{E_s+E}{\gamma E_i}\right)^{\frac{1}{2}}}{E^2\left(1+\dfrac{E_s}{E}\right)^3} & , E < \gamma E_i - E_s \\ = 0\,, E > \gamma E_i - E_s \end{cases} \qquad (4.2)$$

In the above equation, E_s is the surface binding energy of Ga [33] and E is the energy of the sputtered atom. Figure 4.6.B shows the EDF of the sputtered Ga atom calculated from equation (4.2) for an incident Ar^+ and N_2^+ ion energy of 700 eV. There are no Ga atoms sputtered below the surface binding energy of Ga. The sputtered Ga atoms have a minimum energy slightly above their surface binding energy (~ 2.8 eV) and the maximum energy without any limit can go almost up the incident ion energy ~ γE_i [34]. We introduce an important parameter here from the EDF, known as the total average energy of the sputtered atoms ($\overline{E_{Ga}}$). It can be calculated by correlating the Thompson distribution function with the Sigmund distribution function [35]. The integration of the EDF is performed up to the maximum atom energy ($E_{max} \sim \gamma E_i$). More information on the calculations can be found in literature [36] [37], [38]. With several simplifications, we arrive at equation (4.3), which determines the total average energy of the sputtered atom:

$$\overline{E_{Ga}} = 2E_s \ln\left(\frac{\gamma E_i}{E_s}\right) - 3E_s \tag{4.3}$$

It is important to note here that the average energy of sputtered atoms only depends on the surface binding energy and maximum energy of sputtered atoms. For an incident Ar and N_2^+ ion at ~ 700 eV, the average energy of a sputtered Ga atom at the target ($\overline{E_{Ga}}$) from equation (4.3) is calculated to be ~ 22 eV/atom and 17 eV/atom respectively. For confirming the values of the average energy of the sputtered Ga atoms, we used the SRIM software [39]. SRIM is a group of computer programs, which calculate interactions between ions and matter. The core of SRIM is a program called Transport of Ions in Matter (TRIM). The average energy values simulated from TRIM is shown in Figure 4.7. equation (4.3) is useful for comparing the theoretical E_{avg} to the ones obtained from software simulations such as SRIM/TRIM (stopping/transport range in ions and matter) [40].

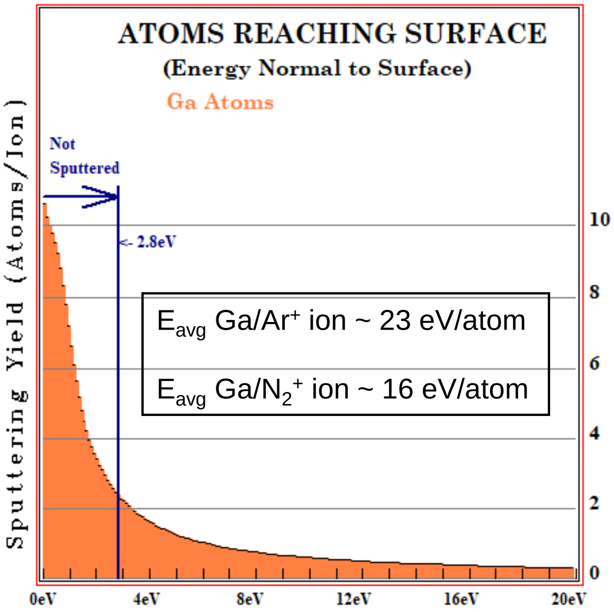

Figure 4.7: Simulations from TRIM for an Ar^+ and N_2^+ ion that calculates the sputter yield and the average energy of the sputtered Ga atom for an ion energy of 700 eV.

We get a good similarity of both the sputter yield *Y(E)* and the average energy per sputtered Ga atom ($\overline{E_{Ga}}$) at the target. These sputtered Ga atoms will experience collisions with the ambient gas and lose part of their kinetic energy modifying their EDF which will not follow the Thompson's distribution [30]. Therefore, the energy at the target and at the substrate will differ significantly depending on the number of collisions suffered. To calculate the average energy at the substrate, the following approach has been used, which considers, in a first approximation, the energy loses along a pathway normal to substrate (without accounting for angular effects) [26], [28], [29], The mean kinetic energy at a distance d from the target is given by the equation:

$$\overline{E_{Ga}^{sub}} = \left(\overline{E_{Ga}} - k_B T_{gas}\right)\left[\frac{E_f}{E_i}\right]^n + k_B T_{gas} \tag{4.4}$$

where $\frac{E_f}{E_i} = 1 - \gamma/2$ the kinetic energy ratio after and before a collision, $n = dP\tau/k_B T_{gas}$ the number of collisions along the path, d the distance between the target and the substrate (~5 cm), P and T_{gas} the sputtering gas pressure and temperature respectively, and τ the collisional cross-section, assuming hard-core interactions[26]. The τ depends mainly on the mass and the interatomic distance and the number of collisions [41]. As the collisional cross-section for the interaction of Ga atoms with an Ar ion is scarcely found in literature , we assume the value of τ to be that of a Copper (Cu)/Ar interaction ~ 25 x 10^{-20} m^2 as the size and mass number of Cu is very close to that of Ga and the interaction of Cu/Ar is commonly used for sputtering model calculations [29].

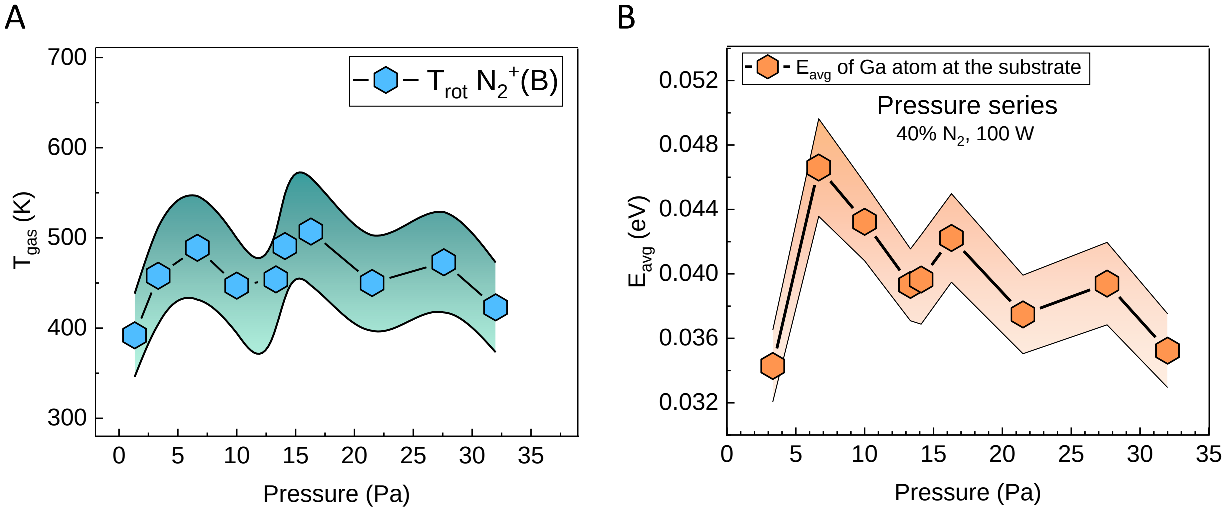

Figure 4.8: A. The trend in gas temperature (T_{gas}) at varying pressure from 1-35 Pa measured from the rotational bands of N_2^+ (B) from OES. B. The average energy of Ga atoms reaching the substrate at varying pressures.

So, the average kinetic energy ($\overline{E_{Ga}^{sub}}$) of the sputtered Ga atoms at the substrate can be estimated from equation (4.4) at different pressures (1-35 Pa) by knowing the gas temperature T_g and $\overline{E_{Ga}}$ (from TRIM simulations). Figure 4.8 shows $\overline{E_{Ga}^{sub}}$ at different pressures (1-35 Pa). The T_g was estimated from the OES measurements of the rotational bands of N_2^+(B) (Chapter 3). The order of magnitude of the $\overline{E_{Ga}^{sub}}$ at the substrate (~ 0.04 eV) is in good agreement with the values obtained in literature from Monte-Carlo simulations for a magnetron sputtering system such as ours at a similar pressure range (~ 1-10 Pa) [42], [43].

Flux of Ga atoms (φ_{Ga})

The flux of sputtered Ga atoms can be estimated if the flux of the Ar^+ and N_2^+ ions incident at the Ga target and their respective sputter yields *Y(E)* are known. We have already calculated the sputter yield of Ga; therefore, we focus now on calculating the flux of the ions at the target. For instance, at an incident ion energy of 700 eV (corresponding to the typical value of the DC self-bias on our target), the Ga sputtering yield *Y(E)* calculated from equation (4.1) for Ar^+ is ~2.4 Ga atoms/ion and for a N_2^+ ion is ~1.5 Ga atoms/ion. Once the sputter yield known, φ_i was determined based on the assumption of a collision-less sheath model [44]. In a collision-less sheath, φ_i is the product of the plasma density at the sheath edge n_s and the minimum velocity of the ions v_{Bohm} at the sheath edge (Bohm velocity)·[44] following the Child-Langmuir theory [24], [45].

$$\varphi_i = n_s v_{Bohm} = \frac{4}{9}\epsilon_0\left(\frac{2e}{M}\right)^{1/2}\frac{V_0^{3/2}}{s^2} \tag{4.5}$$

where V_0 is the difference of potential between the plasma and the cathode, e the electron charge, M the ion mass, ϵ_0 the electrical permittivity in free space and $s = \frac{\sqrt{2}}{3}\lambda_{DS}\left(\frac{2V_0}{T_e}\right)^{3/4}$ the sheath thickness where $\lambda_{DS} = \left({}^{\epsilon_0 T_e}/_{e n_s}\right)^{1/2}$ corresponds to the Debye length. Assuming the quasi-neutrality in the bulk ($n_e \sim n_i$) and that the plasma density at the sheath edge can be calculated by substituting the Bohm Potential into Boltzmann's equations for electrons, we considered $n_s \sim 0.61\ n_e$ [46]. The only other unknown term in the above three equations is the electron temperature (T_e) which has not been directly measured by us. One way is to estimate T_e by knowing the excitation temperature T_{exc} that was measured from the Ar-I emission lines from OES (Chapter 3). To estimate T_e, we mostly relied on values found in the literature, as we did not have access to direct measurement of it. In RF magnetron sputtering systems similar to ours in terms of pressure and gas mixture, T_e ranges from ~1 to 2 eV [47], [48], [49], [50], [51]. Then, to estimate its evolution as a function of the pressure, we assumed that T_{exc} would vary as same as T_e as for non-LTE plasma such as ours, which operates at a low pressure of a few Pa and which exhibits a low electron density ($n_e \sim 10^{10}$ cm^{-3}), 80% of the reactions are governed by direct excitation from the ground state [52]. Figure 4.9.A shows the variation of T_e as a function of the pressure, the error bar being the same as that of T_{exc}. Typically, we estimate that T_e values are in the range of ~1.2 to 1.8 eV for pressures varying from 1.3 to 13.3 Pa.

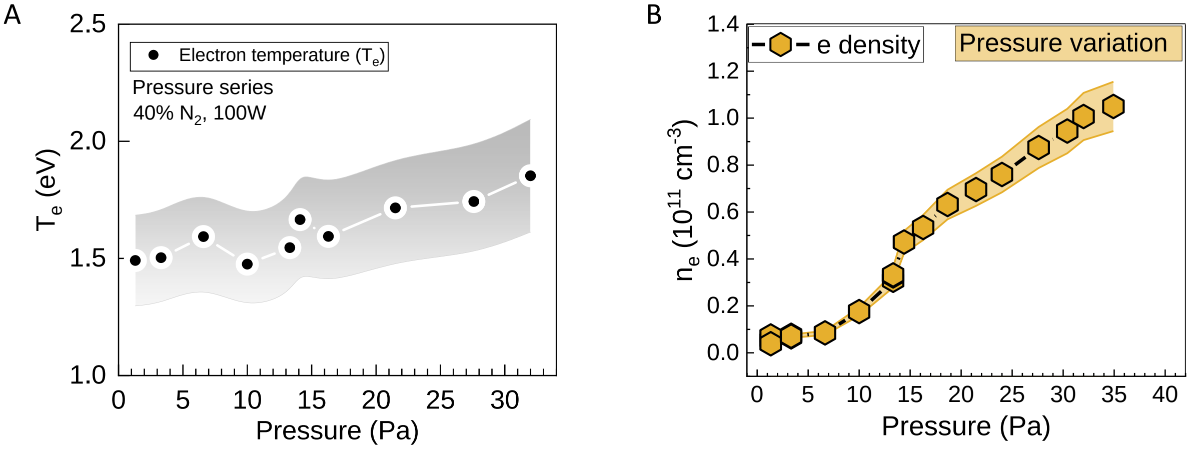

Figure 4.9: A. Trend in the electron temperature (T_e) estimated from the excitation temperatures at varying pressures. B. Trend in the electron density (n_e) calculated from microwave-interferometry at varying pressures.

Overall, knowing T_e and n_e from OES (Figure 4.9.A&B) and MWI interferometry measurements (**Error! Reference source not found.**.d) respectively, we estimated φ_i using equation (4.5). The ratio of the flux of the Ar$^+$ and N$_2^+$ was determined taking into account their partial pressures[27].

Finally, by multiplying the ion fluxes with the sputter yield *Y(E),* we got the flux of the Ga atoms sputtered from the target (φ_{Ga}):

$$\varphi_{Ga} = (\varphi_{Ar^+} * Y(E)_{Ar^+\rightarrow Ga}) + (\varphi_{N_2^+} * Y(E)_{N_2^+\rightarrow Ga}) \tag{1}$$

The flux of the incident ions and the sputtered Ga atoms is shown in Figure 4.10.

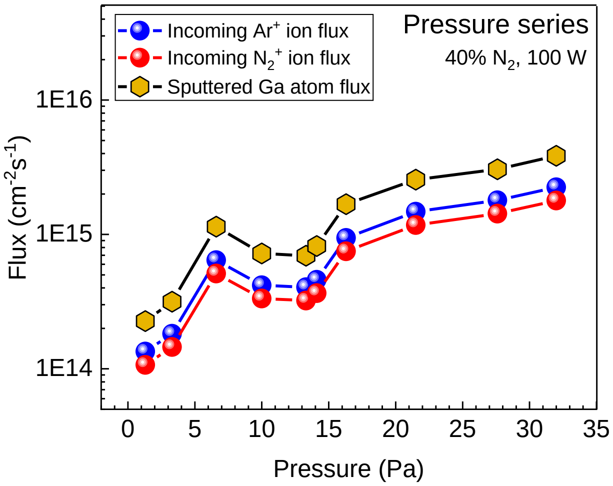

Figure 4.10: The flux of incoming ions at the target: Ar^+, N_2^+ and the sputtered Ga atoms as a function of pressure.

The estimated φ_{Ga} is in the range of 10^{14} ~ 10^{15} $cm^{-2}s^{-1}$. The trend in φ_{Ga} w.r.t pressure is similar to that of the trends of the ion fluxes at the target. The overall flux follows an increasing trend from 1 to 35 Pa with some non-linear variation in the pressure ranges from 3 to 15 Pa. To correlate the φ_{Ga} variation to the GaN film's growth rate and crystalline fraction, we assume that the Ga flux at the target is equal to the Ga flux at the substrate. Of course, the kinetic energy of the sputtered atoms varies from the target to the substrate, but we assume that none of the atoms are lost during the travel from the target to the substrate. Now that we have estimated the plasma parameters (average Ga atom energy at the substrate ($\overline{E_{Ga}^{sub}}$) and the flux of the sputtered Ga (φ_{Ga}) at varying pressures), we aim to analyze the film quality and the growth rate of GaN and investigate their interdependence on the plasma parameters.

4.2.3 Interdependence of the flux & energy of Ga atom on the GaN film structure – pressure effect

Figure 4.11 represents the effect of pressure on four different parameters: a) growth rate (Å/s), b) crystalline fraction ~ F_C(%), c) flux of the sputtered Ga atoms ~ φ_{Ga} ($cm^{-2}s^{-1}$) and d) average kinetic energy of the sputtered Ga atom at the substrate ~ $\overline{E_{Ga}^{sub}}$ (eV). The pressure range that we consider here is from 1-15 Pa, the conditions under which most of the GaN depositions were performed. Figure 4.11 shows that all the four aforementioned parameters follow a similar trend: an increase from 2.3 to 6.6 Pa and a decrease from 6.6 to 10 Pa. Let us first focus on the growth rate variation according to the pressure (Figure 4.11.A).

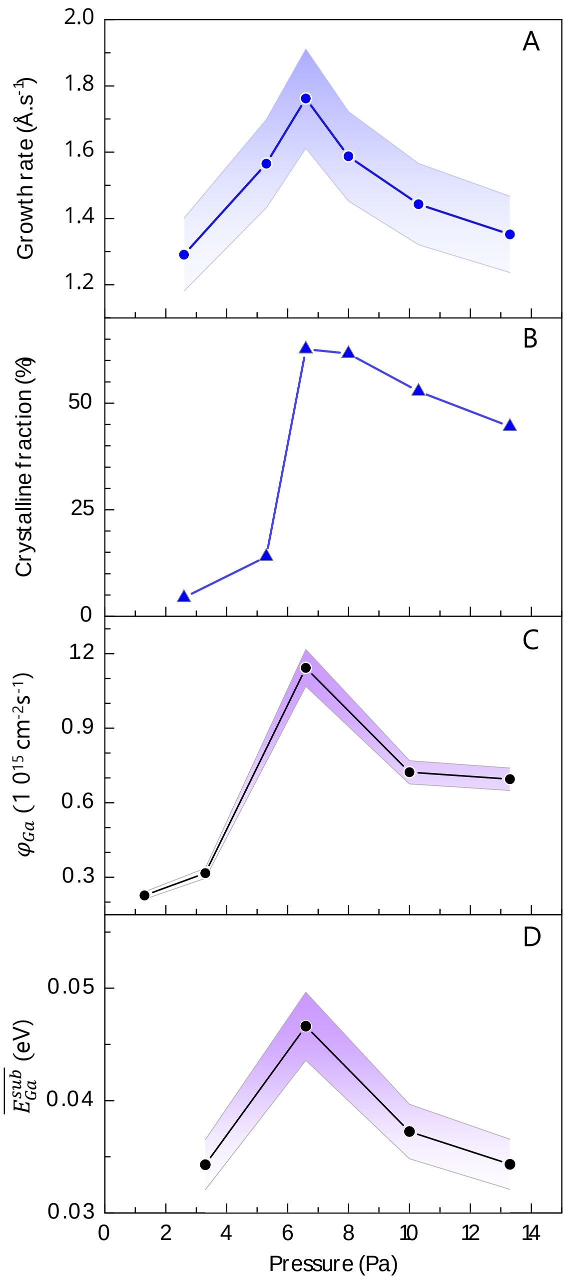

Figure 4.11: The trends in A. growth rate B. Crystalline fraction C. Flux of Ga atom ejecting from the target and D. Average energy of Ga atom reaching the substrate at varying pressures from 0-15 Pa. The RF Power and Ar/N_2 flow were kept constant at 100 W and 12/8 sccm respectively.

The variation of the growth rate can mainly be attributed to the flux of the Ga atoms that reach the substrate. With increasing sputtering pressure from 2.6 – 6.6 Pa, the growth rate increase from 1.2 Å/s to 1.9 Å/s. This trend can be explained by two opposite effects: i) as the pressure increases up to 6.6 Pa, the average mean-free path of the Ar atoms decreases Therefore, the probability of collisions between the Ar and electrons increase, more Ar^+ ions are ionized to bombard the target, which leads to an increase in the number of sputtered target atoms, i.e. the flux of Ga-atoms [53]. This can be verified from Figure 4.11.C where the flux of Ga atoms increases in the pressure range from 1 - 6.6 Pa; ii) at higher pressures (6.6 Pa to 13.3 Pa), the deposition rate decreases since more Ga-atoms suffer collisions and fewer atoms reach the substrate leading to a decrease in the flux and therefore the growth rate [54]. Another reason could be that higher-pressures may result in an enhanced production of active nitrogen species in the plasma along with affecting the directionality of the metal atom flux from the target [55], leading to a decrease in the growth rate. However, since we calculated the flux by assuming interactions normal to the surface, there is no way of confirming the phenomenon.

However, even if several assumptions were made to determine φ_{Ga}, it happens that the estimation of the growth rate from the calculated values is in a quite good agreement with experimental data. For example, if one considers an hexagonal wurtzite GaN structure such as ours, the number of atoms in 1 cm^3 is ~8.9×10^{22} [56]. At 6.6 Pa which corresponds to $\varphi_{Ga} \sim$ 1.1 x 10^{15} $cm^{-2}s^{-1}$, we obtained a growth value of ~2.4 Å/s, which is quite similar to the experimental value ~1.9 Å/s. Note that this deviation might be due to the variation in the flux of N-atoms at the substrate or some contaminants present in the lattice structure. It is worth to note that the increase in growth rate between 2 and 6 Pa is almost doubled while the Ga flux increases by four times. This suggests that the Nitrogen flux predominantly limits the growth rate. This simple approach can be a useful way to guide the experiments toward conditions of high growth rate without performing arduous time consuming experiments and relying on ex-situ characterizations.

Next, we focus on evolution of the crystalline fraction (F_C) and it relation with the Ga-atoms energy impinging the substrate, for which we go back to the Thornton's zone model. As introduced before, the Thornton's zone model [6], [8], [9] considers the final working pressure to be an driving parameter in the structure of the film. Indeed, the pressure has a direct impact on the kinetic energy of Ga-atoms that in result impact the mobility of the adatoms. The adatom mobility governs the formation of crystallites that are bounded by energy-planes during nucleation and coalescence [57]. When we compare the crystalline fraction (Figure 4.11.B) with that of E_{avg} at varying pressures (Figure 4.11.D), we observe a similar trend. As the pressure rises within the range of 2.3 to 6.6 Pa, there is a corresponding increase in the average energy of gallium ($\overline{E_{Ga}^{sub}}$) within GaN, consequently enhancing adatom mobility and facilitating the enhancement of crystalline quality. GaN films subjected to a pressure of 2.6 Pa exhibit a relatively low fraction of crystallinity (FC) ranging from approximately 5% to 10%, indicating amorphous characteristics as evidenced by broad peaks observed in X-ray diffraction (XRD) patterns. The estimated $\overline{E_{Ga}^{sub}}$ at this pressure is approximately 0.035 electron volts (eV). As the pressure increases to 6.6 Pa, the film becomes polycrystalline with Fc ~ 60%. $\overline{E_{Ga}^{sub}}$ at 6.6 Pa is ~ 0.05 eV. The GaN film transitions from an amorphous to a polycrystalline film within the $\overline{E_{Ga}^{sub}}$ range of 0.035 ~ 0.05 eV. Furthermore, the trends in Fc and $\overline{E_{Ga}^{sub}}$ are similar from 6.6 Pa to 13.3 Pa. The F_C value decreases from 60% to 45% and the $\overline{E_{Ga}^{sub}}$ decreases from 0.05 eV to 0.04 eV. This leads us to suggest the average energy of the sputtered Ga atoms that reaches the substrate correlates to an influence on the initial stages of film growth. The growth rate, crystalline fraction, Ga atom flux and the average Ga atom energy, all followed a similar trend as the sputtering pressure increased from 1-13.3 Pa. The best growth rate and the best crystalline fraction were obtained at the same pressure ~ 6.6 Pa. Once again, this intuitive understanding paves way to guiding experiments towards conditions of high crystalline fraction before even performing the depositions and ex-situ characterizations. To explore the credibility of the proposed hypothesis further, while keeping pressure constant, we now analyze the influence of the N_2 flow variation on the GaN film properties.

4.3 Influence of the N_2 gas flow variation

To examine the effects of varying nitrogen concentrations on the resulting GaN film, we conducted a series of depositions while maintaining a constant total gas flow of 20 sccm. Throughout this campaign, the Ar/N_2 flow ratio was adjusted from 10% to 100% of N_2, while the pressure remained at 6.6 Pa and the power at 100W. This deliberate variation in gas composition enables a systematic exploration of the material's properties, providing valuable insights into its behavior across diverse gas phase conditions.

4.3.1 Surface morphology, structure & crystalline fraction

Figure 4.12 depicts the top surface and cross section SEM images of GaN films deposited at N_2 fractions ranging from 10% to 100%. From the surface SEM micrographs (Figure 4.12.A), we clearly see that at higher N_2 fractions (80% and 100%), the nanostructure become smoother with very small nanoscale patterns. These are also the conditions at which the growth rate is the smallest, decreasing from ~ 1.25 Å/s at 60% N_2 flow to ~ 0.5 Å/s at 80% N_2 flow (Figure 4.12.C). The decrease of the grain size could be reasoned by considering the chemical affinity and the reaction kinetics of nitrogen. Indeed, nitrogen, being a smaller and more electronegative atom compared to argon, enhances chemical interactions at the substrate during the deposition process. The increased chemical reactivity of nitrogen promotes the formation of nitride compounds on the substrate surface eventually resulting in a finer grain structure [58]. From Figure 4.12.B, we see that the films become denser at higher N_2 fractions (~ 100%). The densification of the film structure is a consequence of the increased presence of nitrogen and higher nitrogen content that can lead to a more stoichiometric and dense film structure having less voids [59].

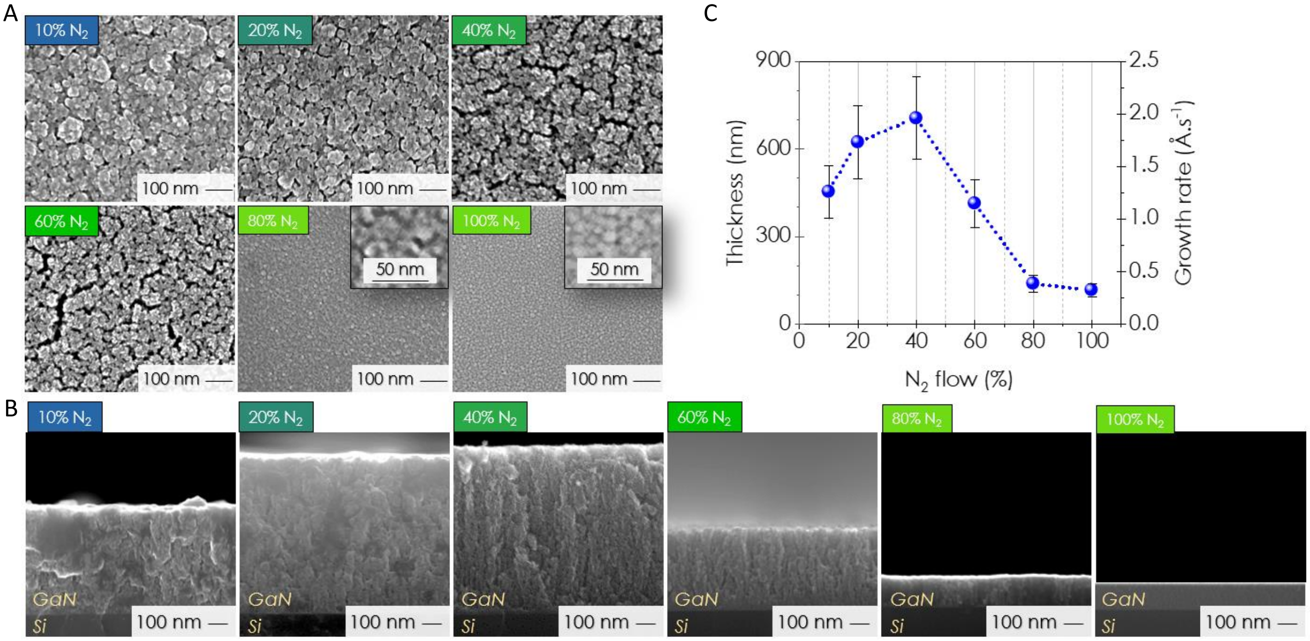

Figure 4.12: SEM images of GaN film on c-Si at varying N_2 fractions from 10-100 %. A. SEM surface micrographs. Insets in the images from 80% and 100% N_2 fraction represents a high-resolution image (50 nm scale) depicting the grain structure. B. SEM cross-section images depicting the thin film & the Si substrate. C. The thickness & growth rate obtained from the cross-section images at varying N_2 fractions. The RF Power and working pressure were kept constant at 100 W and 6.6 Pa respectively.

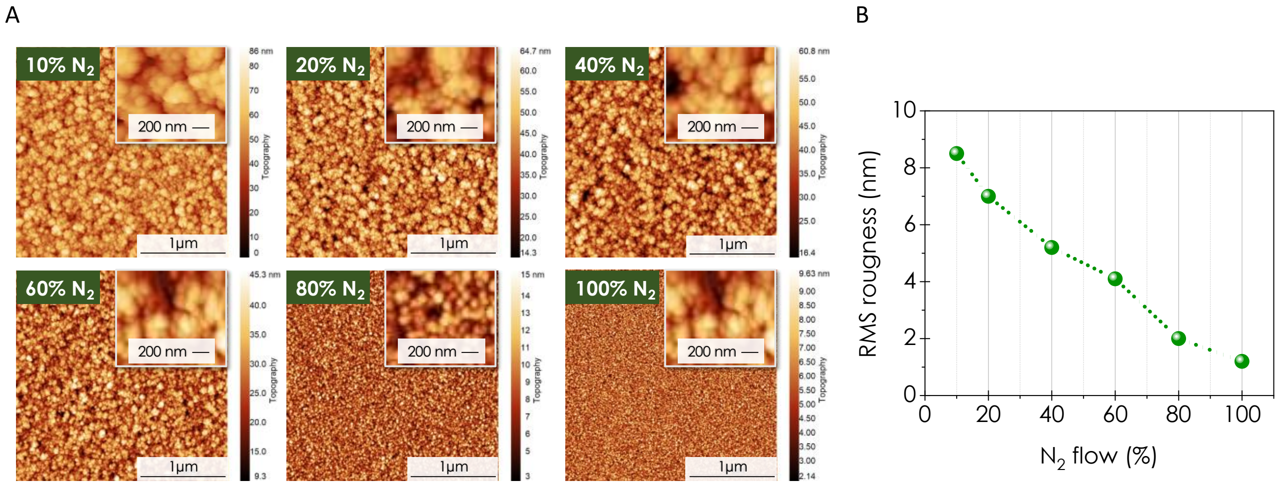

Figure 4.13: AFM images of GaN on Si at varying N_2 fractions from 10-100 %. A. AFM surface micrographs. B. The root mean square (RMS) roughness obtained from AFM topography at varying pressures. The RF Power and working pressure were kept constant at 100 W and 6.6 Pa respectively.

Figure 4.13 represents the AFM images of GaN (A) and the corresponding RMS roughness (B) at varying N_2 fractions, in Figure 4.13.B, we observe that the surface roughness decreases uniformly as the N_2 fraction increases. To explain the trend in roughness, we posit that increasing the N_2 fraction boosts the flux of nitrogen species reaching the substrate. This increase in nitrogen flux can influence the nucleation process, potentially enhancing the density of nucleation sites and promoting a more uniform growth structure, thus leading to smoother film surfaces. Consequently, one can see that at high N_2 fraction (80% and 100%), the films are denser (as seen in Figure 4.13.B with 100% N_2) and are characterized by finer grains (as observed in Figure 4.13.A with 80% and 100% N_2), potentially resulting in fewer and smaller grain boundaries [60]. Smaller grain boundaries typically lead to a better coalescence and hence to a smoother surface, as there are fewer discontinuities or steps on the surface that contribute to roughness. However, a smoother film with a dense compact structure does not necessarily correspond to a higher crystalline quality film. To explore the trends in the crystalline fraction at various N_2 fractions, we further look upon the GIXRD measurements.

Figure 4.14.A presents the GIXRD pattern for different N_2 flows. Two distinct diffraction patterns are observed: i) a broad spectrum from 30^0 to 40^0 indicating amorphous nature without a strong crystalline GaN peak, and ii) a prominent 0002 GaN peak at 34^0 indicating a polycrystalline GaN film. The crystalline fraction (F_C) trends with varying N_2 flow are analyzed similarly to the pressure series, as depicted in Figure 4.14.B.

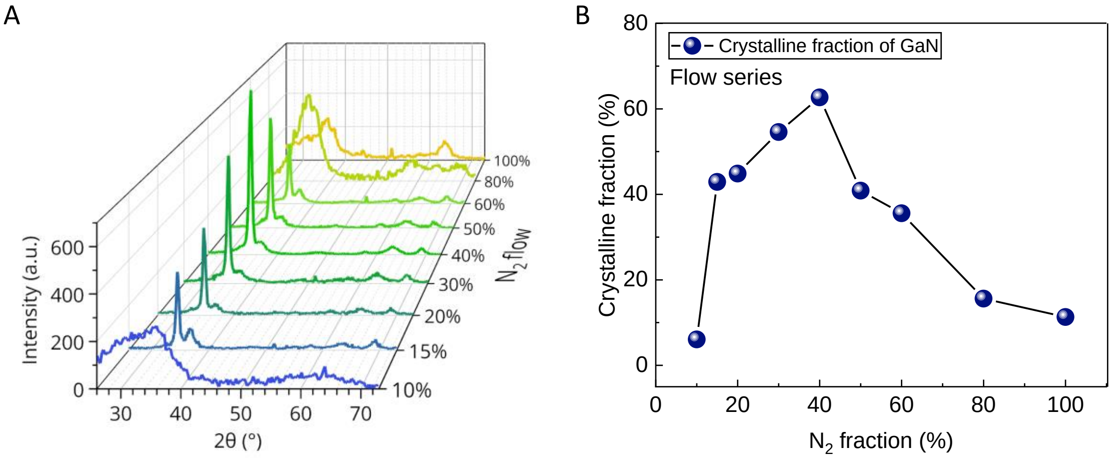

Figure 4.14: A. GIXRD profile at varying N_2 fractions from 10-100 %. B. Crystalline fraction calculated from the corresponding GIXRD spectra.

From Figure 4.14.A, we observe that the thin films at 10%, 80% and 100% N_2 are amorphous. For all the intermediate values, we see the characteristic 0002 peak of GaN peak along with a small (1010) shoulder peak depicting to a polycrystalline film. Typically, those results can be well appreciated by looking at Figure 4.14.B which gives the evolution of the crystalline fraction as a function of N_2 fraction, where the minimal Fc value are those of extrema of N_2 flow % while it is maximal (~60%) at 40% N_2. At this stage, a question arises: what is the reason behind this transition from an amorphous to a polycrystalline layer when the concentration of N is changing? To attempt to address this question, we carried out the same methodology than that used for the pressure series.

4.3.2 Interdependence of the flux & energy of Ga atoms on the GaN film structure – N_2 flow effect

Figure 4.15.A represents the flux of the ions at the target and flux of the sputtered Ga-atoms. Globally, we observe that unlike the pressure series, the flux of the N_2^+ and Ar^+ ions do not follow the same trend. This is because apart from depending on T_e, the flux also depends on the density of the ions (refer equation (4.5)). Therefore, at varying N_2 fractions, the density of the ions depends on the partial pressure of the particular gas (Ar or N_2). At low N_2 fractions, the Ar^+ flux to the target is high and the N_2^+ flux is low. Conversely, as the N_2 fraction increases, the Ar^+ flux decreases. At about 40 % of N_2 fraction in the Ar/N_2 gas mixture, we observe that the flux of Ar^+ and N_2^+ is almost the same ~ 10^{15} $cm^{-2}s^{-1}$.

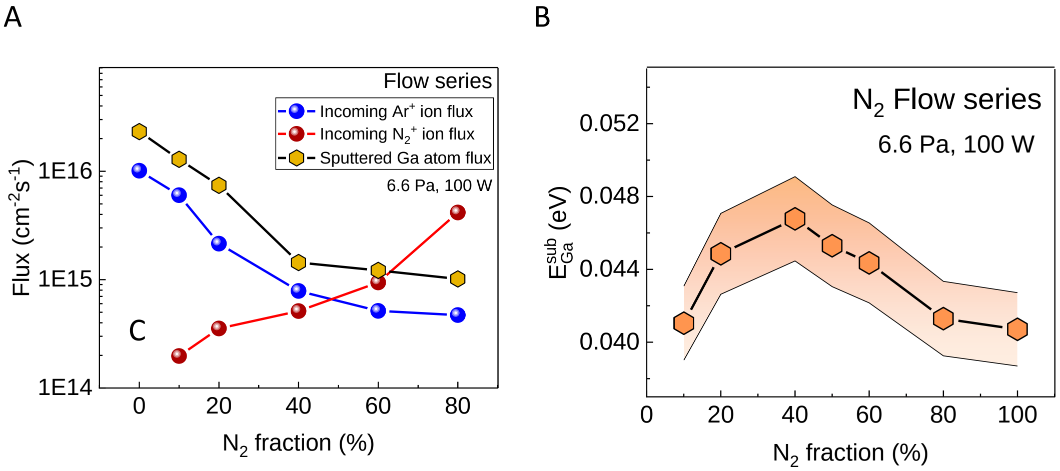

Figure 4.15: A. Trends in the estimated electron temperature (T_e) as a function of varying N_2 fractions from 0-100 %. B. The flux of incoming ions at the target: Ar^+, N_2^+ and the sputtered Ga atom as a function of varying N_2 fractions. C. The average energy of Ga atoms reaching the substrate as a function of varying N_2 fractions.

Figure 4.15.B depicts the average energy of the sputtered Ga atom at the substrate, which is estimated by knowing the sputter yield, the average energy of the sputtered Ga atom at the target, the pressure and the gas temperature. The trends in $\overline{E_{Ga}^{sub}}$ is interpreted from the observation in Figure 4.16.

Figure 4.16 represents the trend in the four parameters, namely the growth rate, Fc, φ_{Ga} and $\overline{E_{Ga}^{sub}}$ as a function of the N_2 flow percentages from (0-100 %), the two later values being calculated using the same procedure as for pressure series. All the gas phase related data needed for the calculations of these values such as Te, Tgas, etc are given in chapter 3. On comparing the trends in the growth rate with the flux of the Ga atoms (Figure 4.16.B), we observe that unlike the pressure series, the growth rate and φ_{Ga} here follows a completely different trend. This discrepancy between the trends of growth rate and Ga-flux might be explained by two phenomena: i) the sputtered yield of Ga (*Y(E))* becomes more dependent on the N_2^+ ions than the Ar^+ ions (scarce) at higher N_2 fractions. Since *Y(E)* of Ga by Ar^+ is higher than that of Ga by N_2^+ (2.4 atoms/Ar^+ ion and 1.6 atoms/N_2^+ ion), it is intuitive that less Ga atoms sputtered at higher N_2 fractions [61] (see Figure 4.16.C); ii) another possible explanation here is that increasing the percentage of N_2 induces poisoning of the Ga target [62] (forming unwanted complex GaN compounds at the target). This could decrease the sputtering efficiency of the Ga atoms from the target, which in turn would result in a decrease in the flux of the Ga atoms (evident from Figure 4.16.C), thereby decreasing the growth rate. The optimal range exists around 40 % N_2 fraction where we observe the highest growth rate. Furthermore, as we reach higher N_2 fractions, we observe that the growth rate decreases. We interpret here that unlike the pressure series, the Ga atom flux alone is not sufficient to comment on the trends in the growth rate at varying N_2 fractions due to the varying sputter yield impacts of Ar^+ and N_2^+ ions on Gallium atoms. A compelling hypothesis here is that from TALIF measurements of N-atom density (Chapter 3), the highest N-atom density was estimated at a N_2 fraction of 50% (N ~ 1.6 x 10^{12} cm^{-3}). Although the nitrogen atom flux and the N-atom density are not comparable parameters, we can still potentially relate to the fact that the condition, which yields us with the highest N-atom density (50% N_2), is very close to the condition that yields us with the highest growth rate (40% N_2). The error in estimation could be because the N-atom density was estimated at a high pressure of 27 Pa whereas the growth flux was estimated at a pressure of 6.6 Pa. This signifies the intuitive understanding of the gas phase chemistry and how it connects well with the growth dynamics of a thin film.

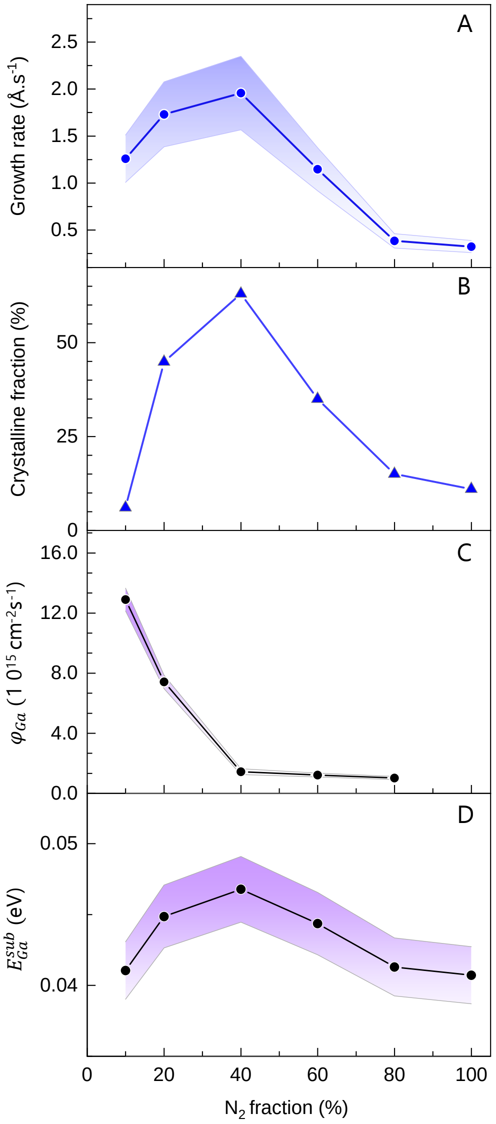

Figure 4.16: The trends in A. growth rate B. Crystalline fraction C. Flux of Ga atom ejecting from the target and D. Average energy of Ga atom reaching the substrate at varying N_2 fractions from 0-100 %. The RF Power and Ar/N_2 flow were kept constant at 100 W and 12/8 sccm respectively.

Examining the crystalline fraction trends in GaN film (Figure 4.16.B), we start by quoting Thornton's zone model for sputtering which depicts that the adatom mobility governs crystallite formation during nucleation and coalescence[9]. The crystalline fraction of GaN increases from as the N_2 flow ratio increases from 10-40%, suggesting an enhanced adatom mobility. The average energy of Ga atoms at the substrate ($\overline{E_{Ga}^{sub}}$ from **Error! Reference source not found.**.b4) mirrors the crystalline fraction's trend, rising from 10-40% N_2. As N_2 fraction increases, reducing Ar species in the plasma, fewer Ga atom/Ar species interactions occur during flight from target to substrate. This increases the energy of Ga atoms at the substrate, enhancing adatom mobility and crystalline fraction. However, from 40-100% N_2, the decreasing crystalline fraction and $\overline{E_{Ga}^{sub}}$ could be explained by examining the Ga atom flux (Figure 4.16.C). At higher N_2 fractions, the sputtering effect by N_2^+ ions become dominant, reducing the energy of sputtered Ga atoms at the target, consequently lowering the $\overline{E_{Ga}^{sub}}$ at the substrate. This decrease in $\overline{E_{Ga}^{sub}}$ reduces the adatom mobility, leading to a reduction in crystalline fraction. An interesting observation here is the striking resemblance of the trends in growth rate, crystalline fraction and $\overline{E_{Ga}^{sub}}$ with varying N_2 flow ratio (Figure 4.16.A, B&D). This indicates a clear grasp of the gas phase chemistry and its coherent alignment with the intricacies of thin film growth dynamics. The thin film with the best growth rate and crystalline fraction was obtained at an N_2 fraction of ~ 40%. By keeping this value constant, we now explore the influence of the RF power.

4.4 Influence of the RF power

In sputtering processes, the injected RF power is another important parameter used to tune the grown film properties. The range under which we performed the experiments from 75 W to 125 W. We fixed this range because below 75 W, the plasma failed to ignite. Conversely, beyond 125 W, challenges arose in maintaining plasma stability for more than 15 minutes, which was to limited regarding our regular deposition of 30 min at minimum.

4.4.1 Surface morphology, structure & crystalline fraction

Figure 4.17 depicts the SEM (A - surface, A' – cross-section) along with the respective growth rates (A") and the AFM images (B) at varying RF powers from 75 W to 125 W and the associated RMS roughness values (B'). Overall, whatever the power, the SEM surface images show porous nanostructured patterns. An interesting observation is from the magnified inset of the surface image at 125 W RF power (Figure 4.17.A) where we observe some droplets of gallium on the film surface stemming from the Ga target.

When it comes to the cross-section of the films (Figure 4.17.A'), we observe a columnar growth that does not significantly differ when RF power is varied within this range. In Figure 4.17.A", B" we observe that both the growth rate and the RMS follows a quite uniform increase with the RF power.

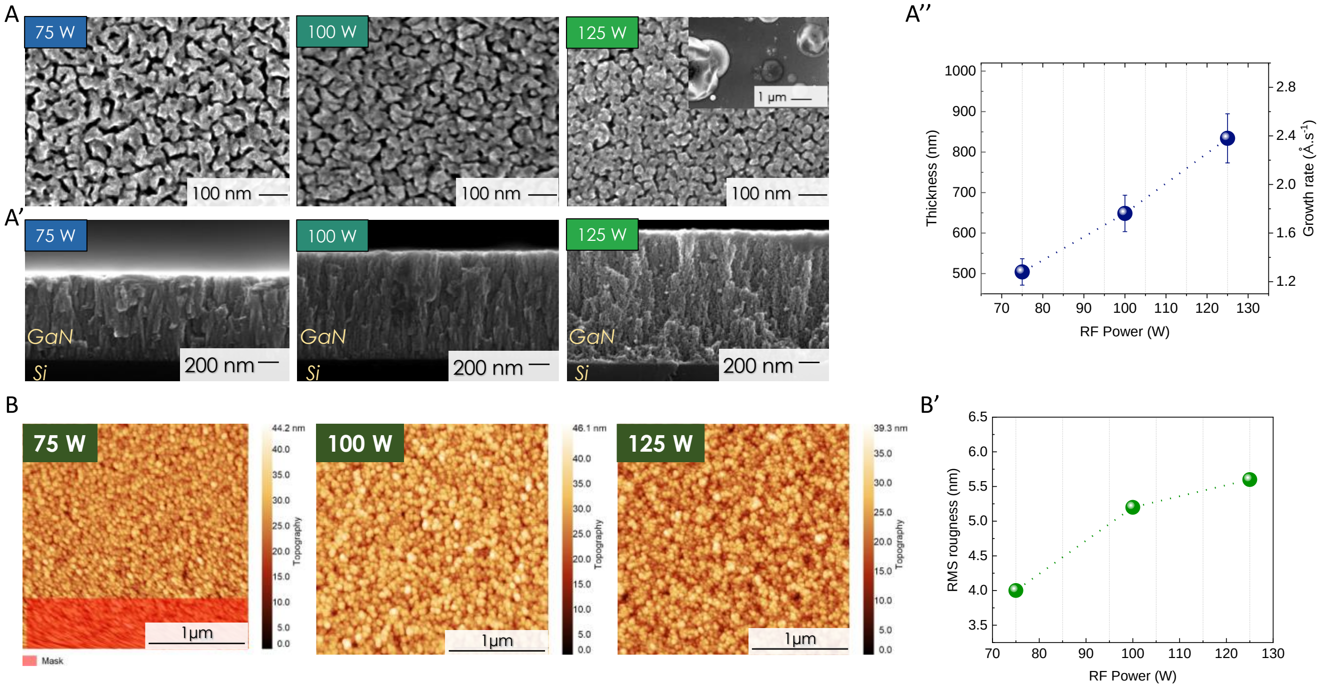

Figure 4.17: SEM & AFM images of GaN on Si at varying RF Power from 75-125 W. **A.** SEM surface micrographs. The inset in the image at 125 W represents a zoomed out low-resolution view showing blisters of Gallium on the surface. **A'.** SEM cross-section images depicting the thin film & the Si substrate. **A''.** The thickness & growth rate obtained from the cross-section images. **B.** AFM surface micrographs. **B'.** The root mean square (RMS) roughness obtained from AFM topography at varying RF Power. The mask mentioned in the first AFM figure just represents the blurred out section of the image, which has been avoided to get a better topography estimate. The Ar/N_2 flow and working pressure were kept constant at 12/8 sccm and 6.6 Pa respectively.

All the above observations including the presence of Ga blisters at the strongest RF power as well as the increase of the growth rate surface roughness when the power increases, could be attributed, for example, to an increase in the self-bias potential that would end up with an increase in the energy and the flux of the ions bombarding the target. Consequently, the growth rate of the thin films tends to rise with elevated RF power due to enhanced Ga-atoms flux. As far as the crystalline structure of the films is concerned, the RF power does not have the same influence as for the growth rate as can be seen in Figure 4.18.A_1 which depicts the F_C extracted from GIXRD, A_1, A_2, A_3 measured at RF powers of 75, 100 and 125W, respectively, for a pressure range from 2.6 Pa to 13.3 Pa at a fixed N_2 fraction of 40 %.

From the GIXRD profiles, we observe that at the lowest power (Figure 4.18.A_1), the intensities of the GIXRD spectra, as a whole is lesser than at a power of 100 W. For the effect of RF power at ~ 6.6 Pa (pressure corresponding to the best film), we observe that as the RF power increases from 75 W to 100 W, the overall intensity of the 0002 peak increases which suggests to an increased crystallinity. This could be reasoned by considering the energy of the atoms at varying powers.

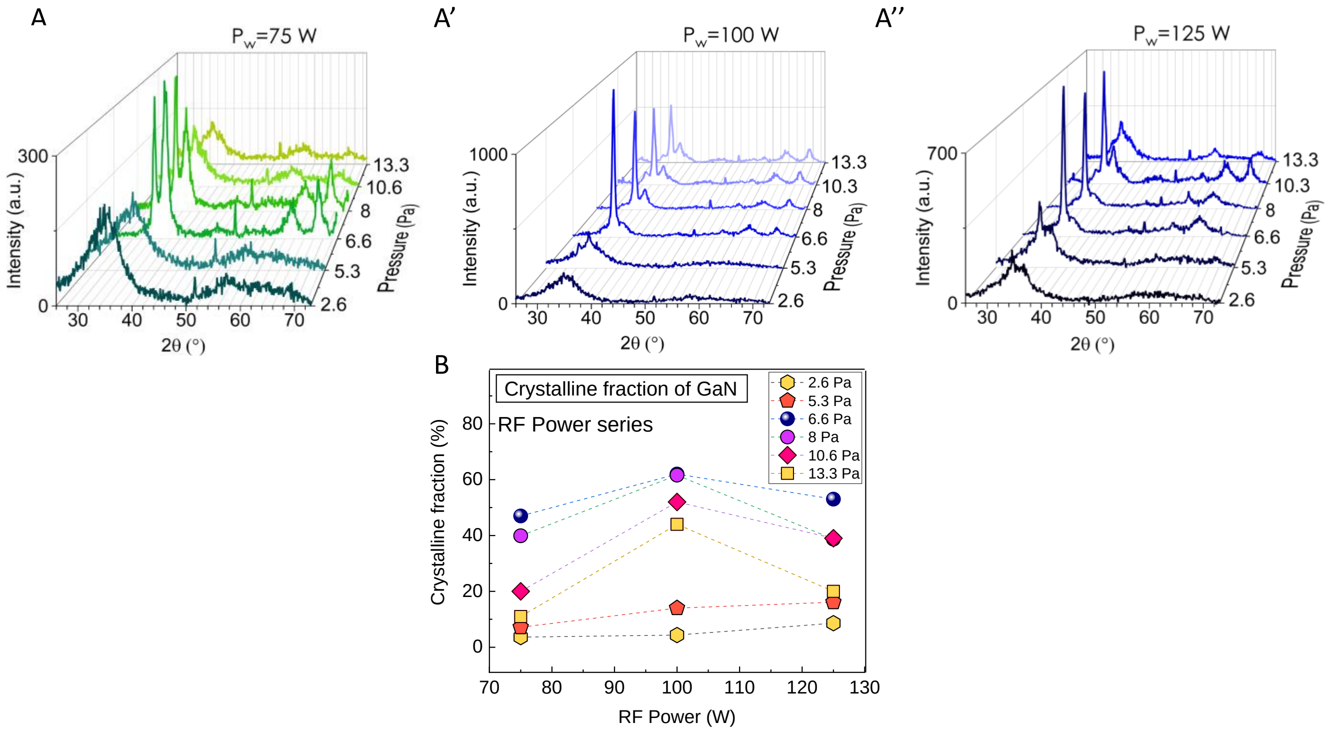

Figure 4.18: A. Crystalline fraction calculated from the GIXRD spectra represented in A_1, A_2, A_3 at varying RF Power – 75 W, 100W & 125 W respectively and at a constant working pressure of 6.6 Pa and an Ar/N_2 flow of 12/8 sccm.

For instance, at a low power of 75 W, the intensity of the 0002 GaN peak is low, which could be attributed to the relatively low energy of the adatoms. Upon examination of the GIXRD profile at 75 W (Figure 4.18.A_1), even under optimal conditions of 6.6 Pa, the peak intensity remains comparable across crystal planes, suggesting a dependence on the energy of the impinging atoms. The crystalline fraction (F_C) increases from approximately 40% to 60% as the RF power is raised from 75 W to 100 W (Figure 4.18.A_2) which could be due to the increase in the energy of the impinging atoms. However, with further power increased to 125 W (Figure 4.18.A_3), contrary to expectations, a decrease in both peak intensity and crystalline fraction is observed. This anomaly could be attributed to the heightened energy of nitrogen ions bombarding the substrate at higher powers [14]. Notably, regardless of RF power, samples deposited at lower pressures exhibit consistently low crystalline fractions (< 15%). Across the RF power range from 75 W to 125 W, a consistent trend of increasing crystalline fraction from 75 W to 100 W followed by a decrease from 100 W to 125 W is observed for pressures ranging from 6.6 Pa to 13.3 Pa. The interpretation from the GIXRD spectra and the corresponding crystalline fraction at varying RF powers leads us to believe that the film deposited at 100W is the best as it provides the best trade off regarding crystallinity without having the issue related to blistering that affects film grown at a superior power. This raises a question on whether this trend in crystallinity at varying RF powers can be correlated with the energy of the sputtered Ga atoms reaching the substrate, paving way to the next sub section.

4.4.2 Interdependence of the flux & energy of Ga atom on the GaN film structure – RF power effect

Using the same methodology as for pressure and flow series, we now correlate the energy and the flux of Ga atoms to the film properties. Figure 4.19 represents the trend in the later parameters along with growth rate and crystallinity varied across RF powers from 75 W to 125 W.

As the RF power escalates from 75 to 125 W, the self-bias potential undergoes a gradual increase from 650 V to approximately 750 V. This increase in self-bias potential significantly affects the energy of Ar^+ and N_2^+ ions, predominantly influencing φ_{Ga} due to enhanced sputter efficiency, as illustrated in Figure 4.19.C. Correspondingly, the average energy ($\overline{E_{Ga}^{sub}}$) of the sputtered Ga atoms also experiences a rise owing to the increased ion energies, as depicted in Figure 4.19.D. Upon comparing the trends in growth rate (Figure 4.19.A) and φ_{Ga} (Figure 4.19.C), a striking similarity becomes evident. However, a notable divergence emerges concerning F_C (Figure 4.19.B) in relation to $\overline{E_{Ga}^{sub}}$. Notably, at RF powers exceeding 100 W, an inverse correlation manifests between F_C and $\overline{E_{Ga}^{sub}}$, indicating that the latter does not directly dictate the former, in contrast to observations in pressure and flow series. This discrepancy underscores the interplay between φ_{Ga}, $\overline{E_{Ga}^{sub}}$,, and F_C. Upon scrutinizing the growth rate and crystalline fraction of GaN thin films under varying RF power, it becomes apparent that unlike the N_2 flow series, the growth rate exhibits a direct dependency on φ_{Ga}, a notion substantiated by nearly equimolar conditions across power variations (40% N_2 at varying RF powers). Moreover, the deviation observed between Fc and $\overline{E_{Ga}^{sub}}$ at higher powers (125 W) suggests a potential correlation with N concentration, aligning with findings from N_2 flow studies where N_2 variation induced the most pronounced deviations. This consistency resembling equimolar GaN mixtures, fortunately results in optimal outcomes regarding growth rate and crystallinity, which emphasizes the validity of our approach.

In summary, the present model, considering factors like φ_{Ga} and $\overline{E_{Ga}^{sub}}$, delivers reliable outcomes concerning both growth rate and crystalline structure of GaN thin films under various process conditions. An intriguing prospect lies in prediction, whereby the model could forecast optimal process conditions by extending the range of considered values. For instance, while our exploration has confined sputtering pressure within the typical 2.3 - 13.3 Pa range, analysis of electron densities (n_e) (MWI) and N-atom densities (TALIF) (Chapter 3) suggests that at equimolar conditions (40% N_2) and an optimal power of 100 W, the ideal pressure exceeds our initial exploration limit (~ 13.3 Pa). Thus, our model predicts an optimized pressure range beyond 13.3 Pa for deposition. Moreover, this model holds potential for investigating sputtering-based depositions of other materials, facilitating the identification of optimized sputtering conditions before conducting ex-situ characterizations.

We have now analyzed the morphology, growth rate and the structure of the GaN thin films at varying process parameters and found out that the best-optimized condition for deposition in terms of crystallinity and growth rate is at a pressure of 6.6 Pa, a N_2 fraction of 40% and an RF power of 100 W. Considering the GaN sample grown at this condition, we now shift our focus towards investigating the chemical composition of our GaN film.

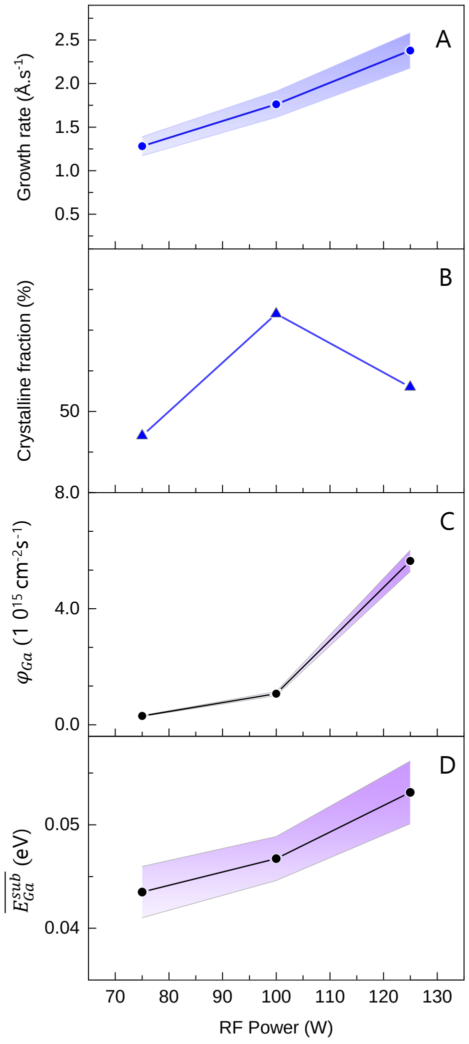

Figure 4.19: The trends in A. growth rate B. Crystalline fraction C. Flux of Ga atom ejecting from the target and D. Average energy of Ga atom reaching the substrate at varying RF Power from 75W to 100W. The working pressure and Ar/N_2 flow were kept constant at 6.6 Pa and 12/8 sccm respectively.

4.5 Chemical composition investigation of polycrystalline GaN films

4.5.1 GaN surface analysis-using XPS

XPS is a powerful technique for studying the chemical composition of materials, chemical states, and elemental binding energies of a material [63]. In this part, we present the XPS analysis of a typical GaN film deposited at the optimized sputtering condition of 6.6 Pa, 100 W and 40% N_2. Figure 4.20.B presents the XPS spectra across the surface of the GaN film starting from the center of the sample (point 1) to one of the diagonal edge of the sample (point 5). It is important to note here that the observed color gradients from Figure 4.20.A illustrates the non-uniformity of the sample. As measured using profilometry, the film is thicker at the center and we gradually become thinner toward the edge of the substrate. Using XPS, we first aim to verify how the composition of the films changes as a function of the thickness.

We should mention that if this non-uniformity can be regarded as a negative point as far applications are concerned, it is however beneficial in a research point of view as it enables to study the influence of the thickness on diverse properties of the films using a single sample.

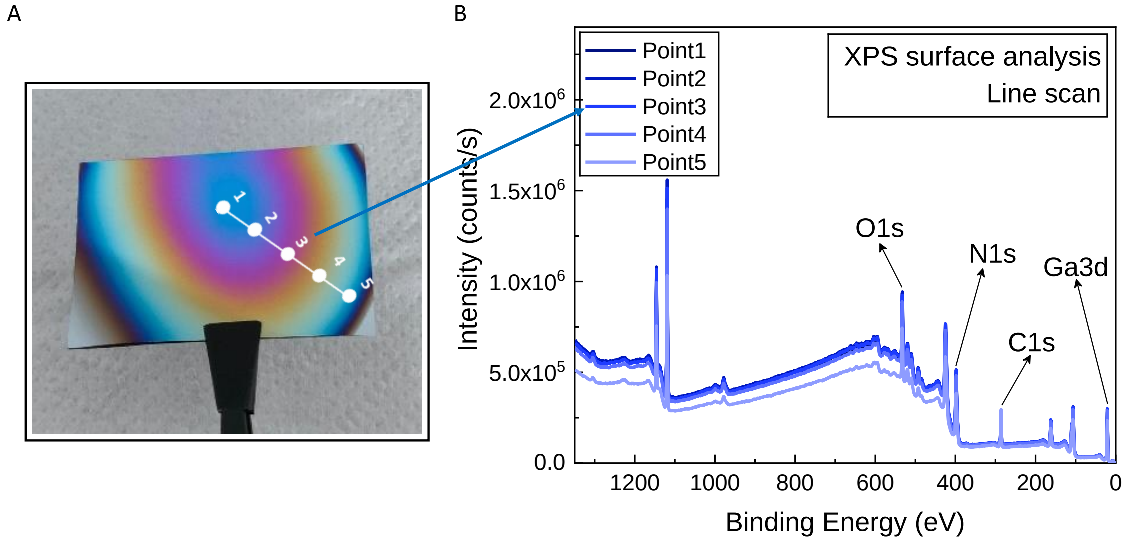

Figure 4.20: A. Real–view image of the GaN on Si. The points (from 1-5) depicts the line scan for which the XPS surface analysis was done. B. XPS surface scan from the center of the GaN sample to a corner (from 1 to 5). The significant elements from the scan were Ga, N, O and C. Sputtering conditions: 6.6 Pa, 100 W and N_2 ~ 40 %.

In Figure 4.20.B, we observe very similar XPS spectra except for point 5 where the film thickness is minimal, which is why the background intensity changes. However, the peaks are identical for all the five points, showing that the change in composition as a function of the thickness is overall minimal, at least within the thickness range of the investigated film (~ 400 nm-point1 to 300 nm-point 5). Therefore, the almost identical intensity of the signal from points 1 to 4 indicates that the sample is uniform across the surface, in terms of its chemical composition. From this surface analysis, we identify the presence of gallium, carbon, oxygen and nitrogen. To calculate the atomic percentages of these elements on the surface, we used a high-resolution spectrum because we needed to fit the overlapped signal from the nitrogen and the Auger peaks of Ga (refer Chapter 2).

Figure 4.21 represents the high-resolution spectra of each of the identified elements (Ga, N, C and O). In Figure 4.21.A, we see that there are two major contributions to the bonding of Ga: Ga-N and Ga-O (also observed in Figure 4.21.D). This is an interesting observation that relates to the fact that OH emission lines were detected in our plasma reactor during the growth of the GaN films (Chapter 3~ plasma contamination). The presence of OH in the plasma was attributed to two phenomena: a) the plasma interacts with the reactor walls which may release a steady supply of adsorbed gases such as water and oxygen [64] and/or b) the use of liquid Ga as a target enables the dissolution of oxygen into the gallium [65], [66] that may contribute to the continuous sputtering of O during plasma operation. In Figure 4.21.D, we observe that the oxygen contributions to Ga peaks attributed to contamination in the GaN film. In the case of Nitrogen (Figure 4.21.B), we find that the major contribution is from the N-Ga bonding. There is also the presence of an N-H bond, which leads us to believe that one of the adsorbed gases that was released from the walls of the reactor is effectively water (H_2O) from which the H species interacts with the nitrogen in the GaN film and from which O could come from. In Figure 4.21.C, we observe that the major contribution to the carbon bonding C-C, which contributes to almost 90% of the total intensity. This is commonly observed in all XPS surface scans where the signal from carbon is mainly attributed to superficial contaminations [67], [68]. The HR-spectra of the GaN surface gave us a stoichiometry of Ga/N ~ 0.95 which is very close to the balanced composition. However, if we include the oxygen signal in the system, we have a total stoichiometry of Ga/N and G/O ~ 0.95/0.68 that corresponds to a film having a composition of a $GaN_{1.05}O_{0.68}$.

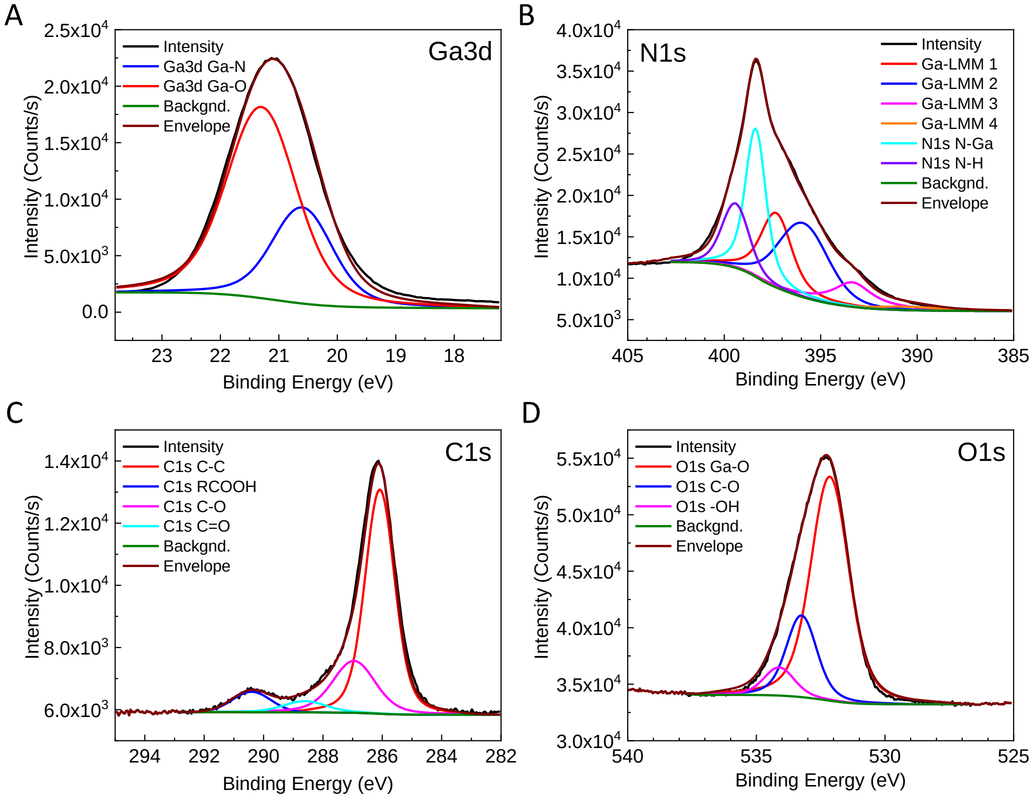

Figure 4.21: XPS surface analysis – high-resolution spectra focusing on the binding energy range corresponding to A. Gallium B. Nitrogen C. Carbon and D. Oxygen. The HR spectra gives us an idea on the strength of bonding between the above-mentioned elements. The above used GaN sample was deposited at 6.6 Pa, 100W and N_2 fraction of 40%.

4.5.2 Composition profile analysis using XPS & SIMS

For more-in depth analysis, we tried to study the composition by etching the GaN layer and comparing the elemental composition along the etched depth profile using XPS. Additionally, we also used SIMS (secondary ion mass spectrometry) to characterize the trends in the depth profile of Ga and N. Figure 4.22.A represents the cross-sectional SEM corresponding to our GaN film on Si. Figure 4.22.A&B represents the SIMS profile for Ga, N, Si and the XPS depth profile of Ga, N, C and O. It is important to note here that although the etch time was similar (~ 600 seconds); the etching rate of SIMS was faster than that of XPS. Therefore, SIMS yielded us a profile that completely etches away the GaN layer and further probes the Si substrate, which was useful for us to comment on the sharpness of the interface. The SIMS profile exhibits a nearly uniform incorporation of Ga and N throughout the film. At the interface with the Si substrate, an abrupt decrease in the Ga and N lines is observed. Consequently, a strong increase in the Si line is observed. In addition, the sharp decrease in the Ga line at the interface depict that melt-back etching [69], [70] does not happen. "Melt back etching" is a phenomenon that usually occurs when the deposition of gallium nitride (GaN) films on silicon (Si) substrates is conducted at high temperatures, such as in MOCVD or MBE processes. At elevated temperatures, the silicon substrate reacts with the GaN layer, forming complexes of Ga and Si with a lower melting point. These complexes potentially melt back into the GaN layer, causing localized etching and degradation of the film's properties, including structural defects and surface roughness. Consequently, as we are deposited at room temperature, we do not observe such phenomena. SIMS could not be used here to determine the chemical composition percentages of the elements, as there was a lack of reference spectrum of GaN for calibration. Therefore, we continued with XPS for a more detailed analysis on the composition profile even though etch depth profile was limited to ~ 50 - 100 nm (limitation of the setup).

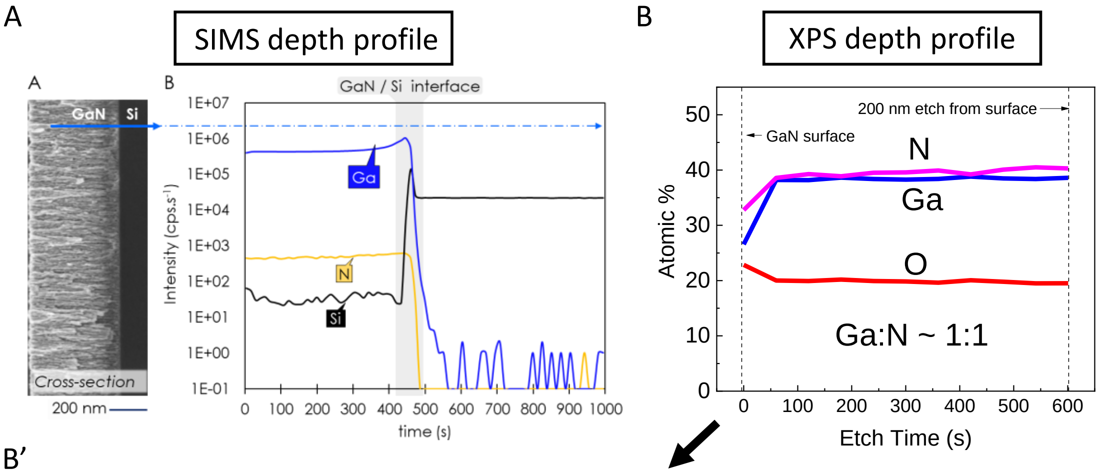

B’

Etch Time (s)	C1s	Ga3d	O1s	N1s	N/Ga	O/Ga
0	17.8	26.6	22.9	32.8	**1.23**	**0.86**
60	3.2	38.2	20.0	38.6	**1.01**	**0.52**
120	2.6	38.2	19.9	39.3	**1.03**	**0.52**
180	2.3	38.6	20.2	38.9	**1.01**	**0.52**
240	2.2	38.4	19.9	39.5	**1.03**	**0.52**
300	2.3	38.3	19.8	39.6	**1.03**	**0.52**
360	2.1	38.4	19.6	39.9	**1.04**	**0.51**
420	1.9	38.8	20.1	39.2	**1.01**	**0.52**
480	1.6	38.5	19.8	40.1	**1.04**	**0.51**
540	1.6	38.4	19.5	40.5	**1.06**	**0.51**
600	1.6	38.6	19.5	40.3	**1.04**	**0.51**

Figure 4.22: The composition/ depth profile of GaN thin film on Si. A. SEM cross-section image and the corresponding composition profile obtained from SIMS that goes beyond the GaN/Si interface. B. XPS depth profile that penetrated ~ 200 nm into the GaN layer. B’. The atomic percentages of elements C, Ga, O and N.

Figure 4.22.B’ represents the composition percentages of C, Ga, O and N along the etch depths from the start to the end. We observe that the carbon contamination decreases from 17 % to ~ 3 % after the first etch (0 to 60 seconds), indicative of a superficial contamination of the surface. For gallium, we observe an increase from ~ 26% to ~ 38% after the first etched layer. This is attributed to a superficial enrichment in Ga due to the bombardment, which is an occasional profile measurement artifact that remains constant, therefore this effect can be ignored and we can say that the Ga has a homogeneous composition along the depth profile. The same effect is observed for nitrogen, the intensity increases from 32% to 38% once the surface is etched, but remains homogenous thereafter. The ratio of Ga/N remains stoichiometric with a value very close to 1. When we look at the oxygen composition, there is a slight decrease after the first etch from 23% to ~ 20% and then remains constant throughout the etch profile. This suggests that the initial 3% decrease could be due to superficial contaminations, but the 20% of oxygen is definitely the proof of the contamination in the bulk. In order to correlate the contaminants with the bulk composition, we further analyze the high-resolution spectra (HR) of each elements and the corresponding etch profiles into the bulk (Figure 4.23).

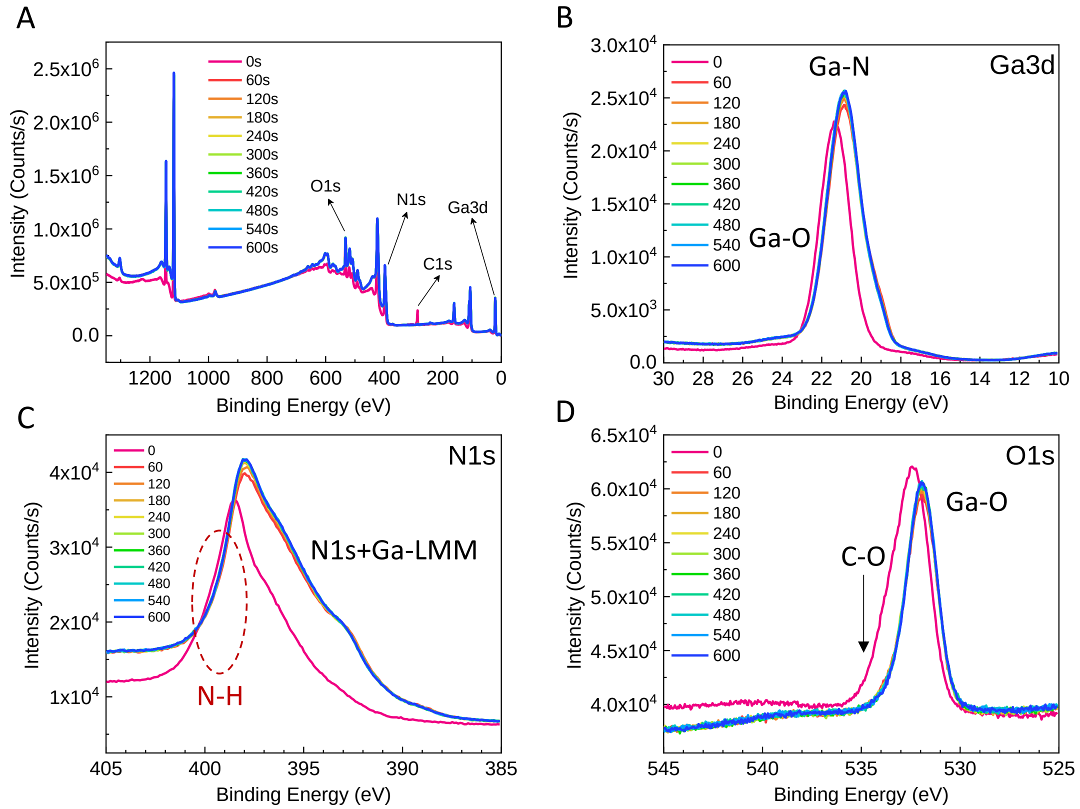

Figure 4.23: A. Single low-resolution XPS spectra at varying etch depths. The etching was carried out for a total of 600 seconds (0-600seconds as represented in the figure)and the corresponding etch depth was approximated at ~ 100 nm. A high-resolution spectra focusing on the binding energy range corresponding to B. Gallium C. Nitrogen and D. Oxygen. The above used GaN sample was deposited at 6.6 Pa, 100W and N_2 fraction of 40%. Note: Most of the peaks in between the etch profile of 0 seconds and 600 seconds overlap with the peak at 600 seconds etch, which is the reason that we don't observe them here.

Figure 4.23.A confirms that the carbon contamination (C1s) disappears after the first etch (0 to 60 seconds). Looking at the Ga spectra in Figure 4.23.B, after the first etch, both Ga-N and Ga-O remain uniform until the end of the depth profile. As far as N is concerned, (Figure 4.23.C), we observe that both N-Ga and N-H are present in the surface at the surface. After the first etch, the N-H disappears suggesting that the contamination of GaN by hydrogen is only effective at the surface and is not present in the layer. For oxygen (Figure 4.23.D), we have contributions from carbon and gallium at the surface. After the first etch, the carbon contribution disappears and the Ga-O bond remains consistent until the end of etch.

Overall, from XPS, we found out that the Ga/N ratio for our sample is close to stoichiometry ~ 1. The depth profile suggests that the elemental distribution of Ga and N is uniform in the layer, which shows that the sputtering process is stable delivering Ga and N, thereby void of any irregularities. When it comes to contaminants, we had identified 3, namely carbon, hydrogen and oxygen, among which carbon and hydrogen have been identified to be superficial. Oxygen contamination is significant both at the surface and inside the layer suggesting that oxygen atoms are present in the lattice structure of GaN. So, there arises a question of how to solve this issue?

4.5.3 Oxygen contamination – do reactor & plasma cleaning help?

In this section, we discuss on the potential effects of the plasma & reactor-cleaning steps that we had proposed in the previous chapter (refer chapter 3). For this purpose, we heated the reactor walls and perform a target cleaning with pure Ar to remove the contaminants. The question is whether the cleaning procedure helps in reducing the oxygen contamination in the GaN film. We aim to explore this with the help of depth profiles from glow-discharge-optical emission spectroscopy (GD-OES). Figure 4.24.B&B' represents the GD-OES depth profiles of the GaN sample before and after the cleaning procedure respectively. Before interpreting on the GD-OES results, it is important to note that atomic percentage on GD-OES spectra have been estimated using EDX measurements as quantitative inputs. Therefore, we can use GD-OES for comparing the trends in Ga, N and O, but the actual composition values should be considered with caution.

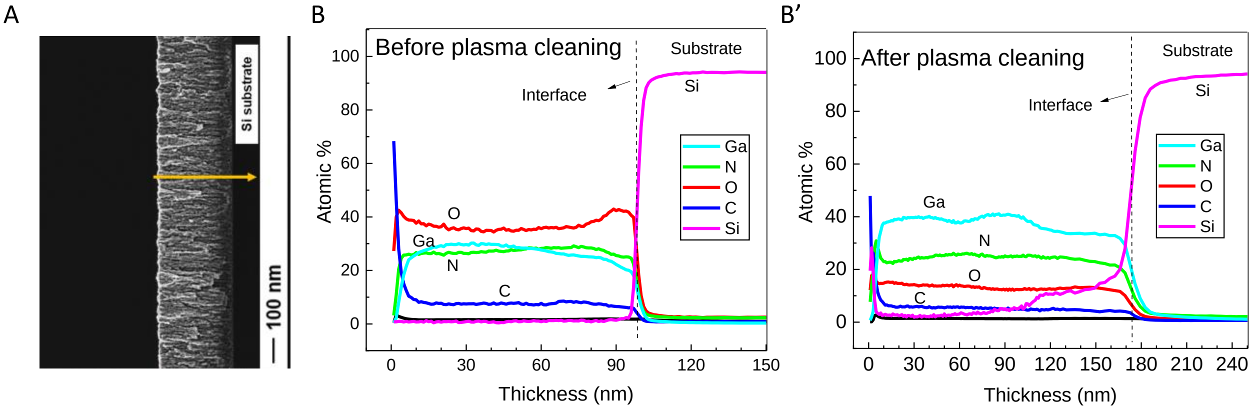

EDX – N (%)	Ga (%)	O (%)
28	41	31

EDX – N (%)	Ga (%)	O (%)
41	46	13

Figure 4.24: The influence of reactor & plasma cleaning on the oxygen contamination in the GaN sample. A. A cross-section SEM image depicting the depth profile that is focused for the GD-OES measurements. B, B'. GD-OES & the corresponding EDX measurements before & after the cleaning process. The Oxygen contamination in the thin film reduced from 31 % to 13 % post cleaning.

From the GD-OES depth profiles, we observe that for the GaN samples before plasma cleaning (Figure 4.24.B), the oxygen content is greater than that of both Ga and N. The Ga, N and the O content is uniform within the GaN layer and we have a sharp interface with the substrate (similar to what we observed from the SIMS spectra). For the sample deposited after plasma cleaning in Figure 4.24.B', we observe that the oxygen composition is ~ 13 %, which is significantly lower when compared to the sample deposited without the cleaning procedure (O ~ 30%). Therefore, until we get a permanent solution for removing O contamination, which is implementing a load-lock system, we used this cleaning procedure to reduce as much as possible the contamination of O in the GaN sample.

4.6 TEM analysis on the crystalline structure of GaN

The microstructure of the polycrystalline type of GaN films (as confirmed from GIXRD) has been studied in detail using Transmission Electron Microscopy (TEM). Figure 4.25 shows the TEM images and structural analysis of a GaN flake obtained from a scratched portion of the thin film deposited at 6.6 Pa, 100 W and at a 40% N_2 fraction. The high-resolution TEM (HR-TEM) images in Figure 4.25.C&D were obtained after tilting a flake in the microscope so that its growth axis is perpendicular to the plane of measurement. In this geometric configuration, some grains were in a $(11\bar{2}0)$ zone axis (Figure 4.25.D-E), which allows us to directly see the stacking of the GaN (0002) compact planes oriented perpendicular to the growth direction.

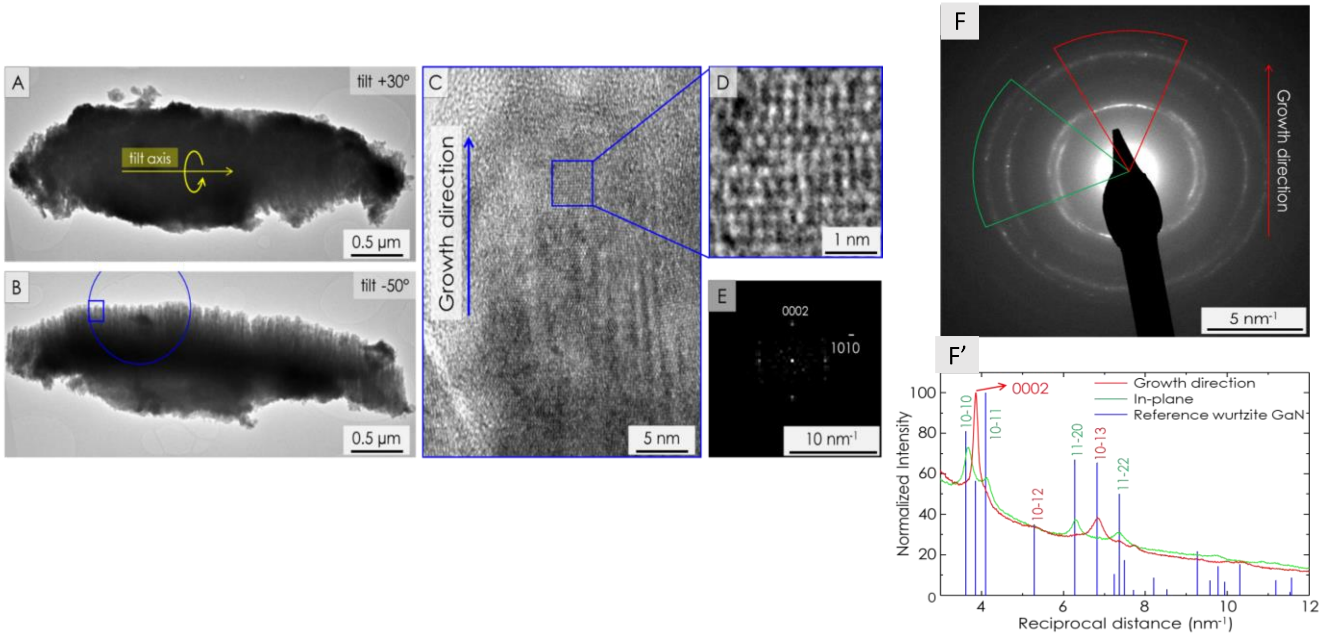

Figure 4.25: TEM of a polycrystalline GaN thin film grown by our Plasma PVD process at 6.6 Pa, 40% N_2 and 100 W. **A, B:** the sample, with its growth axis parallel to the electron beam at a tilt of +30° (A), had that axis almost perpendicular to the beam (in the image plane) at a tilt of -50° (B) (i.e. at a total tilt of -80° with respect to A. The images in **Figure 25 C-E** were recorded in the B orientation. The blue circle in B represents the selected area used for the diffraction pattern displayed in **Figure 25-E**. **C:** High-resolution image of the area blue-squared in B. **D**: Enlargement of the blue squared area in C, showing the stacking of the compact planes perpendicular to the growth direction. **E:** Fast Fourier transform (power spectrum) of D exhibiting a wurtzite stacking of those planes. **F:** Electron diffraction pattern for the GaN sample over the selected area shown by the blue circle in **Figure 25-B**; the growth axis is almost in the plane, in the direction indicated. The red and green spectra in **F'** represent the rotational averages from the red and green sectors in E, respectively, i.e. in the growth direction (red) and in the plane (green).

To confirm this texture effect on a larger scale, selected area diffraction patterns were recorded, as shown in Figure 4.25.F,F'. The latter reveals a powder-pattern shape that confirms the polycrystalline nature of the GaN film, the reciprocal distance between the rings confirming in turn the wurtzite nature of the structure. To qualify the texture detected by GIXRD, rotational average of the diffraction pattern [71] were performed around the growth direction on the one hand (red in Figure 4.25.F,F'), and around an in-plane axis on the other hand (green in Figure 4.25.F,F'). The spectra in Figure 4.25.F' evidence a strong presence of the 0002 peak in the former orientation (in red) and its absence in the latter (in green), indicating a strong (0001) texture.

From chapter 4, until now, we have managed to attain a better control of the process, identify specific contaminants such as oxygen, identify potential solution to mitigate such issues and confirm the polycrystalline and textured nature of our GaN films. From here on, we would also like to explore the optical properties of such films deposited at room temperature, for which we use Cathodoluminescence analysis.

4.7 Cathodoluminescence analysis of GaN films grown at room temperature

Cathodoluminescence (CL) spectra has been recognized as an adequate tool to investigate the structural and optical properties of semiconductors and optoelectronic devices [72], [73]. In this section, we aim to identify the different peaks associated with the CL bands of GaN that we observe from our samples and attempt to reason on the luminescence bands based on the growth conditions. CL is highly sensitive to defects, impurities, and variations in composition within the material. GaN films, especially those grown by sputtering, can contain various types of defects (such as dislocations, vacancies, and interstitials) and impurities as we saw before with oxygen for example, which significantly affect their optical properties. Therefore, with CL, we attempt to understand these defects and their distribution on our GaN films.

4.7.1 Potential origin of the GaN CL peaks in undoped GaN

The band gap of GaN is 3.4 eV, typically associated with the band-edge luminescence (BE-L). Variations in the bandgap, within a range of approximately ±0.1 eV, are attributed to excitons bound to surface-related defects and structural defects, notably stacking faults and c-axis screw dislocations[74]. However, despite this nominal range, the luminescence of undoped GaN samples often span a wide range of energies from 1.7 eV to 3.1 eV. Hence, prior to delving into the CL peaks of GaN, we undertake the classification of luminescence bands based on their emission energies. We can categorize the bands into four spectral regions: **(a) red luminescence (RL) ~ 1.8 to 2.0 eV, (b) yellow luminescence (YL) ~ 2.2 to 2.4 eV, (c) aquamarine luminescence (AL) ~ 2.5 to 2.6 eV and d) blue luminescence (BL) ~ 2.7 – 3.1 eV**. The subsequent analysis discusses the observed peaks and their potential origins. It is important to note that all of the above luminescence bands, in some or the other way are attributed to transitions from a shallow donor to deep acceptors [75]. However, the significance of each band and their observance on specific occurrences related to defects and change in process conditions is detailed below.

We start with the most commonly studied band for an undoped GaN ~ **yellow luminescence (YL)** band centered around 2.2 eV [76]. This YL band has been extensively studied, yet there remains uncertainty regarding the specific defects and their characteristics contributing to this emission [76], [77], [78]. Typically, the YL band in GaN appears broad and nearly Gaussian with a full width at half maximum (FWHM) of about 0.4 – 0.5 eV [79]. It is commonly suggested that this defect-related band arises from transitions between various shallow or deep donors. The native point defects often take the form of vacancies and interstitials. Vacancies are more likely to migrate and form complexes with more stable defects such as impurities and hence are considered as the dominant native point defect in undoped GaN due to their low formation energy[80]. Considering impurities and contaminants in our deposition process, there is a significant presence of oxygen contaminant (~ 30%), confirmed from x-ray photoelectron spectroscopy (XPS) measurements (Figure 4.26.H). Oxygen is considered as a shallow donor in GaN [81]. Therefore, in the presence of gallium vacancies (V_{Ga}), which carry a negative charge of 3, they naturally attract the positively charged donor such as oxygen to form a $V_{Ga}O_N$ complex. Several computational studies have demonstrated that the formation of $V_{Ga}O_N$ complexes are highly stable when compared with complexes from other elements (Ga, Si and N) and it is even more favorable than that of isolated gallium vacancies (V_{Ga}) [80], [82], [83]. Given the prevalence of shallow donors such as oxygen contaminants in our GaN deposition, the YL emission in GaN with a high concentration of these shallow donors could potentially be associated to the transition between shallow donor (oxygen) and deep acceptor (gallium vacancy)[84].

Red luminescence is sporadically observed in undoped GaN, typically appearing as a shoulder to the YL band[85]. Its origin is also linked to transitions from shallow donors to deep acceptors, particularly evident at low emission intensities. It has been suggested that the defects responsible for the RL band are native defects or complexes related to excess Ga which presumable act as deep compensating acceptors[86].

Aquamarine luminescence occasionally occurs in undoped GaN, particularly in samples grown at relatively low temperatures (< 500°C) under Ga-rich conditions[87]. The AL band often manifests as a peak with a narrower full width at half maximum (FWHM) of about 0.2 – 0.3 eV compared to the broader YL band (~ 0.5 eV). Additionally, in certain cases of highly resistive GaN samples grown by molecular beam epitaxy (MBE) under Ga-rich conditions, both RL and AL bands are recurrently observed, overshadowing the exciton emission at the band-edge (~ 3.4 eV)[88].

The **blue luminescence** in undoped GaN is attributed to transitions from shallow donors to deep acceptors, akin to the YL band. While numerous studies have aimed to pin point the nature of defects responsible for the BL bands, a conclusive origin remains elusive, with hypotheses pointing to Gallium vacancy-related complexes arising from impurities [89]. Additionally, the blue luminescence band is often attributed to defects related to dislocations and stacking faults within the GaN crystal structure[90]. It is important to note here that throughout this study, any minor variations in the defect peaks within a shift of ~ ±100 meV is not discussed extensively and is considered to arise from dislocations and structural imperfections in the GaN film because of its polycrystalline nature.

Now that we have defined the potential origin of the peaks in the broad band range from 1.7 ~ 3.5 eV, we set out to correlate the observed CL peaks at different photon energies to the corresponding transitions and understand the effect of the process parameters on the luminescence of GaN.

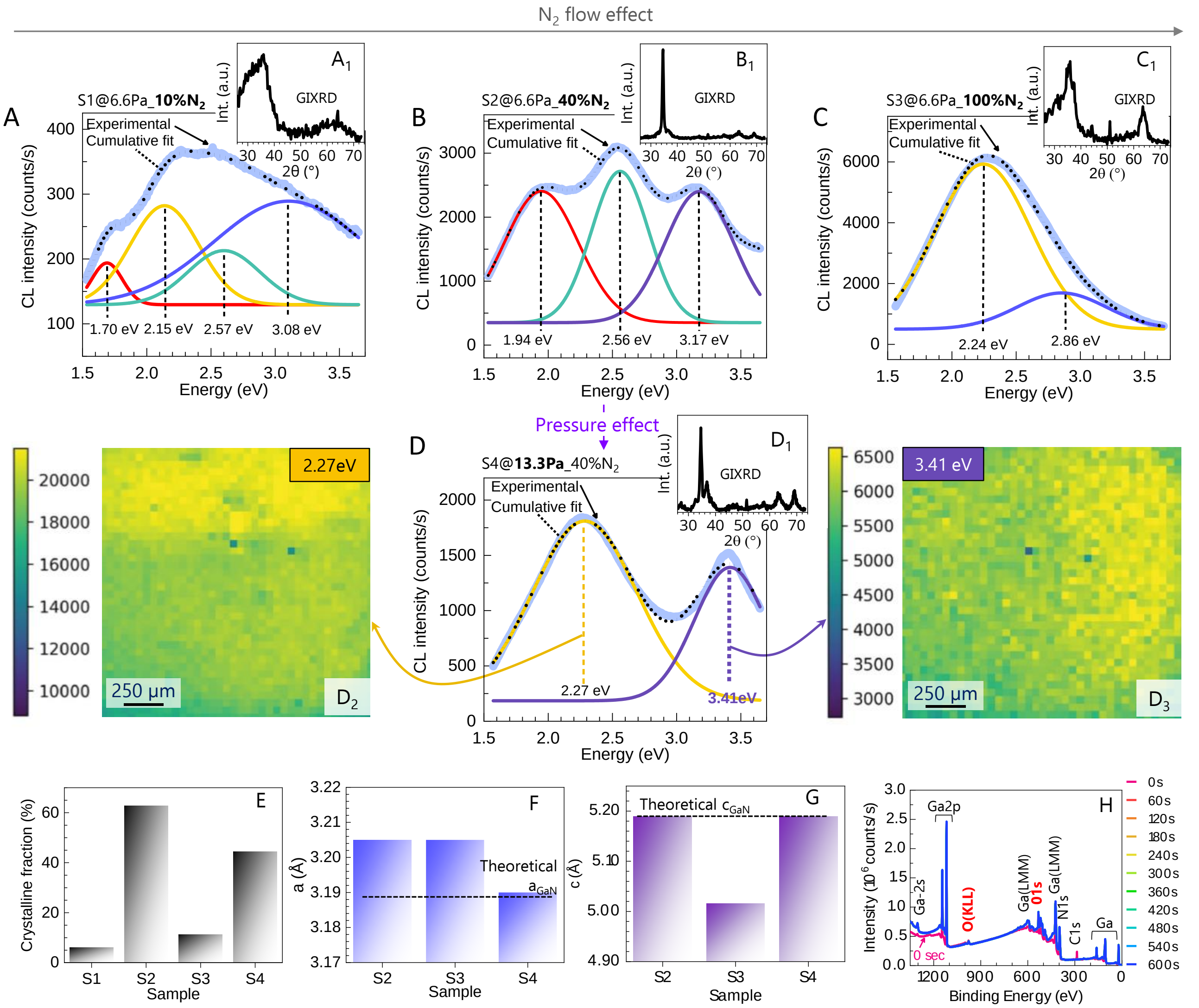

Figure 4.26: A-C. RT Cathodoluminescence (CL) spectra for GaN samples deposited at RT: 10% N_2 (sample 1), 40% N_2 (sample 2) and 100% N_2 (sample 3). Samples 1,2,3 were deposited at a constant pressure of 6.6 Pa; D. Sample 4 deposited at 40% N_2 at a higher pressure of 13.3 Pa. The insets represented as A_1-D_1 depicts the GXRD spectra of the corresponding GaN films; D_1 & D_2. 2D CL surface mapping for sample 4 at a photon energy of 2.27 eV and 3.41 eV respectively; E, F & G. Crystalline fraction (F_C) and the lattice parameters 'a' and 'c' of samples 2,3 & 4 obtained from the XRD spectra respectively corresponding to the hexagonal structure of GaN; H. High resolution XPS spectra of the GaN films at various etch depths ranging from 0 to ~ 200nm (0-600 seconds) revealing the significance of oxygen contaminants in the thin film.

4.7.2 Observations & analysis of the CL peaks of GaN grown at room temperature

Figure 4.26.$A_{(1)}$-$D_{(1)}$ respectively present the CL spectra and GIXRD patterns of the GaN samples deposited at different conditions of Ar/N_2 ratio: Sample 1 – S1: 10% of N_2 ($A_{(1)}$); S2: 40% of N_2 ($B_{(1)}$); S3: 100% of N_2 ($C_{(1)}$), at a fixed pressure of 6.6 Pa, while $D_{(1)}$ corresponds to S4: 13.3 Pa at a fixed ratio of 40% N_2. Typically, by comparing Figure 4.26.$A_{(1)}$-$B_{(1)}$-$C_{(1)}$, one can observe the effect of the variation in N_2 flow fraction whereas comparing Figure 4.26.$B_{(1)}$&$D_{(1)}$ illustrates the effect of pressure at a fixed N_2 flow. From GIXRD patterns (Figure 4.26.A_1-D_1), it clearly

appears that S1 and S3 are of amorphous phase while S2 and S4 are polycrystalline. To have a better appreciation of it, Figure 4.26.E is plotted to show the crystalline fraction values of S1 to S4. Regarding CL spectra (Figure 4.26.A-D), each spectrum has been de-convoluted to visualize the peaks associated with the bands corresponding to RL, YL, AL, BL and BE-L [75]. Important to be pointed out here is that all the four investigated films have been found to exhibit uniform luminescence across its surface as shown in Figure 4.26.D_2&D_3 that depicts the 2-D mapping of the CL spectra of S4 at photon energies corresponding to the YL(d_1) and BE-L(d_2). The mappings reveal that the CL peak intensity spread is uniform throughout the sample across a range of ~ 250μm.

Upon considering the effect of N_2 flow (Figure 4.26.$A_{(1)}$-$B_{(1)}$-$C_{(1)}$), one can observe distinct CL spectra when varying N_2 fractions (10%, 40% & 100%). Overall, three major observations are emerging from N_2 flow series:

I. It appears that only S2 (40% N_2) exhibits a BE-L (3.17 eV), even though it shifts from the theoretical value of 3.4 eV, as can be seen in Figure 4.26.B_1. By looking at Figure 4.26.E, one can notice that S2 is the film that exhibit the highest F_C of ~60% in comparison with S1 and S3 that respectively present a F_C ~ 5% and ~10%. The presence of well-defined crystal grains in S2 therefore allows for efficient electron-hole recombination near the band edge. As a result, band edge luminescence may be significantly weakened if not occurring for S1 and S3.

II. S1 (10% N_2) and S2 (40 %N_2) exhibit both RL and AL emission as can be respectively seen in

III. .a and b in comparison to S3 (Figure 4.26.C) that does not reveal none of these peaks. Several studies that relate the defects and luminescence features of GaN have highlighted that the presence of a RL accompanied by an AL band is frequently observed in cases where the deposition involves a Ga-rich growth environment[85], [86], [87], [88, p. 680]. This would mean that S1 and S2 are very likely to be Ga-rich.

IV. If one focuses on the changes in amplitude of the CL spectra of S1, S2 and S3, one can clearly see that the S1 grown at 10% N_2 (Figure 4.26.A) shows the weakest luminescence, peaking at a maximum of ~ 300 counts/sec, almost ten time lower than that of sample 2 (Figure 4.26.B). In this particular case, one may intuitively correlate it to the increase of F_C (Figure 4.26.E) that is occurring when changing the N_2 flow fraction from 10% (S1) to 40 % (S2). Indeed, the higher crystallinity of S2 (40% N_2) allows for more efficient charge transport resulting in a higher proportion of electron-hole pairs that contribute to radiative recombination so leading to higher CL intensity. In addition, the relatively prominent BL peak observed for the amorphous sample S1 (Figure 4.26.A) is often the mark of a highly defective sample that has stacking faults and dislocations[90]. By considering the same reasoning, one may expect to see S2 (Figure 4.26.B) having a higher CL intensity than S3 (Figure 4.26.C) considering its lower F_C (Figure 4.26.E), the inverse trend is however observed. Indeed, S3 displays the highest intensity of all the investigated samples. To explain this unintuitive tendency, one may consider discussing the potential effect of the grain boundaries in pc-film [91]. The sample with a lower crystalline fraction (S3) likely has a higher density of grain boundaries and defects that can act as non-radiative recombination centers but they are also more prone to be passivated taking into account the high amorphous fraction of the film[92]. Passivation of these defects may allow more charge carriers to undergo radiative recombination and emit photons, leading to higher luminescence intensity [93]. We should mention that this can only be true for samples having grain boundaries. Clearly, if we compare the GIXRD spectra of S1 & S3 (Figure 4.26.A_1&C_1), it happens that S3 has a more defined crystalline peak at ~34° and therefore could have more grain boundaries leading to efficient passivation so resulting in a higher CL intensity.

Considering now the effect of working pressure, we compare S2 and S4 (Figure 4.26.$B_{(1)}$&$D_{(1)}$) deposited at 6.6 Pa and 13.3 Pa, respectively. From these two CL spectra, one can notice the disappearance of the RL and the AL band only for S4 (13.3Pa), suggesting that S2 (6.6 Pa) was deposited under Ga-richer conditions[85], [86], [87], [88, p. 680]. This is consistent with our recent study conducted in the same reactor as discussed here, in which we have shown that when the pressure decreases, the density of nitrogen-atoms in the gas phase (plasma) also decreases (linearly with pressure). Another important observation in the case of S4 (Figure 4.26.D) is the position of the BE-L peak (~ 3.41 eV) which is extremely close to the theoretical value of GaN crystal (3.4 eV). What is relatable here is the evolution of the lattice parameters *a* and *c* (Figure 4.26.F&G) with the BE-L peak shifting for S2 and S4. Intuitively, the S4 that has a the BE-L peak closest to that of GaN crystal also has lattice parameters (a = 3.19 Å & c = 5.19 Å) which are equal to the theoretical values of GaN[94]. It is noteworthy that if the lattice parameter *c* is equal for S2 and S4 (Figure 4.26.G), the parameter *a*, although minimal, deviates for S2 from 3.19 Å to 3.21 Å. Hence, in terms of global luminescence features, S4 exhibits the most promising CL spectrum, that would resemble a highly defective GaN epitaxial film grown at high temperature. However, if one would only considers, the XRD pattern and F_C as indicators of the overall quality of the film, S2 would have been considered the best sample over the other ones (Figure 4.26.B_1&E). Therefore, a question arises: why does S4 exhibit the best luminescent features? For this purpose, scrutinizing the samples at the nanoscale using HR-TEM has been seen as a valuable way to address this point, especially by focusing on observing the nanostructure of the different samples. For instance, larger grain sizes in pc-films would tend to reduced grain boundary density thus improving charge carrier mobility and by the way improving CL features[93], [95], [96].

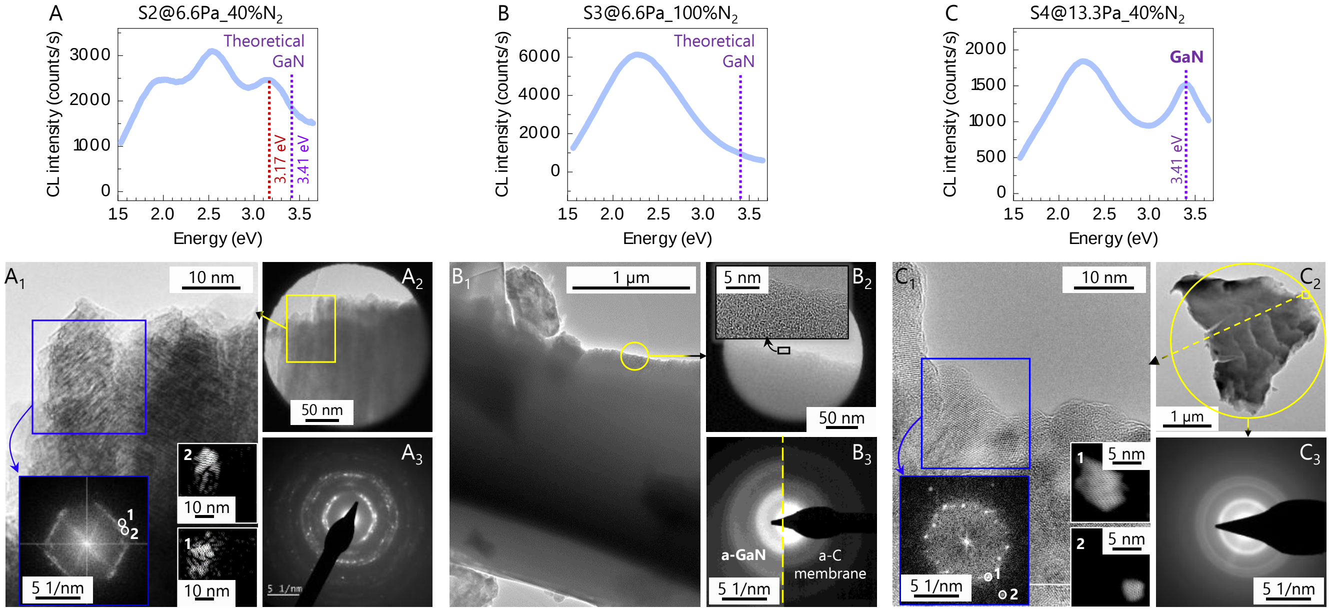

Figure 4.27: A, B & C. RT Cathodoluminescence (CL) spectra for GaN samples deposited at RT with process conditions: 6.6 Pa, 40% N_2 (A – Sample 2) ~ polycrystalline, 6.6 Pa, 100% N_2 (B – Sample 3) ~ amorphous and 13.3 Pa, 40% N_2 (C – Sample 3) ~ polycrystalline. : $A_{(x)}$, $B_{(x)}$ & $C_{(x)}$ corresponds to the TEM measurements of the aforementioned samples. The notations 1 & 2 represent the focused area of the sample taken for measurement and 3 depicts the diffraction patterns corresponding to the film.

Figure 4.27 shows a panorama of TEM images of three samples: the two samples that present the highest crystalline fraction, namely S2_6.6 Pa/40%N_2 (A) and S4_6.6Pa/100%N_2 (C) along with one of the amorphous sampleS4_13.3 Pa/40%N_2 (B) that displays the strongest (overall) luminescence intensity. The corresponding CL spectra of those samples are presented again for convenience. For all the samples, similar images and processing were done so we rely hereafter on S2 (Figure 4.27$A_{(x)}$) to detail the methodology. As shown in Figure 4.27.A&A_1, a large scale image was acquired and a zoom of it was done, the later on which a selective area diffraction (SAED) was performed (Figure 4.27.A_2). The processed insets in Figure 4.27.A gives access to the grains size in the GaN thin film. Overall, from TEM analysis shown in Figure 4.27, two main observations can be raised:

I. Diffraction patterns of both S2 (Figure 4.27.A_2) and S4 (Figure 4.27.C_2) brings confirmation of their polycrystalline nature while (Figure 4.27.C_2) depicts to an amorphous GaN film, coherent with our results from GIXRD measurements (Figure 4.26.$B_{(1)}$, $C_{(1)}$&$D_{(1)}$).

II. The grain size in the pc-films S2 (Figure 4.27.A) is larger (~20 nm) than that of S4 (Figure 4.27.B), which is about 5nm.

The smaller grains size found in S4 can be one possible explanation of why it has the best CL features. Indeed, smaller grain sizes imply having a higher density of grain boundaries, but these boundaries may be more continuous and smoother compared to larger grains. As a result, scattering at grain boundaries can be reduced, allowing carriers to move more freely, leading to higher mobility [97]. Moreover, we previously showed that the amorphous phase can act as passivation of the grains explaining why S3 has the strongest luminescence intensity even though it does not show B-EL. In the case of S4, it has a crystalline fraction of about 45% (Figure 4.27.E) so one may invoke the fact that this mix phase along with the presence of small grains would be the right combination that makes this sample having this desired BE-L feature.

When it comes to the other pc-film S2 (Figure 4.27), the red shift of the band edge (to ~ 3.2 eV) that could be due to the larger grain size, can typically result in an increased lattice strain within the material [98] as evidenced by the deviation of its lattice parameter *a* (Figure 4.27.F). At the inverse, S4 shows a lattice parameters almost equal to that of theoretical GaN as mentioned previously (Figure 4.27.F&G). As far as the amorphous film S3 (Figure 4.27.B) is concerned, the absence of luminescence at 3.4 eV can be naturally attributed to its disordered structure and lack of a well-defined band structure typical of a crystalline material. As a result, the energy distribution of electronic states in the amorphous film is continuous, leading to a lack of distinct luminescence features at specific energy levels [99]. Evidently, the lattice parameters values for sample 3 (Figure 4.27.F&G) also exhibits a relatively significant deviation from the theoretical GaN values.

In conclusion, our investigation comparing films of different structures sheds light on the interplay between deposition conditions, crystallinity, related defects and luminescence characteristics. The observed CL spectra variations, particularly impacted by the changes in N_2 fraction (10%, 40% and 100% N_2) and working pressure (6.6 Pa and 13.3 Pa), underscore the profound influence of growth environment on the optical properties of GaN films. At lower N_2 fractions, we observe a decrease in the luminescence intensity and broader peaks, indicative of higher percentages of defects and reduced crystallinity. Conversely, increasing the N_2 fraction from 10% to 40% leads to enhanced crystallinity, as evidenced by sharper peaks from GIXRD and higher overall CL intensity. Notably, the presence of specific luminescence bands (RL, YL, AL) reflects the prevailing growth conditions with defects, with Ga-rich environments favoring the emergence of certain intrinsic point defects associated with the RL and the AL bands. Sample deposited at 100% N_2, even though mostly amorphous and without BE-L peak, shows the strongest CL intensity, suggesting an amorphous passivation of grains that might be at the origin of this high intensity. On the other hand, samples deposited at higher pressures exhibit distinct luminescence peaks, even though persistent intrinsic point defects are observed. TEM analysis corroborates our CL findings, revealing a correlation between grain size, crystallinity, and luminescence properties. Larger grain sizes (~20 nm for sample deposited at 6.6 Pa) are associated with red shifts in the band-edge luminescence, potentially attributed to increased lattice strain. Conversely, smaller grain sizes (~ 5nm for sample deposited at 13.3 Pa) associated to a potential passivation due to the presence of a significant amount of amorphous phase (F_C of 45%), exhibit closer alignment with the theoretical band edge of GaN, indicative of reduced defect density and enhanced carrier mobility.

4.8 A summary of the qualification of GaN on Si at room temperature

Figure 4.28 illustrates a panorama of the main experimental results gained from the characterizations of the films (growth rate, surface roughness and the crystalline fraction) of the GaN film as a function of the working pressure, the N_2 flow and the RF power. The findings and learnings for GaN films deposited at RT are depicted below.

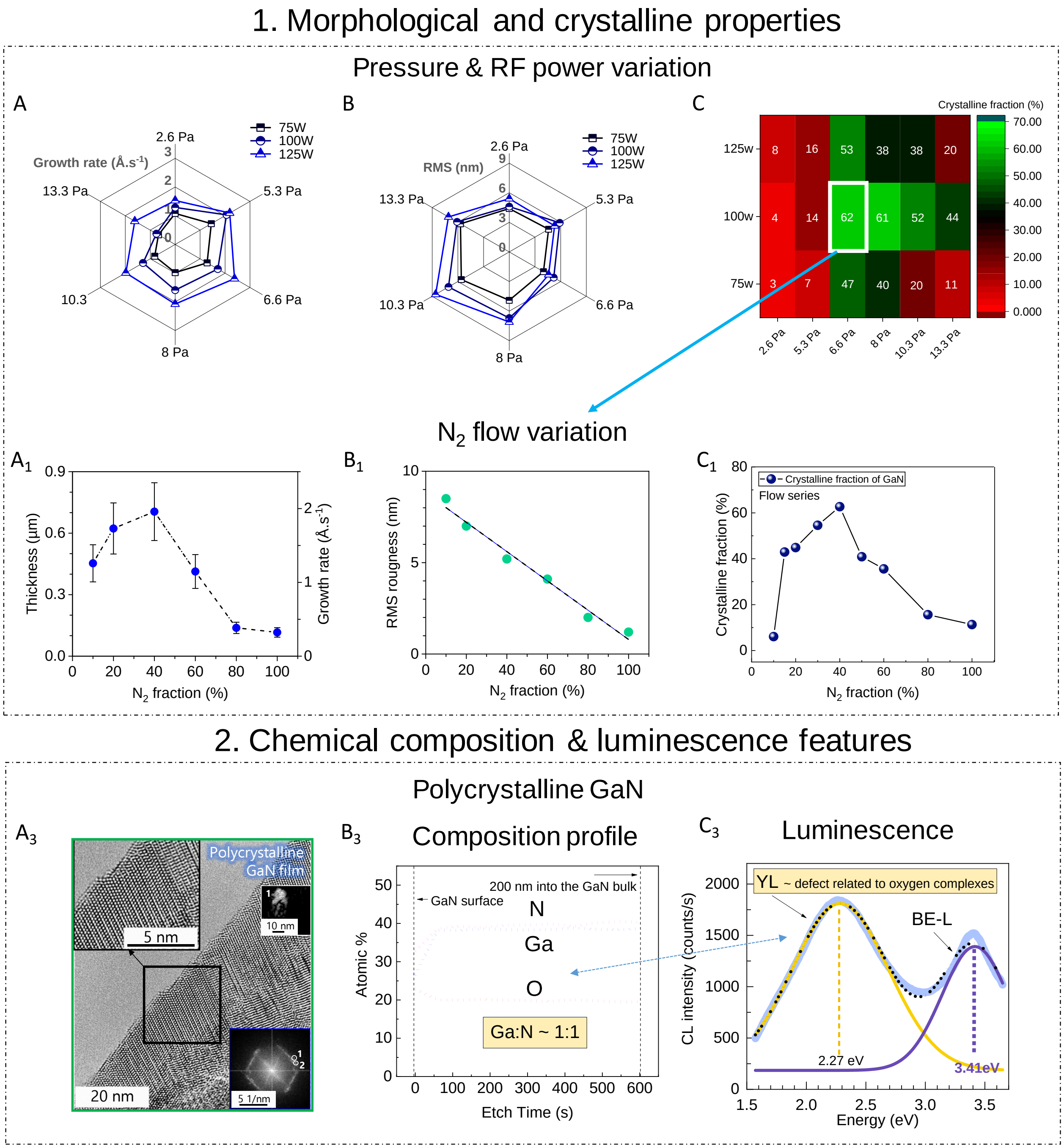

Figure 4.28: Illustration of the characterized data depicting the influence of working pressure (Pa), RF Power (W) and N_2 flow variation (percentage) for the GaN sample deposited at room temperature on Si. A, B & C: The growth rate (Å/s), RMS roughness and the crystalline fraction at different working pressure & RF power. A', B' & C'. The growth rate (Å/s), RMS roughness and the crystalline fraction at different N_2 fractions in an Ar/N_2 gas mixture.

I. **Polycrystalline GaN with a strong orientation towards the c-axis, which resembled a hexagonal wurtzite GaN** structure. Morphology revealed nanostructured grains with columnar cross-sections.

II. Through this study, **we defined the optimized sputtering condition: 6.6 Pa pressure, 40% N_2 fraction and 100W power, which yielded a hexagonal wurtzite polycrystalline GaN with the highest growth rate (~ 2 Å/s) and the best crystalline fraction (~ 62%).**

III. From the plasma diagnostics, we introduced two plasma parameters – the Ga atom flux (φ_{Ga}) and the average Ga atom energy at the substrate ($\overline{E_{Ga}^{sub}}$). Upon observing the trends in the growth rate and the crystalline fraction by varying all the process parameters (pressure, flow and power), we found that **$\boldsymbol{\varphi_{Ga}}$ is a good indicator that correlates with the growth rate trends and $\overline{\boldsymbol{E_{Ga}^{sub}}}$ was found to be a good indicator that directly correlates with the crystalline fraction of the GaN film.**

IV. Regarding the chemical composition, based on XPS analysis, **our sample exhibits a Ga/N ratio close to stoichiometry, approximately 1, indicating balanced elemental composition.** The depth profile confirms uniform distribution of Ga and N throughout the layer, indicative of stable sputtering processes yielding consistent delivery of Ga and N atoms without irregularities. Regarding contaminants, we identified carbon, hydrogen, and oxygen, with carbon and hydrogen primarily present on the surface. **Oxygen contamination is notable both at the surface and within the layer, suggesting its incorporation into the GaN lattice structure.**

V. To alleviate the oxygen contamination in the film, we investigated the depth profile before and after a plasma & reactor cleaning procedure using GD-OES. The results were promising and the oxygen composition in the GaN film was reduced from 30% to ~ 13%. We suggest the cleaning procedure as a temporary solution for reducing the effects of oxygen contamination and point out to the fact that the permanent solution could be the implementation of a load-lock system in our reactor.

VI. Cathodoluminescence (CL) analysis into GaN film structures reveals the profound influence of deposition conditions on optical properties. Varying N_2 fractions (10%, 40%, and 100%) and working pressures (6.6 Pa and 13.3 Pa) notably influence the optical properties. Lower N_2 fractions result in decreased luminescence intensity and broader peaks, indicating higher defect percentages and reduced crystallinity. Conversely, increasing N_2 fraction enhances crystallinity, leading to sharper peaks and higher overall luminescence intensity. **Specific luminescence bands (RL, YL, AL) correlate with growth conditions and defects, with Ga-rich environments favoring certain intrinsic point defects.** Despite being mostly amorphous, samples deposited at 100% N_2 exhibit strong luminescence, suggesting amorphous grain passivation. TEM analysis confirms a correlation between grain size, crystallinity, and luminescence properties.

We have seen that we are able to finely tune and control the discharge to obtain polycrystalline GaN films which exhibits luminescence at room temperature. We now want to investigate the effect of the substrate temperature on the morphology, growth rate, crystalline structure, chemical composition and the optical properties of GaN films to compare with the films obtained at room temperature and provide a comprehensive understanding on the thermal effects related to the growth properties of the film.

REFERENCES

[1] R. Jenkins, T. G. Fawcett, D. K. Smith, J. W. Visser, M. C. Morris, and L. K. Frevel, "JCPDS—International centre for diffraction data sample preparation methods in X-ray powder diffraction," *Powder Diffr.*, vol. 1, no. 2, pp. 51–63, 1986.

[2] A. L. Patterson, "The Scherrer Formula for X-Ray Particle Size Determination," *Phys. Rev.*, vol. 56, no. 10, pp. 978–982, Nov. 1939, doi: 10.1103/PhysRev.56.978.

[3] V. Lemos, C. A. Argüello, and R. C. C. Leite, "Resonant Raman scattering of TO(A1), TO(E1) and E2 optical phonons in GaN," *Solid State Commun.*, vol. 11, no. 10, pp. 1351–1353, 1972, doi: https://doi.org/10.1016/0038-1098(72)90541-8.

[4] A. G. Milekhin *et al.*, "Raman scattering study of GaN nanostructures obtained by bottom-up and top-down approaches," *J. Phys. Condens. Matter*, vol. 18, no. 26, pp. 5825–5834, Jul. 2006, doi: 10.1088/0953-8984/18/26/003.

[5] M. S. Kumar and J. Kumar, "XRD, XPS, SEM, PL and Raman scattering analysis of synthesised GaN powder," *Mater. Chem. Phys.*, vol. 77, no. 2, pp. 341–345, 2003.

[6] J. A. Thornton, "The microstructure of sputter-deposited coatings," *J. Vac. Sci. Technol. Vac. Surf. Films*, vol. 4, no. 6, pp. 3059–3065, 1986.

[7] A. Nikiforov, C. Ma, A. Choukourov, and F. Palumbo, "Plasma technology in antimicrobial surface engineering," *J. Appl. Phys.*, vol. 131, p. 011102, Jan. 2022, doi: 10.1063/5.0066724.

[8] E. Alfonso, J. Olaya, and G. Cubillos, "Thin Film Growth Through Sputtering Technique and Its Applications," in *Crystallization - Science and Technology*, M. Andreeta, Ed., InTech, 2012. doi: 10.5772/35844.

[9] J. A. Thornton, "Structure-zone models of thin films," in *Modeling of Optical Thin Films*, SPIE, 1988, pp. 95–105.

[10] J. A. Thornton, "High Rate Thick Film Growth," *Annu. Rev. Mater. Sci.*, vol. 7, no. 1, pp. 239–260, Aug. 1977, doi: 10.1146/annurev.ms.07.080177.001323.

[11] 7_B A. Movchan, "Study of the structure and properties of thick vacuum condensates of nickel, titanium, tungsten, aluminium oxide and zirconium dioxide," *Phys Met Met.*, vol. 28, no. 4, pp. 83–90, 1969.

[12] H. F. Huq, R. Y. Garza, and R. Garcia-Perez, "Characteristics of GaN Thin Films Using Magnetron Sputtering System," *J. Mod. Phys.*, vol. 07, no. 15, pp. 2028–2037, 2016, doi: 10.4236/jmp.2016.715178.

[13] Z. Yang, L. K. Li, and W. I. Wang, "GaN grown by molecular beam epitaxy at high growth rates using ammonia as the nitrogen source," *Appl. Phys. Lett.*, vol. 67, no. 12, pp. 1686–1688, Sep. 1995, doi: 10.1063/1.115057.

[14] K. P. Biju, A. Subrahmanyam, and M. K. Jain, "Low-temperature growth of polycrystalline GaN films using modified activated reactive evaporation," *J. Cryst. Growth*, vol. 311, no. 8, pp. 2275–2280, 2009.

[15] T. Miyazaki, T. Fujimaki, S. Adachi, and K. Ohtsuka, "Properties of GaN films deposited on Si (111) by radio-frequency-magnetron sputtering," *J. Appl. Phys.*, vol. 89, no. 12, pp. 8316–8320, 2001.

[16] M. Sobanska *et al.*, "Plasma-assisted MBE growth of GaN on Si(111) substrates," *Cryst. Res. Technol.*, vol. 47, no. 3, pp. 307–312, Mar. 2012, doi: 10.1002/crat.201100408.

[17] G. E. Abrosimova, A. S. Aronin, and N. N. Kholstinina, "On the determination of the volume fraction of the crystalline phase in amorphous-crystalline alloys," *Phys. Solid State*, vol. 52, pp. 445–451, 2010.

[18] P. Losbichler and C. Mitterer, "Non-reactively sputtered TiN and TiB2 films: influence of activation energy on film growth," *Surf. Coat. Technol.*, vol. 97, no. 1–3, pp. 567–573, 1997.

[19] A. Anders, "Tutorial: Reactive high power impulse magnetron sputtering (R-HiPIMS)," *J. Appl. Phys.*, vol. 121, no. 17, 2017, Accessed: Dec. 05, 2023. [Online]. Available: https://pubs.aip.org/aip/jap/article/121/17/171101/945026

[20] V. Suendo, "Physico-Chimie des plasmas de silane pour la formation de nacocristaux de silicium a tempétature ambiante: application à des dispositifs.," PhD Thesis, Ecole Polytechnique X, 2005. Accessed: Nov. 28, 2023. [Online]. Available: https://pastel.hal.science/pastel-00001909/

[21] A. Palmero, E. D. Van Hattum, W. M. Arnoldbik, A. M. Vredenberg, and F. Habraken, "Characterization of the plasma in a radio-frequency magnetron sputtering system," *J. Appl. Phys.*, vol. 95, no. 12, pp. 7611–7618, 2004.

[22] J. W. Bradley, S. Thompson, and Y. A. Gonzalvo, "Measurement of the plasma potential in a magnetron discharge and the prediction of the electron drift speeds," *Plasma Sources Sci. Technol.*, vol. 10, no. 3, p. 490, 2001.

[23] H. Kakati, A. R. Pal, H. Bailung, and J. Chutia, “Sheath and potential characteristics in rf magnetron sputtering plasma,” *J. Appl. Phys.*, vol. 100, no. 8, 2006, Accessed: Dec. 05, 2023. [Online]. Available: https://pubs.aip.org/aip/jap/article/100/8/083303/930365

[24] A. Palmero, E. D. Van Hattum, W. M. Arnoldbik, and F. Habraken, “Argon plasma modelling in a RF magnetron sputtering system,” *Surf. Coat. Technol.*, vol. 188, pp. 392–398, 2004.

[25] W. Möller and D. Güttler, “Modeling of plasma-target interaction during reactive magnetron sputtering of TiN,” *J. Appl. Phys.*, vol. 102, no. 9, 2007, Accessed: Dec. 05, 2023. [Online]. Available: https://pubs.aip.org/aip/jap/article-abstract/102/9/094501/1030070

[26] P. Brault, A.-L. Thomann, and M. Cavarroc, “Theory and molecular simulations of plasma sputtering, transport and deposition processes,” *Eur. Phys. J. D*, vol. 77, no. 2, p. 19, Feb. 2023, doi: 10.1140/epjd/s10053-023-00592-x.

[27] S. Mahieu and D. Depla, “Reactive sputter deposition of TiN layers: modelling the growth by characterization of particle fluxes towards the substrate,” *J. Phys. Appl. Phys.*, vol. 42, no. 5, p. 053002, 2009.

[28] K. Meyer, I. K. Schuller, and C. M. Falco, “Thermalization of sputtered atoms,” *J. Appl. Phys.*, vol. 52, no. 9, pp. 5803–5805, 1981.

[29] A. Gras-Marti and J. A. Valles-Abarca, “Slowing down and thermalization of sputtered particle fluxes: Energy distributions,” *J. Appl. Phys.*, vol. 54, no. 2, pp. 1071–1075, 1983.

[30] J.-H. Hsieh and C. Li, “Calculation of Sputtering Rate during a Plasma-Assisted Process,” *Jpn. J. Appl. Phys.*, vol. 42, no. Part 1, No. 8, pp. 5295–5298, Aug. 2003, doi: 10.1143/JJAP.42.5295.

[31] Y. Kudriavtsev, A. Villegas, A. Godines, and R. Asomoza, “Calculation of the surface binding energy for ion sputtered particles,” *Appl. Surf. Sci.*, vol. 239, no. 3–4, pp. 273–278, Jan. 2005, doi: 10.1016/j.apsusc.2004.06.014.

[32] M. Kaminsky, Ed., *Radiation Effects on Solid Surfaces*, vol. 158. in Advances in Chemistry, vol. 158. WASHINGTON, D. C.: AMERICAN CHEMICAL SOCIETY, 1976. doi: 10.1021/ba-1976-0158.

[33] C. Adelmann, J. Brault, G. Mula, B. Daudin, L. Lymperakis, and J. Neugebauer, “Gallium adsorption on (0001) GaN surfaces,” *Phys. Rev. B*, vol. 67, no. 16, p. 165419, Apr. 2003, doi: 10.1103/PhysRevB.67.165419.

[34] N. Mahne, M. Čekada, and M. Panjan, “Energy Distribution of Sputtered Atoms Explored by SRIM Simulations,” *Coatings*, vol. 13, no. 8, p. 1448, 2023.

[35] P. Sigmund, “Theory of Sputtering. I. Sputtering Yield of Amorphous and Polycrystalline Targets,” *Phys. Rev.*, vol. 184, no. 2, pp. 383–416, Aug. 1969, doi: 10.1103/PhysRev.184.383.

[36] N. Mahne, M. Čekada, and M. Panjan, “Total and Differential Sputtering Yields Explored by SRIM Simulations,” *Coatings*, vol. 12, no. 10, p. 1541, 2022.

[37] J. Held, A. Hecimovic, A. Von Keudell, and V. Schulz-von der Gathen, “Velocity distribution of titanium neutrals in the target region of high power impulse magnetron sputtering discharges,” *Plasma Sources Sci. Technol.*, vol. 27, no. 10, p. 105012, 2018.

[38] J. P. Biersack and W. Eckstein, “Sputtering studies with the Monte Carlo Program TRIM.SP,” *Appl. Phys. Solids Surf.*, vol. 34, no. 2, pp. 73–94, Jun. 1984, doi: 10.1007/BF00614759.

[39] J. F. Ziegler and J. P. Biersack, “The Stopping and Range of Ions in Matter,” in *Treatise on Heavy-Ion Science*, D. A. Bromley, Ed., Boston, MA: Springer US, 1985, pp. 93–129. doi: 10.1007/978-1-4615-8103-1_3.

[40] J. F. Ziegler, M. D. Ziegler, and J. P. Biersack, “SRIM–The stopping and range of ions in matter (2010),” *Nucl. Instrum. Methods Phys. Res. Sect. B Beam Interact. Mater. At.*, vol. 268, no. 11–12, pp. 1818–1823, 2010.

[41] A. Palmero, H. Rudolph, and F. Habraken, “One-dimensional analysis of the rate of plasma-assisted sputter deposition,” *J. Appl. Phys.*, vol. 101, no. 8, 2007, Accessed: Dec. 06, 2023. [Online]. Available: https://pubs.aip.org/aip/jap/article-abstract/101/8/083307/916191

[42] Y. Yamamura and M. Ishida, “Monte Carlo simulation of the thermalization of sputtered atoms and reflected atoms in the magnetron sputtering discharge,” *J. Vac. Sci. Technol. Vac. Surf. Films*, vol. 13, no. 1, pp. 101–112, 1995.

[43] G. M. Turner, I. S. Falconer, B. W. James, and D. R. McKenzie, “Monte Carlo calculations of the properties of sputtered atoms at a substrate surface in a magnetron discharge,” *J. Vac. Sci. Technol. Vac. Surf. Films*, vol. 10, no. 3, pp. 455–461, 1992.

[44] H.-B. Valentini, “Bohm criterion for the collisional sheath,” *Phys. Plasmas*, vol. 3, no. 4, pp. 1459–1461, 1996.

[45] M. S. Benilov, “The Child–Langmuir law and analytical theory of collisionless to collision-dominated sheaths,” *Plasma Sources Sci. Technol.*, vol. 18, no. 1, p. 014005, 2008.

[46] H. S. Butler and G. S. Kino, “Plasma Sheath Formation by Radio-Frequency Fields,” *Phys. Fluids*, vol. 6, no. 9, p. 1346, 1963, doi: 10.1063/1.1706905.

[47] B. Fritsche, T. Chevolleau, J. Kourtev, A. Kolitsch, and W. Möller, "Plasma diagnostic of an RF magnetron Ar/N2 discharge," *Vacuum*, vol. 69, no. 1–3, pp. 139–145, 2002.

[48] A. Bousquet, L. Spinelle, J. Cellier, and E. Tomasella, "Optical Emission Spectroscopy Analysis of Ar/N2 Plasma in Reactive Magnetron Sputtering," *Plasma Process. Polym.*, vol. 6, no. S1, pp. S605–S609, 2009, doi: 10.1002/ppap.200931602.

[49] I. Petrov, A. Myers, J. E. Greene, and J. R. Abelson, "Mass and energy resolved detection of ions and neutral sputtered species incident at the substrate during reactive magnetron sputtering of Ti in mixed Ar+ N2 mixtures," *J. Vac. Sci. Technol. Vac. Surf. Films*, vol. 12, no. 5, pp. 2846–2854, 1994.

[50] R. Pintaske, T. Welzel, M. Schaller, N. Kahl, J. Hahn, and F. Richter, "Spectroscopic studies of a magnetron sputtering discharge for boron nitride deposition," *Surf. Coat. Technol.*, vol. 99, no. 3, pp. 266–273, 1998.

[51] M. S. Mohammed, "Spectroscopic plasma diagnosis of V2O5 at a Variable of Operating Power and Pressure With Radio Frequency Magnetron Sputtering," in *IOP Conference Series: Materials Science and Engineering*, IOP Publishing, 2020, p. 072150. Accessed: Dec. 06, 2023. [Online]. Available: https://iopscience.iop.org/article/10.1088/1757-899X/928/7/072150/meta

[52] A. Kais, J. Lo, L. Thérèse, and Ph. Guillot, "Heating power at the substrate, electron temperature, and electron density in 2.45 GHz low-pressure microwave plasma," *Phys. Plasmas*, vol. 25, no. 1, p. 013504, Jan. 2018, doi: 10.1063/1.5005592.

[53] S. Lin, J. Zhang, R. Zhu, S. Fu, and D. Yun, "Effects of sputtering pressure on microstructure and mechanical properties of ZrN films deposited by magnetron sputtering," *Mater. Res. Bull.*, vol. 105, pp. 231–236, 2018.

[54] A. Büttner *et al.*, "Influence of sputtering pressure on microstructure and layer properties of iridium thin films," *Thin Solid Films*, vol. 662, pp. 41–46, 2018.

[55] A. Prabaswara, J. Birch, M. Junaid, E. A. Serban, L. Hultman, and C.-L. Hsiao, "Review of GaN Thin Film and Nanorod Growth Using Magnetron Sputter Epitaxy," *Appl. Sci.*, vol. 10, no. 9, p. 3050, Apr. 2020, doi: 10.3390/app10093050.

[56] A. Denis, G. Goglio, and G. Demazeau, "Gallium nitride bulk crystal growth processes: A review," *Mater. Sci. Eng. R Rep.*, vol. 50, no. 6, pp. 167–194, Jan. 2006, doi: 10.1016/j.mser.2005.11.001.

[57] I. Petrov, F. Adibi, J. E. Greene, L. Hultman, and J.-E. Sundgren, "Average energy deposited per atom: A universal parameter for describing ion-assisted film growth?," *Appl. Phys. Lett.*, vol. 63, no. 1, pp. 36–38, 1993.

[58] T. Motomura, T. Tabaru, Y. Fujio, and T. Okuyama, "Influence of nitrogen gas flow ratio on gallium nitride film growth using high-density convergent plasma sputtering device at room temperature," *J. Vac. Sci. Technol. A*, vol. 39, no. 1, p. 013001, Dec. 2020, doi: 10.1116/6.0000677.

[59] M. Wen *et al.*, "Effects of nitrogen flow rate on the preferred orientation and phase transition for niobium nitride films grown by direct current reactive magnetron sputtering," *J. Phys. Appl. Phys.*, vol. 42, no. 3, p. 035304, 2008.

[60] K. Chakrabarti, J. J. Jeong, S. K. Hwang, Y. C. Yoo, and C. M. Lee, "Effects of nitrogen flow rates on the growth morphology of TiAlN films prepared by an rf-reactive sputtering technique," *Thin Solid Films*, vol. 406, no. 1–2, pp. 159–163, 2002.

[61] K. Pingen *et al.*, "High growth rate magnetron sputter epitaxy of GaN using a solid Ga target," *Vacuum*, p. 112852, 2023.

[62] A. El Farsy, J.-F. Pierson, T. Gries, L. de Poucques, and J. Bougdira, "On the correlation between the TiN thin film properties and the energy flux of neutral sputtered atoms in direct current magnetron discharge," *J. Phys. Appl. Phys.*, vol. 55, no. 50, p. 505203, 2022.

[63] J. D. Andrade, "X-ray Photoelectron Spectroscopy (XPS)," in *Surface and Interfacial Aspects of Biomedical Polymers*, J. D. Andrade, Ed., Boston, MA: Springer US, 1985, pp. 105–195. doi: 10.1007/978-1-4684-8610-0_5.

[64] E. C. Knox-Davies, J. M. Shannon, and S. R. P. Silva, "The properties and deposition process of GaN films grown by reactive sputtering at low temperatures," *J. Appl. Phys.*, vol. 99, no. 7, 2006.

[65] M. Dinescu, P. Verardi, C. Boulmer-Leborgne, C. Gerardi, L. Mirenghi, and V. Sandu, "GaN thin films deposition by laser ablation of liquid Ga target in nitrogen reactive atmosphere," *Appl. Surf. Sci.*, vol. 127, pp. 559–563, 1998.

[66] C. Lehrer, L. Frey, S. Petersen, M. Mizutani, M. Takai, and H. Ryssel, "Defects and gallium-contamination during focused ion beam micro machining," in *2000 International Conference on Ion Implantation Technology Proceedings. Ion Implantation Technology-2000 (Cat. No. 00EX432)*, IEEE, 2000, pp. 695–698. Accessed: Nov. 02, 2023. [Online]. Available: https://ieeexplore.ieee.org/abstract/document/924248/

[67] H. W. Choi, M. A. Rana, S. J. Chua, T. Osipowicz, and J. S. Pan, "Surface analysis of GaN decomposition," *Semicond. Sci. Technol.*, vol. 17, no. 12, p. 1223, 2002.

[68] M. Mishra *et al.*, "New approach to clean GaN surfaces," *Mater. Focus*, vol. 3, no. 3, pp. 218–223, 2014.

[69] A. Dadgar, "Sixteen years GaN on Si," *Phys. Status Solidi B*, vol. 252, no. 5, pp. 1063–1068, May 2015, doi: 10.1002/pssb.201451656.

[70] A. Dadgar, A. Krost, and B. Gil, "Epitaxial growth and benefits of GaN on silicon," *III-Nitride Semicond. Their Mod. Devices*, vol. 18, p. 78, 2013.

[71] D. R. G. Mitchell, "DiffTools: Electron diffraction software tools for DigitalMicrograph™," *Microsc. Res. Tech.*, vol. 71, no. 8, pp. 588–593, Aug. 2008, doi: 10.1002/jemt.20591.

[72] J. Schreiber, S. Hildebrandt, W. Kircher, and T. Richter, "Optical investigations of surface and interface properties at III–V semiconductors," *Mater. Sci. Eng. B*, vol. 9, no. 1, pp. 31–35, Jul. 1991, doi: 10.1016/0921-5107(91)90144-K.

[73] S. Hildebrandt, J. Schreiber, W. Hergert, and V. I. Petrov, "Determination of the absorption coefficient and the internal luminescence spectrum of GaAs and GaAs1- xPx (x= 0.375, 0.78) from beam voltage dependent measurements of cathodoluminescence spectra in the scanning electron microscope," *Phys. Status Solidi A*, vol. 110, no. 1, pp. 283–291, 1988.

[74] G. D. Chen *et al.*, "Photoluminescence studies of band-edge transitions in GaN epitaxial layers grown by plasma-assisted molecular beam epitaxy," *J. Appl. Phys.*, vol. 79, no. 5, pp. 2675–2683, 1996.

[75] M. A. Reshchikov and H. Morkoç, "Luminescence properties of defects in GaN," *J. Appl. Phys.*, vol. 97, no. 6, 2005, Accessed: Jan. 12, 2024. [Online]. Available: https://pubs.aip.org/aip/jap/article/97/6/061301/984603

[76] E. Calleja *et al.*, "Yellow luminescence and related deep states in undoped GaN," *Phys. Rev. B*, vol. 55, no. 7, pp. 4689–4694, Feb. 1997, doi: 10.1103/PhysRevB.55.4689.

[77] C. B. Soh, S. J. Chua, H. F. Lim, D. Z. Chi, S. Tripathy, and W. Liu, "Assignment of deep levels causing yellow luminescence in GaN," *J. Appl. Phys.*, vol. 96, no. 3, pp. 1341–1347, 2004.

[78] T. Ogino and M. Aoki, "Mechanism of yellow luminescence in GaN," *Jpn. J. Appl. Phys.*, vol. 19, no. 12, p. 2395, 1980.

[79] M. A. Reshchikov, "On the Origin of the Yellow Luminescence Band in GaN," *Phys. Status Solidi B*, vol. 260, no. 8, p. 2200488, Aug. 2023, doi: 10.1002/pssb.202200488.

[80] J. Neugebauer and C. G. Van de Walle, "Gallium vacancies and the yellow luminescence in GaN," *Appl. Phys. Lett.*, vol. 69, no. 4, pp. 503–505, 1996.

[81] H. Wang and A.-B. Chen, "Calculation of shallow donor levels in GaN," *J. Appl. Phys.*, vol. 87, no. 11, pp. 7859–7863, 2000.

[82] T. Mattila and R. M. Nieminen, "Point-defect complexes and broadband luminescence in GaN and AlN," *Phys. Rev. B*, vol. 55, no. 15, pp. 9571–9576, Apr. 1997, doi: 10.1103/PhysRevB.55.9571.

[83] Z. Xie, Y. Sui, J. Buckeridge, A. A. Sokol, T. W. Keal, and A. Walsh, "Prediction of multiband luminescence due to the gallium vacancy–oxygen defect complex in GaN," *Appl. Phys. Lett.*, vol. 112, no. 26, 2018, Accessed: Feb. 09, 2024. [Online]. Available: https://pubs.aip.org/aip/apl/article/112/26/262104/35613

[84] G. A. Slack, L. J. Schowalter, D. Morelli, and J. A. Freitas Jr, "Some effects of oxygen impurities on AlN and GaN," *J. Cryst. Growth*, vol. 246, no. 3–4, pp. 287–298, 2002.

[85] K. Fujii *et al.*, "Deep-level luminescence at 1.93 eV in GaN prepared by ammonothermal growth," *Phys. Status Solidi A*, vol. 204, no. 10, pp. 3509–3513, Oct. 2007, doi: 10.1002/pssa.200723188.

[86] M. A. Reshchikov and H. Morkoc, "Unusual properties of the red and green luminescence bands in Ga-rich GaN," *MRS Online Proc. Libr. OPL*, vol. 831, 2004, Accessed: Feb. 09, 2024. [Online]. Available: https://www.cambridge.org/core/journals/mrs-online-proceedings-library-archive/article/unusual-properties-of-the-red-and-green-luminescence-bands-in-garich-gan/75127451BCF001EB3EF8BF61E261FCDF

[87] M. A. Reshchikov, L. He, R. J. Molnar, S. S. Park, K. Y. Lee, and H. Morkoç, "Aquamarine Luminescence Band in Undoped GaN," *MRS Proc.*, vol. 831, p. E9.8, 2004, doi: 10.1557/PROC-831-E9.8.

[88] M. A. Reshchikov, R. J. Molnar, and H. Morkoç, "Photoluminescence and Excitation Spectra of Deep Defects in GaN," *MRS Online Proc. Libr. OPL*, vol. 680, pp. E5-6, 2001.

[89] S. Li *et al.*, "Study of the blue luminescence in unintentional doped GaN films grown by MOCVD," *J. Lumin.*, vol. 106, no. 3–4, pp. 219–223, 2004.

[90] S. Li *et al.*, "Relationship between structure characteristic and blue luminescence in unintentional doped GaN layers," *Mater. Sci. Eng. B*, vol. 122, no. 1, pp. 72–75, 2005.

[91] I. Shalish *et al.*, "Grain-boundary-controlled transport in GaN layers," *Phys. Rev. B*, vol. 61, no. 23, pp. 15573–15576, Jun. 2000, doi: 10.1103/PhysRevB.61.15573.

[92] J. T. Asubar, Z. Yatabe, D. Gregusova, and T. Hashizume, "Controlling surface/interface states in GaN-based transistors: Surface model, insulated gate, and surface passivation," *J. Appl. Phys.*, vol. 129, no. 12, 2021, Accessed: Feb. 12, 2024. [Online]. Available: https://pubs.aip.org/aip/jap/article/129/12/121102/905430

[93] H. Yoo *et al.*, "Understanding luminescence properties of grain boundaries in GaN thin films and their atomistic origin," *Appl. Phys. Lett.*, vol. 112, no. 13, 2018, Accessed: Feb. 12, 2024. [Online]. Available: https://pubs.aip.org/aip/apl/article/112/13/131901/34757

[94] V. Darakchieva, B. Monemar, and A. Usui, "On the lattice parameters of GaN," *Appl. Phys. Lett.*, vol. 91, no. 3, 2007, Accessed: Feb. 12, 2024. [Online]. Available: https://pubs.aip.org/aip/apl/article/91/3/031911/117993

[95] G. Nouet, P. Ruterana, H. Tampo, and H. Asahi, "Polycrystalline GaN: Analysis of the Defects," *Phys. Status Solidi C*, no. 1, pp. 409–412, Jan. 2003, doi: 10.1002/pssc.200390075.

[96] T. Barfels *et al.*, "Structure and luminescence of GaN layers," *Appl. Surf. Sci.*, vol. 179, no. 1–4, pp. 191–195, 2001.

[97] Y. Wang, W. Tang, and L. Zhang, "Crystalline size effects on texture coefficient, electrical and optical properties of sputter-deposited Ga-doped ZnO thin films," *J. Mater. Sci. Technol.*, vol. 31, no. 2, pp. 175–181, 2015.

[98] E. J. Mittemeijer and U. Welzel, "The 'state of the art' of the diffraction analysis of crystallite size and lattice strain," *Z. Für Krist.*, vol. 223, no. 9, pp. 552–560, Sep. 2008, doi: 10.1524/zkri.2008.1213.

[99] G. Yue, J. D. Lorentzen, J. Lin, D. Han, and Q. Wang, "Photoluminescence and Raman studies in thin-film materials: Transition from amorphous to microcrystalline silicon," *Appl. Phys. Lett.*, vol. 75, no. 4, pp. 492–494, Jul. 1999, doi: 10.1063/1.124426.

Chapter 5 – Characterization of GaN thin films on Si at various growth temperatures

Table of Contents

Chapter 5 – Characterization of GaN thin films on Si at various growth temperatures **118**

5.1 Influence of the substrate temperature **118**

5.1.1 Effect of growth temperature on the surface morphology 119

5.1.2 Effect of growth temperature on the crystalline structure 120

5.1.3 Effect of temperature on the chemical structure 121

5.1.4 Impact of growth temperature on the luminescence features of the films 123

5.2 A summary of the growth temperature series of GaN thin film deposition on Si **125**

REFERENCES **127**

Chapter 5 presents the characterization of a GaN thin film deposited at varying substrate temperatures ranging from room temperature up to 500°C.
The chapter comprises of single section (**section 1**) which presents the results, examining the impact of growth temperature on GaN film properties akin to Chapter 4. We aim to find the best temperature for achieving the highest growth rate, lowest surface roughness, and improved crystal quality. Utilizing morphological, structural, and XPS analyses, we evaluate surface chemistry, Ga/N ratio, and contaminants. Composition profile analysis focuses on uniformity and lattice structure influence. CL study aims to identify films with minimal defects and highest luminescence intensity at 3.4 eV. A concise summary correlates findings, elucidating the temperature's influence on plasma PVD-deposited GaN thin film quality.

5.1 Influence of the substrate temperature

In the previous chapter, we investigated GaN crystalline quality at room temperature deposition, finding optimal conditions at 6.6 Pa, 100W, and 40% N_2, yielding the best growth rate (~ 2Å/s). However, we also noticed a significant amount of oxygen present in our films. Increasing the deposition temperature could help in reduce oxygen contamination in GaN films. Higher temperatures promote outgassing of residual oxygen and strengthen chemical bonds in the film, reducing susceptibility to contamination [1], [2]. Moreover, we are interested to investigate the effect of substrate temperature on the crystallinity and the morphology of the thin films. Our goal is to find an optimal temperature range below conventional (700-1000ºC) which ideally provides us with a film with a high quality. In this section, we base our quality levers on the above four parameters – growth rate, crystalline fraction, chemical composition and luminescence to evaluate the quality of our GaN thin films.

5.1.1 Effect of growth temperature on the surface morphology

Figure 5.1.A&B shows the SEM surface micrographs and the cross-sectional images of the GaN films grown on Si at temperature ranging from RT to 500°C, respectively. From the surface micrographs, we observe that similar to the RT depositions, the films are nanostructured with features sizes varying as a function of the growth temperature. The features become larger as the temperature reaches 400ºC while a subtle change in the size and shape can be seen from RT to 300ºC. Interestingly, the features shape at 500ºC is completely different and consists of flakes rather than nanostructured grains. An important point to note is that for all the depositions except for the one at 500ºC, the base pressure after plasma cleaning was kept at ~ 3 x 10^{-7} mbar. However, in the case of 500ºC, the minimum base pressure that we could reach even after hours of waiting was ~ 1 x 10^{-6} mbar and although minimal, there was always a potential residue of OH lines observed from the OES. This means that the oxygen contamination for the samples grown at 500ºC would eventually be larger than the samples deposited at lower growth temperatures. A possible explanation of the irregular grain structure for the samples at 500ºC could be the increased contamination (introduces defects or impurities that could affect the film's structural integrity).

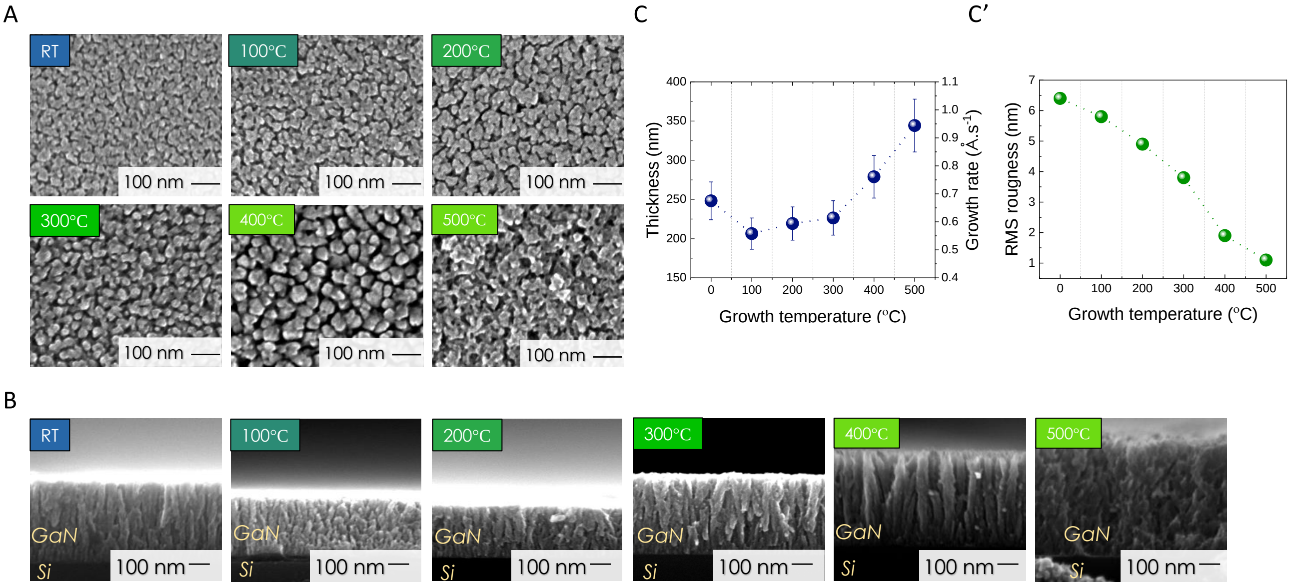

Figure 5.1: SEM images of GaN on Si at varying growth temperatures from room temperature to 500ºC. A. SEM surface micrographs. B. SEM cross-section images depicting the thin film & the Si substrate. C. The thickness & growth rate obtained from the cross-section images. C'. The root mean square (RMS) roughness obtained from AFM topography. The working pressure, RF power and Ar/N_2 flow rates were kept constant at 6.6 Pa, 100 W and 12/8 sccm respectively.

The cross-section images (Figure 5.1.B) reveal the columnar structure of the films except for the highest temperature of 500ºC that also here differs from the rest by exhibiting a 'flake-like' structure. This could mean that the expected increase in adatom mobility would still not be sufficient in our process to enhance a higher degree of binding among the columns and the borders between the columns to form a uniform dense structure that is not columnar [3].

In terms of growth rate (Figure 5.1.C), apart from a small exception from the RT to 100ºC where we observe a decrease, the growth rate increases with the temperature, while inversely, the surface roughness (Figure 5.1.C') decreases. The tendency in the growth rate could be explained by the fact that an improved adatom mobility, promoted by higher temperature, allows for an efficient incorporation into the growing crystal lattice, resulting in a higher growth rate [4], [5]. Moreover, on considering the surface roughness, the reduction in surface diffusion barriers - the movement of adatoms on the substrate surface is governed by surface diffusion [6]. At elevated temperatures, the energy barrier for surface diffusion is reduced. Lower barriers mean that adatoms can more easily overcome obstacles and find optimal lattice positions, leading to smoother and uniform growth with reduced defect densities.

Thornton (refer Chapter 4) depicted that the formation of large grains even with grain boundaries (columnar structures) at elevated temperatures could crystallize and produce a better crystalline structure [7]. To confirm the influence of the growth temperature on the effect of crystallization, we performed GIXRD.

5.1.2 Effect of growth temperature on the crystalline structure

.A shows the GIXRD spectra of GaN films grown from RT to 500°C. The corresponding crystalline fraction is depicted in .B. In Figure 2-A, as expected, we observe a drastic increase of the crystalline fraction that goes from 60% at room temperature deposition up to ~ 95% at 400°C, which is the maximal value reached within this T range. With increased surface mobility, the atoms are less likely to be trapped in positions other than the lattice structure, which can reduce the defects thus minimizing the occurrence of dislocations or vacancies [8].

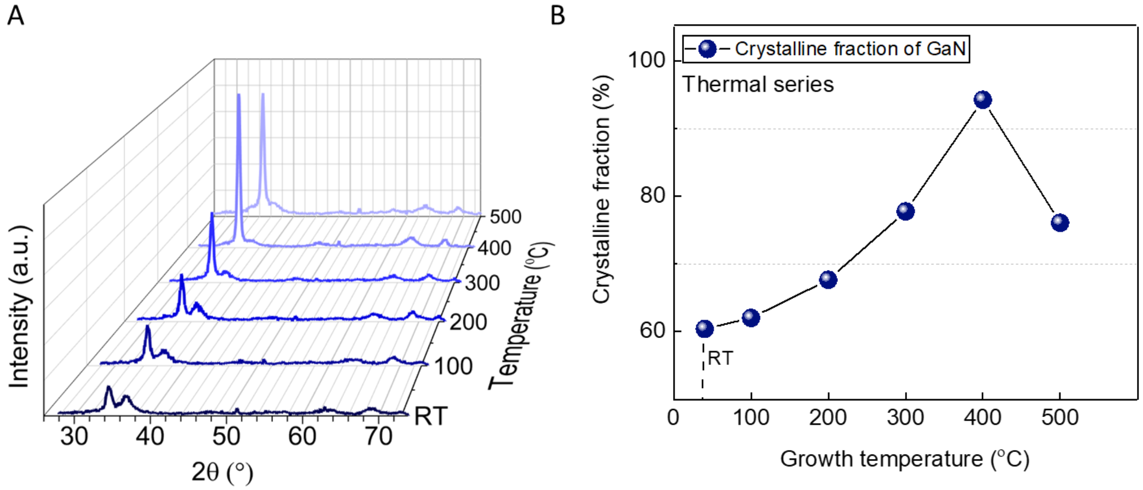

Figure 5.2: A. GIXRD profile at varying growth temperatures from room temperature to 500°C. B. Crystalline fraction calculated from the corresponding GIXRD spectra from A. The working pressure, RF power and the Ar/N_2 flow were kept constant at 6.6 Pa, 100 W and 12/8 sccm respectively.

However, at 500°C, we observe that the F_C decreases which would be the results of the presence of oxygen contaminants as mentioned in the previous section [9], [10]. Another explanation could be related to the strain relaxation of the film while cooling down. Indeed, the large difference in the thermal expansion coefficients between GaN and Si could potentially worsen the strain relaxation process and could induce defects in the crystal lattice that leads to a lower crystalline fraction [11].

Going back to the increase in crystalline fraction as the temperature increases up to 400°C, one could also comment on the energy barriers and reduced contaminants [12]. The additional thermal energy at higher temperatures helps the system to overcome energy barriers that hinder atoms from settling into the crystalline lattice positions. Elevated temperatures can facilitate desorption of impurities or contaminants from the substrate surface, leading to films with fewer defects. However, to verify the effect of elemental contributions to the surface and the bulk of GaN, it requires a better insight of the chemical composition of the films deposited at higher temperatures.

5.1.3 Effect of temperature on the chemical structure

In this subsection, we first analyze the surface chemistry of the GaN film and then proceed with the composition profile within the bulk.

Surface analysis

To begin with, we conducted XPS analysis on the GaN film deposited under optimized sputtering conditions but at 500 °C, specifically at 6.6 Pa, 100 W, and 40% N_2. Figure 5.3 illustrates the XPS spectra spanning the GaN film's surface, commencing from the sample center (point 1) extending to the diagonal edges (point 2). It is important to recall that the color gradients observed in Figure 5.3.A depicts the thickness variation across the surface of the film.

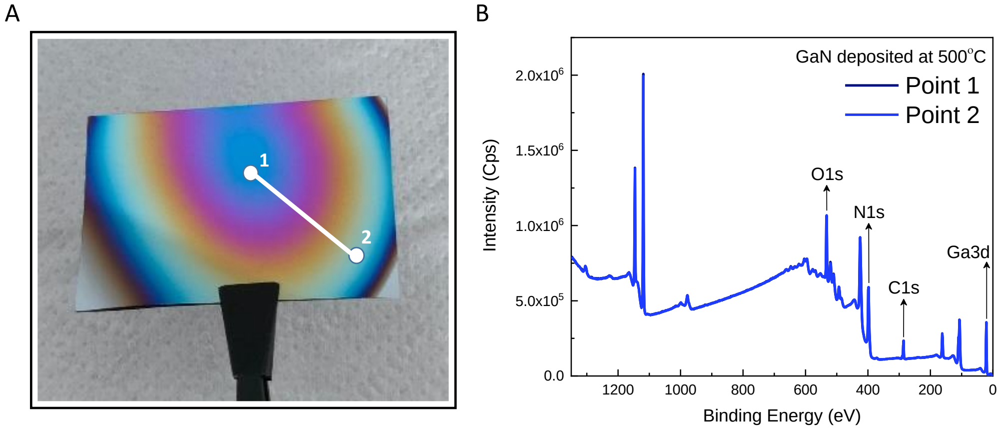

Figure 5.3: A. Real–view image of the GaN on Si. The points 1&2 depicts the line scan for which the XPS surface analysis was done. B. XPS surface scan from the center of the GaN sample to a corner (from 1 to 2). The significant elements from the scan were Ga, N, O and C. Sputtering conditions: 6.6 Pa, 100 W and N_2 ~ 40 % and the growth temperature was kept at 500°C.

In Figure 3.B, the observed color gradient solely reflects a variation on the thickness and not on the composition chemistry as the XPS spectra is identical at points 1 and 2. This implies that increasing the growth temperature does not have any effect on the composition uniformity across the surface of the sample.

Through surface examination, we detect the presence of gallium, carbon, oxygen, and nitrogen in the film. In order to determine the atomic percentages of these elements on the surface, we employed a high-resolution spectrum, necessary to analyze the overlapped signals from nitrogen and the Auger peaks of gallium (Chapter 2).

Figure 5.4 illustrates the high-resolution spectra corresponding to each of the identified elements, C (A), O (B), N (C) and Ga (D), the corresponding table composition is presented in Figure 5.4.E. From the surface spectra in Figure 5.4.A, we observe that the carbon signal, which is attributed to superficial contaminations (Chapter 4), decreases as the growth temperature increases from RT to 500°C. The composition reduces from 18% to 12% at the surface. This could be attributed to an obvious reason - increased desorption of contaminates at elevated temperatures - higher temperatures enhance desorption of adsorbed species from the material's surface [13]. Furthermore, the reduction in carbon content could also be an impact of improved diffusion – elevated temperatures could enhance the diffusion of impurities within the material which may help in moving the carbon atoms away from the surface, thereby reducing the presence of superficial carbon [14]. Following in the footsteps of enhanced desorption or diffusion of superficial elements on the surface at elevated growth temperatures, we could expect that the oxygen contamination also reduce as the growth temperature increases. Surprisingly, we observe that the oxygen concentration (Figure 5.4.E) was not reduced at higher temperature, even though one may expect such phenomenon (efficient outgassing of residual oxygen from the substrate, formation of stronger chemical bonds within the GaN film)[15] . The incorporation of oxygen in the GaN surface slightly varies from 30% to ~ 32% as the temperature increases from RT to 500°C. This suggests that a variation in growth temperature does not have a significant impact on the composition [16].

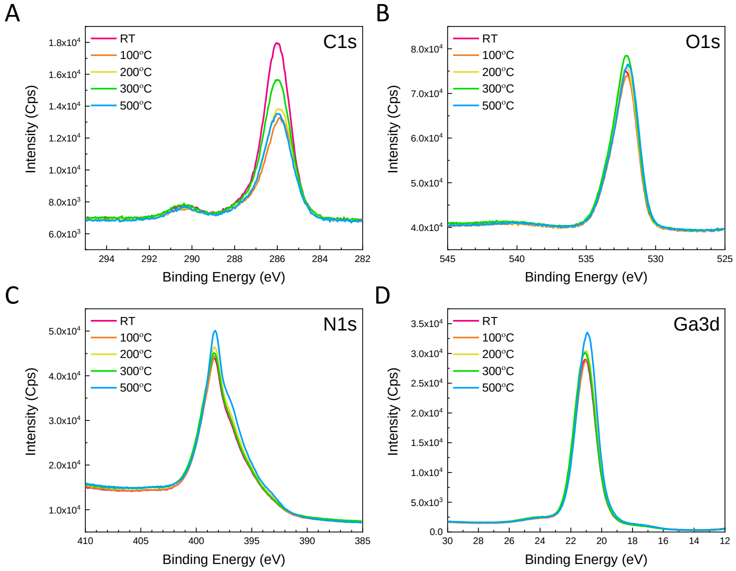

E

HR-Atomic %	RTA	S100	S200	S300	S500
C1s	17.7	12.2	12.8	14.7	12.1
Ga3d	25.7	27.5	27.7	26.4	28.8
N1s	26.0	28.5	27.9	26.1	27.2
O1s	30.6	31.7	31.6	32.8	31.9
O/Ga	1.19	1.15	1.14	1.24	1.11
N/Ga	1.01	1.04	1.01	0.99	0.95
C/Ga	0.69	0.44	0.46	0.56	0.42

Figure 5.4: XPS surface analysis – high-resolution spectra focusing on the binding energy range corresponding to A. Carbon B. Oxygen C. Nitrogen and D. Gallium. The HR spectra gives us an idea on the strength of bonding between the above-mentioned elements. The above used GaN sample was deposited at 6.6 Pa, 100W and N_2 fraction of 40% and the growth temperature was varied. E. The composition percentages calculated from the XPS measurements of the elements at varying growth temperatures.

Figure 5.4.C&D depicts the XPS spectra of N and Ga, respectively. We see that the intensity of the spectra remains almost constant except for the sample deposited at 500°C, which exhibits a slightly intense emission. Nevertheless, in Figure 5.4.E, we observe that the composition variation across different substrate temperatures is minimal, the N and Ga composition almost remaining uniform. The stoichiometry ratio of N/Ga remains within the range of 0.95 to 1.01. The slight increase of the Ga & N composition at 500°C could be attributed to increase in surface migration at the substrate at higher temperatures. To understand the GaN bulk chemistry, we investigate the composition profile of GaN specifically at a moderate growth temperature of 300°C.

Bulk composition profile

Figure 5.5.A represents the composition profile of all the elements for GaN grown at a temperature of 300°C. The mapping of the individual elements throughout the etch profile is represented in Figure 5.5.B-F. Unlike the etch profile observed for room temperature deposited samples (refer chapter 4), the sputtering was conducted until the Si substrate was reached. From Figure 5.5.A, we observe that near the surface (etch time 0 to 100 seconds); the gallium and nitrogen composition uniformly increase by almost 10 %. This could be attributed to the superficial enrichment of gallium and nitrogen, which is an occasional profile measurement artifact from XPS. Therefore, composition values in the bulk ~ 30% for both gallium and nitrogen.

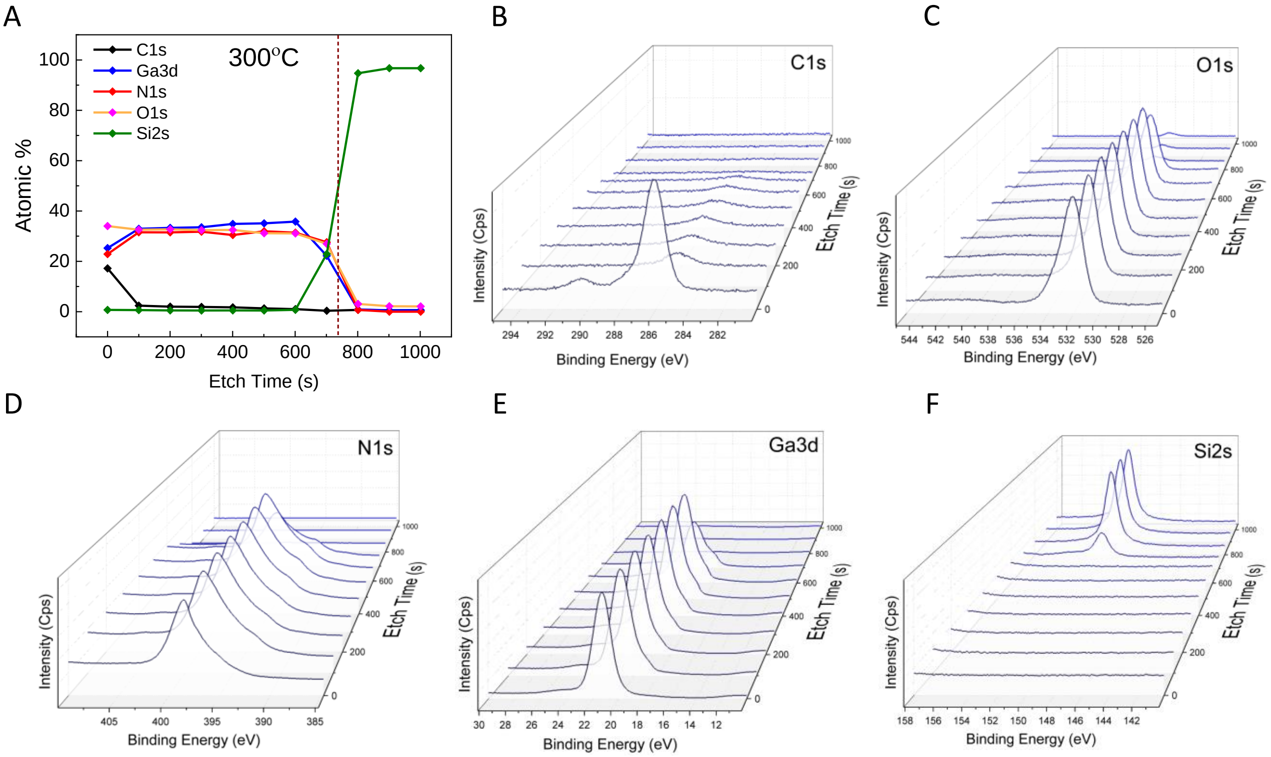

Figure 5.5: A. The composition/ depth profile of GaN thin film on Si deposited at 300°C. B-F. The HR-spectra for each element taken at an interval of 100 seconds for a total etch time of 1000 seconds. The elements are carbon, oxygen, gallium, nitrogen and the substrate silicon respectively in that order. The working pressure, RF power and the Ar/N_2 flow rates were kept constant at 6.6 Pa, 100 W and 12/8 sccm respectively.

Oxygen on the other hand remains consistent from the surface to the bulk and its content is similar to that of gallium and nitrogen ~ 30%. This points out to the fact that increasing the growth temperature does not necessarily reduce the contamination of oxygen in the bulk. Surface contaminants such as carbon do not extend into the bulk (Figure 5.5.B), but oxygen extended from the surface to the bulk down to the interface with the c-Si substrate (Figure 5.5.C). This result undoubtedly shows the presence of a huge amount of oxygen in our samples, independent of the growth temperature. However, this does not necessarily mean that there is no impact of the growth temperature elevation on the quality of the GaN film as we showed previously when it comes to the crystalline fraction that reaches up to 95% at 400°C (.B). To explore the potential impact of the substrate temperature on the defects and optical properties, we investigated the luminescence features of the films.

5.1.4 Impact of growth temperature on the luminescence features of the films

Figure 5.6 shows the CL spectra of GaN films deposited at 200°C, 300°C, 400°C and 500°C. The spectra were measured in the energy range from 1- 4.5 eV. The luminescence peaks appearing at each conditions are evidenced directly in the figure.

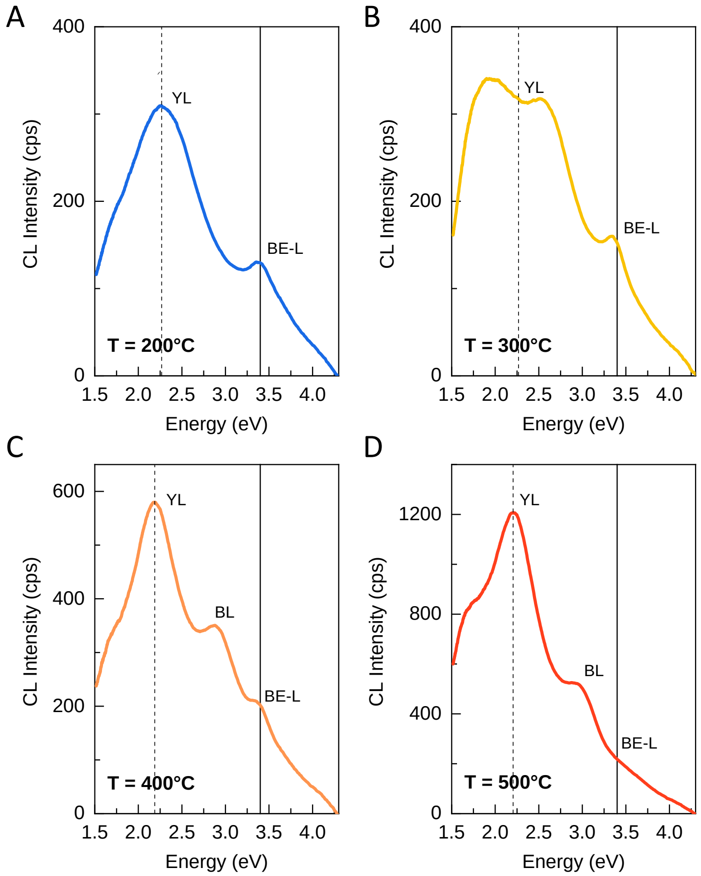

Figure 5.6: Cathodoluminescence (CL) spectra of at varying growth temperatures from 200°C to 500°C (A-D). The working pressure, RF power and the Ar/N_2 flow were kept constant at 6.6 Pa, 100 W and 12/8 sccm respectively.

Overall, the first observation that we can make is the increase in total luminescence intensity as the temperature increases. Let us first consider the case of the samples grown at 200°C, 300°C and 400°C (Figure 5.6.A-C). We see a gradual increase in the intensity of the band-edge luminescence (BE-L) at 3.4 eV (from 150 to 400 counts/s), which could point out to an improved material quality as the growth temperature increases. However, if we observe the YL band, we see that from 200°C to 400°C, the intensity of the YL peak increases almost two fold (from 300 - 600 counts/s). From Chapter 4, we defined the origin of the YL band to defects related to the Ga and O complexes. This would mean that an increase in growth temperature leads to two processes related to defects: i) the donor bound exciton (D^oX) transition is more prominent –the increase in thermal energy leads to an increase in the mobile concentration of energy (i.e. the exciton energy), hence, the luminescence intensity increases. The D^oX transition is associated to deep donor states [17], [18]; ii) enhanced formation of the Ga vacancies and Ga-O complexes – as the temperature increases, the oxygen from the surface associates with the Ga vacancy more rapidly due to an enhanced diffusion. The stable $V_{Ga}O_N$ complexes thus emits the YL band with a higher intensity. The shift of the YL and the BL peaks of GaN at 300°C could be attributed to a residual compressive strain of the film and other confinement effects [17].

Finally, when considering the sample at 500°C (Figure 5.6.D), we notice a significant increase in the YL and the BL peaks and surprisingly, the BE-L at 3.4 eV is missing. We could correlate this with the deposition process itself (increased oxygen contamination at 500°C) and suggest that the increased intensity of the YL and the BL bands could be due to an increase in the point defects arising from vacancies and impurities, which could potentially suggest that this sample is the most defective one [19], [20]. This is in agreement with the GXRD spectra where we observe a decrease in the crystalline fraction at 500°C. Since the BE-L peak is visualized as a shoulder embedded in the strong YL band, a significant increase in the YL band intensity could potentially mask the luminescence from the BE-L band [21].

Overall, from the CL spectra at varying temperatures, we could say that the sample at 400°C has the best BE-L at 3.4 eV. However, this comes at a cost as the YL defect band is also significant here confirming that the oxygen contamination in our sample is significant.

5.2 A summary of the growth temperature series of GaN thin film deposition on Si

In this chapter, we presented the characterization results of GaN films grown by plasma PVD at varying temperatures ranging from room temperature to 500°C. Our aim was to identify the optimum temperature for deposition and analyze the growth features in terms of morphology, growth rate, crystalline fraction, chemical composition and the luminescence. From the morphology study, the surface micrographs revealed nanostructured films with varying grain sizes when the growth temperature increase or decrease. Notably, at 500°C, a distinct flake-like grain structure was observed unlike the other films. Cross-sectional SEM images showed a consistent columnar structure except for the sample deposited at 500°C (flake like structure), suggesting that despite the higher temperature, adatom mobility may not be sufficient to enhance binding among columns. The trends in the growth rate and the surface roughness align with the principles of increased thermal energy as the temperature increases.

In a structural point of view, an increase in the crystalline fraction is operated with rising temperature. The crystallinity of the films improved from 60% at room temperature to about 95% at 400°C. This phenomenon was attributed to the increased temperatures, which imparted greater kinetic energy to the atoms. This increased energy facilitates their movement across the substrate surface, enabling them to attain energetically favorable positions. Consequently, this results in a more organized atomic structure and a decrease in defect formation. However, with the temperature increase from 400°C to 500°C, the crystalline fraction drops from 90% to about 75%. This decrease could potentially be due to an increase in the oxygen contaminant in the plasma during deposition or due to the strain in the lattice while the sample was cooling down post deposition.

As far as the chemical composition of the films is concerned, the increase of the growth temperature does not affect the composition uniformity across the film's surface. The analysis shows a decrease in surface carbon contamination with rising temperatures, which is attributed to enhanced desorption and diffusion of impurities. When it comes to the bulk, C is no present anymore. However, we show that oxygen contamination on the surface as well as in the bulk always occur (up to 30 at%) independently of the growth temperature. Despite the oxygen contamination, the increase in growth temperature is seen to keep the Ga/N stoichiometry intact and could improve the diffusion of elements. What does this mean for defects? The impact of defects caused by contaminants like oxygen on the film's quality was further explored through cathodoluminescence (CL) studies.

Key observations from CL studies included an overall increase in luminescence intensity with rising growth temperatures. Specifically, the BEL at 3.4 eV, which becomes more intense up to 400°C, suggesting improved material quality at higher temperatures, in agreement with the evolution of the crystalline fraction. However, the intensity of the YL peak also significantly increased from 200°C to 400°C, indicating an increase in point defects. This suggests two parallel processes: an increase in D^0X transition (donor bound exciton transition) intensity and enhanced formation of vacancies and Ga-O complexes at higher temperatures. An increase in growth temperature did not have an impact on the peak position of the BE-L as it was almost close to the ideal GaN value of 3.4 eV
Overall, the sample with the best growth rate and the least-surface roughness was the one deposited at 500°C. The GaN film deposited at 400°C exhibited the highest crystalline fraction and most favorable luminescence spectra, suggesting an optimal growth temperature around 400°C. However, while this temperature did not significantly alter the CL features of the films, it underscores the already promising quality of the room temperature (RT) sample, which can be further enhanced through oxygen reduction and additional optimizations. Upon comprehensive examination of the data

presented throughout Chapter 4, a notable technical challenge emerges. The incorporation of a load lock system into the reactor, facilitating deposition without exposure to air between processes, holds promise for significantly enhancing the luminescence spectra of samples. This improvement is anticipated to include a reduction in the YL band intensity, favoring a more pronounced intensity of the BE-L band, even at room temperature.

REFERENCES

[1] E. C. Knox-Davies, J. M. Shannon, and S. R. P. Silva, “The properties and deposition process of GaN films grown by reactive sputtering at low temperatures,” *J. Appl. Phys.*, vol. 99, no. 7, p. 073503, Apr. 2006, doi: 10.1063/1.2186380.

[2] F. Schubert, S. Wirth, F. Zimmermann, J. Heitmann, T. Mikolajick, and S. Schmult, “Growth condition dependence of unintentional oxygen incorporation in epitaxial GaN,” *Sci. Technol. Adv. Mater.*, vol. 17, no. 1, pp. 239–243, Jan. 2016, doi: 10.1080/14686996.2016.1178565.

[3] E. Alfonso, J. Olaya, and G. Cubillos, “Thin Film Growth Through Sputtering Technique and Its Applications,” in *Crystallization - Science and Technology*, M. Andreeta, Ed., InTech, 2012. doi: 10.5772/35844.

[4] C. N. De Carvalho, A. B. Do Rego, A. Amaral, P. Brogueira, and G. Lavareda, “Effect of substrate temperature on the surface structure, composition and morphology of indium–tin oxide films,” *Surf. Coat. Technol.*, vol. 124, no. 1, pp. 70–75, 2000.

[5] M. Einollahzadeh-Samadi and R. S. Dariani, “Effect of substrate temperature and deposition rate on the morphology and optical properties of Ti films,” *Appl. Surf. Sci.*, vol. 280, pp. 263–267, 2013.

[6] Z. Weng, F. Zhang, C. Xu, and J. Zhou, “The effect of incident energy, incident angle and substrate temperature on surface morphology and atomic distribution of NiTi films,” *Mater. Des.*, vol. 187, p. 108350, 2020.

[7] J. A. Thornton, “Structure-zone models of thin films,” in *Modeling of Optical Thin Films*, SPIE, 1988, pp. 95–105.

[8] X.-Y. Li *et al.*, “Effect of substrate temperature on the structural and optical properties of ZnO and Al-doped ZnO thin films prepared by dc magnetron sputtering,” *Opt. Commun.*, vol. 282, no. 2, pp. 247–252, 2009.

[9] G. C. Hua, N. Otsuka, W. Xie, D. C. Grillo, M. Kobayashi, and R. L. Gunshor, “Growth and Characterization of ZnSe/ZnCdSe Diode Structures on (In, Ga)As Buffer Layers,” *MRS Proc.*, vol. 242, p. 221, 1992, doi: 10.1557/PROC-242-221.

[10] M. Zajac *et al.*, “Basic ammonothermal growth of Gallium Nitride – State of the art, challenges, perspectives,” *Prog. Cryst. Growth Charact. Mater.*, vol. 64, no. 3, pp. 63–74, Sep. 2018, doi: 10.1016/j.pcrysgrow.2018.05.001.

[11] A. Bourret, C. Adelmann, B. Daudin, J.-L. Rouvière, G. Feuillet, and G. Mula, “Strain relaxation in (0001) AlN/GaN heterostructures,” *Phys. Rev. B*, vol. 63, no. 24, p. 245307, Jun. 2001, doi: 10.1103/PhysRevB.63.245307.

[12] K. M. Tracy, W. J. Mecouch, R. F. Davis, and R. J. Nemanich, “Preparation and characterization of atomically clean, stoichiometric surfaces of n-and p-type GaN (0001),” *J. Appl. Phys.*, vol. 94, no. 5, pp. 3163–3172, 2003.

[13] C. H. Seager, A. F. Wright, J. Yu, and W. Götz, “Role of carbon in GaN,” *J. Appl. Phys.*, vol. 92, no. 11, pp. 6553–6560, 2002.

[14] J. Falta *et al.*, “Cleaning and growth morphology of GaN and InGaN surfaces,” *Phys. Status Solidi B*, vol. 248, no. 8, pp. 1800–1809, Aug. 2011, doi: 10.1002/pssb.201046574.

[15] G. A. Slack, L. J. Schowalter, D. Morelli, and J. A. Freitas Jr, “Some effects of oxygen impurities on AlN and GaN,” *J. Cryst. Growth*, vol. 246, no. 3–4, pp. 287–298, 2002.

[16] D. Majchrzak, M. Grodzicki, P. Ciechanowicz, J. G. Rousset, E. Piskorska-Hommel, and D. Hommel, “The influence of oxygen and carbon contaminants on the valence band of p-GaN (0001),” *Acta Phys Pol A*, vol. 136, pp. 585–588, 2019.

[17] F. B. Nasr, A. Matoussi, R. Salh, S. Guermazi, H.-J. Fitting, and Z. Fakhfakh, “Cathodoluminescence study of undoped GaN films: Experiment and calculation,” *Phys. E Low-Dimens. Syst. Nanostructures*, vol. 41, no. 3, pp. 454–459, 2009.

[18] A. Alemu, B. Gil, M. Julier, and S. Nakamura, “Optical properties of wurtzite GaN epilayers grown on A-plane sapphire,” *Phys. Rev. B*, vol. 57, no. 7, p. 3761, 1998.

[19] R. Armitage *et al.*, “Contributions from gallium vacancies and carbon-related defects to the ‘yellow luminescence’ in GaN,” *Appl. Phys. Lett.*, vol. 82, no. 20, pp. 3457–3459, 2003.

[20] J. Lähnemann, U. Jahn, O. Brandt, T. Flissikowski, P. Dogan, and H. T. Grahn, “Luminescence associated with stacking faults in GaN,” *J. Phys. Appl. Phys.*, vol. 47, no. 42, p. 423001, 2014.

[21] M. A. Reshchikov, “On the Origin of the Yellow Luminescence Band in GaN,” *Phys. Status Solidi B*, vol. 260, no. 8, p. 2200488, Aug. 2023, doi: 10.1002/pssb.202200488.

Summary & perspectives

Summary

The collaborative research from this doctoral thesis explored Plasma-based Physical Vapor Deposition (PVD) as a promising alternative to conventional methods such as MOCVD and MBE. Low-temperature processing reduces challenges like thermal mismatch-induced strain, caters to temperature-sensitive applications, and reduces energy consumption. From an ecological standpoint, plasma-assisted growth methods offer advantages in terms of reduced material consumption and waste production. The utilization of plasma allows for precise control over deposition parameters, leading to higher material utilization efficiency and minimizing the generation of harmful byproducts. Additionally, the absence of toxic precursor gases commonly associated with conventional techniques reduces environmental impact and potential health hazards. On the economic front, plasma-assisted growth methods can offer cost savings over time. Improved material utilization and reduced energy consumption translate into lower operational costs and increased productivity. Additionally, the ability to deposit high-quality films at lower temperatures can extend the lifespan of equipment and reduce maintenance expenses.

The introductory chapter discussed on three important aspects relevant to the context of this thesis: i) properties and importance of GaN, ii) the deposition processes, iii) low pressure plasmas for deposition. **Chapter 2** focused on the plasma PVD process and introduced the custom-built reactor system and its functionalities. Several ex-situ solid-state characterization techniques were elaborated which were used to examine the quality of the GaN thin films.
Chapter 3 provided an extensive overview of three plasma diagnostic methodologies employed to characterize our Ar/N_2 plasma: Two-Photon Absorption Laser-Induced Fluorescence (TALIF), Microwave Interferometry (MWI), and Optical Emission Spectroscopy (OES). Each technique targeted a specific plasma characteristic, serving as valuable tools in our analysis. TALIF was utilized to ascertain the absolute N atom density, despite encountering challenges posed by the low-intensity N fluorescence signal characteristic of the low-pressure conditions at which our plasma discharge operates. We employed a Peak Excitation Method (PEM) to determine the absolute atomic density, enabling us to focus solely on temporally integrated fluorescence signals, thereby neglecting the quenching rate's influence. Notably, we found that the measured N-atom density ranges from approximately 10^{11} to 10^{12} cm^{-3}. MWI served to determine the electron density within the discharge, revealing values typically ranging from 10^{10} to 10^{11} cm^{-3}. Comparing density measurements from TALIF and MWI aids in characterizing plasma attributes across varying working pressures, with electron and N atom densities showing similar dependence upon process parameters. In terms of qualification, OES served a dual purpose: identifying trends in emissive species concerning process conditions and monitoring efficient sputtering of Ga-atoms. Additionally, OES facilitated the detection of oxygen-based contaminants (OH) in the plasma, crucial for mitigating potential detrimental effects on the growth process. Introducing a plasma and reactor cleaning solution helped to alleviate contamination impacts on the films. Another important use of OES was to determine the plasma characteristic temperatures. While rotational temperature measurements provide a reliable estimate of gas temperature (~450 K), direct determination of electron temperature proved challenging. Alternative measurements, such as vibrational and excitation temperatures, yielded estimates ranging from 2000 K to 8000 K and approximately 4000 K, respectively. The comprehensive plasma qualification undertaken at various growth pressures laid the groundwork for subsequent thin film characterization under these process conditions.

In **chapter 4**, we meticulously analyzed the influence of working pressure, N_2 flow variation, and RF power on key film characteristics - morphology, growth rate, and crystalline structure. Through a deep analysis, we navigated the intricate parameter space, endeavoring to uncover optimal conditions conducive to superior GaN film quality.
Our quest for optimization lead us to the identification of a paramount sputtering set of parameters characterized, i.e. a pressure of6.6 Pa, 60%/40% Ar/N_2 fraction, and 100W RF power. Within this regime, GaN films manifested a hexagonal wurtzite crystalline structure, exhibiting a growth rate of ~ 2 Å/s and a crystalline fraction of ~ 60%. This

optimized condition represented a pivotal milestone in our journey, laying the groundwork for enhanced GaN film fabrication processes. Moreover, our exploration extended beyond mere parameter optimization, delving into the underlying mechanisms governing film growth. Introducing two important plasma parameters - the Ga atom flux (φ_{Ga}) and average Ga atom energy at the substrate ($\overline{E_{Ga}^{sub}}$) - we unveiled their profound impact on the GaN film properties. The φ_{Ga} emerged as a reliable indicator of growth rate trends, offering valuable insights into sputtering dynamics. It was found that the growth rate estimated through calculations was in good agreement with the experiments (~ 2.4 Å/s), highlighting the validity of our method. Concurrently, $\overline{E_{Ga}^{sub}}$ emerged as a potent determinant of crystalline quality, elucidating the relationship between energy deposition and film structure. Beyond the domain of process parameters, our analysis extended to the chemical composition of GaN films, shedding light on intrinsic and extrinsic factors influencing film quality. While Ga and N constituted the primary constituents, our investigation unearthed the presence of contaminants—carbon, hydrogen, and notably, oxygen. Oxygen, in particular, emerged as a significant impurity, with its incorporation posing challenges to film integrity and performance. To mitigate oxygen contamination and enhance film quality, we employed a multifaceted approach, encompassing target cleaning using Ar plasma and reactor cleaning procedures. Leveraging techniques such as Glow Discharge Optical Emission Spectroscopy (GD-OES), we traced and to an extent rectified oxygen-induced anomalies, culminating in a substantial reduction in oxygen composition from ~ 30% to ~ 13% within the GaN film. Further insights into film properties are gleaned through advanced characterization techniques, including Transmission Electron Microscopy (TEM) and Cathodoluminescence (CL). TEM analysis unveiled an ordered atomic stacking of GaN planes, confirming the polycrystalline nature of the films. Concurrently, CL studies provided a perception into the distinctive luminescence profiles of GaN films, thereby giving insights into their optical properties and defect characteristics. Notably, the presence of specific luminescence bands (Red (RL), yellow (YL), aquamarine (AL), blue (BL) and band-edge (BE-L) luminescence) reflected the prevailing growth conditions, with Ga-rich environments favoring the emergence of certain intrinsic point defects associated with the RL and the AL bands. Operating at room temperature and utilizing silicon substrates, our study scrutinized the intricate interplay between process parameters and resultant film properties, unraveling critical insights poised to redefine GaN film fabrication.

In **chapter 5**, we had examined the characteristics of GaN films across a spectrum of substrate temperatures, ranging from room temperature to 500^{o}C. Our objective was to discern the most favorable deposition temperature while examining various aspects usinf the same methodology as presented in chapter 4. Microscopic analysis of the surface morphology unveiled nanostructured films exhibiting diverse grain sizes dependent upon the deposition temperature. Particularly noteworthy was the emergence of a distinct flake-like grain structure at 500^{o}C, contrasting with other temperature regimes. Despite the elevated temperature, cross-sectional SEM imaging depicted a consistent columnar architecture as that of the sample grown at RT, implying that adatom mobility might not be sufficient to foster inter-column binding. The growth rate exhibited a direct correlation with rise in temperature, indicative of enhanced adatom mobility, while surface roughness exhibited a converse trend owing to reduced surface diffusion barriers, aligning with principles of increased thermal energy. X-ray diffraction analysis revealed an increasing crystalline fraction when temperature increases, up to 400^{o}C, beyond which a decline was observed. This decline could potentially be ascribed to heightened oxygen contamination or lattice strain during post-deposition cooling. XPS analysis elucidated surface chemistry uniformity across varying temperatures, with a reduction in carbon contamination noted at higher temperatures, attributable to enhanced impurity desorption. Oxygen contamination, however, remained invariant.

Cathodoluminescence studies underscored an overall enhancement in luminescence intensity with temperature elevation, albeit accompanied by an increase in point defects. The peak position of the BE-L remained stable across temperatures, underscoring the reliability of GaN film deposition. In summary, while the GaN film deposited at 500^{o}C exhibited superior growth kinetics and surface characteristics, the film fabricated at 400^{o}C demonstrated optimal crystalline integrity and luminescence properties, indicative of its superior quality. Hence, we propose that the optimal growth temperature for GaN film deposition lies around 400^{o}C.

In summary, this work offers a comprehensive exploration of the challenges, techniques, and progress towards the low-temperature deposition of GaN thin films using Plasma PVD, providing concrete insights into its optimization and control.

Perspectives

The current thesis highlights the work done towards the deposition of GaN films by plasma PVD at LPICM. The final chapter focused on the effect of 'substrate temperature' parameter and the analysis was based on how good the GaN film quality was in terms of structural, optical, morphological and chemical properties. However, a complete investigation on the influence of substrate temperature is still pending. Building on this premise, the first perspective would be thoroughly analyzing the impact of substrate temperature on the GaN film quality but having as ultimate goal of low temperature deposition.

Overall, several area of improvement have progressively emerged during this thesis. For instance, if we focus on the betterment of the reactor system, we build on finding potential solutions to current problems such as the high level of oxygen contamination (~ 30%) in the thin film. The obvious solution here is to implement a load-lock system, which prevents the reaction chamber and the Ga target to be exposed to the atmosphere between successive depositions. Another solution to mitigate oxygen contamination would be to introduce hydrogen (H_2) in the reactor chamber. The highly reactive hydrogen species can chemically react with oxygen-containing compounds, transforming them down into simpler molecules (H_2O) [1], [2], which could potentially help to remove oxygen contaminants from the chamber walls, surfaces, and vacuum system [3], [4]. Currently, we have already installed the hydrogen lines in our plasma PVD reactor and some initial tests are ongoing.

Focusing on the current findings from this research, we have obtained polycrystalline GaN at room temperature. An important question arises on what can be done using such thin films and which applications to target? In terms of photovoltaics, there have been a few works, where they use polycrystalline GaN thin films to serve as an electron transport layer (ETL) for perovskite solar cells [5], [6]. The emphasis is mainly on low temperature process here as the GaN layers had been deposited on fluorine-doped tin oxide (FTO) which is thermally sensitive. The use of GaN as an ETL enhanced the efficiency of the solar cells from 10% to ~ 15%.

In microelectronics, polycrystalline GaN have been used in thin film transistors with bottom gate configuration on sapphire substrates which exhibits n-type field effect characteristics. The entire TFT device fabrication process temperature was below 250°C for this process [7]. Our work could pave way for TFTs with an even lower thermal budget.

Another field of application, which has often been scarcely explored in terms of GaN, is electrochemical detection and sensing. Porous polycrystalline GaN layers grown by MOCVD at "low-temperatures (600°C)" has been employed for catalyst-free electrochemical detection of H_2O_2 [8]. The emphasis was based on low temperature growth since it can generate rich N-vacancies, which greatly improves the catalytic activity and electrical conductivity of the material. Although, this work does not provide much information about Ga and N vacancies or in terms of electrical conductivity, the low-temperature growth with high levels of crystallinity could still be an interesting avenue to explore in terms of sensing. This also facilitates the need for a thorough electrical characterization of our thin films.

As the current applications related to pc-GaN are limited, the focus shifts towards ways to improve the film quality, i.e. potential epitaxy of GaN which has a plethora of applications ranging from light-emitting diodes (LEDs), laser diodes (LDs), power electronics and RF devices such as amplifiers, switches and oscillators [9], [10]. The perspective to build upon is how to obtain high quality epitaxial growth of GaN from the current results. The area to explore would be to mitigate the effects due to defects present in our thin films which stems from impurities and threading dislocations [11], [12], which arises from lattice mismatched substrates such as Si. Potential explorations include investigating the homoepitaxy of GaN or the growth of GaN on lattice matched buffer layers over Si substrates such as aluminum nitride (AlN) and silicon nitride (SiN) using low temperature plasma PVD. An interesting route within this context would be to explore nitrogen mediated crystallization of GaN films deposited on Si [13]. Generally, during deposition, the influx of numerous high-energy particles toward the substrate promotes the formation of densely packed and randomly oriented nuclei during the initial phase of deposition. This phenomenon could potentially lead to a decrease in grain size and the development of large crystal mosaics. Conversely, with the nitrogen-mediated crystallization method, the nucleation density can be diminished as nitrogen atoms adsorbed on the growth surface interfere with the crystallization process of GaN. Consequently, GaN films tend to exhibit well-aligned crystal orientation and possess relatively larger grain sizes.

An extension of reactor improvement would be to use it for the deposition of other important materials such as Ga_2O_3 and III-V materials such as GaAs. Owing to the ever-present oxygen in our reactor system, its use can be modified if we stop treating it as a contaminant and treat it as a precursor material. Take the case of gallium oxide (Ga_2O_3). This material has several important uses across various fields such as power electronics, optoelectronics and gas sensing. Ga_2O_3 is highly attractive for power electronic devices due to its wide bandgap (~4.5 eV), which enables operation at high voltages and temperatures [14]. It can be used in the fabrication of high-power, high-frequency transistors, diodes, and rectifiers for applications like electric vehicles, renewable energy systems, and power grid infrastructure. The wide bandgap of Ga_2O_3 also makes it suitable for optoelectronic applications such as UV photodetectors, solar-blind photodetectors, and transparent conductive coatings for UV optoelectronic devices [15]. It can be used in gas sensors for detecting harmful gases like hydrogen, carbon monoxide, and nitrogen dioxide. Its high surface-to-volume ratio and ability to interact with gas molecules make it a promising material for environmental monitoring, industrial safety, and healthcare applications.

Focusing on the III-V group materials, GaAs is an important semiconductor in the photovoltaic industry and has paved way towards record breaking solar cell conversion efficiency [16]. The practicality of using such a semiconductor has drastically increased ever since the research on III-V/Si tandems boomed [17]. What could be interesting from the perspective of a GaAs PVD deposition is to give equal weightage towards plasma characterization using similar diagnostic techniques such as ours and potentially construct a parametric investigation of GaAs deposition on suitable substrates at low temperatures by plasma PVD.

Overall, the work presented in this doctoral thesis on thin film and plasma characterization of GaN films at low temperatures paves way to explorations related to several important aspects that are currently necessary towards obtaining high quality GaN thin films towards applications such as power electronics, photovoltaics and even electrochemical sensing, which are all in some way or the other associated with the semiconductor industry that strives towards improving the technology for the 21st century.

REFERENCES

[1] R. E. Thomas, M. J. Mantini, R. A. Rudder, D. P. Malta, S. V. Hattangady, and R. J. Markunas, "Carbon and oxygen removal from silicon (100) surfaces by remote plasma cleaning techniques," *J. Vac. Sci. Technol. Vac. Surf. Films*, vol. 10, no. 4, pp. 817–822, 1992.

[2] L. Oren and R. J. Taylor, "Trapping and removal of oxygen in tokamaks," *Nucl. Fusion*, vol. 17, no. 6, p. 1143, 1977.

[3] A. Belkind and S. Gershman, "Plasma cleaning of surfaces," *Vac. Coat. Technol. Novemb.*, pp. 46–57, 2008.

[4] F. Waelbroeck, J. Winter, and P. Wienhold, "Cleaning and conditioning of the walls of plasma devices by glow discharges in hydrogen," *J. Vac. Sci. Technol. Vac. Surf. Films*, vol. 2, no. 4, pp. 1521–1536, 1984.

[5] H. Wei *et al.*, "Plasma-enhanced atomic-layer-deposited gallium nitride as an electron transport layer for planar perovskite solar cells," *J. Mater. Chem. A*, vol. 7, no. 44, pp. 25347–25354, 2019, doi: 10.1039/C9TA08929B.

[6] P. Qiu *et al.*, "Plasma-enhanced atomic layer deposition of gallium nitride thin films on fluorine-doped tin oxide glass substrate for future photovoltaic application," *Ceram. Int.*, vol. 46, no. 5, pp. 5765–5772, Apr. 2020, doi: 10.1016/j.ceramint.2019.11.026.

[7] S. Bolat, C. Ozgit-Akgun, B. Tekcan, N. Biyikli, and A. K. Okyay, "Low temperature thin film transistors with hollow cathode plasma-assisted atomic layer deposition based GaN channels," *Appl. Phys. Lett.*, vol. 104, no. 24, 2014, Accessed: Feb. 20, 2024. [Online]. Available: https://pubs.aip.org/aip/apl/article-abstract/104/24/243505/385128

[8] S. Chen *et al.*, "Direct Growth of Polycrystalline GaN Porous Layer with Rich Nitrogen Vacancies: Application to Catalyst-Free Electrochemical Detection," *ACS Appl. Mater. Interfaces*, vol. 12, no. 48, pp. 53807–53815, Dec. 2020, doi: 10.1021/acsami.0c15824.

[9] K. J. Chen *et al.*, "GaN-on-Si power technology: Devices and applications," *IEEE Trans. Electron Devices*, vol. 64, no. 3, pp. 779–795, 2017.

[10] T. J. Flack, B. N. Pushpakaran, and S. B. Bayne, "GaN Technology for Power Electronic Applications: A Review," *J. Electron. Mater.*, vol. 45, no. 6, pp. 2673–2682, Jun. 2016, doi: 10.1007/s11664-016-4435-3.

[11] X. J. Ning, F. R. Chien, P. Pirouz, J. W. Yang, and M. A. Khan, "Growth defects in GaN films on sapphire: The probable origin of threading dislocations," *J. Mater. Res.*, vol. 11, no. 3, pp. 580–592, 1996.

[12] A. Sakai, H. Sunakawa, and A. Usui, "Defect structure in selectively grown GaN films with low threading dislocation density," *Appl. Phys. Lett.*, vol. 71, no. 16, pp. 2259–2261, 1997.

[13] N. Itagaki *et al.*, "Crystallinity control of sputtered ZnO films by utilizing buffer layers fabricated via nitrogen mediated crystallization: Effects of nitrogen flow rate," in *International Conference on Plasma Surface Engineering*, 2012, pp. 84–87. Accessed: Feb. 20, 2024. [Online]. Available: https://wcc.ep.liu.se/index.php/PSE/article/view/398

[14] M. Higashiwaki, K. Sasaki, A. Kuramata, T. Masui, and S. Yamakoshi, "Development of gallium oxide power devices," *Phys. Status Solidi A*, vol. 211, no. 1, pp. 21–26, Jan. 2014, doi: 10.1002/pssa.201330197.

[15] N. S. Jamwal and A. Kiani, "Gallium oxide nanostructures: A review of synthesis, properties and applications," *Nanomaterials*, vol. 12, no. 12, p. 2061, 2022.

[16] M. Bosi and C. Pelosi, "The potential of III-V semiconductors as terrestrial photovoltaic devices," *Prog. Photovolt. Res. Appl.*, vol. 15, no. 1, pp. 51–68, Jan. 2007, doi: 10.1002/pip.715.

[17] H. Liu, Z. Ren, Z. Liu, A. G. Aberle, T. Buonassisi, and I. M. Peters, "The realistic energy yield potential of GaAs-on-Si tandem solar cells: a theoretical case study," *Opt. Express*, vol. 23, no. 7, pp. A382–A390, 2015.

Scientific contributions

Publications

1. Lakshman Srinivasan, Cyril Jadaud, François Silva, Jean-Charles Vanel, Jean-Luc Maurice, Erik Johnson, Pere Roca i Cabarrocas, Karim Ouaras; **Reactive plasma sputtering deposition of polycrystalline GaN thin films on silicon substrates at room temperature.** *J. Vac. Sci. Technol. A* 1 September 2023; 41 (5): 053407. https://doi.org/10.1116/6.0002718

2. Lakshman Srinivasan, Laurent Invernizzi, Swaminathan Prasanna, Kristaq Gazeli, Nicolas Fagnon, Pere Roca i Cabarrocas, Guillaume Lombardi, Karim Ouaras; **Nitrogen atoms absolute density measurement using two-photon absorption laser induced fluorescence in reactive magnetron discharge for gallium nitride deposition.** *Appl. Phys. Lett.* 4 March 2024; 124 (10): 104101. https://doi.org/10.1063/5.0192748

3. Lakshman Srinivasan, Kristaq Gazeli, Swaminathan Prasanna, Pere Roca i Cabarrocas, Guillaume Lombardi, Karim Ouaras; **Gallium Nitride Deposition via Sputtering: Linking Plasma-Surface Interactions and Thin Film Crystalline Features.** Submitted to **Vacuum.** February 16, 2024.

4. Lakshman Srinivasan, Jean-Luc Maurice, Stefano Pirotta, Stéphane Collin, Pere Roca i Cabarrocas, Karim Ouaras; **Room Temperature Plasma Sputtering Enabling Growth of Luminescent GaN thin films on Si substrates.** (Under finalization).

5. Lakshman Srinivasan, Kristaq Gazeli, Swaminathan Prasanna, Pere Roca i Cabarrocas, Guillaume Lombardi, Karim Ouaras; **Plasma temperature & density characterization in an Ar/N_2 discharge: underlying process, control and optimization of GaN thin film growth via reactive sputtering.** (Under finalization).

6. Lakshman Srinivasan, Jean-Luc Maurice, Pere Roca i Cabarrocas, Karim Ouaras; **Influence of the process parameters on the structure and morphology of polycrystalline GaN thin films deposited at room temperature by Reactive Plasma Sputtering.** (Under preparation).

Conferences

1. Lakshman Srinivasan, Pere Roca i Cabarrocas, Karim Ouaras; Plasma enhanced physical vapor deposition of III-V materials (GaN); **GDR Emili** plasma conference, 2021 (poster).

2. Lakshman Srinivasan, Pere Roca i Cabarrocas, Karim Ouaras; Plasma enhanced physical vapor deposition of III-V materials (GaN); **Journees Nationales du Photovoltaique (JNPV)** 2021, (poster).

3. Lakshman Srinivasan, Pere Roca i Cabarrocas, Karim Ouaras; Plasma enhanced physical vapor deposition of polycrystalline GaN thin films at low temperature; **European conference on crystal growth (ECCG7)**, 2022 (oral).

4. Lakshman Srinivasan, Cyril Jadaud, François Silva, Jean-Charles Vanel, Jean-Luc Maurice, Erik Johnson, Pere Roca i Cabarrocas, Karim Ouaras; Plasma enhanced PVD of GaN at low temperature; **World conference on photovoltaic energy (WCPEC) 2022** (poster).

5. Lise Watrin, Lakshman Srinivasan, F. Silva, C. Jadaud, P. Bulkin, J-C. Vanel, E.V.Johnson, K.Ouaras, Pere Roca i Cabarrocas; Low temperature plasma deposition processes for GaN thin films; **International conference on amorphous and nanocrystalline semiconductors (ICANS30)** August 2024 (to come)

ECOLE
DOCTORALE

Titre : Dépôt plasma à basse température de semi-conducteurs III-V (GaN) sur Si

Mots clés : nitrure de gallium, plasma, sputtering, polycristalline, spectroscopie, III-V semiconducteur.

Résumé : L'importance du dépôt de couches minces de Nitrure de Gallium (GaN) sur des substrats de silicium à des températures réduites (< 500°C) découle de la demande croissante de l'industrie des semi-conducteurs pour atténuer les inconvénients associés au traitement à haute température, tels que la diffusion d'atomes et les contraintes mécaniques dues à l'incompatibilité thermique entre le film et le substrat. En effet, les méthodes conventionnelles comme la MOCVD (Metal Organic Chemical Vapor Deposition) et la MBE (Molecular Beam Epitaxy) impliquent généralement des températures élevées, ce qui peut entraîner des défauts structurels et une dégradation des dispositifs. Ainsi, la recherche de méthodes alternatives de dépôt à basse température devient cruciale pour améliorer l'intégrité des dispositifs électroniques et optoélectroniques à base de GaN.
Cette thèse, réalisée en collaboration avec le LPICM et l'IPVF, explore une méthodologie de croissance à basse température pour le dépôt de GaN. Elle se concentre sur le Dépôt Physique en Phase Vapeur (PVD) assisté par plasma (pulvérisation) basé sur un magnétron (RF), qui se présente comme une voie prometteuse pour contourner les limitations des techniques de croissance traditionnelles. Le réacteur PVD-plasma, récemment développé au LPICM, est conçu pour explorer le dépôt de semi-conducteurs III-V à faible coût par plasma, rendant ce projet un nouvel axe de recherche novateur au laboratoire.
Ce travail repose sur une approche méthodologique systématique, intégrant la compréhension des processus de dépôt en couplant les diagnostics plasma, la caractérisation des matériaux et les stratégies d'optimisation de la croissance des films de GaN à température ambiante (RT). Les diagnostics plasma ont été déployés pour analyser le plasma Ar-N_2 utilisé. La décharge de plasma a été caractérisée par des techniques avancées telles que la spectroscopie d'émission optique (OES), la fluorescence induite par laser à deux photons (TALIF) et l'interférométrie micro-ondes (MWI). Ces techniques ont permis d'obtenir des paramètres cruciaux liés aux températures et à la densité du plasma, fournissant une compréhension approfondie des mécanismes de dépôt. Les données obtenues ont permis d'estimer deux paramètres critiques pour la croissance : le flux des atomes de Ga pulvérisés et leur énergie moyenne au niveau du substrat. Cette estimation a facilité l'étude de l'interaction entre les caractéristiques du plasma et les propriétés des films de GaN déposés, telles que le taux de croissance et la fraction cristalline. La caractérisation des films minces de GaN, déposés à température ambiante, a été réalisée à l'aide de techniques variées telles que la microscopie électronique à balayage (SEM), la microscopie à force atomique (AFM), la diffraction des rayons X en incidence rasante (GIXRD), la spectroscopie de photoélectrons X (XPS) et la cathodoluminescence (CL).
Parmi les résultats notables, nous avons obtenu des couches minces de GaN polycristallin de structure wurtzite hexagonale avec des taux de croissance de ~ 2 Å/s et des fractions cristallines de ~ 60 % dans des conditions de pulvérisation optimisées : une pression de travail de 6,6 Pa, un ratio de 60/40 % Ar/N_2 et une puissance RF de 100 W. En outre, l'influence de ces paramètres a été systématiquement étudiée, mettant en évidence leur rôle crucial dans les propriétés morphologiques, structurales et optiques des films déposés.
Il a été démontré que la vitesse de croissance estimée par les calculs (~ 2,4 Å/s) concordait bien avec celle déterminée expérimentalement, confirmant l'efficacité de notre méthode. De plus, nous avons montré que l'énergie moyenne des atomes de Ga au substrat est corrélée avec la fraction cristalline des films de GaN déterminée expérimentalement. Une étude approfondie de l'influence de la température du substrat (de RT à 500°C) a révélé le rôle essentiel de l'énergie thermique dans l'amélioration de la mobilité des atomes déposés et de la qualité cristalline, la meilleure fraction cristalline de près de ~ 95% étant obtenue à une température de substrat de 400°C.
Globalement, cette thèse, essentiellement expérimentale, a permis de mieux comprendre les défis, les méthodologies et les progressions qui sous-tendent le traitement à basse température des films minces de GaN par PVD-plasma. Elle offre des aperçus concrets sur l'optimisation et le contrôle de la qualité du dépôt, ouvrant ainsi la voie à des développements futurs dans le domaine des semi-conducteurs à basse température. En intégrant des diagnostics plasma avancés et des techniques de caractérisation sophistiquées, ce travail contribue à l'avancement des connaissances et des technologies dans le domaine du dépôt de GaN, avec des implications significatives pour l'industrie des semi-conducteurs.

Title : Low temperature plasma deposition of III-V semiconductors (GaN) on Si

Keywords : Gallium Nitride, plasma, sputtering, polycrystalline, spectroscopy, III-V semiconductors.

Abstract : The importance of the deposition of Gallium Nitride (GaN) thin films on Silicon substrates at reduced temperatures (< 500°C) stems from the increasing demand of the semiconductor industry in mitigating inherent drawbacks associated with high-temperature processing arising from the thermal mismatch between the film and the substrate. This doctoral thesis, done at LPICM in collaboration with IPVF, undertakes a comprehensive exploration of a low-temperature processing methodology, focusing on Plasma based Physical Vapor Deposition (PVD) as a promising avenue for circumventing the constraints of conventional growth techniques such as MOCVD and MBE. The newly custom-built plasma PVD reactor paves way to explore low-cost III-V deposition by plasma, which is a novel topic at the lab. The work delineates a systematic approach encompassing deposition processes, plasma diagnostics, material characterization, and growth optimization strategies for GaN films deposited at room temperature (RT). Plasma diagnostics play a pivotal role when investigating the intricate nuances of Ar-N_2 plasmas used in the deposition process. The plasma discharge is characterized via optical emission spectroscopy (OES), two-photon absorption laser-induced fluorescence (TALIF), and microwave interferometry (MWI) to obtain parameters related to plasma temperatures and density. From the plasma diagnostics, two important parameters were estimated - the flux of the sputtered Ga atoms (φ_{Ga}) and their average energy at the substrate ($\overline{E_{Ga}^{sub}}$). This allowed us to address the interplay between plasma characteristics and GaN film properties such as their growth rate and crystalline fraction. The assessment of GaN thin films deposited at room temperature was done using characterization techniques such as SEM, AFM & GIXRD, XPS and Cathodoluminescence (CL).
Noteworthy findings include the successful growth of hexagonal wurtzite polycrystalline GaN exhibiting growth rates of ~ 2 Å/s and crystalline fractions of ~ 60% at an optimized sputtering condition (6.6 Pa, 40% N_2 and 100 W), elucidating the profound influence of process parameters such as the working pressure, RF power and the N_2 flow rate on the morphological, structural & optical properties. It was found that the growth rate estimated through calculations (~ 2.4 Å/s) was in good agreement with experiments, highlighting the validity of our method. Similarly, $\overline{E_{Ga}^{sub}}$ of Ga correlated well with the crystalline fraction of the GaN films. Further investigation into the influence of substrate temperature from RT to 500°C emphasized the role of thermal energy in enhancing adatom mobility and crystalline quality with the best crystalline fraction of almost ~ 95% obtained at a substrate temperature of 400°C. Overall, this doctoral thesis provides an extensive understanding of the challenges, methodologies, and advancements underpinning the low-temperature processing of GaN thin films via Plasma PVD, by offering tangible insights into its optimization and control.